Mass composition of ultra-high energy cosmic rays based on air shower universality

Zur Erlangung des akademischen Grades eines

Doktors der Naturwissenschaften

von der Fakultät für Physik des
Karlsruher Instituts für Technologie (KIT)

genehmigte

Dissertation

von

Dipl.-Phys. Detlef Maurel

aus Blaubeuren

Abstract

The subject of this thesis is the measurement of the mass composition of ultra-high energy cosmic rays. The Pierre Auger Observatory detects cosmic rays indirectly by observing the development of particle cascades created in the Earth's atmosphere. The energy deposit of these *extensive air showers* in the atmosphere is measured by fluorescence telescopes (*fluorescence detector* - FD). The density of secondary particles on ground is sampled by an array of water Cherenkov detectors (*surface detector* - SD). The FD can only measure in very dark and clear atmospheric conditions and hence has a duty cycle of only 13 % while the duty cycle of SD is nearly 100 %. In order to make unambiguous statements about the source and propagation scenarios of cosmic rays, it is essential to measure the mass of the primary particle on a single event basis. The aim of this thesis was to benefit from the large data sample collected by the SD and to develop a method for an event-based measurement of the primary mass.

The main achievements are:

- Development of a model that describes the signal response of the SD. The model is based on the concept of air shower universality. It uses the total energy E, the depth of maximum of the air shower cascade X_{max}, the depth of first interaction X_0 and the overall muon content N_μ to predict the average time-dependent signal in the water Cherenkov detectors (WCD).

- Development of a new reconstruction algorithm that uses the time traces of the WCDs to reconstruct X_{max} and N_μ. These observables are used to discriminate showers by primary mass and to distinguish hadronic and photon-induced showers.

- Measurement of the shower maximum and muon content with the SD on a single event basis. The average and fluctuations of X_{max} as well as the average and fluctuations of N_μ consistently show a trend to heavy mass composition in the energy range 10^{19}eV to 10^{20}eV. The FD measurement was confirmed and extended to higher energy.

- Correlations with astrophysical sources. The arrival directions of the highest energy events were compared with the positions of active galactic nuclei from the VCV catalog. Indications for a strong correlation of light particles and possibly an energy-dependent onset of the correlation were found.

- A search for photon primaries was started. Ultra-high energy photons are expected as by-products of the GZK effect on protons or from photo-dissociation of heavy nuclei with the cosmic microwave background. It was shown that, using N_μ, X_{max} and the shape of the lateral signal distribution, photon showers can be discriminated from proton showers.

Zusammenfassung

Thema dieser Arbeit ist die Messung der Massenzusammensetzung der ultra-hochenergetischen kosmischen Strahlung. Das Pierre-Auger-Observatorium beobachtet die ausgedehnten Luftschauer die von kosmischer Strahlung in der Atmosphäre der Erde erzeugt werden. Dabei wird die Anregung von Atomen der Luft durch Sekundärteilchen entlang der Schauerachse mit Fluoreszenzteleskopen vermessen. Die Teilchendichte auf der Erdoberfläche wird mit einem Feld aus Wasser-Cherenkov-Detektoren gemessen (*surface detector* - SD). Die Fluoreszenzmessung erfordert eine dunkle und klare Atmosphäre und kommt deshalb nur in 13 % der Gesamtmesszeit zum Einsatz. Im Gegensatz dazu misst der SD nahezu ununterbrochen. Um klare Aussagen über die Mechanismen der Produktion und Ausbreitung der kosmischen Strahlung treffen zu können ist es unerlässlich, die Masse des Primärteilchens für jedes einzelne Ereignis zu bestimmen. Ziel dieser Arbeit war, den großen Datensatz zu nutzen, der vom SD erzeugt wird und eine Methode zur Bestimmung der Primärmasse im Einzelereignis zu entwickeln.

Die wichtigsten Ergebnisse sind:

- Entwicklung eines Modells zur Beschreibung des Signals im SD. Das Modell basiert auf dem Konzept der Schauer-Universalität. Mittels der Gesamtenergie E, der Tiefe des Schauermaximums X_{max}, der Tiefe der ersten Wechselwirkung X_0 und des Myonanteils N_μ erlaubt das Modell eine Vorhersage des zeitabhängigen Signals in den Wasser-Cherenkov-Detektoren.

- Entwicklung eines neuen Algorithmus zur Rekonstruktion von X_{max} und N_μ aus Messungen der WCDs. Diese Observablen ermöglichen eine Klassifikation von Schauern nach ihrer Primärmasse.

- Messung von X_{max} und N_μ mit dem SD im Einzelereignis. Sowohl der Mittelwert als auch die Streuung von X_{max} und N_μ weisen mit ansteigender Energie konsistent einen Trend zu schwerer Massenzusammensetzung auf. Die Ergebnisse der Fluoreszenzmessung wurden bestätigt und zu höherer Energie hin erweitert.

- Korrelationen mit astrophysikalischen Quellen. Die Ankunftsrichtungen der höchstenergetischen Ereignisse wurden mit den Positionen aktiver galaktischer Kerne aus dem VCV-Katalog verglichen. Anzeichen einer starken Korrelation leichter Elemente und möglicherweise ein energieabhängiger Anstieg der Korrelation wurden gefunden.

- Eine Analyse zur Suche nach Photon-induzierten Schauern wurde begonnen. Ultrahochenergetische Photonen werden als Nebenprodukte der Streuung von Protonen oder Atomkernen an der Strahlung des kosmischen Mikrowellenhintergrunds erwartet. Es wurde gezeigt, dass mittels N_μ, X_{max} und der Form der lateralen Dichteverteilung des SD-Signals hadronische von Photon-induzierten Schauern unterschieden werden können.

Contents

1

Introduction

Cosmic rays were first discovered in 1912 by the observation that the speed of discharge of electroscopes mounted on balloons increases with the altitude. This was the first proof that, in addition to radiation stemming from radioactive isotopes in the Earth, there are energetic particles coming from outside the Earth's atmosphere, called *cosmic rays*. Soon, a dependence of the flux on the incoming direction with respect to the orientation of the geomagnetic field was found, showing that cosmic rays are charged particles. When approaching the Earth, cosmic rays interact with the atomic nuclei in the atmosphere (mainly nitrogen and oxygen). The energy of the initial particle is distributed by breaking up the nuclei. The fragments of this process in turn interact with other atoms and produce a cascade of secondary particles, called an *extensive air shower*. This cascade continues to multiply until the average energy of secondaries is so small that the ionization of air molecules starts to dominate and the cascade is absorbed. If the energy is high enough, the cascade can traverse the whole atmosphere and reach the Earth's surface. When the cascade reaches the ground it can contain more than 10^{10} particles (at 10^{19} eV) and cover an area of many km^2.

With the development of fast electronics, it became possible to detect coincidences on short time scales in detectors separated by large distances. Starting in 1938, the first air showers were detected with a setup of only two detectors separated by a few hundred meters. At this time, cosmic rays were a valuable tool for the understanding of particle physics. The primary energy of cosmic rays exceeded by far what could be achieved in particle accelerators. This lead to the discovery of the muon, the pion and the positron.

Nowadays, particle accelerators can reach equivalent center of mass energies of 10^{17}eV and offer a very controlled environment in contrast to the random flux of cosmic rays. Nevertheless, the most energetic cosmic rays measured today actually reach macroscopic scales. The energy exceeds by far what can be reached in man-made machines by several orders of magnitude. The size of an accelerator able to produce 10^{20} eV particles would be in the order of the solar orbit of Mercury. Hence, cosmic rays could be the only way to study physics at these extreme energies for the foreseeable future.

There are compelling indications that cosmic rays up to 10^{15}eV are accelerated in shock fronts of supernova explosions within our own galaxy. Above that energy, the situation becomes more obscure. While the all-particle energy spectrum is well known up to 10^{20}eV, the

astrophysical processes that can explain these extreme energies are not clear at all. There are many theories on the sources of cosmic rays and their propagation in the universe. These theories make different predictions on the dependence of the chemical composition on primary energy. Some theories are strongly disfavored because the predicted flux of ultra-high energy photons and neutrinos would be too large. To discriminate and possibly falsify theories, a measurement of the primary mass of each cosmic ray event is essential.

The flux of cosmic rays falls extremely rapidly with increasing energy. Below 10^{14}eV, the flux is so large that detectors with sizes in the order of $1\,\mathrm{m}^2$ can quickly gather large data samples (e.g. using calorimeters and tracking detectors). The detectors need to be placed above the bulk of the atmosphere (on balloons or satellites) because the primary energy is too small for the shower to reach the Earth's surface. These detectors can easily measure the mass, charge and energy as well as the arrival direction of a cosmic ray. Above 10^{14}eV, the flux becomes so low that direct measurements in a reasonable time period become impossible. One needs to resort to the indirect measurement of extensive air showers on ground. Several experiments have been built for this purpose. They measure the emission of fluorescence light, Cherenkov radiation and electromagnetic radiation in the MHz up to the GHz range and sample the distribution of secondary particles on ground.

The Pierre Auger Observatory is the largest ground-based cosmic ray detector. It covers an area of $3000\,\mathrm{km}^2$. The fluorescence detector (FD) uses the Earth's atmosphere as an electromagnetic calorimeter. It measures the emission of ultraviolet light along the incoming direction of the particle. Hence, it can observe the whole longitudinal development of the particle cascade. The density of secondary particles on ground is sampled by an array of water Cherenkov detectors (WCD), called the surface detector (SD).

The longitudinal development measured by the FD, in particular the depth of shower maximum, is correlated to the primary mass. However, the FD can only be operated in dark, moonless nights with clear atmospheric conditions. As a result, the number of events collected by the FD is about ten times smaller than by the SD. In particular, the FD data sample in the most interesting region above 10^{19}eV becomes very small.

The aim of this work is the measurement of the mass composition of cosmic rays with energies above 10^{19}eV. To fully benefit from the large data sample taken by the SD, the analysis is designed to be independent of the FD. The thesis is structured as follows. In Chapter 2, a brief introduction to the state of the art of cosmic ray research is given. Chapter 3 describes the detectors of the Pierre Auger Observatory. Because the SD is the main tool for this analysis, it is described in more detail. In Chapter 4, based on the concept of shower universality, a model for the description of the signal in the SD is developed. For the reconstruction of SD events, a completely new algorithm is shown. It uses the time distribution of secondary particles measured by the SD to reconstruct mass-dependent parameters of the primary cosmic ray. The details are presented in Chapter 5. The reconstruction makes heavy use of shower universality. The models are validated and the accuracy is tested using simulated (Chapter 6) and real events (Chapter 7). The reconstruction is applied to data in Chapter 8. Using several observables, the mass composition of ultra-high energy cosmic rays (UHECR) at the highest energies is studied. Chapter 9 summarizes the results and gives an outlook on possible further improvements of the method presented in this thesis.

Cosmic rays and extensive air showers

2.1 Cosmic rays

Cosmic rays are high-energy particles that reach the earth from extraterrestrial space. The earth is subject to a continuous, mainly isotropic flux of charged and neutral particles with energies starting at a few MeV and reaching more than 10^{20}eV. These are the highest particle energies ever measured. The equivalent center of mass energy is a factor 100 larger than what can be achieved at particle accelerators like the LHC. Since their discovery in 1912, cosmic rays are a field of intense research. At low and intermediate energies, cosmic rays are quite well understood. Their chemical composition is well known and there are suitable models to describe the production and propagation through space. At the highest energies, the situations becomes more obscure. Because the mass measurement becomes increasingly difficult, it is not possible to discriminate different source and propagation scenarios. The nature of the sources and the propagation processes is mainly unknown (although there are many promising theories).

This section summarizes the current status of ultra-high energy cosmic ray research. It is based on the extensive review articles [1] and [2] and references therein.

The all-particle spectrum of cosmic rays is shown in Fig. 2.1. The spectrum is rather featureless with a few exceptions. The flux follows a power law $dN/dE \propto E^{\gamma}$ over the entire energy range. Between 10^{15}eV and 10^{16}eV, the spectral index changes and a steepening (called the *knee*) of the spectrum is observed. A second yet less pronounced *knee* might occur around 4×10^{17}eV. Between 10^{18}eV and 10^{19}eV, the spectrum flattens. This feature is called the *ankle*. At 5.5×10^{19}eV, a sharp cutoff is observed [3].

The flux ranges from several 1000 particles per square meter and second at GeV energies to less than one particle per square kilometer and century at 10^{20}eV. Up to 10^{14}eV a direct detection with small-scale balloon- or satellite-borne detectors is possible due to the intense flux. The mass, charge and energy of individual isotopes can be measured directly. At higher energies, the flux becomes so low that direct measurements on a reasonable time scale are impossible. The only option is the indirect measurement through the detection of extensive showers of secondary particles that are created in the atmosphere. This technique employs
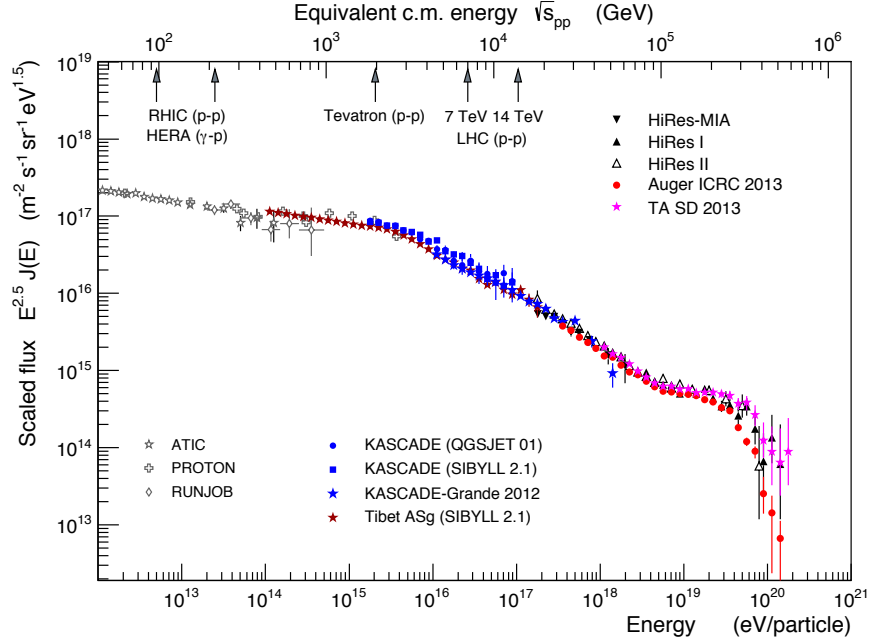
Figure 2.1: Combined energy spectrum of cosmic rays. The results of balloon, space and ground-based experiments are shown. A direct detection of cosmic rays is possible up to 10^{14}eV. At higher energies, the measurement is done with ground arrays and fluorescence detectors. The spectrum follows a power law $dN/dE \propto E^\gamma$. The flux is scaled with $E^{2.5}$ to emphasize the change of the spectral index γ below 10^{16}eV (the *knee*), at 10^{19}eV (the *ankle*) and the suppression at 6×10^{19}eV. Equivalent center of mass energies are shown to compare with particle accelerators. From [2].

the atmosphere as a calorimeter, which collects the energy deposit of air showers. In this picture, the calorimeter is read out along the shower track by fluorescence detectors and at a single level by ground detectors (the latter corresponds to reading out the calorimeter only once after several interaction lengths). Mass and charge of the primary cosmic ray can not be measured directly and need to be estimated from the collective distribution of secondary particles. An overview of extensive air showers is given in Section 2.2.

The properties of air showers need to be interpreted based on the predictions of simulation algorithms. Hence, the results are very susceptible to uncertainties in the modeling of hadronic interactions at the highest energies. The lower energy regime is well understood and is described within perturbative QED. The predictions can be validated with particle accelerator data. For the first few interactions in an air shower, the high-energy regime becomes important. The predictions are difficult, in particular because hadronic multiparticle production can not be calculated within the framework of QCD. Instead, one needs to resort to phenomenological models that are tuned to accelerator data and extrapolate the measurements up to air shower energies. For the case of the LHC, this data is available up to a corresponding rest frame energy of $\approx 10^{17}$eV. Different assumptions in interaction models (e.g. QGSJet II-03, EPOS 1.99) lead to systematic uncertainties above the energy range of the LHC. The forward region of accelerator data is of special importance because the particle
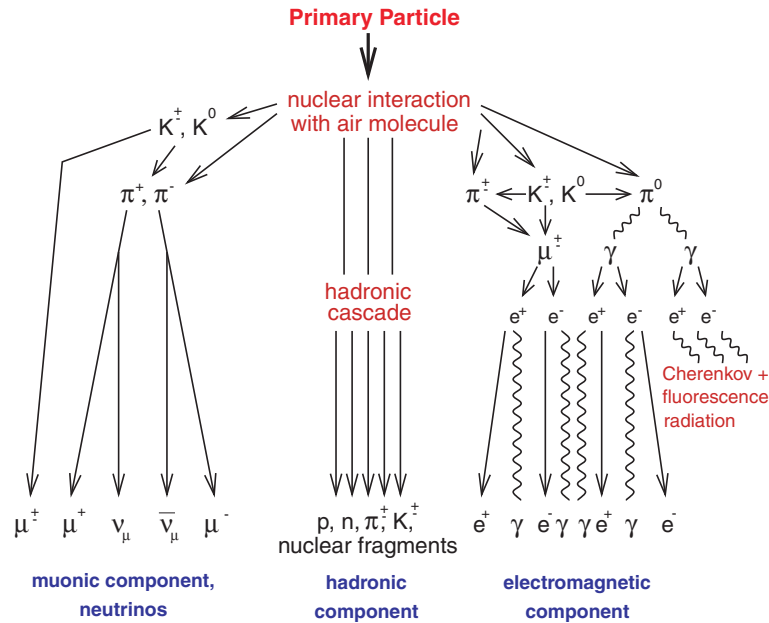
Figure 2.2: Schematic view of an extensive air shower. The shower is initiated by the fragmentation of nuclei in the Earth's atmosphere. The primary energy is transformed to create charged and neutral mesons (usually pions and kaons). These mesons decay or re-interact to produce a cascade of muons as well as electrons, positrons and photons. From [4].

production in an air shower is strongly boosted forward in the direction of the shower axis. For an accurate description of this high rapidity region, additional detectors have been built at the LHC to measure the forward region of particle production (e.g. CASTOR, LHCf).

2.2 Extensive air showers

When a high-energy particle enters the Earth's atmosphere, it interacts with an air nucleus (in most cases nitrogen or oxygen). The kinetic energy is transformed to create new particles, called *secondaries*. Each secondary particle in turn interacts with other particles. A particle cascade (an *extensive air shower*) is formed. At the highest energies, a shower originating from a single subatomic particle extends over an area of many km^2. The number of secondary particles at the maximum of the cascade is in the order of 10^{10}. A schematic view of the particle cascade is shown in Fig. 2.2.

The particles in an extensive air shower can be regarded as three sub-components: The muonic, the electromagnetic and the hadronic component. In most interactions with air nuclei, charged and neutral pions ($\pi^{\pm}, \pi^0$) are produced. Less frequently, heavier mesons (e.g. $K^{\pm}, K^0$), protons, neutrons and other heavy baryons are created. Neglecting the small contribution of heavier mesons and baryons, 2/3 of the energy is transferred to charged pions and 1/3 to neutral pions.

Neutral pions have a very short mean life time of 10^{-16} s. A π^0 usually decays into two photons before it can re-interact with an air nucleus (the distance it travels before it decays is $c\tau = 25$ nm). Charged pions interact before decaying ($c\tau = 7.8$ m) until the pion energy is < 30 GeV (or equivalently, until the decay time in the rest frame of the pion becomes comparable to the interaction length). The decay modes of charged pions are

$$\pi^+ \to \mu^+ + \nu_\mu \quad \text{and} \quad \pi^- \to \mu^- + \bar{\nu}_\mu \,.$$

This is the *muonic cascade*.

Interactions of neutrinos with air nuclei are extremely rare due to the small interaction cross section. Hence, they are not detected directly (although neutrinos can induce extensive air showers in very rare cases). Muons are only weakly absorbed by the atmosphere and undergo very few interactions. The transverse momentum w.r.t. the shower axis gained at production is essentially conserved. Because muons are produced very high in the atmosphere, they can reach the ground level at large distances from the shower core.

Neutral pions decay to two photons:

$$\pi^0 \to \gamma\gamma \,.$$

In most cases, photons convert to e^+e^--pairs in the Coulomb field of air nuclei. The electrons and positrons in turn produce bremsstrahlung photons. The ensemble of electrons, positrons and photons is called the *electromagnetic cascade*.

The growth of the cascade continues until the energy loss from bremsstrahlung equals the loss due to ionization of air molecules. This happens at the *critical energy* $E_c = 86$ MeV. The atmospheric depth of this point is called the *depth of shower maximum* $X_{\max}$. After the maximum, the cascade is attenuated exponentially through ionization.

Although Monte Carlo simulation codes are needed to understand the details of the development of the particle cascade, some general features of purely electromagnetic showers can already be described in a very simple analytical model (known as the *Heitler model* [5]). The basic assumption is that particles move freely for one interaction length until an interaction happens. Each time, two new particles are produced. The multiplication continues until the critical energy is reached. Hence, the number of particles growth exponentially with the atmospheric depth X: $N(X) = 2^{X/\lambda}$, where λ is the mean free path between subsequent interactions. At the maximum of the cascade development, there are $N_{\max} = E_0/E_c$ secondary particles where E_0 is the energy of the primary particle. The depth of maximum is given by $X_{\max} = \lambda \log_2(E_0/E_c)$.

In this very simple model, the details of the cascade are certainly not described accurately. Nevertheless, it shows that the number of particles at maximum is proportional to the primary energy and that the depth of maximum increases logarithmically with energy. This is also the result of detailed simulations (for the latter, see Fig. 2.9).

With more detailed considerations, it can be shown that many features of the electromagnetic cascade (e.g. energy spectrum and angular distribution of secondaries) can be described in terms of the primary energy and the *shower age s*, where

$$s = \frac{3X}{X + 2X_{\max}} \,. \tag{2.1}$$

The shower age is defined such that $s = 0$ at the boundary of the atmosphere and $s = 1$ at shower maximum. The number of particles $N(X)$ at a given depth X is described by a *Gaisser-Hillas* profile

$$N(X) = N_{\max} \left(\frac{X - X_0}{X_{\max} - X_0} \right)^{\frac{X_{\max} - X}{\Lambda}} \exp \left(\frac{X_{\max} - X}{\Lambda} \right) .$$

The lateral shape w.r.t. the shower axis of the cascade is given by

$$\frac{dN_e}{r\, dr\, d\phi} = C(s) N_e(X) \left(\frac{r}{r_1} \right)^{s-2} \left(1 + \frac{r}{r_1} \right)^{s-4.5} ,$$

where $C(s)$ is a normalization constant depending on the shower age and ϕ denotes the polar angle in the plane perpendicular to the shower axis.

Showers initiated by protons or atomic nuclei (*hadronic showers*) can be described by a similar approach. The main difference is that, in each hadronic interaction with air nuclei, *many* secondaries (usually pions) are produced. The number of secondary mesons (*multiplicity*) is model-dependent. For n_{tot} pions, $n_{\text{ch}} = \frac{2}{3} n_{\text{tot}}$ charged pions are created. Charged pions usually decay to muons. The number of muons after n generations reads as

$$N_\mu = (n_{\text{ch}})^n = \left(\frac{E_0}{E_{\text{dec}}} \right)^\alpha ,$$

where E_{dec} is the critical energy where decay is preferred over re-interaction and α depends on the hadronic interaction model.

The energy in the hadronic and electromagnetic cascade is given by

$$E_{\text{had}} = \left(\frac{2}{3} \right)^n E_0 \qquad E_{\text{em}} = E_0 - E_{\text{had}} .$$

Clearly, the fraction of energy transferred to the electromagnetic cascade increases with the number of generations, and hence with the primary energy.

The results of these simple considerations are confirmed by detailed MC simulations. The properties of showers initiated by heavy nuclei can be derived from proton showers using the superposition model. The model states that a heavy nucleus of mass A and energy E can be viewed as a superposition of A independent nucleons with energy $E_h = E/A$. It is justified because the kinetic energy per nucleon is much larger than the typical nuclear binding energy. One obtains that the number of particles $N_{\max}^A$ at the shower maximum is independent of the primary mass,

$$N_{\max}^A \approx A \cdot \frac{E_h}{E_c} = \frac{E_0}{E_c} = N_{\max} ,$$

the depth of maximum $X_{\max}^A$ is inversely proportional to the mass,

$$X_{\max}^A \approx X_{\max} \cdot \frac{E_0}{A} ,$$

and the number of muons N_μ^A is proportional to the mass,

$$N_\mu^A \approx A \cdot \left(\frac{E_0/A}{E_{\text{dec}}} \right)^\alpha = A^{1-\alpha} \cdot N_\mu .$$
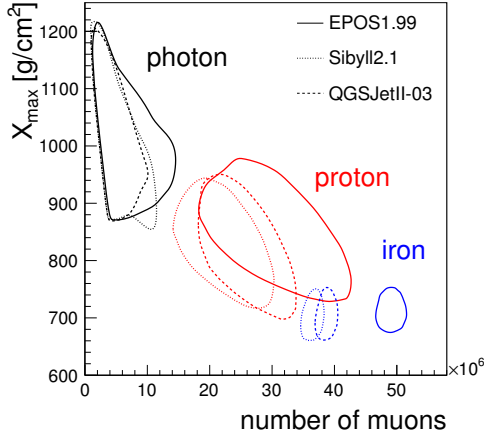
Figure 2.3: Model predictions of X_{max} and the number of muons at ground level for $E = 10^{19}$eV. The contour lines indicate the region that contains 90 % of the simulated showers. Photon showers develop mainly in the electromagnetic cascade due to the small cross section for photo-nuclear interaction. Hence, the number of muons is smaller and the shower maximum is deeper. Furthermore, photon showers are less dependent on systematic uncertainties of hadronic interaction models, as opposed to proton- and iron-induced showers. From [6].

The cross section for interaction of photons and atomic nuclei is comparatively small. Hence, the number of muons in photon-induced showers is small, the development of the cascade is slower and the depth of maximum is larger than for hadronic showers. The results of detailed simulations are shown in Figs. 2.3, 8.1 and 8.19.

The Pierre Auger Observatory has shown that the amount of muons in air showers is larger than the model predictions (see e.g. [7, 8, 9, 10]). This is true even with the most extreme assumptions. The size of the discrepancy depends on which interaction model is used. This is due to different assumptions when accelerator data is extrapolated up to the highest energies. The predicted number of muons can be increased by changing the properties of hadronic interactions, e.g. multiplicity, inelasticity and cross section. The effect on X_{max} and N_{μ} of changing these parameters is shown in Fig. 2.4. The number of muons also depends on the baryon multiplicity and on the type of secondary mesons. For example, the amount of energy transferred to the muonic cascade can be increased if the ratio of ρ mesons to pions is increased. While π^0 contribute to the electromagnetic cascade, ρ mesons decay to $\pi^+\pi^-$ pairs that contribute to the muonic cascade.

The fact that the average properties of the cascade can be described in terms of energy and shower age only is called *shower universality*. There is no direct dependence on the primary mass or the zenith angle. This is a very remarkable result. Despite the vast number of interactions in an air shower, its overall shape can be described very well with very few measurable quantities. So far, this holds only for purely electromagnetic showers. In Chapter 4 it is shown that the concept can be extended to hadronic showers as well by introducing one additional parameter, the muon scale N_{μ}. The result is a model that describes showers initiated by protons, nuclei up to iron as well as photon showers using only three parameters: E, X_{max} and N_{μ}.

In this thesis, two different quantities are denoted with the same symbol, N_{μ}. For the discussion of the particle cascade, it denotes the number of individual muons that reach the Earth's surface. In the following chapters (starting from Chapter 4), N_{μ} is the amount of muons relative to the prediction from proton QGSJet II-03 simulations. This is done for consistency with previous publications. Although this is not very convenient, there is little room for confusion because the first definition is not used anywhere except in this section.
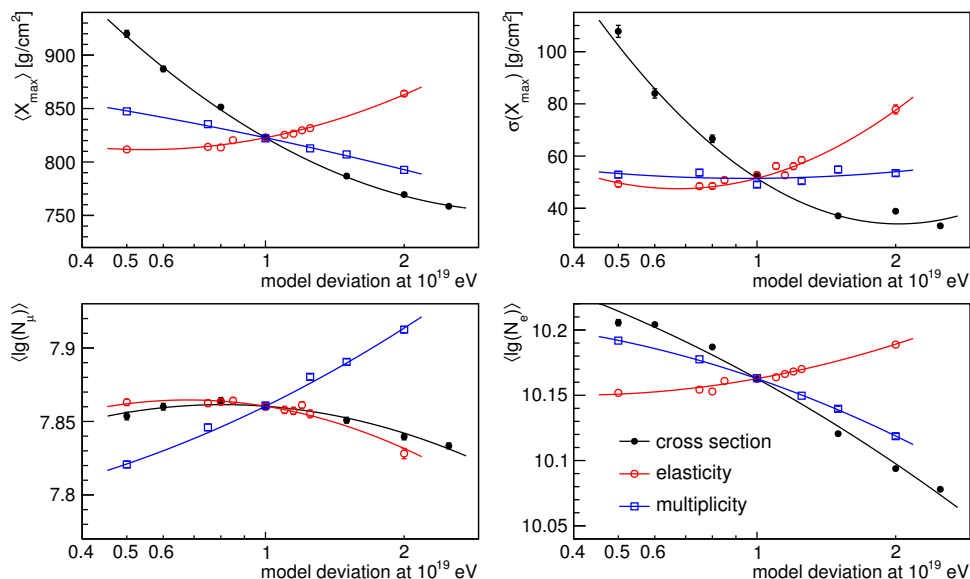
Figure 2.4: Influence of the properties of hadronic interactions on air shower observables. For example, the mean and fluctuations of X_{max} (top) depend strongly on the interaction cross section. The number of muons on ground (bottom) is strongly correlated to the multiplicity of hadronic multiparticle production. From [6].

2.3 Astrophysical scenarios

At the lowest energies starting in the MeV range, cosmic rays are produced within the solar system. The flux is strongly dominated by proton and helium, although all isotopes of the periodic table up to uranium have been measured. At higher energies cosmic rays are of galactic or extragalactic origin.

Supernova explosions are very good candidates for the acceleration of cosmic rays up to the knee region. Particles from the interstellar medium gain energy by repeated reflection from the front and back surfaces of the expanding shell of the supernova remnant. This happens by a first order Fermi acceleration process. The energy gain is proportional to $\beta = v/c$ where v is the velocity of the shell. The shell forms a shock front because its velocity is much larger than the velocity of sound in the interstellar medium. At each encounter with the boundary of the shock, a particle can leave the region. With increasing number of reflections and therefore with increasing energy, a particle is more probable to leave the acceleration site. This leads naturally to a steeply falling power law distribution of the energy. The energy attainable in this process is limited by the lifetime of the shell ($\approx 10^5$ years) and by its size. Common supernova remnants can provide energies up to 10^{15}eV. According to some recent calculations [11], if the matter density is high enough and the amplification of the magnetic field in the shock by cosmic rays is taken into account, even maximum energies up to 10^{17}eV are possible.
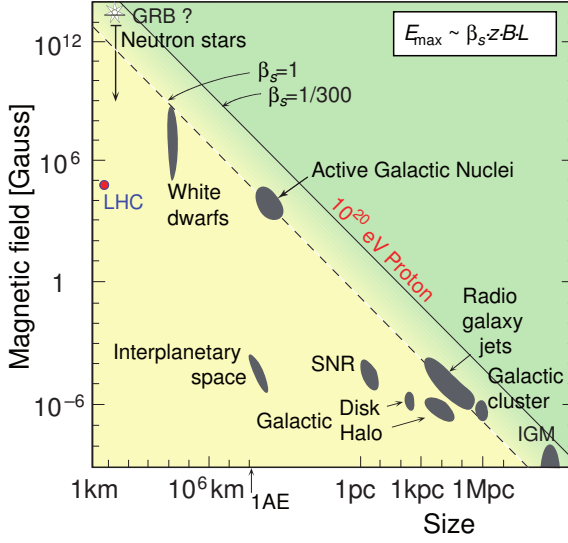
Figure 2.5: Hillas plot [12] of possible sources for the acceleration of UHECR. The diagonal lines show the requirements on the magnetic field strength and the size of the source to confine particles long enough in the source region. $\beta_s = v_s/c$ is the velocity of the shock front. Objects below the solid (dashed) line are not able to accelerate protons (iron nuclei) up to 10^{20}eV. From [13].

Once a particle leaves the acceleration site, it is deflected by the galactic magnetic field. The radius of the circular motion of a charged particle with mass m and charge q in a magnetic field (*Larmor radius*) is given by

$$r_L = \frac{mv_\perp}{|q|B},$$

where B is the magnetic flux density. For protons in the galactic magnetic field this reads as

$$r_L = 1.08\text{pc}\frac{E/\text{PeV}}{Z \cdot B/\mu\text{G}}.$$

With increasing rigidity ($\propto E/Z$), the Larmor radius exceeds the size of the galaxy and the particles can no longer be confined (*leakage*). It can be shown that a few supernova explosions per century in the galaxy are enough to compensate for the leakage and account for the measured flux. The KASCADE experiment has measured the energy spectrum for several mass groups and has shown that the position of the knee might be correlated with the primary mass. Hence, the knee can be understood as a rigidity-dependent leakage from the galaxy or a rigidity-dependent maximum energy at the acceleration sites.

Above the knee, the sources of cosmic rays are presumably located outside of our galaxy. The Larmor radius becomes larger than the thickness of the galaxy. Hence, the apparent isotropic distribution of arrival directions can not be explained with galactic sources only.

The sources of charged particles are divided in two classes of models. The first are *bottom-up* scenarios where charged particles are accelerated continuously from rest within a small region of space. Possible sources of cosmic rays above 10^{19}eV are given by the *Hillas plot* (Fig. 2.5). The maximum energy E_max a particle can attain in the source is given by its charge, the size of the source and the magnetic field strength at the source,

$$E_\text{max} \simeq 10^{18}\text{eV} \cdot Z \left(\frac{R}{\text{kpc}}\right)\left(\frac{B}{\mu\text{G}}\right).$$
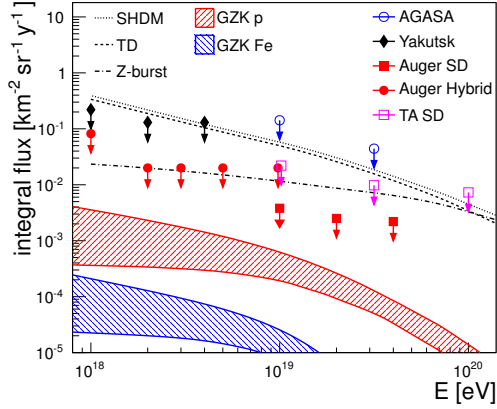
Figure 2.6: Limits on the photon flux derived by different experiments. The strongest limits are set by Auger calculated from the distribution of X_{max} and the lateral shape of the signal on ground [19]. Top-down models are strongly disfavored (e.g. decay of super-heavy dark matter particles or topological defects). The shaded areas indicate the prediction for the flux of GZK photons. From [6].

This is a necessary requirement to confine charged particles long enough during the acceleration process. In practice, the maximum energy is smaller when radiative losses, the efficiency of the acceleration process and interactions within the source are taken into account.

Active galactic nuclei (AGN) and gamma-ray bursts are popular source candidates. The jets produced by AGNs extend over distances of 1 pc and have magnetic fields of several Gauss. The cores of AGNs are much smaller but have magnetic fields over several thousand Gauss. In principle, AGNs are capable of accelerating protons and heavy nuclei up to 10^{20}eV in optimal conditions.

The second class of sources are *top-down* scenarios. In these models, cosmic rays are produced in decays of exotic super-heavy particles (at least 10^{23}eV to 10^{24}eV). Candidates are X bosons predicted by grand unified theories (GUT) [14], relic particles from the inflationary epoch in the expansion of the universe or topological defects [15]. While decaying to standard model particles, a large number of ultra-high energy photons and neutrinos are produced. So far, no ultra-high energy photons have been detected. Although most air shower experiments are not optimized for photon searches, they were able to derive limits on the photon flux (Fig. 2.6). The strongest limits are set by the Pierre Auger Observatory [16, 17, 18]. Top-down models are strongly disfavored. However the sensitivity is not sufficient to exclude models that predict photons created by the GZK effect.

The suppression of the flux above 5.5×10^{19}eV can be explained by the interaction of charged particles with photons from the cosmic ray microwave background (CMB) and subsequent energy loss. One possibility is the excitation of protons by CMB photons with subsequent emission of pions (GZK effect [20, 21]),

$$p + \gamma_{CMB} \rightarrow \Delta^+ \rightarrow p + \pi^0 \rightarrow p + \gamma\gamma$$

or

$$p + \gamma_{CMB} \rightarrow \Delta^+ \rightarrow n + \pi^+ \rightarrow n + \mu^+ + \nu_\mu$$

where $m(\Delta^+) = 1232$ MeV. The conversion to protons is preferred energetically because the final state products are lighter. Taking into account that part of the kinetic energy is transferred to the pion, the energy of the onset of suppression is 5×10^{19}eV. Similarly, nuclei are
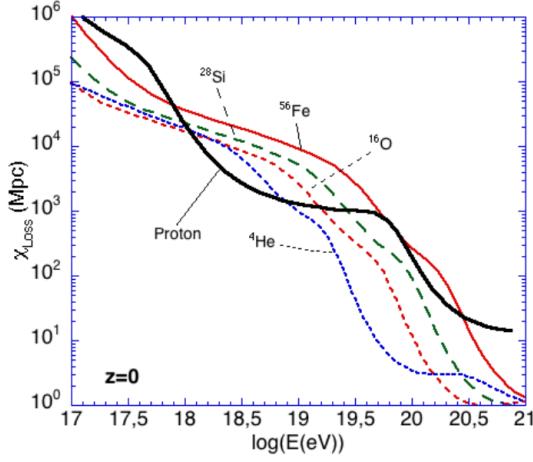
11

Figure 2.7: The energy loss length χ_{loss} for cosmic rays in the cosmic microwave background (CMB) for elements from proton to iron. Cosmic rays lose energy in inelastic interactions with CMB photons. The first dip is caused by e^+e^- pair production, the second by the GZK suppression. The energy loss length is largest for iron due to the high binding energy per nucleon. From [22].

excited (giant dipole resonance) and broken up to lighter fragments (*photo-disintegration*). The GZK effect implies a maximum distance that can be traversed by cosmic rays without interaction and subsequent energy loss. The energy loss length for particles above 10^{19}eV ranges from 100 Mpc to 1 Gpc (Fig. 2.7).

The ankle could be caused by a transition from galactic to extragalactic sources. In this scenario, the cutoff is caused by a rigidity-dependent maximum energy at the accelerators. Similar to the knee, this would naturally explain the transition from light to heavy composition. In an alternative scenario, the ankle is due to interaction with the CMB and subsequent production of e^+e^- pairs, the cutoff is caused by the GZK effect and photo-dissociation of heavy nuclei. Incidentally, the expected energy spectra at the cutoff are very similar for proton and iron although the energy loss processes are completely different. A more exotic scenario is a pure proton composition and drastic changes of particle physics at the highest energies. By changing the cross sections and multiplicity of hadronic interactions, X_{max} and the number of muons on ground can be changed in such a way to obtain an apparent increase of the primary mass (Fig. 2.4).

The mass composition is not well known above 10^{15}eV. Without a precise knowledge of the mass composition (preferably on a single event basis) no firm conclusions on possible source and propagation scenarios can be drawn. A comparison of two possible scenarios for the energy range of Auger is shown in Fig. 2.8.

The best estimator for the primary mass is the depth of shower maximum X_{max}. The Auger measurement along with the model predictions is shown in Fig. 2.9. The mean and fluctuations of X_{max} tend towards lighter composition up to 3×10^{18}eV. Above that and up to 4×10^{19}eV there is a clear trend towards heavier composition, although the model systematics become important. The X_{max} measurement can be visualized in the so-called *umbrella plots* Fig. 2.10. The trend to heavier composition is apparent. The energy evolution is the same for all models. However, it is not possible to exclude any models due to the large systematic uncertainties.
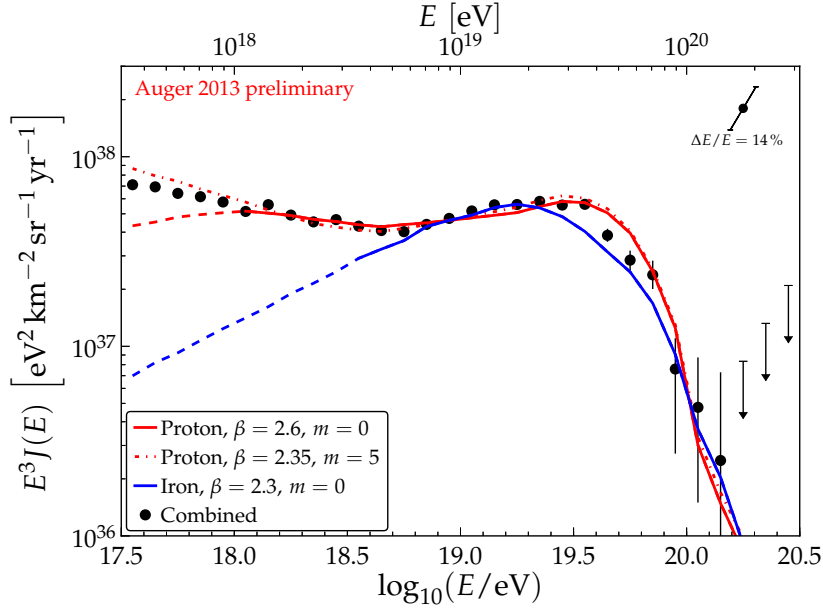
Figure 2.8: Ambiguity in the spectrum at the highest energies. Without a direct measurement of the mass, it is impossible to distinguish between different source scenarios. **Red:** Proton dominated flux with e^+e^- pair production and GZK suppression, **Blue:** Iron dominated flux - the ankle is due to the transition to extragalactic sources. From [23].

In addition to the X_{max} measurement, there are several mass-dependent observables that are estimated from the secondary particles on ground. The ratio of the number of muons to electromagnetic particles is correlated to the primary mass and to the properties of hadronic interactions (Section 2.2). This ratio can be estimated from the slope of the lateral density of secondary particles and from the time structure of the shower front [24, 25, 26, 27]. The results from all these observables is compatible with the X_{max} measurement, the average mass composition tending from light towards heavier composition on average.

There are indications for a correlation of the highest energy events ($E > 57 \times 10^{18}$eV) with the nearby (distance < 75 Mpc) matter distribution [28], although the significance is only $\approx 3\sigma$ [29, 30]. The correlation suggests a light mass composition. This is not in direct contradiction to the X_{max} measurement (Fig. 2.9), because although the X_{max} data suggests a trend to heavier masses, it allows for 10 % to 15 % protons [31].

The deflection in magnetic fields depends on the ratio of charge to mass. Therefore, light particles are expected to correlate stronger to their source (if point sources exist). So far, the primary mass was not taken into account in the correlation study. In Section 8.5 the SD data is classified as light or heavy using N_μ and X_{max}. The correlation study is repeated for these two classes.
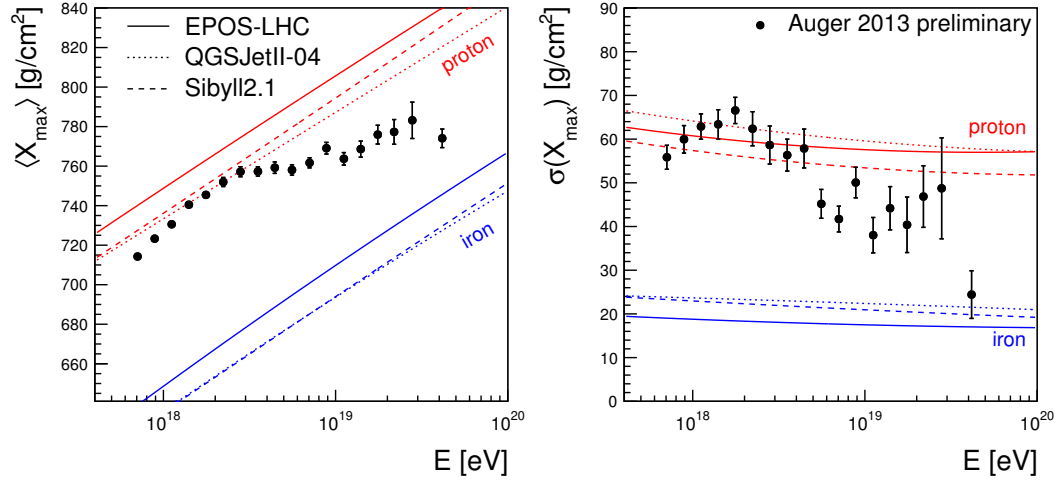
Figure 2.9: The mean (left) and fluctuations (right) of the shower maximum compared to the model predictions. Above 4×10^{18}eV, a clear trend to heavier composition is apparent. From [32, 33].
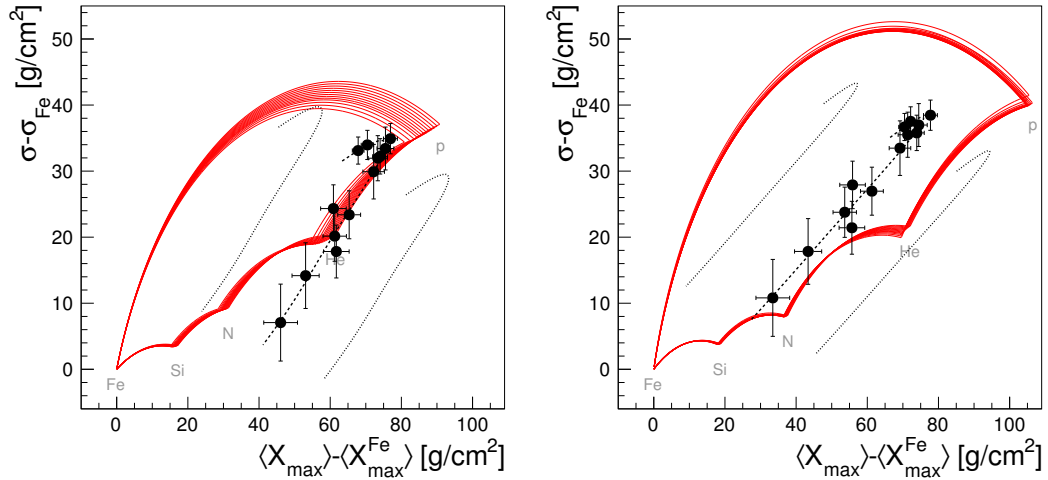
Figure 2.10: Comparison of X_{max} data with the model predictions for QGSJet II-03 (left) and EPOS 1.99 (right). The energy of the data points increases from top to bottom. The area enclosed by the red contour contains all possible transitions from light to heavy composition including elements between proton and iron. If only proton and iron are present in the data, X_{max} follows the upper contour. The lower contour shows how X_{max} evolves if there is a continuous increase of the mass from proton to iron. Both models are compatible with the data if the systematic uncertainties from the model predictions are taken into account (indicated by the gray lines). From [6, 34, 35].

3

The Pierre Auger Observatory

It is known since a long time that the cosmic ray energy spectrum extends above 10^{20}eV [36]. The Pierre Auger Observatory was built to measure extensive air showers created in the Earth's atmosphere by ultra-high energy cosmic rays. It has been designed to measure the energy spectrum, the distribution of arrival directions and the chemical composition above 10^{17}eV [37]. Considering the size of the observatory and the steeply falling energy spectrum, the energy range 10^{17}eV to 10^{20}eV can be measured with high statistical significance. The density of secondary particles on ground is sampled by an array of water Cherenkov tanks that are placed on a triangular grid at a distance of 1.5 km, called the *surface detector* (SD). The energy deposit in the atmosphere is measured by several fluorescence telescopes, called the *fluorescence detector* (FD). This *hybrid* design allows to measure the lateral particle distribution as well as the longitudinal development of an air shower. The *full efficiency threshold* denotes the energy above which the detector is triggered by every shower regardless of its orientation w.r.t. the observatory. The corresponding energy of full efficiency is $10^{18.5}$eV for the standard SD and $10^{19.0}$eV for the FD. In certain conditions, much lower energies can be measured, e.g. when the impact point is close to a fluorescence telescope or to a SD station. The threshold denotes the energy above which the efficiency is independent of the geometry w.r.t. the detector.

The layout of the observatory is shown in Fig. 3.1. An air shower that was recorded in coincidence by the SD and all four fluorescence detectors is shown in Fig. 3.2.

In the following sections, the parts of the observatory that are of particular relevance for this thesis are presented in detail. Future enhancements that are still in the design or commissioning phase are discussed together with possible benefit for the method presented in this thesis.

3.1 Surface Detector

3.1.1 Detector description

The surface detector comprises more than 1600 water Cherenkov detectors (referred to as *tanks*) distributed uniformly on a triangular grid with a spacing of 1.5 km over an area of more than 3000 km^2 (Fig. 3.1) [40]. Each tank contains 12 000 l of highly purified water. The
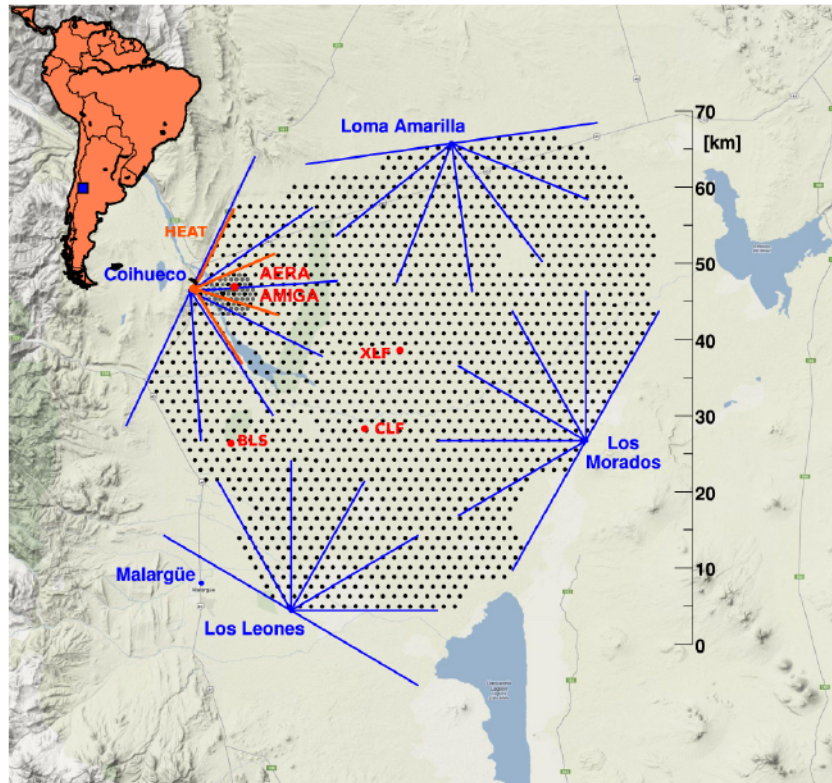
Figure 3.1: The Pierre Auger Observatory is located at the eastern border of the Andes mountains in the vicinity of the town of Malargüe (the location of Auger is indicated by the blue square on the map of South America). It covers an area of $3000\,km^2$ that is equipped with an array of water Cherenkov detectors. The volume above the ground is overlooked by 27 fluorescence telescopes. Their field of view is indicated by the blue lines. The atmosphere is monitored by measuring the transmission of the light produced by UV lasers (CLF, XLF). The longitudinal development of lower energy showers (above 10^{17}eV) is measured by HEAT (high-elevation Auger telescopes). Their energy deposit on ground is measured by a part of the array with denser detector spacing (AMIGA). Adapted from [38].

water is contained in a reflective shell, which in turn is contained by a solid plastic shell for mechanical stability and screening of light from the outside. The electronic equipment of the detector is powered by a solar panel and a battery, which makes the system autonomous. The schematic structure of the tank is shown in Fig. 3.3.

As the secondary particles travel through the detector, they polarize the water molecules. The particle speed exceeds the speed of light in water. This leads to polarization of the water molecules and subsequent emission of light along the track (*Cherenkov effect*). The amount of light is proportional to the energy and the track length. Electromagnetic particles are usually completely absorbed inside the tank. Muons traverse the whole tank regardless of the incoming direction. The track length, and hence the energy deposit depends on the zenith angle (for details, see Fig. 4.4). Almost all the light is reflected diffusely on the inner Tyvek coating. After a few reflections, the light in the tank is completely isotropized. The
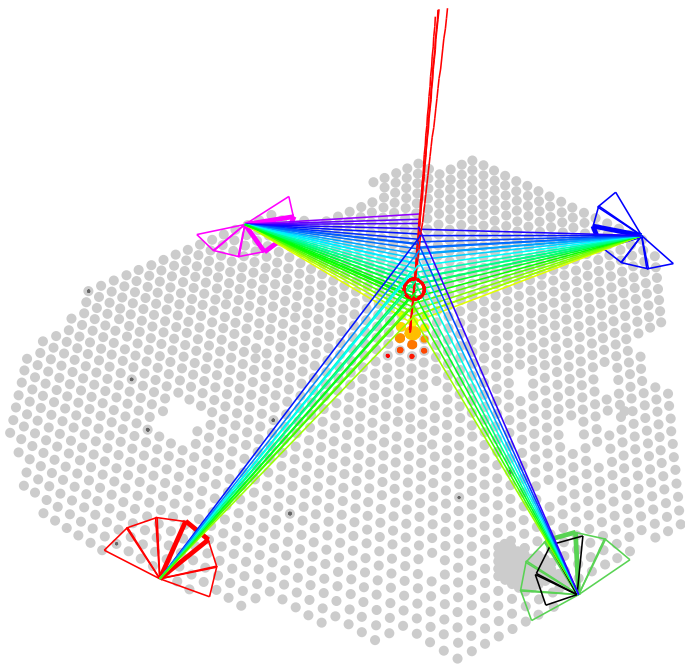
Figure 3.2: Example of an air shower recorded in coincidence by the surface detector and all four fluorescence detectors. The primary energy is reconstructed to 5×10^{19}eV. The path of the fluorescence light from the shower axis to the telescopes is indicated by the colored lines. The particle density on ground is indicated by the size of the colored surface detectors. From [39].

time to create the light is in the order of a few nanoseconds. The light is collected by three photomultiplier tubes mounted at the top of the tank looking downwards into the water. The light collection can be characterized by an exponential with a decay constant of ≈ 65 ns [41]. The signal of the photomultiplier is sampled at 40 MHz and a dynamic range of 10 bit. Due to the steeply falling lateral distribution of the particle density a large dynamic range is necessary. The dynamic range is extended by a factor 32 by sampling the signal at the next to last (*low gain*) as well as the last dynode (*high gain*) of the PMT. This is done to cover both the region close to the core where several thousands of particles are recorded in a very short time period as well as regions far from the core that are hit by only a few particles.

3.1.2 SD Calibration

Each water tank has a background rate of ≈ 3000 Hz from atmospheric muons and low energy extensive air showers. This background is a nuisance that needs to be minimized at the same time as it is essential for the calibration of the detector [42]. The relative unit for the tank signal is given by the average signal that is produced by a vertically centered incident muon that traverses the whole water volume. In the detector simulation, this average is calculated by injecting a large number of 1 GeV muons exactly in the center of the tank and propagating them downwards vertically. The calibration for the tanks in the field is derived from a test detector equipped with two additional scintillators placed on top and below the tank. This setup allows to select particles within a narrow angular window around the vertical direction. Vertical through-going muons are selected by requiring coincident signals in both scintillators. For the tanks in the field, the selection of vertical muons is not possible. The average signal is shifted to higher values (Fig. 3.4) because the signal produced by a muon is proportional to its track length in the water.
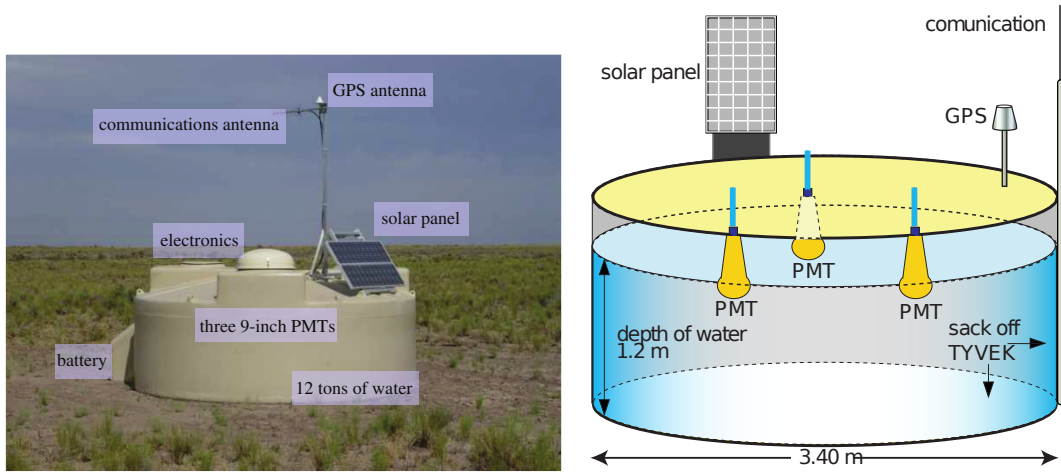
Figure 3.3: A water Cherenkov detector in the field and the schematic structure (see text for a detailed description of the detector components). From [40].
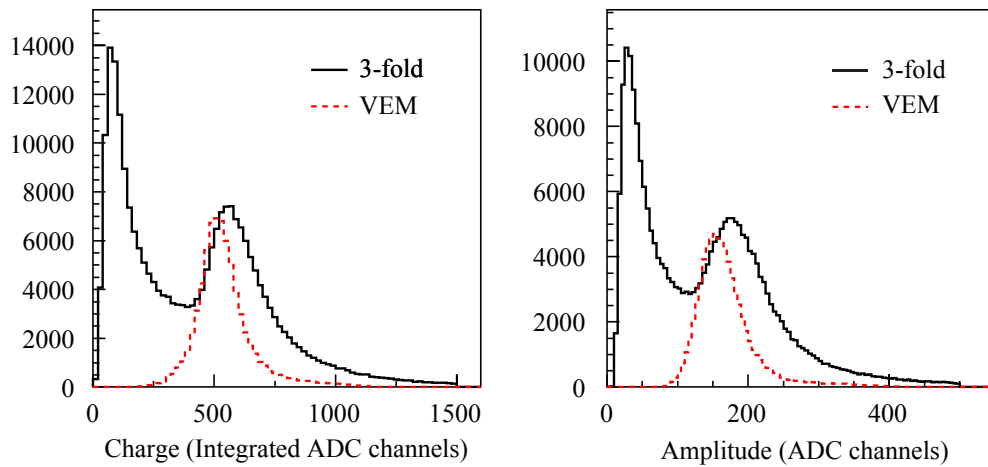
Figure 3.4: Measurement of the charge and pulse height distribution in the water Cherenkov tanks. The black line is produced by all particles created in the atmosphere. The first peak stems from the convolution of the trigger and the spectrum of low-energy particles. Using additional scintillators on top and below the tank, vertical muons that traverse the whole water volume are selected to measure the true VEM. The peak positions are shifted due to the different average track lengths of vertical and inclined muons. From [42].

3.1.3 SD Trigger

The surface detector is read out via a wireless network. The limited network bandwidth does not allow to read out each detector in real time. The network allows to transmit the data of roughly one event per hour and tank. This requires a strong suppression of the background from atmospheric muons while keeping as many real air shower events as possible.

The single detector rate of 3000 Hz is reduced to a counting rate of 3×10^{-5} Hz through a hierarchical trigger system. This trigger is fully efficient (it selects all physics events) above 3×10^{18} eV in the zenith angle range from 0° to 60° independent of the position of the impact point of the shower w.r.t. the array[43]. The trigger algorithm for showers above 60° (*very inclined showers*) is described in [44].

In the first step, shower candidates are selected by the local trigger. This is done autonomously by each station. Different parts of the shower front have distinctive time structure. The *threshold trigger* (Thr) is designed to catch short, sharp peaks created in the FADC trace mainly by muons. This trigger catches muons from air showers as well as atmospheric muons. The *time over threshold* (ToT) trigger is designed to catch the signal from the electromagnetic part of the shower, which is more spread out in time. It is very efficient in the rejection of single background muons. There are two additional triggers that are already implemented in the local station software but not yet used in the standard reconstruction. These are the *time over threshold deconvolved* (ToTd) and the *multiplicity of positive steps* (MoPS). These triggers are designed to catch small signals far from the core [45, 46]. An example of the different parts of the signal is shown in Fig. 4.13.

Once a local trigger (T1, T2) is formed, the type of the trigger and a time stamp is transmitted over the wireless connection to the central facility. At this stage, the detailed time information is not yet transferred. It is stored for 10 s locally in case an array trigger (a shower candidate) is found. The stream of local triggers is checked for spatial and temporal correlations by the central facility. If a shower candidate is found, an array trigger (T3) is formed and the detailed time traces as well as the calibration histograms of all possible candidate stations are transferred. The details of the first three stages of the trigger chain are shown in Fig. 3.5.

At this stage, the criteria for station selection are still very permissive. Hence, there is still a large number of background muons in the selected events. A large number of chance coincidences is expected due to the large number of possible combinations of single detectors. The aim of the T4 (*physics trigger*) is to reject these background signals as well as to select real shower events. The start time of the stations with the highest signal in a compact configuration (Fig. 3.6) is fitted with a planar front. Coincidences from background muons are rejected by requiring the start times of the remaining stations to be compatible with the arrival time of the planar front. Furthermore, stations that have no active neighboring stations within 3000 m (*lonely stations*) are rejected.

In the last stage (T5, *quality trigger*), showers are selected to ensure the accuracy of the reconstruction of the core and the energy. This is done by requiring all stations around the station with the highest signal to be in data acquisition at the time of the event. The main purpose is to exclude events falling on the border of the array where the reconstructed energy and core position can be unreliable.
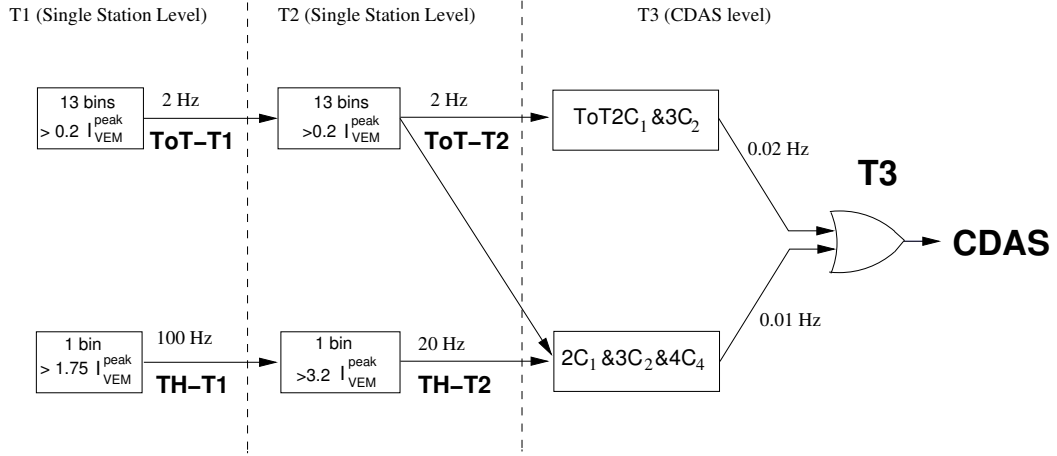
Figure 3.5: Hierarchical structure of the SD trigger. The first two stages are done autonomously by each station. The aims are to reject as many atmospheric background muons as possible and to catch all stations triggered either by electromagnetic particle or by muons. A time stamp of the local trigger is submitted to the central data acquisition system. If several local triggers correlate in space and time, an array trigger (T3) is formed. From [43].

(a) 3ToT

(b) 4C1

Figure 3.6: Station configurations of the physics trigger (T4). Three stations with a time over threshold trigger (3ToT) or four stations with a threshold trigger in the first crown around the station with the largest signal (4C1) are required. The start times are fitted to a planar front. Stations that are not compatible with the planar front are rejected. From [47].

(a) Plane shower front   (b) Curved shower front

Figure 3.7: Fit of the shower front to the start times of the individual stations. From [47].

3.1.4 SD Reconstruction

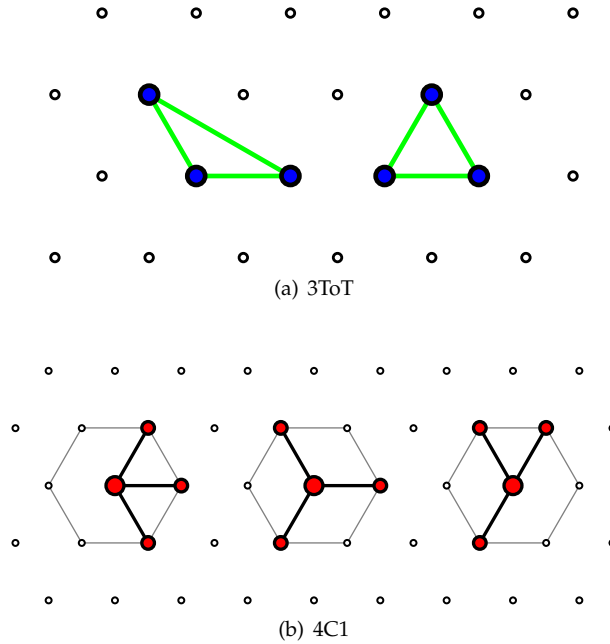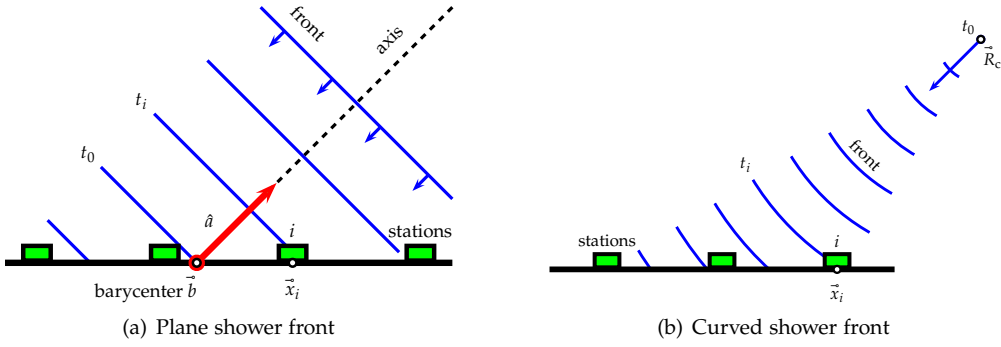The stations that are compatible in space and time with the propagation of a plane shower front are selected (marked as *candidates*) for the full reconstruction. The first stage consists of finding approximate initial values for the shower core and arrival direction. The signal weighted average (called *barycenter*) of the positions of the candidate stations [48] determines the initial value for the core as well as the origin of the coordinate system used further on in the reconstruction.

The arrival direction is approximated by fitting a planar shower front to the start times of the signals (Fig. 3.7(a)). In the second stage, the radius of curvature of the shower front is fitted, assuming a spherical shape (Fig. 3.7(b)). The resolution on the arrival direction is typically in the order of $1°$ [49].

The variance of the start time is needed to fit the curvature. It is based on a model as described in [50], which in turn depends on the *rise time* of the signal (the time it takes the signal to rise from 10% to 50% of its total value). Far from the core, single muons hitting the detector can result in a very short rise time. This can cause the variance of the start time to be underestimated and distort the curvature fit. This issue and a possible solution is discussed further in Section 5.2.

The total signals S_i are fitted with a modified NKG function [51, 52],

$$S(r) = S_{1000} \left(\frac{r}{r_{1000}} \right)^{\beta} \left(\frac{r + r_{700}}{r_{1000} + r_{700}} \right)^{\beta + \gamma} . \tag{3.1}$$

An example of the signals in an SD event is shown in Fig. 3.8(a). The fit of the lateral distribution to the signals is shown in Fig. 3.8(b).

The uncertainty of the signal is estimated from real data using *twin stations*. Those are stations at a distance of $10\,\mathrm{m}$ that are not used in the standard reconstruction. Assuming the same expected signal if both stations are part of an event, the uncertainty is estimated from the difference of the signals (for more details, see [53]).

The signal uncertainty is modeled as a function of zenith angle as [53]

$$f_S(\theta) = 0.34 + 0.46 / \cos \theta \tag{3.2}$$

$$\sigma_S(\theta) = f_S(\theta) \sqrt{S} . \tag{3.3}$$

The LDF fit is based on a log likelihood maximization. This allows to account for non-triggering stations where the signal can be below the trigger threshold. The signal of saturated stations is recovered based on a model of the pulse shape and the electronic undershoot in the late part of the signal trace [54]. If the saturated station is not too close to the core, the recovered signal is used. Otherwise the saturated signal sets a lower limit to the LDF. Stations with $S < 30$ VEM contribute to the likelihood with a Poisson term based on the expected number of particles. The number of particles per VEM depends on the zenith angle: Because of the attenuation in the atmosphere, muons dominate at large θ and muons produce larger signals on average. Furthermore, the average signal of a muon depends on its track length inside the water volume. This is not the case for electromagnetic particles. The number of particles is parametrized as

$$n = p\,S$$

$$p = p(\theta) = \begin{cases} f_S(\theta)^{-2} & \text{for } f_S(\theta) \geq 1 \\ 1 & \text{for } f_S(\theta) < 1 \end{cases} .$$

The signal factor $f_S(\theta)$ is taken from Eq. (3.2).

Originally, the NKG function was designed to describe the lateral density for purely electromagnetic showers.

For purely electromagnetic showers, the normalization of Eq. (3.1) is given by the shower age (see Eq. (2.1) on page 6). For the case of hadronic showers, the normalization S_{1000} is fitted independently to account for the amount of muons on ground. Muons are produced in the early stage of the cascade and undergo very few interactions. Due to the large transverse momentum, muons typically reach further out from the axis than the electromagnetic part. This results in a flatter lateral shape of the LDF.

From the lateral fit, the position of the shower core is obtained. Eq. (3.1) does not depend on the azimuth angle in the shower plane. Signal asymmetries caused by attenuation and detector effects are ignored. The signal in the late region of the shower (above the shower axis) is smaller than in the early region (below the axis) due to the attenuation of the electromagnetic part in the atmosphere. Ignoring this effects leads to a systematic shift of the core to the early region by up to 50 m depending on the zenith angle [55]. In this thesis, a better description of the ground signal based on shower universality is developed (Section 4.5). In Sections 6.2 and 7.3 it is shown that this model gives a bias-free estimate of the core position.

The shower size S_{1000} is an estimator of the total energy. The estimated signal at 1000 m is used because at this distance the dependence on the type of the lateral distribution function and on the primary mass is minimized while the correlation to the primary energy is maximized.

The shape parameters β, γ are taken from a parametrization derived from high-multiplicity events. The parametrization is derived from events where enough stations are distributed
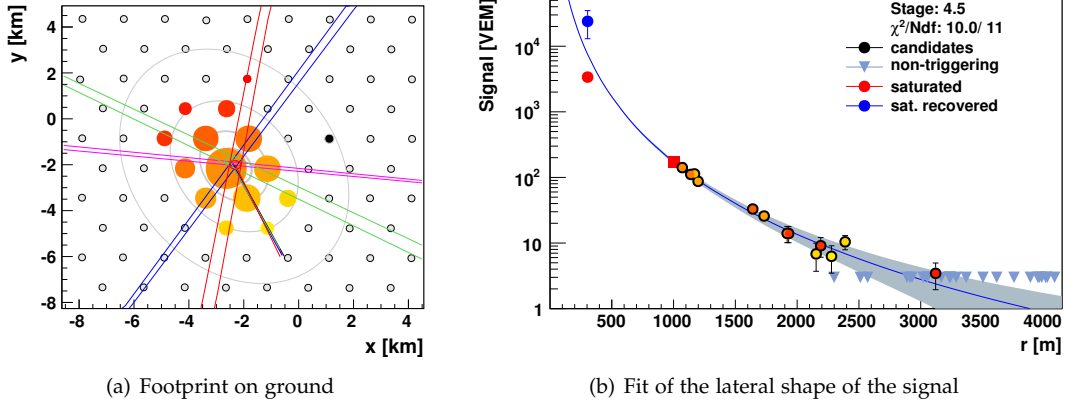
(a) Footprint on ground

(b) Fit of the lateral shape of the signal

Figure 3.8: Footprint on ground of the shower in Fig. 3.2 and the reconstruction of the lateral distribution function (LDF). The signal size is indicated by the size of the circles. The arrival time is color coded from yellow to red. The colored lines are estimates of the shower detector plane of each fluorescence telescope. From [39].

equally over the whole distance range. This is required to ensure a sufficiently long lever arm for the fit of the lateral distribution. An example of such a model for hadronic showers is given in [56]. The lateral shape of photon-induced showers is steeper. A shape model for photons is given in [57].

At a fixed primary energy, S_{1000} depends on the zenith angle (because of the attenuation in the atmosphere). Hence, the shower size is converted to the value the shower would have, had it arrived at the median angle ($\theta = 38°$). This method assumes isotropic arrival directions (*constant intensity cut - CIC*). The zenith-independent shower size estimator $S_{38°}$ is obtained as

$$S_{38°} = \frac{S_{1000}}{1 + ax - bx^2} \,.$$

where $x = \cos^2 \theta - \cos^2 38°$ and the coefficients taken from [58],

$$a = 0.87 \pm 0.04$$
$$b = 1.49 \pm 0.20$$

In hybrid events, the correlation of $S_{38°}$ and the total energy E_{FD} is measured. This correlation is applied to pure SD events to calculate the energy,

$$E/\text{EeV} = A \cdot S_{38°}{}^{B} \,.$$

where [23]

$$A = 0.190 \pm 0.005$$
$$B = 1.025 \pm 0.007$$

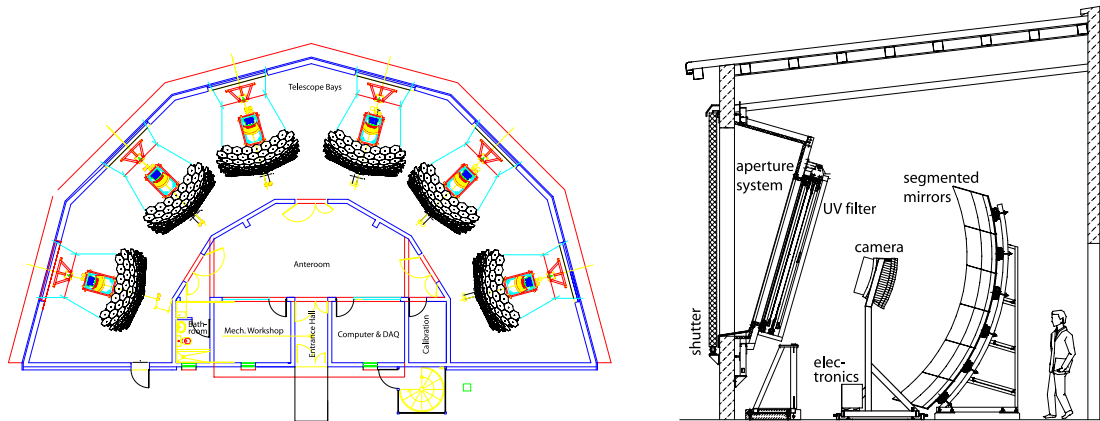More details on the calibration are given in Section 3.2.2.

Figure 3.9: Schematic view of a FD building with six telescopes (left) and a telescope with the mirror and camera (right). From [59].

3.2 Fluorescence Detector

3.2.1 Detector description

When the charged secondary particles of an extensive air shower traverse the atmosphere, they excite nitrogen molecules, which in turn emit ultraviolet fluorescence light at 300 nm to 430 nm [59]. The light emission is proportional to the energy deposit. The light is recorded at 4 detector buildings (*eyes*) that are situated at the border of the array (Fig. 3.1). Each building contains 6 fluorescence telescopes. Each telescope monitors a field of view of $30° \times 30°$. These telescopes are designed to measure the longitudinal development of showers above 10^{19}eV. In addition, three telescope buildings are situated at the western border of the array, designed to measure lower energy showers that develop higher in the atmosphere (*High Elevation Auger Telescopes - HEAT*). A schematic view of the telescope buildings is shown in Fig. 3.9. The FD is only operated in clear, moonless nights to minimize the amount of background light. This amounts to a duty cycle of $\approx 13\,\%$. Above 10^{19}eV, the trigger efficiency is $100\,\%$ over the whole SD array.

Each telescope is equipped with a UV filter to suppress the strong background of visible light that is present even in good observation conditions. The light is focused by a $10\,m^2$ mirror onto a camera of 440 photomultiplier light sensors (*pixels*). Each pixel has a field of view of $1.5°$. The light pulses in the pixels are digitized every 100 ns.

The longitudinal development of the shower is projected on the camera as a line of activated pixels. The pulse time of the pixels follows the time development in the atmosphere. A variable threshold is set on the signal of each pixel to maintain a trigger rate of 100 Hz per pixel (first level trigger - FLT). Each camera is scanned for tracks of at least five triggered pixels (second level trigger - SLT). Such tracks are found at a rate of 0.1 Hz to 10 Hz per camera. A third level trigger (TLT) is implemented to reject tracks generated by lightnings, muons hitting the camera and random coincidences. This is done using pattern recognition based on a shower library obtained from real data. At the end of the chain, the trigger rate is 0.02 Hz per building.

Once a shower candidate is found, a T3 trigger is formed and sent to the central data acquisition system (CDAS). The T3 from the FD acts as an external trigger for the SD. If a SD station is found in coincidence by CDAS, a hybrid trigger is generated and data of even a single station is read out. This is done even if the multiplicity or the station configuration is insufficient to form a separate SD trigger because even a single SD station improves the FD reconstruction.

3.2.2 FD Reconstruction

The first step in the FD reconstruction is the determination of the shower-detector plane (SDP). The SDP is determined by the location of the FD building and the projection of the shower axis on the camera (Fig. 3.10). The location of the shower axis within the SDP and its orientation with respect to the telescope can not be obtained from a geometrical fit of the pixel track. It can be estimated from the timing of the pixel pulses. If only FD data is used (*mono reconstruction*), the uncertainty in the arrival direction and core position is very large. Hence, the distance of the axis to the telescope is not known precisely and therefore the attenuation of the fluorescence light cannot be estimated correctly. This leads to a large uncertainty in the calorimetric energy. Because the SD has a duty cycle of close to 100 %, usually a triggered station is available for each FD trigger. The start time of the signal in one SD station is enough to place a strong constraint on the geometry of the shower (*hybrid reconstruction*). In Fig. 3.11, the reconstruction a shower in mono and hybrid mode is compared. The accuracy of the hybrid reconstruction is 50 m on the core position and $0.6°$ on the shower axis.

Once the geometry of the shower is known, the light at each pixel is converted to the light production at the shower. Using the geometry and the pulse time, the energy deposit dE/dX is calculated as a function of the slant depth X and is fitted with a Gaisser-Hillas function [60] (Fig. 3.12). The integral of this shape is the calorimetric energy of the shower. It is corrected for the *missing energy* that is carried by muons and neutrinos, which is not seen by the FD. This correction is derived from simulations for different interaction models and primary particles [61, 62, 63]. The systematic uncertainty on the missing energy due to the unknown mass composition is in the order of a few percent.

In a subset of events, when the energy is large enough, the FD and the SD trigger independently. Data from this sample is called *golden hybrid events*. It is used for the validation of analyses based on the SD (Chapter 7) and for the energy calibration of the SD. The calibration of the shower size with the calorimetric energy is shown in Fig. 3.13 for vertical and inclined events.
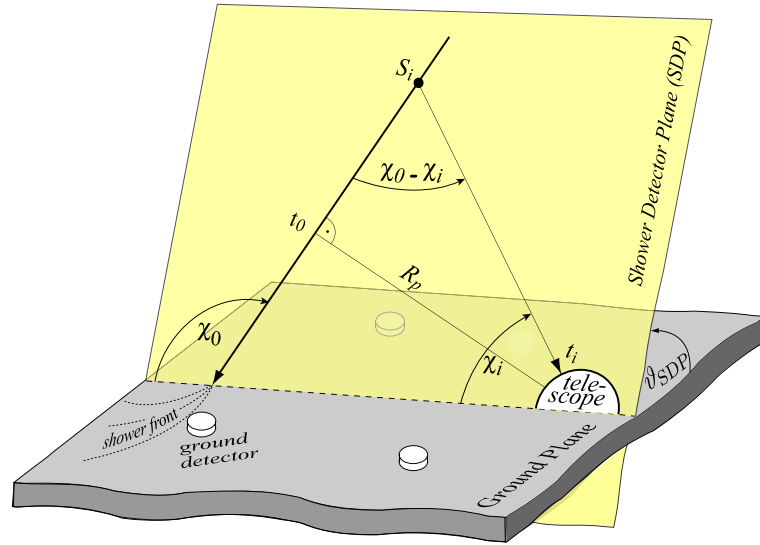
Figure 3.10: Schematic view of the geometrical shower reconstruction. The shower detector plane (SDP) is determined by the position of the detector building and the track of triggered pixels. From [59].
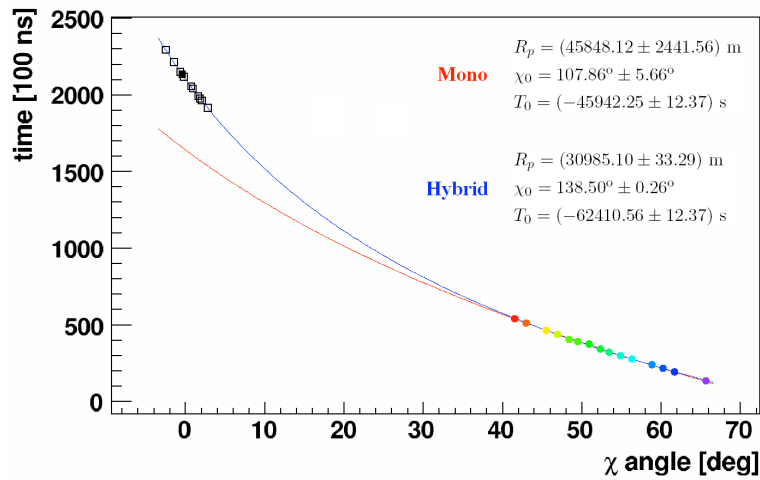
Figure 3.11: Reconstruction of the shower geometry. Comparison of the reconstruction of the shower axis in monocular (only FD) and hybrid mode (at least one SD station). FD data (colored points) and SD data (black points) are superimposed to the monocular (red line) and hybrid (blue line) reconstruction fits. The start times of the SD stations allow to place a strong constraint on the arrival direction and the core position (compare the uncertainties in R_p and χ_0). This improves the uncertainty in the energy reconstruction. From [59].
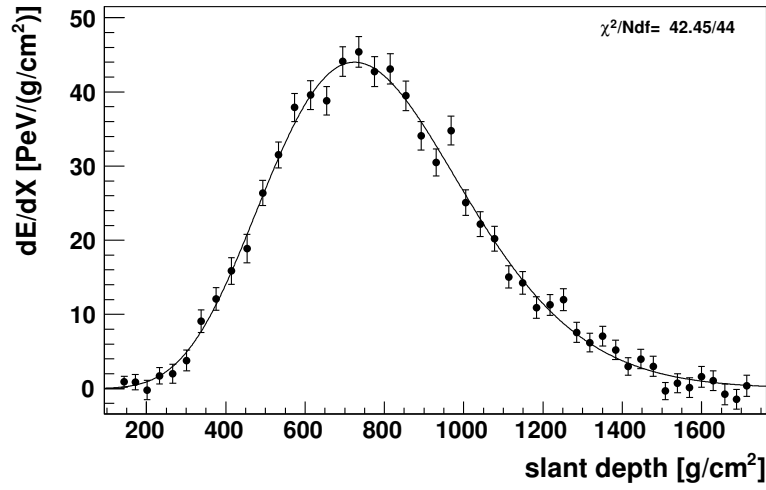
Figure 3.12: Reconstruction of the longitudinal energy deposit. From [59]. Once the shower geometry is known, the light of each pixel is converted to the energy deposit at the shower axis based on the light attenuation in the atmosphere. The energy deposit dE/dX is given as a function of slant depth X. The shape is fitted with a Gaisser-Hillas function. From the fit, the maximum of the longitudinal development X_{max} and the calorimetric energy is obtained. The reconstructed energy for this shower is 3×10^{19}eV. From [59].
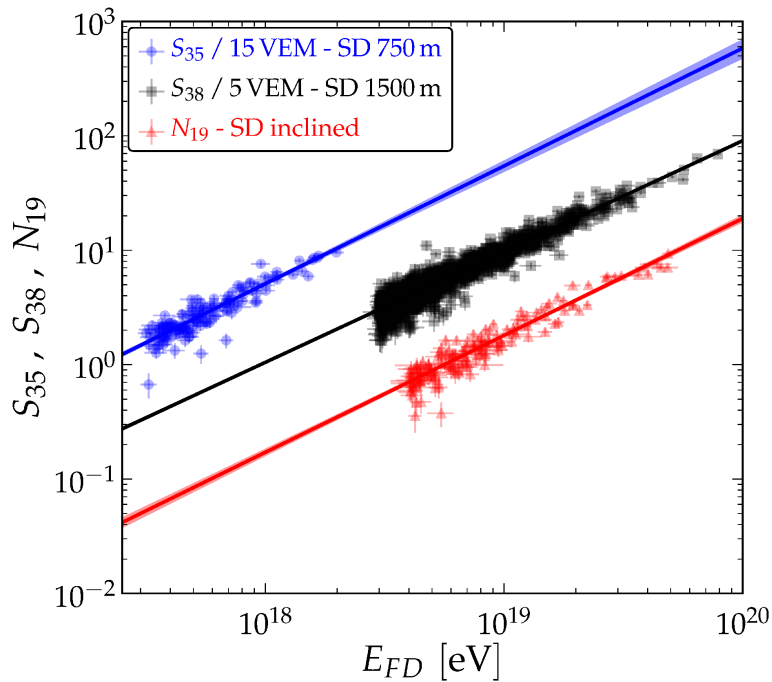
Figure 3.13: SD energy calibration derived from golden hybrid events. The shower size is corrected for the zenith-dependent attenuation in the atmosphere (infill array: S_{35}, regular array S_{38}, showers above $60°$: N_{19}) and correlated with the calorimetric energy. From [23]. The correlation is described by a power law.

3.3 Extensions of the observatory

Since the commissioning of the SD and the FD, several extensions have been deployed or are being developed.

The energy of full trigger efficiency of the SD was lowered to 3×10^{17} eV with a denser detector spacing in a part of the ground array (*infill array*). The same energy range is aimed at with the *high-elevation Auger telescopes* (HEAT). Placed in the vicinity of the Coihueco telescope at the western border of the array, these telescopes look above the field of view of the standard telescopes to measure the fluorescence emission in the upper atmosphere [64].

Underground scintillation detectors are being deployed in the area of the infill array [65, 66]. This extension will permit a direct measurement of the muon density along with each water Cherenkov detector. It will improve the sensitivity to the primary mass and allow for a better discrimination of hadronic interaction models. Knowledge of the muon density will help to validate the models based on shower universality presented in Chapter 4.

The Auger Engineering Radio Array (AERA) [67, 68] is built to measure the radio emission from charged particles along the shower track in the energy range of the infill array. It operates in the frequency range from 30 MHz to 80 MHz. The radio measurement allows to measure the longitudinal development of the shower at $E > 10^{17}$ eV.

Furthermore, extensions to the FD are being discussed. The aim is to increase the duty cycle and to extend the sensitivity to lower energies. This will be especially helpful for the search of photons around 10^{18} eV.

Extensions of the SD to improve the sensitivity to the muonic and electromagnetic parts of the particle cascade are being discussed. An overview and the potential benefits for this thesis is given in Sections 4.11 and 5.7.

4

Air shower universality and shower models

An extensive air shower contains a very large number of secondary particles. In a typical proton shower at $E = 10^{19}$eV (the energy relevant for this thesis) more than 10^{10} particles reach the depth of the surface detector (SD). Nevertheless it is possible to describe the average properties of the air shower cascade as a function of a very small set of parameters. For purely electromagnetic showers, it is enough to know the total energy E and the depth of shower maximum X_{max}. With these parameters, one can predict the longitudinal and lateral development, the energy spectrum and the angular distribution of secondary particles around the shower axis [69, 70]. This remarkable property is called *shower universality*: Despite the vast number of particles and interactions, the general features of an air shower are determined by only a few measurable quantities. There is no direct dependence on primary mass, incoming direction or any other individual feature.

This approach can also be applied to air showers initiated by hadronic primaries (i.e. protons and nuclei up to iron) [71, 72]. Those showers contain a large number of muons due to hadronic interactions with air molecules leading to the production and subsequent decay of charged pions. The muonic component is accounted for in the universality description by introducing an overall factor for the muon scale, N_μ[1] (Section 4.5). This scale accounts for the difference in the amount of muons depending on the primary mass and hadronic interaction model.

In this approach, an extensive air shower is described completely by measurable quantities. The main goal of this thesis is to measure N_μ and X_{max} from the large data sample collected by the SD, thereby assuming that universality gives an accurate description of the measurement. The model predictions can be validated with data if the universality parameters are known, i.e. measured independently. This is done based on a smaller data set where additional information from the fluorescence detector (FD) is available (Chapter 7).

In this section, a model of the signal in the water Cherenkov detectors (WCDs) is developed. Its aim is to predict the time dependent signal $S(t)$. Note that, although this section

---

[1]Here, N_μ denotes the amount of muons relative to the reference of proton QGSJet II-03 showers. For consistency with previous publications, N_μ also denotes the number of individual muons that reach the ground level. The second definition is only used in Section 2.2. From here on, N_μ is always the relative quantity.
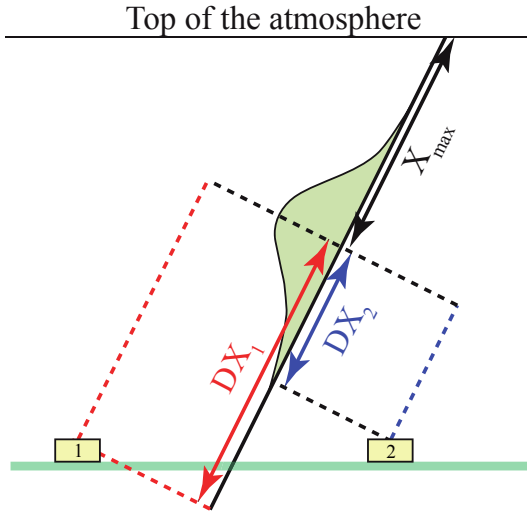
Top of the atmosphere

Figure 4.1: Calculation of the distance to X_{max} (DX). The density of the atmosphere is integrated from the shower maximum to the projected position of the station on the shower axis. The azimuthal asymmetry in the signal is accounted for automatically due to the difference in depth of late and early stations (DX_1 and DX_2).

focuses on WCDs, shower universality allows to predict the signal in any kind of detector (e.g. scintillators, RPCs) at any point of the cascade [73]. Where necessary, the models for a different detector need to be adapted to account for geometrical detector effects. This implies that, once E, X_{max} and N_μ are measured using the SD, the FD or a combination of both, the signal in a different detector would be completely determined (and vice versa).

Air showers are seen from below by the SD. Hence, the relevant quantity to describe the longitudinal development is the atmospheric grammage between a point on ground and the position of the shower maximum (Fig. 4.1),

$$DX = X_{station} - X_{max}.$$

For the case of a flat atmosphere, the grammage along the shower axis (*slant depth*) is obtained from the vertical depth as

$$X_{slant} = X_{vertical} / \cos\theta.$$

This is a very good approximation to the real (curved) atmosphere for $\theta < 60°$ (the relevant zenith angle range for this thesis).

The density of the atmosphere follows an exponential decrease. At several heights, however, the slope of the exponential changes. These features can be modeled to very good accuracy with a five layer atmosphere. The height of the layer boundaries depend on the state of the atmosphere. A good approximation of the real condition is given by the Malargüe monthly models [74]. In the lower four atmospheric layers, the relation between the mass overburden X in g/cm^2 and the height h is given by

$$X(h) = a_i + b_i \cdot e^{-h/c_i} \quad i = 1\dots4.$$

In the fifth layer the mass overburden decreases linearly with height,

$$X(h) = a_5 - b_5 \cdot h/c_5.$$

In the following sections, the simulation of extensive air showers initiated by ultra-high energy cosmic rays is described. An overview of the method to obtain ground particle distributions is given. The simulation of the response of the WCDs is described in detail. Finally, a model for the time-dependent tank response based on shower universality is built.

4.1 Shower Simulation

The simulation of extensive air showers is performed using CORSIKA 6.900 [74]. It allows the simulation of the particle cascade in the atmosphere initiated by various types of cosmic rays such as protons, atomic nuclei or photons. CORSIKA handles all relevant processes like the propagation of particles, their deflection in the earth magnetic field, interactions with the constituents of the atmosphere, energy losses, particle decay and so forth. The primary energies considered here are several orders of magnitude higher than what can be achieved at particle accelerators. This makes predictions of the physical processes at the highest energies uncertain because measurements at much lower energies need to be extrapolated. For the description of hadronic interactions at the highest energies several models are available. In this work the predictions of the models QGSJet II-03 [75] and EPOS 1.99 [76] are studied in detail.

The number of secondary particles in a shower is proportional to the primary energy. Simulating the whole particle cascade becomes very time-consuming above a primary energy of 10^{16}eV. This is solved by *thin sampling*. If the sum of energies of all secondary particles falls below an adjustable fraction of the primary energy

$$\epsilon_{th} E_0 > \sum_j E_j$$

where

$$\epsilon_{th} = E/E_0$$

is the ratio of the particle energy E and the total energy E_0, all but one particle are discarded. The probability p_i for a particle to remain is computed according to its energy E_i

$$p_i = E_i / \sum_j E_j$$

It is attributed a weight $w_i = 1/p_i$ to ensure energy conservation. Due to this mechanism, the number of particles that are actually simulated remains rather constant with respect to the primary energy. In general, the secondary particles that reach the ground have a weight $w > 1$. The technique to recover the actual distributions in space and time from the weighted particles is shown in Section 4.3.

4.2 Shower libraries

This work is based on two distinct sets of simulated showers called *shower libraries*. The first library contains showers at fixed zenith angles and primary energies. Proton and iron primaries are simulated using the high-energy hadronic interaction models QGSJet II-03 and EPOS 1.99. The primary energies are fixed at $10^{18.6}$eV, $10^{19.0}$eV, $10^{19.5}$eV and $10^{20.0}$eV. The zenith angle of the arrival direction was set to fixed values of $0°$, $12°$, $25°$, $36°$, $45°$, $53°$ and $60°$
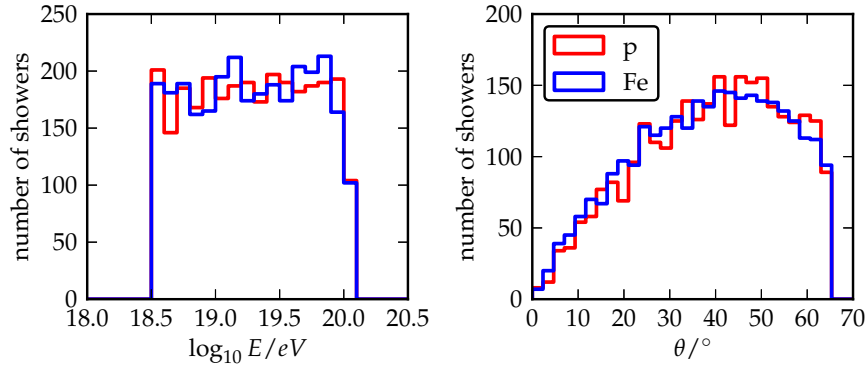
Figure 4.2: Distribution of primary energy and zenith angle in the continuous shower library. The energy is sample uniformly in $\log_{10} E$. The zenith angle is sampled to match the distribution in data, $dN/d\theta \propto \sin\theta \cos\theta$, according to an isotropic flux projected on a flat surface.

while the azimuth angle was sampled uniformly in $\phi = 0° \dots 360°$. The Malargüe monthly models for the description of the atmosphere are used [74]. For each set of those parameters, 10 showers are simulated. In total, 13440 showers are available. Fixed angles and energies are convenient to study the mean values and fluctuations of observables on ground. This library is referred to as the *fixed library*.

The second library aims to reflect the properties of showers in real data. The distribution of zenith angle and energy is shown in Fig. 4.2. It is based on `CORSIKA` showers that were transferred from the computing center in Lyon (`QGSjetII_Proton_SRB`[2] and `QGSJet_Iron_SRB`[3]) The zenith angle is distributed proportional to $\sin\theta \cos\theta$. This corresponds to an isotropic flux projected on a flat detector surface. The energy follows a E^{-1} flux. This is a compromise between the much steeper real spectrum and the computing time to obtain a large enough simulation sample. The Malargüe seasonal models are used for the description of the atmosphere. This library is referred to as the *continuous library*.

The results in the following chapters (e.g. reconstruction accuracy of X_{max}) are checked with both libraries. In general the results are compatible. It shows that the models developed in this section have no strong dependence on one specific set of simulations. Depending on the situation, one of both libraries is more convenient. The accuracy of the geometry reconstruction is estimated from the fixed library while the resolution and bias of X_{max} are based on the continuous library.

---

[2]http://augerdb.lal.in2p3.fr:8080/augerdb/simdb/Library-en.do?libraryId=11963710
[3]http://augerdb.lal.in2p3.fr:8080/augerdb/simdb/Library-en.do?libraryId=9136660

4.3 Simulation of the detector response

The $\overline{\text{Off}\underline{\text{line}}}$ software framework [77] is used to simulate the time-dependent response of the WCDs in the SD array. The simulation starts with the ground particle files produced by COR-SIKA. Each file contains information on the secondary particles of an air shower that reach the height of the detector (*observation level*). For each particle (amongst other information) the type, energy, momentum and arrival time are stored.

The WCDs cover only a small fraction of the ground surface. The fraction of weighted particles that actually hit the position of a specific tank is very small. To obtain a significant sample, all particles within a region much larger than the actual tank surface are used (*sampling area*). However, if the sampling area is too large, the particle distribution is no longer representative for the specific detector position, e.g. due to the steeply falling lateral density. As a compromise, the radial extent is usually set to $\pm 10\,\%$ of the distance of the station to the shower core. For example, the sampling region for station placed at 1000 m ranges from 900 m to 1100 m.

Most ground particles have a weight $w > 1$. The method to obtain the actual particles is called *unthinning* or *resampling* [78]. For each weighted particle, the number of *unthinned* particles is obtained from a Poisson distribution with a mean w. The arrival times of the unthinned particles are smeared to avoid creating artificial peaks that could be misinterpreted as muon peaks. The true positions of the original particles are unknown, because most of them are discarded during the simulation. Therefore, the resampled particles are distributed uniformly over the projected surface of the tank as seen by the weighted particle.

In the next step, the response of the WCD to each incident particle is simulated using Geant4 [79]. The production of Cherenkov photons along the particle track and the light propagation in the water volume the reflection on the inner Tyvek surface and the collection by the photomultipliers is calculated. This is by far the most time-consuming part of the detector simulation. Close to the core, more than 10^6 particles can be injected onto the tank surface, which makes the full tank simulation very time-consuming. To avoid the full Geant4 simulation for each secondary particle, an interpolation procedure was developed (Section 4.4).

The Cherenkov photons that are not absorbed by the water, hit the entry of a photomultiplier tube and produce photoelectrons at its cathode. Their number and arrival time is recorded. The final steps in the detector simulation are the amplification and time delay introduced by the dynode chain of the photomultiplier tube and the digitization in the FADC. The signals obtained in the last step are converted to the VEM signal using a pre-calculated calibration function (the calibration of the SD is described in Section 3.1.2).

In the standard simulation the arrival time of the light at the entry of the PMT is stored in the form of time distributions using a bin width of 1 ns. During digitization and filtering, this signal is sampled every 25 ns. The high resolution time distribution of the PMT response is discarded afterward to save space because it is not needed anymore. Usually this is done for all the stations at once but it has a huge memory footprint. This can be avoided by changing the order of the simulation and processing the whole electronics chain for one station at a time. For this purpose, the $\overline{\text{Off}\underline{\text{line}}}$ configuration is modified.
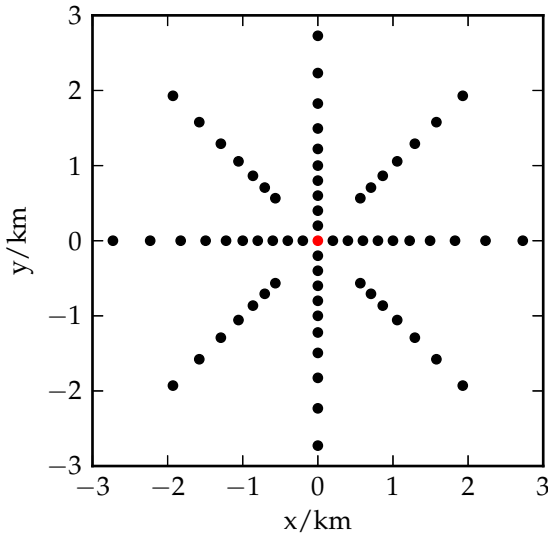
Figure 4.3: The models are based on a virtual (*dense*) array of surface detector stations. In contrast to the real array with fixed geographic positions, stations in the dense array (black markers) are placed at fixed locations w.r.t. the shower core (red marker). Thereby, geometrical effects due to the triangular structure of the array are avoided in the derivation of the models.

The syntax for the modified module sequence is

```
<loop numTimes="unbounded" pushEventToStack="no">
  <module> SdPMTSimulatorOG              </module>
  <module> SdFilterFADCSimulatorMTU      </module>
</loop>
```

In addition the option `LimitStationsPerCycle` is set to 1 in the `SdPMTSimulator`. The option `StoreBaseSignals` is set to no in the `SdFilterFADCSimulator`.

$\overline{\text{Off}}\underline{\text{line}}$ allows to place detectors at fixed positions referring to the shower axis such that the detector response is always simulated at the same positions regardless of the shower geometry and the position of the shower in the surface array. The setup of those *dense* stations is depicted in Fig. 4.3. Dense stations are placed at 200 m, 400 m, 600 m, 800 m, 1000 m, 1222 m, 1494 m, 1826 m, 2232 m and 2728 m from the shower core and in steps of 45° around the shower axis (for details on the coordinate system, see Fig. A.1).

4.4 Pre-calculation and interpolation of the tank response

Close to the shower core, the full tank simulation with Geant4 becomes too time consuming due to the large number of particles hitting the detector. Therefore, the tank response is derived from a pre-calculated tabulation [80]. The tank response, i.e. the number of photoelectrons at the cathode of each PMT is simulated with Geant4 for muons, electrons and photons. The particles enter the tank at angles between 0° and 88°. Electrons are simulated from 1 MeV to 100 GeV, photons from 0.1 MeV to 100 GeV and muons from 10 MeV to 2500 GeV. The entry position of a particle is sampled uniformly in the projected area of the tank. For muons, the probability to decay inside the tank is calculated as a function of energy. For each configuration of particle species, energy and incident angle, the tank response is calculated several times to achieve an accuracy better than 1 %. The mean and fluctuations of
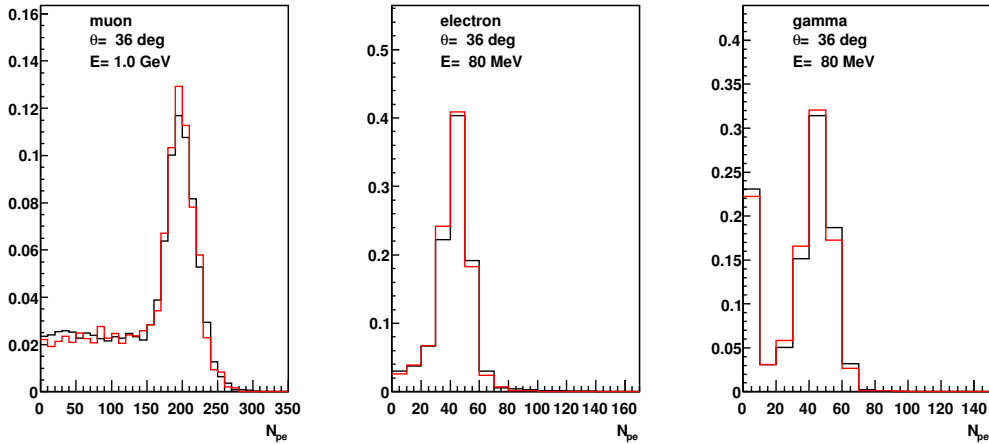
Figure 4.4: Distribution of the number of photoelectrons (N_{pe}) created in the photomultiplier by Cherenkov light for (anti-)muons, electrons/positrons and photons at $\theta = 36°$. For the muons, there is a long tail at small N_{pe} due to particles entering the detector close to the edge (*corner clipping*). From [80].

the pre-calculated values are stored in a table that allows a very fast simulation of the tank response. This method reproduces the fluctuations in the number of photoelectrons due to impact parameter, fluctuations in the light production and from photo-statistics correctly. The response of the full detector simulation convolved with the energy spectrum of particles in the shower is reproduced to an accuracy better than 5 %.

In Fig. 4.4 the number of photoelectrons from the full simulation is compared to the interpolated values obtained from the tabulation. In this case, the tank was simulated directly with Geant4 (without using the $\overline{\text{Off}\underline{\text{line}}}$ framework).

The WCD signals are simulated with $\overline{\text{Off}\underline{\text{line}}}$, both with the full Geant4 simulation and the interpolation. The difference is shown in Fig. 4.5. Again, the signal is reproduced well within 5 %, but a systematic difference of 1 % to 2 % is observed. This issue has not been solved completely. It is possible that the tank geometry used to produce the interpolation tables is not exactly the same as the one used in the $\overline{\text{Off}\underline{\text{line}}}$ module (e.g. in the ratio of radius to height). This could introduce a nonlinear deformation of the distribution of the number of photoelectrons that is not compensated by the calibration procedure. For electromagnetic particles, the difference is expected to be very small because they are usually absorbed within a few cm. For muons, the geometry of the tank becomes important. The amount of light produced in the tank depends strongly on incident angle and position due to corner clipping and the average track length. Depending on the zenith angle this could introduce a systematic error in the mean expected number of photoelectrons. Note that this difference is very likely not the cause for the *DX*-dependent effect shown in Fig. 4.12 and discussed in Section 4.6.

4.5 Model of the integrated ground signal

Ideally, a universal model describes the electromagnetic signal by a function $S = f(X_{max}, E)$, independent of primary mass or hadronic interaction model, i.e. with no dependence on the
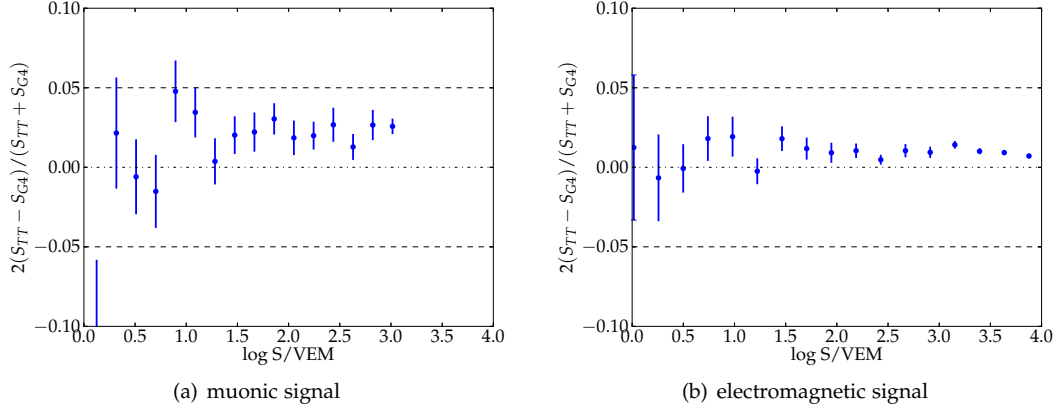
(a) muonic signal

(b) electromagnetic signal

Figure 4.5: Comparison of the VEM signal from the full Geant4 simulation S_{G4} to the value from the interpolation S_{TT}. Both signals are based on exactly the same resampled particles.

overall muon content. The size of the muonic part is given by an overall scaling factor N_μ. Its size is given by the muonic signal simulated for a specific primary and interaction model referred to the expectation of the reference model (proton showers simulated with QGSJet II-03),

$$N_\mu = \frac{S_\mu}{S_\mu^{\text{ref}}} \, .$$

In previous works (e.g. [81]) a universal description of the signals on ground was attempted with three signal components: The muonic component, the purely electromagnetic component and the electromagnetic component stemming from muon interactions and muon decay (*muon halo*). However, in this approach, the electromagnetic component has a strong dependence on N_μ and shows differences of up to 40 % (Fig. 4.6). Universality of the purely electromagnetic component is violated.

Simulations show that a significant fraction of the purely electromagnetic component stems from hadronic interactions at low-energy. This fraction is called the electromagnetic component from low-energy hadrons or the *jet component*. The size of this fraction is directly proportional to the muon content. In a very late stage of the shower development (close to the ground), jets with a high transverse momentum are produced. Those jets have a large angle with respect to the shower axis and point to stations far from the core. The particles created by those jets can be distinguished from the rest of the electromagnetic cascade using the projected impact point of their *mother particles* (Fig. 4.7).

The information of the two preceding particle generations are recorded in CORSIKA if the *history* option is switched on. The particles stemming from hadron jets have a low thinning weight compared to the rest of the cascade. By placing a cut on the projected radius, the two components are effectively separated (Fig. 4.8). However, in most CORSIKA simulations performed in the past, the information on the particle history is not available. In this case the separation is done by cutting on weight and hadronic generation of the particle. The shape of the lateral distribution of the four signal components was studied for both approaches. Both methods lead to practically the same results in terms of the LDF (Fig. 4.9).
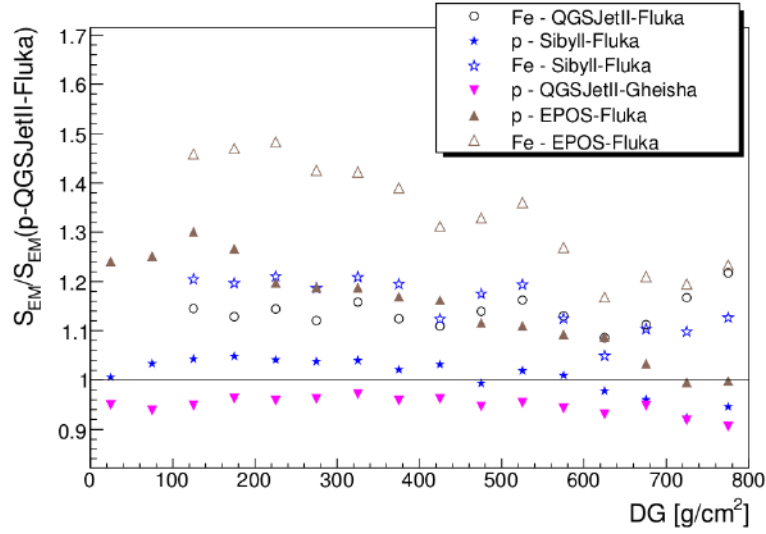
Figure 4.6: Violation of universality of the electromagnetic signal in the three-component approach [81]. One important feature of a universal signal model is that the electromagnetic signal is given by $S = f(X_{max}, E)$, with no dependence on the muon content. Specifically, it has to be the same for different hadronic interaction models and primary particles. In this model however, the predictions for the electromagnetic signal differ by up to 40 %. This is due to a dependence on the muon content of part of the electromagnetic signal.
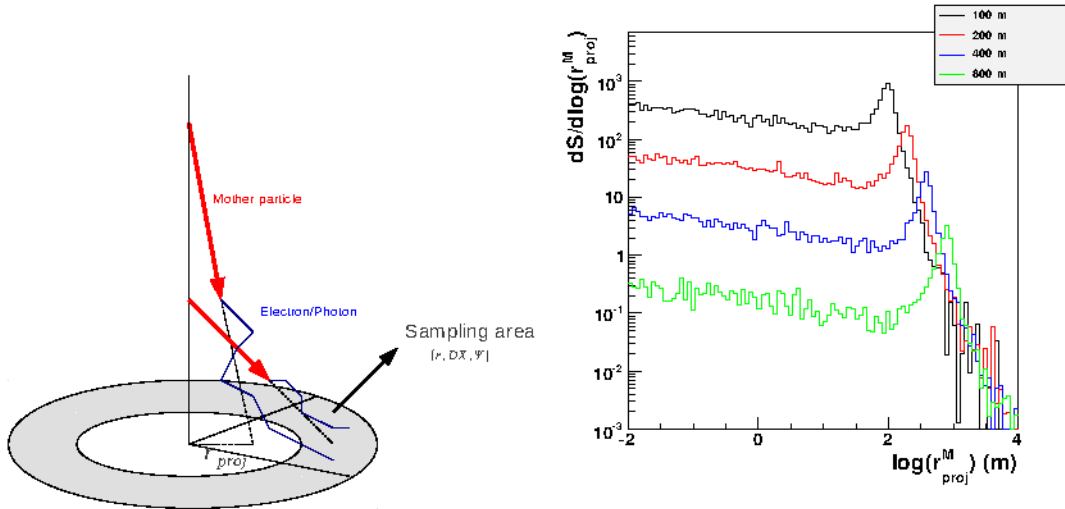

Figure 4.7: Left: The electromagnetic component from hadron jets is distinguished from the rest of the cascade by the projected impact point of the mother particle. **Right:** The distribution of the projected radius for electromagnetic particles. There is a clear peak for the jet component. From [72].
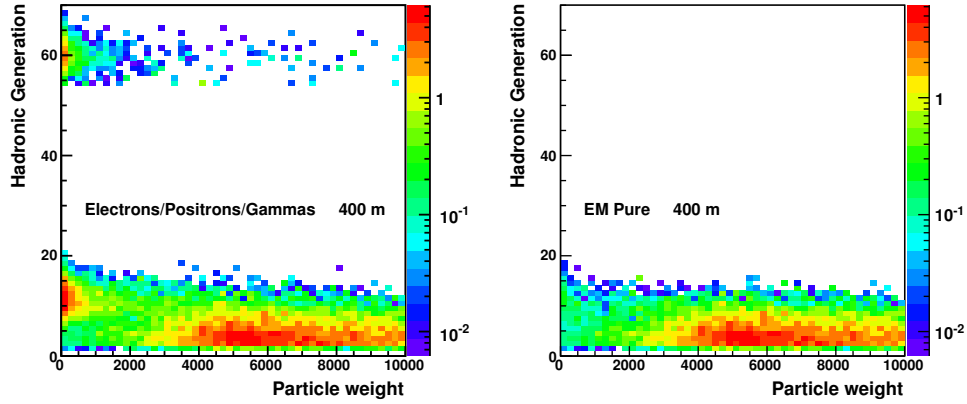
Figure 4.8: Left: The distribution of hadronic generation vs. particle weight for electromagnetic particles. Particles stemming from muon decay in the upper part, the jet component in the lower left and the rest of the cascade in the lower right. **Right:** The distribution after applying the cut on projected radius. From [72].
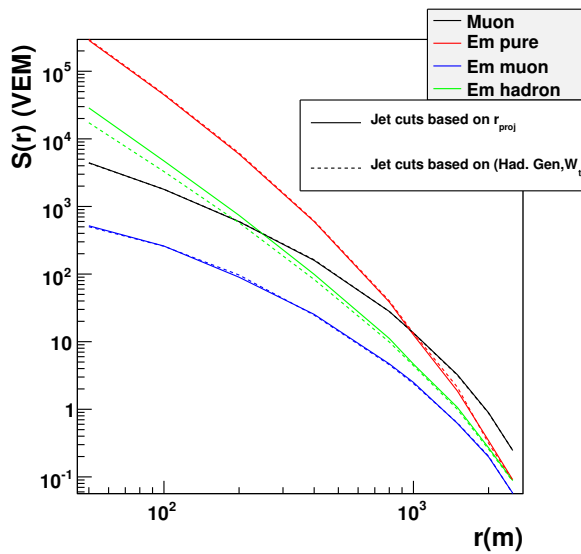

Figure 4.9: The lateral distribution of the signal in the universal model. The cuts to separate the hadron jet component from the pure electromagnetic component based on the projected radius (solid lines) give similar results as the cuts based on hadronic generation and particle weight (dashed lines). From [72].

For the derivation of the signal model the simulations with fixed energy and zenith angle as described in Section 4.2 are used. The response of the WCDs is simulated based on the interpolation tables. The properties of incident particles depend on where a detector is located referred to the shower axis. The angular distribution of particles hitting detectors below the shower axis (early region) is more centered around the vertical axis than for detectors above the shower axis (late region). Furthermore, a part of the shower in the late region is absorbed
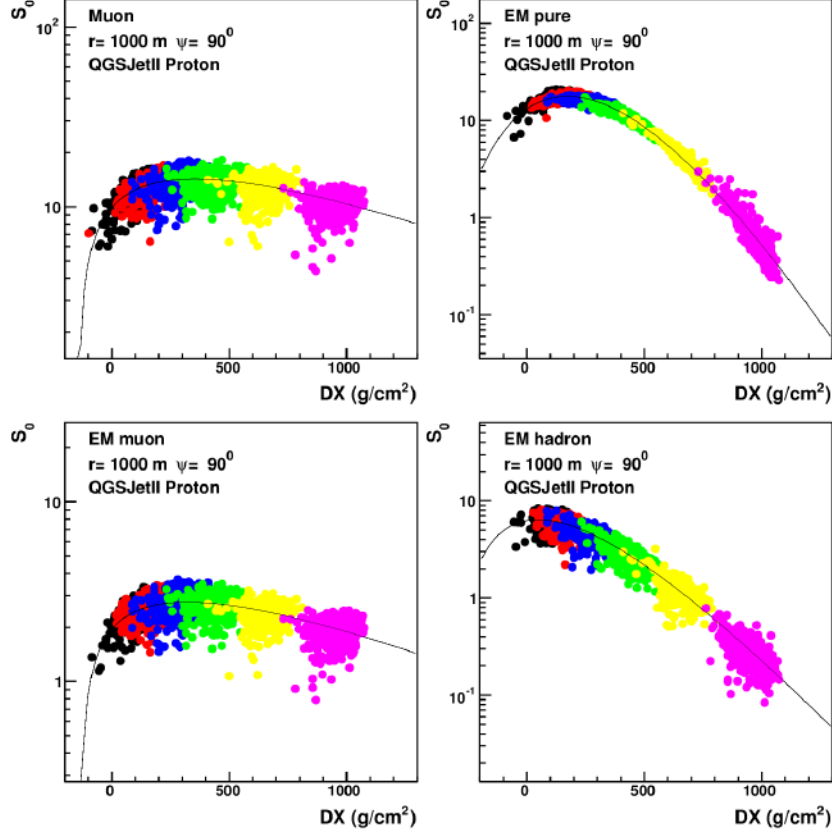
Figure 4.10: DX-dependence of the signal components. Zenith angles between 0° and 60° are color coded. Each point correspond to one simulated shower. The signals at different energies have been normalized to 10^{19} eV. The lines are the result of fit of the signals to the Gaisser-Hillas profile. From [72].

(*truncated*) by the ground before it can reach the detector. In addition to these geometric effects, early and late detectors see the shower at different development stages. These purely detector-related effects are corrected for in the first step to obtain the signal S_0. This is the signal that would be measured by a free-floating spherical detector without ground screening.

At a fixed distance to the shower core the signal S_0 of each component is parametrized with a Gaisser-Hillas function [60] (Fig. 4.10) as

$$S_0(DX, E) = S_{max} \left(\frac{E}{10^{19} \text{eV}} \right)^{\gamma} \left(\frac{DX - DX_0}{DX_{max} - DX_0} \right)^{\frac{DX_{max} - DX_0}{\lambda(E)}} \exp \left(\frac{DX_{max} - DX}{\lambda(E)} \right) .$$

S_{max}, γ, DX_0, DX_{max} and λ are parametrized as a function of distance to the core. This is done separately for all four components. The resulting model describes the longitudinal as well as the lateral shape of the shower. It gives an analytical parametrization of the spectrum of particles convolved with the detector response.
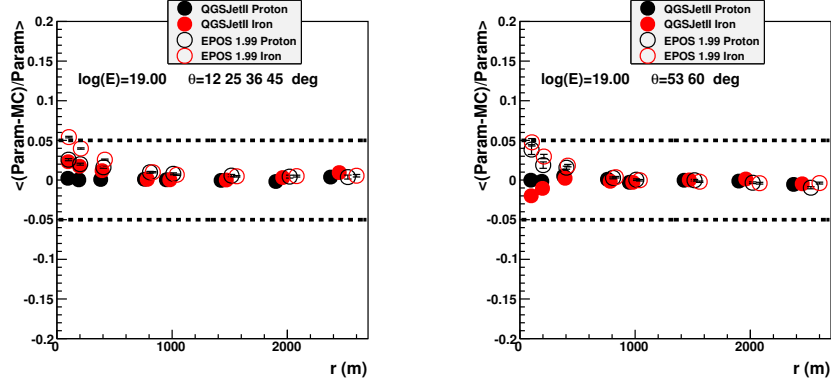
Figure 4.11: The average difference of the standalone tank simulation and the signal model. **Left:** 12°, 25°, 36° and 45°, **Right:** 53° and 60°. The difference of the signal and the model prediction is at most 5 %. From [72].

The integrated signal of a specific component at a position r, ψ is given by

$$S_0(\mathrm{N}_\mu, DX, E, \theta, r, \psi) = S_{0\,\mathrm{em}}^{\mathrm{ref}} + \mathrm{N}_\mu \left(S_{0\,\mu}^{\mathrm{ref}} + S_{0\,\mathrm{em}_\mu}^{\mathrm{ref}} f_{\mathrm{em}_\mu} \right) + \mathrm{N}_\mu^{\gamma_f(r)} S_{0\,\mathrm{em}_{had}}^{\mathrm{ref}} f_{\mathrm{em}_{had}} .$$

The muon scale N_μ is given by the ratio of the muonic signal compared to the reference model (proton QGSJet II-03) at a distance to ground of $DX = 400\,\mathrm{g/cm^2}$,

$$\mathrm{N}_\mu^{ref}(E) = \frac{S_{0,\mu}(r = 1000\,\mathrm{m}, DX = 400\,\mathrm{g/cm^2}, E)}{S_{0,\mu}^{\mathrm{ref}}(r = 1000\,\mathrm{m}, DX = 400\,\mathrm{g/cm^2}, E)} .$$

The signals are corrected for asymmetries caused by the detector and ground screening and the attenuation in the atmosphere is taken into account. Hence, the model is able to predict the signal on ground accurately. It gives a good prediction over the whole range of zenith angles θ and r, ψ coordinates in the shower plane. This property is very important for the reconstruction algorithm presented in Chapter 5 and the reconstruction of the shower geometry shown in Section 6.2.

4.6 Validation of the signal model with simulations

The tank signals that are used to derive the signal model are calculated based on the same resampling algorithm and the same code for the tank response as used in $\overline{\mathrm{Off}\underline{\mathrm{line}}}$. However, this implementation is independent of the framework. The residuals are shown in Fig. 4.11. The tank simulation and the signal model is in very good agreement.

When the WCDs are simulated with $\overline{\mathrm{Off}\underline{\mathrm{line}}}$ (using the same resampling algorithm and tank response) there is a systematic difference of $\approx 13\,\%$ (Fig. 4.12). There is no dependence of this difference on energy, zenith angle and geometry. There is also a systematic trend with DX of the residuals. The trend is the same for each fixed zenith angle and it is much more pronounced for the signals that depend on the muon scale. This suggests that the model can
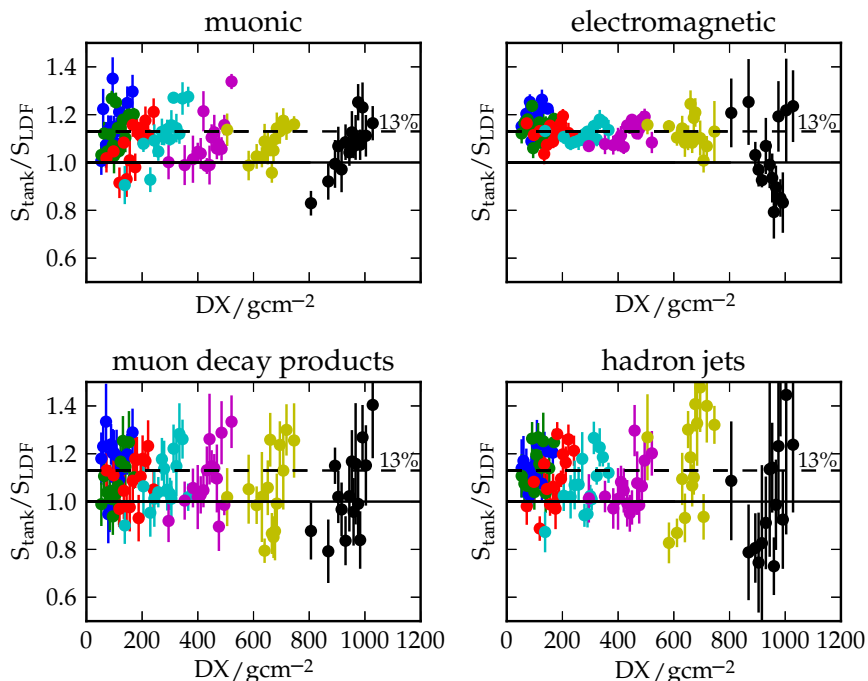
Figure 4.12: The residuals calculated from the $\overline{\text{Off}\underline{\text{line}}}$ tank simulation. The 13 % difference is corrected in the reconstruction. There is an additional correlation with DX within each zenith angle bin. Proton showers at $10^{19.5}$eV are used. The zenith angle is color-coded ($0°$, $12°$, $25°$, $36°$, $45°$, $53°$ and $60°$).

be improved by parametrizing the signals as a function of the maximum depth of the muonic cascade $X_{\max}^{\mu}$. This is discussed further in Section 6.3.1.5. The $\overline{\text{Off}\underline{\text{line}}}$ tank response and the signal model are calculated with different implementations. Hence, there are many possible sources of discrepancies. However, the resampling algorithms in both implementations as well as the number of photoelectrons at the PMT base are compared on the level of single particles and found to be exactly the same. The DX-dependence of the residuals is only visible in the comparison to the $\overline{\text{Off}\underline{\text{line}}}$ implementation. It could, nevertheless, also be present in the other implementation. Because in Fig. 4.11, only one value is given for each zenith angle, it is possible that the dependence on DX is present but averaged out. The differences between the two implementations are not yet fully understood. For now, an overall rescaling is applied to the signal model to make it compatible with the simulations (see also Chapter 5).

4.7 Time dependence of the signal

Muons and electromagnetic particles have different propagation characteristics in the atmosphere. Between the production point and the ground, muons are rarely deflected while electromagnetic particles scatter 10-50 times (the interaction length is $\approx 37\,\text{g/cm}^2$). As a result, the bulk of electromagnetic particles is delayed with respect to the muonic part and is
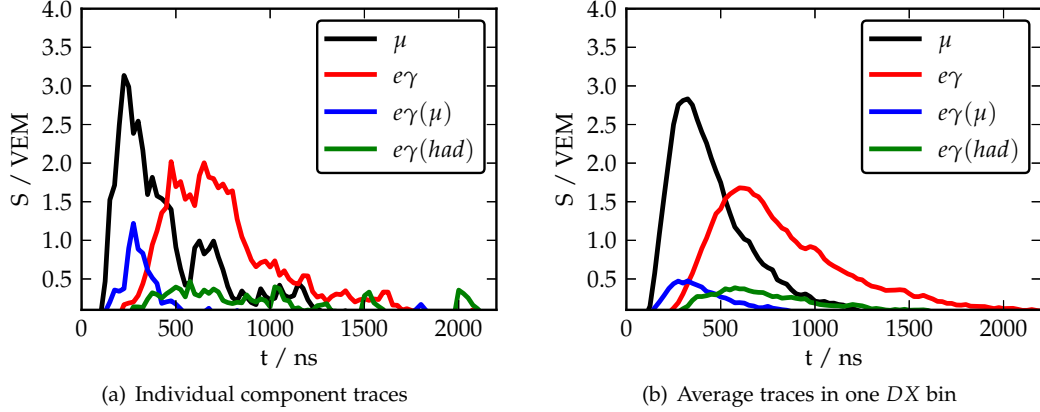
(a) Individual component traces

(b) Average traces in one *DX* bin

Figure 4.13: Time dependence of the signal (*component traces*) in the WCDs for proton showers at $10^{19.5}$eV simulated with QGSJet II-03. In this case, the signal of the hadron jet component is comparatively small. It is larger for muon-rich showers, which leads to the discrepancy shown in Fig. 4.6.

spread out in time. This difference is very important for the reconstruction of X_{max} and allows to discriminate deep from shallow showers. The time structure of the four signal components depends on X_{max} and distance to the core. The detailed dependence is shown in this section. An example of the individual component traces in a station and the average of all traces within one bin of *DX* is shown in Fig. 4.13.

The resampled traces are usually based on a rather small number of particles. Moreover, several time corrections are applied to the resampled particles. This could in principle introduce systematic errors in the estimate of the time shape. In a separate study [82], the time profiles of unthinned simulations are studied (all secondary particles are propagated to the ground). No systematic effects of the resampling on the shape of the time profiles was found. This is very expensive in terms of computing time and storage and is usually not done.

Due to the limited number of particles in a station (except for small distances to the core), stations with the same θ, r, ψ are grouped by their distance to the shower maximum *DX*. At this stage, it is assumed that the time shape does not depend on primary mass, energy or hadronic interaction model. Therefore, the traces of all available models, primaries and energies are combined. The assumption is not entirely true. The systematic effect caused by this assumption is studied in more detail in Sections 4.9 and 6.7. In the next step, the stations are binned by *DX* such that each bin contains the same number of entries. The binning is shown in (Fig. 4.14). The time parametrization was derived also with much smaller bins, with very similar results. Therefore, to save space and computing time, five bins are chosen. All the traces in the same bin are normalized. For each bin, the average trace is calculated. The mean of all *DX* values in the same bin is used further on.

There is a subtle detail that has to be considered when the mean of the traces within one bin is calculated. In general, the clocks of different stations are not in phase, i.e. the boundaries of the FADC bins do not coincide (this behavior is reproduced in the simulation by adding a random time offset). To calculate the mean trace, the bin contents are added partially
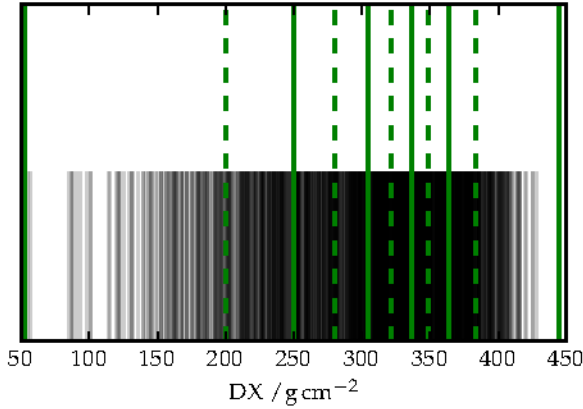
Figure 4.14: Distribution of DX for $\theta = 36°$, $r = 1000\,\mathrm{m}$, $\Psi = 90°$. Each simulated stations is indicated by a black line. The bin boundaries are chosen such that each bin contains the same number of entries. The solid green lines indicate the bin boundaries, the dashed green lines are the mean value of the DX distribution in one bin. Although the first bin is comparatively large, the parametrization with finer binning gives very similar results.
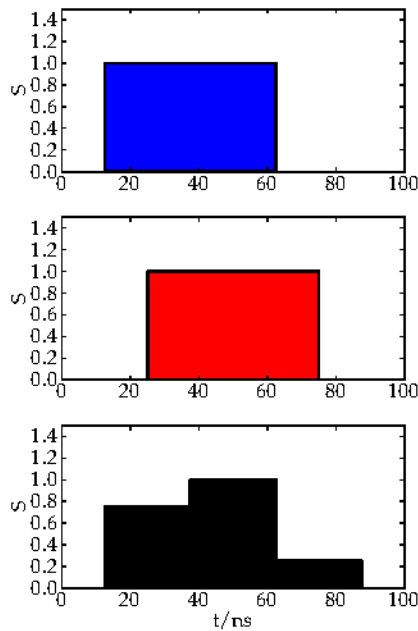

Figure 4.15: Calculation of the average component VEM trace. In general, the clocks of different stations are not in phase. To calculate the mean bin content of several traces, the individual entries are distributed over neighboring bins of the average trace. This is shown in a toy example of two traces that contain two bins with the same bin content (blue and red). The start times are shifted by half the width of a bin. The bin boundaries of the upper trace are taken as the reference to calculate the average (lower plot). The amount of overlap of each bin of the second trace with the bin boundaries of the first determines how the bin content of the second trace is distributed.

according to the phase shift (Fig. 4.15).

Several functional shapes were studied to describe the time-dependence (Moyal distribution, Gamma distribution, etc.). Most of them are not suited to describe the fast rise of the traces. The lognormal distribution describes the time shape accurately over a very wide range of distances to the core, DX and for all energies and primaries relevant for this thesis. Adjusted to this application, it has the form

$$f(t;t_0,m,s) = \begin{cases} \dfrac{1}{\frac{t-t_0}{\mathrm{ns}} \cdot s \cdot \sqrt{2\pi}} \exp\left(-\dfrac{\left(\ln \frac{t-t_0}{\mathrm{ns}} - m\right)^2}{2s^2} \right) & \text{for } t > t_0 \\ 0 & \text{for } t \leq t_0 \end{cases}$$

where m is a measure for the mean, s for the spread of the distribution. The shape of the
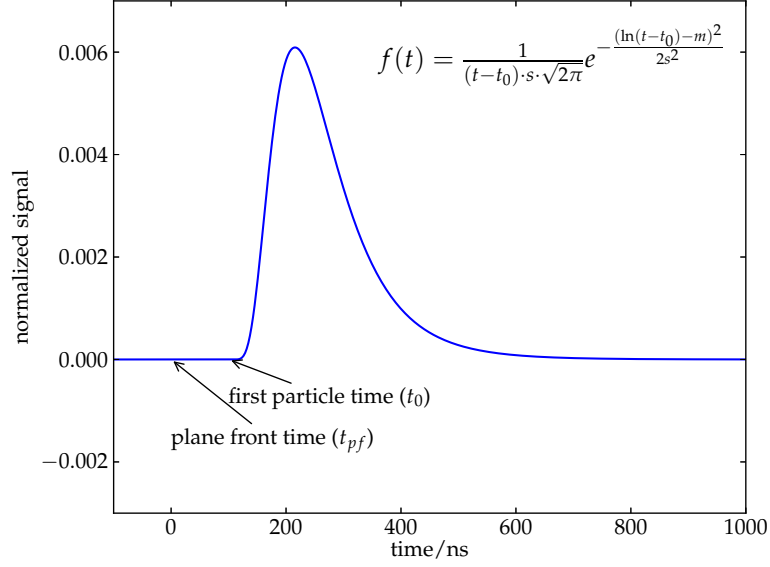
Figure 4.16: The functional shape used for the description of the shape of the component VEM traces is a lognormal distribution with three parameters t_0, m, s. The time is referred to the arrival of the plane front at the station. The starting time t_0 is given by the distance of the station to the point of first interaction X_0 (for the derivation, see Eq. (4.1)).

function is shown in Fig. 4.16.

The start time t_0 is calculated from the point of first interaction X_0. The height of first interaction is obtained from the density profiles defined in CORSIKA. The distance of the station to the point of first interaction determines the earliest possible time when any particle can arrive at a station. It follows from Fig. 4.17 that the time delay $c\delta t$ between the plane and curved shower front is

$$c\delta t = d' - d = \sqrt{d^2 + r^2} - d$$
$$= d\left(\sqrt{1 + \frac{r^2}{d^2}} - 1\right).$$

The point of first interaction is typically several tens of km away so the approximation

$$\sqrt{1 + x^2} = 1 + \frac{x^2}{2} - \frac{3x^4}{4!} + \dots$$

can be used for small x. It follows

$$c\delta t = d\frac{(r/d)^2}{2} = \frac{r^2}{2d}.$$

Rearranging and substituting the position of the station $\vec{P}_{\text{station}}$, the position of the point of first interaction $\vec{P}_{\text{first}}$ and $\delta t = t_0$, one obtains

$$t_0 = \frac{1}{2c}\frac{r^2}{|\vec{P}_{\text{station}} - \vec{P}_{\text{first}}|}. \tag{4.1}$$
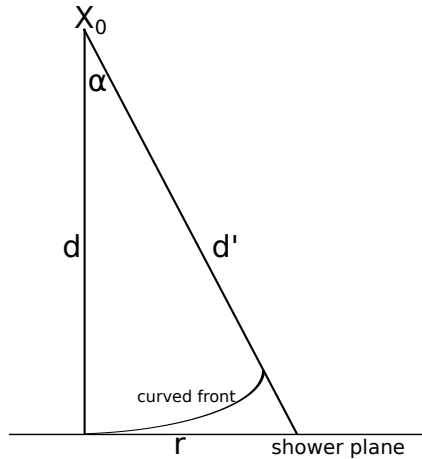
Figure 4.17: The earliest possible time for any particle to arrive at a station is determined by the geometric distance d' of the station to the point of first interaction X_0.

4.8 Functional form of the time shape parameters

The lognormal distribution is described by a time shift t_0 and two shape parameters, m and s. The time shift corresponds to the start time obtained from the first interaction. t_0 is fixed, while the shape parameters are fitted for each DX bin.

The m parameter is fitted with a smoothly broken power law function

$$m(DX) = p_0 \left(\frac{DX}{\mathrm{g/cm^2}} + p_3 \right)^{-p_1} \left[1 + \left(\frac{\frac{DX}{\mathrm{g/cm^2}} + p_3}{p_4 + p_3} \right)^{p_5} \right]^{-p_2/p_5}. \tag{4.2}$$

The dependence of m on DX can be attributed to p_1 and p_2 alone. Leaving the remaining parameters free does not improve the description. On the contrary, it adds unnecessary complication to the model. Therefore, the parameters are fixed to $p_0 = 10^6$, $p_3 = 4000$, $p_4 = 500$ and $p_5 = 2$.

The s parameter is fitted with a linear function

$$s(DX) = q_0 + q_1 \cdot \frac{DX}{\mathrm{g/cm^2}}. \tag{4.3}$$

Each fit is done for all four signal components and for all combinations of r, ψ. An example of the fits for the purely muonic component at $\psi = 90°$ is given in Fig. 4.18.

The longitudinal profile is simulated only to the height of the ground surface. As a result, the Gaisser-Hillas fit done by `CORSIKA` for very deep near to vertical showers can be unreliable because only the rising part of the profile can be used in the fit, i.e. the true X_{max} might be even below the ground. In such cases, the estimate of the true X_{max} (and hence also DX) can be wrong. Such showers are rejected by requiring X_{max} to be at least $50\,\mathrm{g/cm^2}$ above the ground along the shower axis. Note that this concerns only a small fraction of near-vertical proton showers.
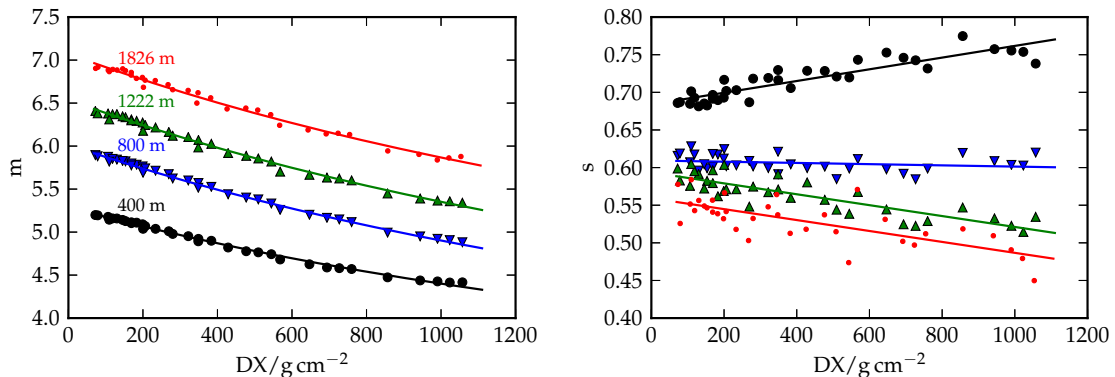
Figure 4.18: The parameters *m* (left) and *s* (right) of the lognormal for the purely muonic component for $\psi = 90°$ (see Eqs. (4.2) and (4.3) for the functional form). The distance to the shower axis is color coded (only four distances are shown while the actual model is based on 9 distances from 200 m to 2232 m). Time traces from showers of all energies, primaries and hadronic interaction models are used (as in the model used for the standard reconstruction).

The time model is based on proton and iron showers simulated with QGSJet II-03 and EPOS 1.99. It is referred to as the *reference model*.

The time model was made available in an internal publication [83] and a standalone version of the code was created [84] for use within the collaboration.

4.9 Deviations from universality in the time model

The model described here has no dependence on energy, primary particle or interaction model. It is universal in the sense that it depends only on DX and r, ψ in the shower plane. As a test for deviations from universality, the time model was derived separately for different interaction models and primary particles and the difference to the reference model is calculated. The residuals of the *m* parameter are shown in Figs. 4.19, A.3 and A.4. For the case of the time model built only with photon showers, the residuals are shown in Fig. A.2.

It is apparent that the time shape is not completely independent of mass, model and energy. Those universal-violating features are similar for all four signal components and at all azimuth angles. The purely muonic component at $\psi = 90°$ was chosen as a representative case. The importance of the universality violation is judged based on the systematics introduced in the reconstruction algorithm. It is shown in Section 6.7 that these model systematics are the smallest contribution to the overall systematic uncertainty.
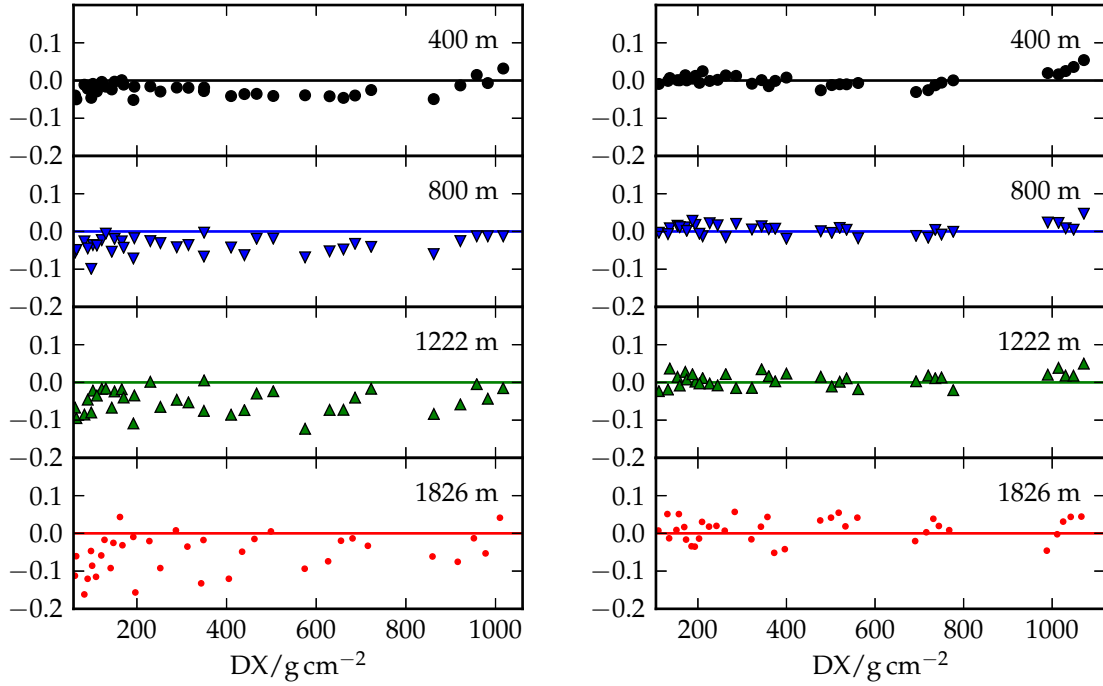
(a) Average component trace based on QGSJet II-03 proton

(b) Average component trace based on QGSJet II-03 iron

Figure 4.19: Violation of universality of the time shape of the purely muonic component. Each points corresponds to one average component trace. The difference of the *m* parameter of the lognormal to the prediction of the reference model (proton and iron, QGSJet II-03 and EPOS 1.99 mixed) is shown.

4.10 Validation of the time model

The time model predicts the simulated time traces accurately. This was checked by comparing the time quantiles obtained from the model and the traces. The time quantiles are given by the inverse of the c.d.f $F_c(t)$

$$F_c(t) = \int_0^q f_c(t)dt$$

where $q = 0.1, 0.3, 0.5, 0.9$ for the purpose of this study. The checks are done separately for each signal component. For the prediction of the quantiles in the simulated traces, the true geometry, X_{max}, X_0 etc. is used. The fitting routines are not used. The start time t_0 is obtained from the distance to the first interaction (see Eq. (4.1)).

The rise time of the trace is of special interested because this observable is often used in analyses of the mass composition (e.g. [85, 86, 87]). It is defined as the time that it takes for the trace to rise from 10 % to 50 % of its total integrated value. An example of the rise time calculated from the model is shown in Fig. 4.20. Overall, the description of the rise time by the model is very good. Small discrepancies are visible for very small and very large *DX*. A more thorough test of the model is the prediction of the absolute quantiles (because it shows

whether the absolute timing is predicted correctly). It is shown in Figs. A.5 to A.7. The 10 % and 50 % quantiles are predicted accurately while there is a large offset for the 90 % quantile. The discrepancy in the prediction of t_{90} can be explained due to the fact that the lognormal distribution falls off too quickly compared to the simulated trace.

The comparison shows that the timing of the shower front is predicted well except for the very late part of the trace. The systematic uncertainty coming from the assumption that the time model is universal in interaction model, primary and energy is shown in Fig. 4.21. For the comparison, the same showers are used to build the time model as for the comparison i.e. this is a check of self-consistency (in this case, proton showers at 10^{20}eV simulated with QGSJet II-03 are used). If the quantiles are predicted using the reference model (mixed composition), a systematic shift of the time quantiles occurs. This shift is responsible for the uncertainties that are studied in more detail in Section 6.7.

The time model gives an accurate description of the simulated signal. The validation based on real data is shown in Section 7.2.

4.11 Discussion and outlook

In this chapter, it was shown that the WCD signal and its time dependence can be described based on the concept of shower universality with three variables E, X_{max} and N_μ. These *time models* have been validated with a setup of simulated showers and WCDs created by the $\overline{\text{Off}}\underline{\text{line}}$ framework. The model predictions are also tested with real data (Chapter 7) using events with both SD and FD information (*golden hybrid events*).

With the current detectors design of the Pierre Auger Observatory, the the muon density on ground can be estimated with different methods, but a direct measurement of individual particles is not possible. Hence, to test shower universality, the muon content has to be fitted and the comparison is not completely independent of the reconstruction algorithm. All other parameters except for N_μ that define the shower can be taken from FD data to predict SD data.

Several extensions of the Pierre Auger Observatory are planned or being deployed. One of the main goals is to improve the sensitivity of the detector to the mass of the primary particle with a direct muon measurement. All these measurements rely on the shielding of the electromagnetic cascade. This is achieved by absorption in (part of) the WCD itself or in the ground. The reconstruction algorithm presented in this thesis will profit from a direct measurement of the muon number in each detector. With this information, the primary energy and the muon content can be determined at the same time without relying on a (model-dependent) energy calibration. Furthermore, it will be possible to validate shower universality without relying on the reconstruction algorithm.
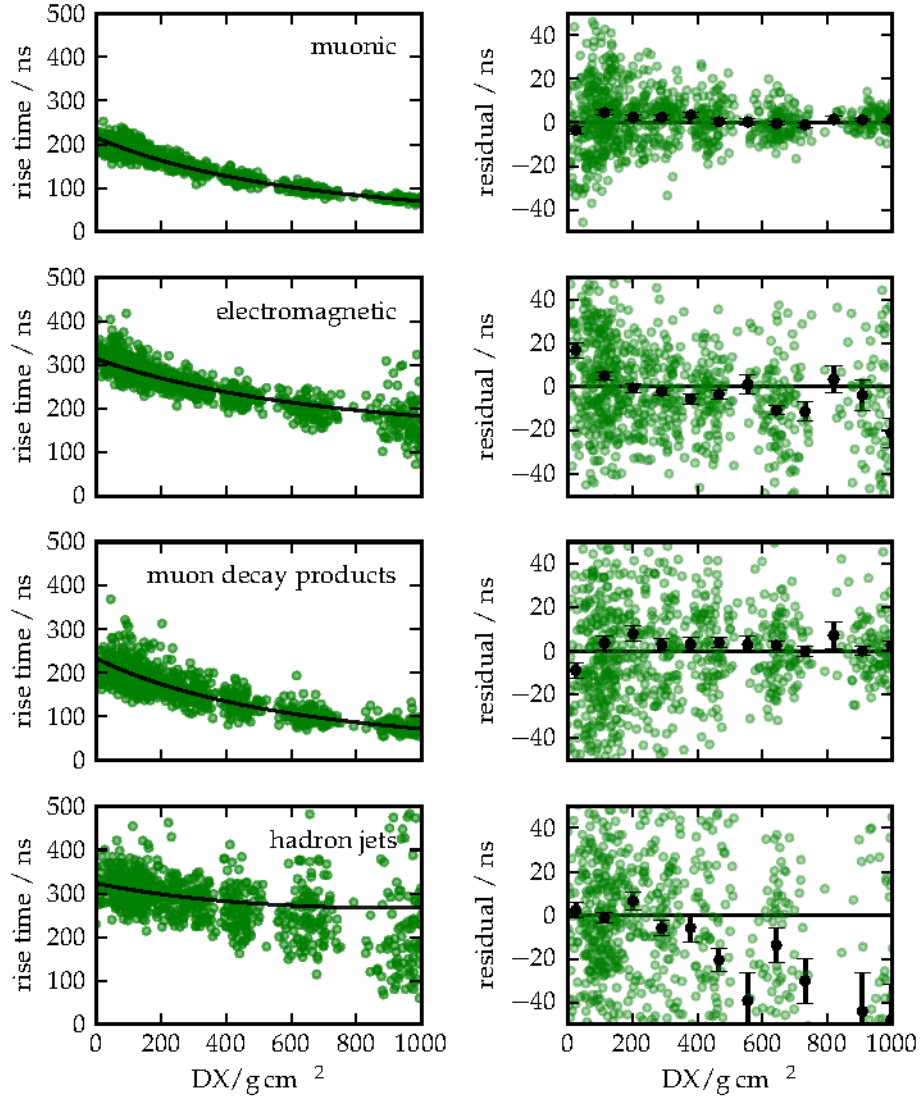
Figure 4.20: The rise time obtained from the simulated traces (green points) and the model prediction (solid black line). Dense stations at $r = 800\,\mathrm{m}$ and $\Psi = 90°$ are used. The residuals ($S_{\mathrm{simulation}} - S_{\mathrm{prediction}}$) are shown on the right.

(a) Rise time, self-consistency check

(b) Rise time, prediction from reference model

(c) t_{50}, self-consistency check

(d) t_{50}, prediction from reference model

(e) t_{90}, self-consistency check
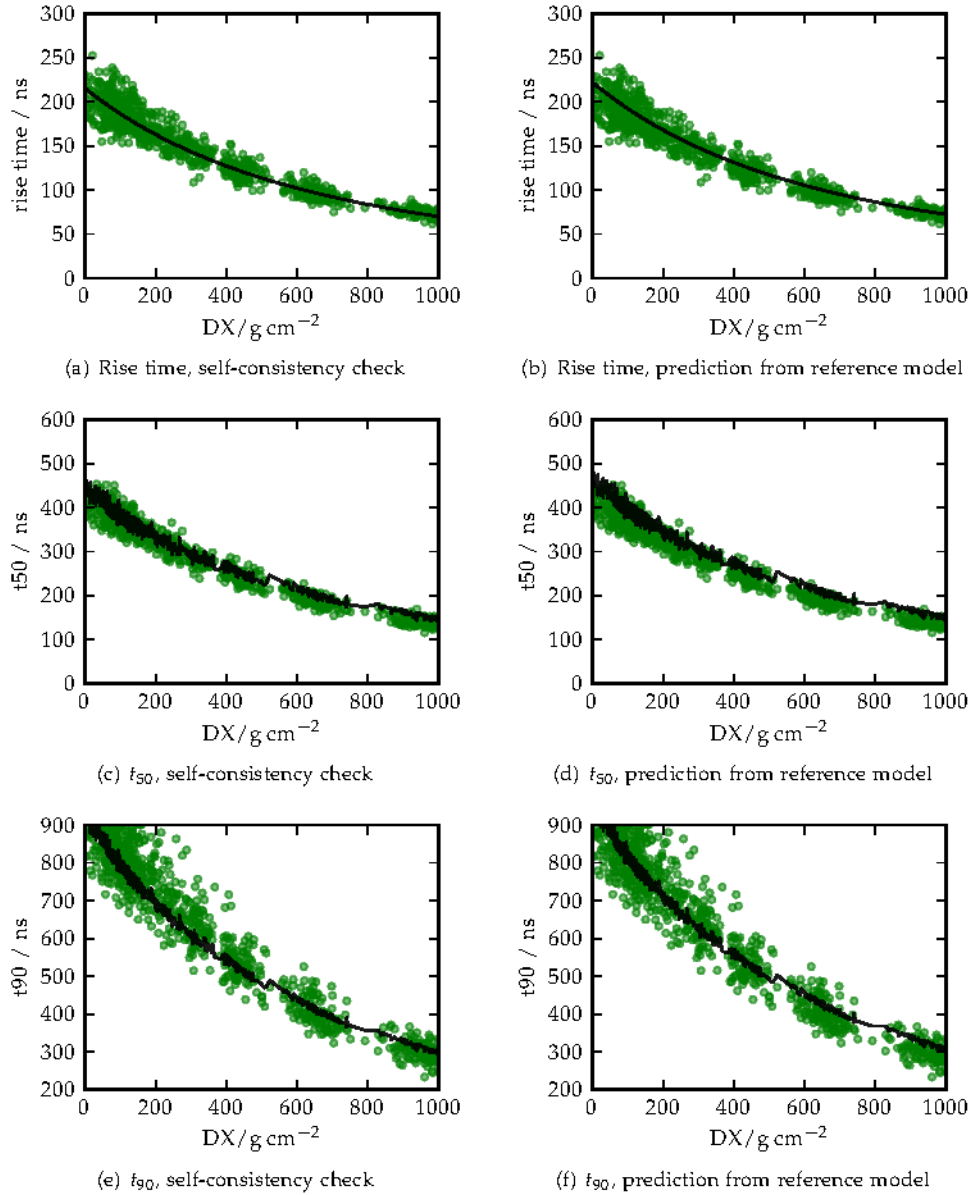
(f) t_{90}, prediction from reference model

Figure 4.21: Deviation from universality in the prediction of the time quantiles of the purely muonic component for proton QGSJet II-03 showers at 10^{20}eV. Dense stations at $r = 800$ m and $\Psi = 90°$ are used. **Left:** The prediction is based on the exact same showers (self-consistency). **Right:** The reference model was used, and the effect of violation of universality is apparent. The reference model is based on a mixture of models and primaries, hence there is an overall shift in the prediction of the start time. This is due to the model dependence of X_0 (see also Fig. A.9 and Appendix A.3).

5

Reconstruction of surface detector data based on air shower universality

A new algorithm for the reconstruction of extensive air showers has been implemented in the context of this work. It represents a new way of looking at the data measured by the surface detector.

The standard algorithm used for the SD reconstruction in $\overline{\text{Off}\underline{\text{line}}}$ is based on an NKG-type lateral distribution function to describe the lateral shape of the signal (Section 3.1.4). The arrival time of the shower front at the individual detectors is described by a spherical shower front. The parameters obtained from the standard reconstruction are the slope and normalization of the lateral distribution of the signals, the curvature of the shower front and the rise time of the signals. These parameters are correlated with the type of the primary particle and its energy. However, it is not possible to directly infer the mass and the properties of hadronic interactions at the highest energies. Furthermore, those variables are highly dependent on the specific detector design.

The shower models based on air shower universality allow to describe the signal on ground as a function of physical variables that are directly connected to the nature of the primary particle and the properties of hadronic interactions at the highest energies. These parameters are the muon content N_μ, the depth of shower maximum $X_{\max}$ and the depth of first interaction X_0. This is a more fundamental and also detector-independent way of describing a shower. Many phenomenological parameters that are used up to now (LDF slope, rise time) can be predicted by this model. The aim of the model is to provide a description that is independent of the detector. It is based on fundamental variables that describe the entire shower. In principle the reconstruction presented herein can be easily extended by data obtained from other types of detectors (see Chapter 9).

In this section, the details of the new reconstruction algorithm are described. It uses the models based on shower universality shown in Sections 4.5 and 4.7 to derive the geometry of the shower, $X_{\max}$ and N_μ. The core routines are implemented as a C++ class based on `Minuit2` [88, 89] and the $\overline{\text{Off}\underline{\text{line}}}$ geometry routines [77]. It can be interfaced to the $\overline{\text{Off}\underline{\text{line}}}$ framework to integrate the analysis in the standard reconstruction chain. In addition, an interface based

on `Python` and `SWIG` [90] was developed. In this way, the performance of a compiled language is combined with the flexibility and the rapid development cycle of a dynamically typed language. This is especially useful for the quickly evolving algorithms used for the analyses in this thesis. All the results presented herein are obtained using this approach.

The algorithm is implemented as a multi-parameter maximum likelihood fit. The initial parameters for the geometry and energy of the shower are taken from the standard $\overline{\text{Off}\underline{\text{line}}}$ reconstruction. N_μ is initially set to 1.0, while X_{max} is set to the mean value of the energy-dependent parametrization (Section 6.3). For some analyses of hybrid events (Section 7.2), the results from the FD reconstruction (Section 3.2.2) are used.

The stability of the reconstruction was tested by varying the initial values of the parameters. The algorithm is very robust. The result of the reconstruction has little to no dependence on the initial values. For example, in the standard configuration the initial value of X_{max} is set to the energy-dependent expectation of the mean of proton and iron showers (usually $700\,\text{g/cm}^2$ to $800\,\text{g/cm}^2$). However, even if the initial value is changed by several hundred g/cm^2, or even set to zero, the reconstructed X_{max} changes by less than $1\,\text{g/cm}^2$. This is especially important for the photon search (Section 8.6) because the difference of the initial and true parameters is larger.

5.1 Criteria for station selection

The fitting algorithm is based on three likelihood contributions. The first two parts are essentially a χ^2 fit of the total signals to the signal model and a χ^2 fit of the VEM trace to the time model. The third part is the likelihood to obtain the measured start time, given the prediction of the time model for the total trace and the number of particles in a station. All three contributions are formulated as log likelihood. The mathematical details are described in Section 5.2. Depending on the size and shape of the VEM trace a station contributes with the total signal, the start time or the content of individual bins. The average number of stations that contribute to the fit is shown in Fig. 5.1.

The first cut is imposed by the range of validity of the signal model. A station is used if its distance to the initial shower axis is at most $r = 2600\,\text{m}$. The same radial cut is used for the start time.

Stations that have at least 5 bins above 1 VEM, contribute bin-by-bin to the fit (*shape fit*). The assumption of Gaussian-distributed values is not valid at too low values. Hence only bins above 1 VEM contribute to the likelihood. This cut also reduces the dependence on the tails of trace that is known to be underestimated by the model. The remaining stations contribute with the LDF and start time fit if they pass the radial cut. Saturated stations have a very well-defined start time due to the large signal. They contribute only to the start time fit but not to the LDF or shape fit because of the cut-off. The influence of the precise value of the selection thresholds was checked. The reconstruction results (e.g. resolution of X_{max}) are found to be stable under a change of the thresholds.
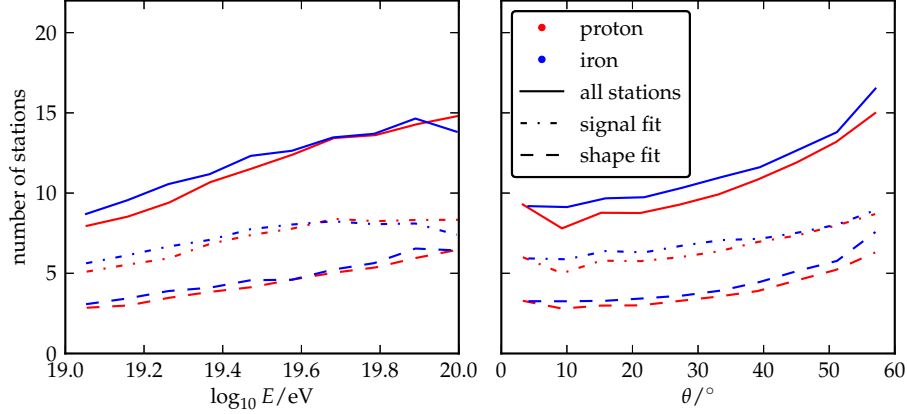
Figure 5.1: Average number of stations that are considered for the bin-by-bin time fit (*shape fit*) and the fit of the total signal (*signal fit*).

5.2 Construction of the likelihood

The likelihood is a function of nine parameters. The core position x, y, z, core time t_{core}, axis θ, ϕ. The coordinates of the core position refer to the weighted vector sum of the station positions (*barycenter*) [48]. t_{core} refers to the initial value (usually the fitted core time of the curvature fit in the `LDFFinderKG` module). X_{max}, N_μ and X_0. The height of the core z is always fixed. It was introduced so it can be easily changed in the future. The core time is fitted independently. It can be constrained to maintain compatibility with the initial core position and the speed of light. X_0 is coupled to X_{max} if not otherwise specified (Section 5.5). In general, all parameters can be fixed or left free depending on the type of analysis.

The total log likelihood is written as

$$\ln L_{total} = f(N_\mu, E, X_{max}, X_0, x, y, z, t_{core}, \theta, \phi) \,.$$

There are two main contributions: *station-based* (i.e. signal and time information), and *event-based* contributions (usually optional constraints on E and X_0).

Each station selected for the bin-by-bin time fit, contributes with $\ln L^k_{shape}$. The remaining stations contribute with the total signal and start time, $\ln L^i_{signal} + \ln L^i_{start}$. The total likelihood reads as

$$\ln L_{total} = \sum_{\text{stations k}} \ln L^k_{shape}$$
$$+ \sum_{\text{stations i}} \ln L^i_{signal} + \ln L^i_{start} \,.$$

Additional terms can be added to the likelihood to constrain E, X_0 or X_{max}.

The integrated signal S_c of a component c at a position r, ψ in the shower plane is given by the universal model (Section 4.5) as

$$S_c = f(N_\mu, E, DX, \theta, r, \psi)$$

where S_c is multiplied by 1.13 to account for the discrepancy shown in Fig. 4.12. The normalized signal at the time t_{PF} of a component c given by

$$s_c = f(\mathrm{DX}, \mathrm{DX}_0, \theta, r, \psi, t_{\mathrm{PF}}),$$

which is simply a lognormal function with the parameters m and s as derived in Section 4.7 and a time offset between the plane and curved front t_0,

$$s_c = \mathrm{lognormal}(m, s, t_0).$$

The method to calculate the start time t_0 from the geometric distance to the first interaction DX_0 is described in Eq. (4.1) on page 44. The parameters of the lognormal are stored for the distances given in Section 4.3 and for $\psi = 0°, 90°, 180°$. The values of m and s for the actual detector position are obtained from a linear interpolation first in ψ and then in r.

The total expected signal at the time t_{PF} is a weighted sum of the component signals and time shapes,

$$S_{\mathrm{tot}}(t_{\mathrm{PF}}) = \sum_{\mathrm{comp.}\, c} S_c \cdot s_c(t_{\mathrm{PF}}).$$

Using the standard normal distribution

$$f_{\mathrm{G}}(x, \mu, \sigma) = \frac{1}{\sqrt{2\pi}\,\sigma} \exp\left(-\frac{(x-\mu)^2}{2\sigma^2}\right)$$

the bin-by-bin time contribution of a station k with the measured signal S_k^m in the bin m to the likelihood reads as

$$\ln L_{\mathrm{shape}}^k = \sum_{\mathrm{bins}\, m} \ln f_G\left(S_k^m, S_{\mathrm{tot}}^m, \sigma(S_{\mathrm{tot}}^m)\right).$$

This is essentially a chi-square fit of the traces to the time model summed over all stations selected for the shape fit.

The uncertainty $\sigma(S)$ of the total signal reads as

$$\sigma_S(\theta) = f_S(\theta)\,\sqrt{S},$$

where

$$f_S(\theta) = 0.34 + 0.46/\cos\theta.$$

This is referred to as the *signal uncertainty model* [53]. It is obtained from the signal spread of twin stations (for more details, see Section 3.1.4).

Using the standard signal uncertainty model for individual bins can be criticized due to the comparatively low (>1 VEM) bin content. Furthermore, correlations of neighboring bins due to signal decay time are ignored in the current state. In general, ignoring those correlations leads to an underestimated χ^2.

The total signal S_{tot} is written as

$$S_{\mathrm{tot}} = \sum_{\mathrm{comp.}\, c} S_c.$$

The likelihood contribution of the total integrated signal reads

$$\ln L_{\text{signal}}^i = \ln f_G\left(S^m, S_{\text{tot}}, \sigma(S_{\text{tot}})\right).$$

Again, this corresponds to a chi-square fit written in the form of a log likelihood.

The start time of the signal determines the arrival direction and the curvature of the shower front. In the standard reconstruction, the start times are used to fit a spherical shower front. This fit uses a time variance model where the uncertainty of the start time is a function of the rise time (the time it takes the integrated trace from 10 % to 50 % of its total value). This becomes problematic at large distances from the core when a station samples only a few particles. The rise time can become too low. In the most extreme case it is the rise time of the muon peak. At large distances, the particles in the shower front are spread out widely in time, while the calculation based on the rise time gives a very low value.

The situation can be improved with the time model presented in Section 4.7. The time model describes the arrival times of particles in the shower front. The p.d.f. $f_1(t)$ for the arrival time of the first particle is from the time shape $f(t)$ by extreme value transformation [50]. The individual particle arrival times can be reordered such that

$$t_1 < t_2 < t_3 \cdots < t_n.$$

Where n is the number of detected particles. The probability of t_1 being less than some given t is complementary to the probability of all t_i being larger,

$$F_1(t) = 1 - (1 - F(t))^n.$$

Using the cumulative distribution function $F(t)$

$$F(t) = \int_0^t f(t)\, dt$$

the distribution of t_1 is obtained from the derivative of $F(t)$ evaluated at t_1,

$$\begin{aligned} f_1(t_1) &= dF_1/dt|_{t=t_1} \\ &= n(1 - F(t_1))^{n-1} f(t_1). \end{aligned}$$

In a given tank, the start time is identified with the arrival time of the first particle,

$$f_1(t_{\text{start}}) = n\left(1 - \int_0^{t_{\text{start}}} f(t')dt'\right)^{n-1} f(t_{\text{start}}). \tag{5.1}$$

Provided that $f(t)$ is an unbiased estimate of the time distribution of ground particles, $f_1(t)$ automatically gives the correct time variance. The underestimation of the variance of the start time is solved.

Due to the exponent in Eq. (5.1), the width of $f_1(t)$ becomes smaller than the FADC bin width if more than a few particles hit the station. Hence, the arrival time of the curved front has to match the prediction derived from f_1 in a very narrow (unphysical) time interval. To
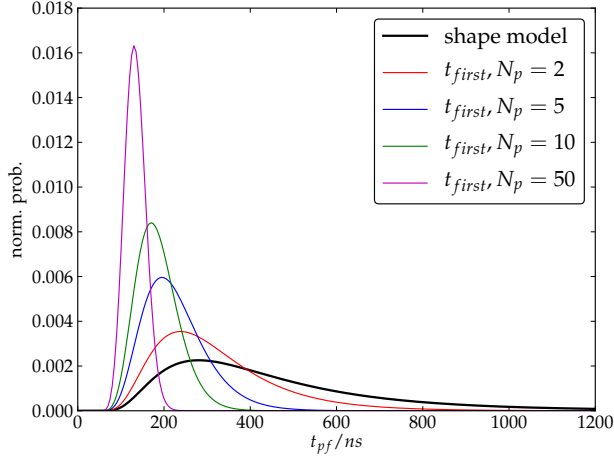
Figure 5.2: Using the shape model $f(t)$ (black line), a p.d.f. for the arrival time of the first particle $f_1(t)$ is obtained by extreme value transformation. $f_1(t)$ is shown for different numbers of particles N_p (colored lines).
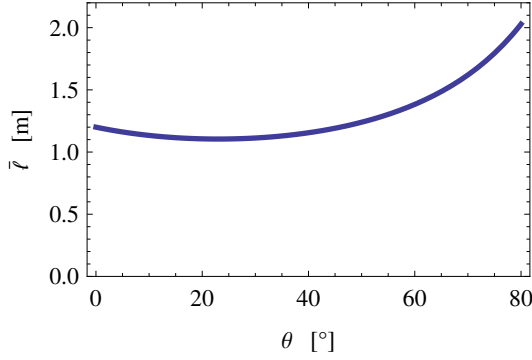

Figure 5.3: The relative track length $\bar{l}$ (RTL) of a muon in a water Cherenkov detector (height $h = 1.2$ m, radius $r = 1.8$ m). For vertical muons, the average corresponds to the height of the detector. The average decreases up to $20°$ because of corner-clipping particles. Above that, muons start to cross the detector (almost) horizontally.

account for the uncertainty on the GPS time and for the finite bin width, $f_1(t)$ is smeared by a Gaussian $g(\mu = 0, \sigma = 25 \text{ ns})$ according to

$$f_1(t)_{\text{smeared}} = \int_{-\infty}^{\infty} f_1(t - \tau) g(\tau) d\tau .$$

The smearing is applied in each iteration of the fit. For performance reasons, the folding integral is approximated by a discrete sum,

$$f_1(t)_{\text{smeared}} \approx \sum_i f_1(t - \tau_i) g(\tau_i) \Delta\tau \qquad \text{where } -3\sigma < \tau_i < 3\sigma .$$

The step size is set to $\Delta\tau = 2$ ns.

An example of the p.d.f. for the first particle with different numbers of particles is shown in Fig. 5.2. The expected variance of the start time is calculated from $f_1(t)$. A comparison to the simulation and the prediction of the standard time variance model [50] is shown in Fig. 5.7.

For the reconstruction, it is assumed that the early part of the shower front consists mainly of muons because the time delay of muons due to scattering is very small. Hence, the time model for the pure muonic component may be used. The number of particles is obtained from the expected muonic signal S^μ_{model}. Because the signal produced by a muon depends on

the track length in the water, n is obtained as

$$n = S^{\mu}_{\text{model}}/\text{RTL}(\theta_s)$$

where h is the height and r the radius of the tank and $\text{RTL}(\theta_s)$ is the relative track length [91]

$$\text{RTL}(\theta_s) = \left(\cos\theta_s + \frac{2h\sin\theta_s}{\pi r} \right)^{-1}$$

where θ_s denotes the incident angle of the shower front at the station. The relative track length as a function of the incoming angle of the particle is shown in Fig. 5.3.

Finally, one obtains for the start time contribution of a station j

$$\ln L_{\text{start}} = \ln \left[n_j \left(1 - \int_0^{t_{\text{start}}} s^{\mu}(t')dt' \right)^{n_j-1} s^{\mu}(t_{\text{start}}) \right].$$

5.3 Correction for the missing energy

The energy used for the universality reconstruction is taken from the shower size estimate S_{1000}, which in turn is calibrated to the calorimetric energy measured in hybrid events. The fluorescence light is mainly generated by the electromagnetic cascade. Therefore, the energy carried by muons and neutrinos is not visible (called *missing energy*). The average amount of this energy is parametrized as a function of the calorimetric energy to obtain the total energy (Section 3.2.2). However, the approach up to version v9r1 of the official reconstruction code was only correct on average. The amount of missing energy depends also on the distance of the shower to the ground due to the absorption in the atmosphere. From v9r3 on, this is correctly taken into account [92, 63]. For v9r1, the missing energy needs to be rescaled according to N_{μ}. The correction factor for the missing energy in the standard reconstruction depends on assumptions on primary mass and hadronic interaction model and thus on the muon content of the shower. If $N_{\mu} \neq 1$, the correction obtained from proton simulations using QGSJet II-03 is incorrect. Therefore, the missing energy factor has to be rescaled. This is done in each iteration of the fit, because the factor depends on N_{μ} (which is also fitted). The correction factor f is defined as

$$f = \frac{E_{\text{tot}}}{E_{\text{cal}}}$$

or, equivalently

$$E_{\text{tot}} = f \cdot E_{\text{cal}}.$$

With the missing energy denoted by ΔE, one obtains

$$E_{\text{tot}} = E_{\text{cal}} + \Delta E.$$

For $N_{\mu} \neq 1$, and assuming that the missing energy scales linearly with N_{μ}, the total energy E'_{tot} after rescaling is

$$\begin{aligned}
E'_{\text{tot}} &= E_{\text{cal}} + N_{\mu}\Delta E \\
&= E_{\text{cal}} + N_{\mu}(E_{\text{tot}} - E_{\text{cal}}) \\
&= (1 - N_{\mu})E_{\text{cal}} + N_{\mu}E_{\text{tot}} \\
&= (1 - N_{\mu})E_{\text{cal}} + fN_{\mu}E_{\text{cal}} \\
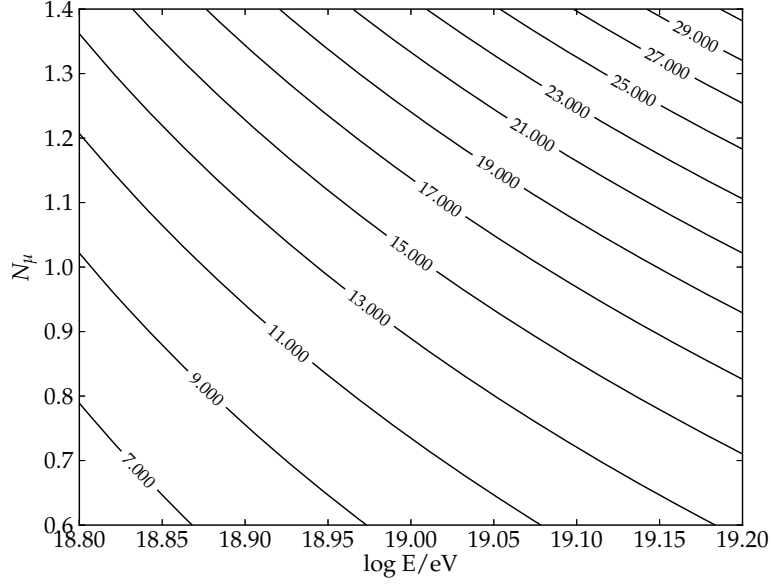&= (1 + N_{\mu}(f - 1))E_{\text{cal}}.
\end{aligned}$$

Figure 5.4: N_μ and E are correlated because muonic and electromagnetic part of the signal is not measured separately by the WCD. With only one detector in an event, the muonic signal can be obtained by every combination N_μ-E on the corresponding contour line. The degeneracy is considerably reduced because the ratio of signal components depends on the distance of the detector to the shower core.

In [61], the missing energy is parametrized as a function of E_{cal},

$$\frac{E_{\text{cal}}}{E_0} = p_0 - p_1 \left(\frac{E_{\text{cal}}}{1\text{EeV}} \right)^{-p_2} . \tag{5.2}$$

The values are obtained from the parametrization for proton showers simulated with QGSJet01 [93, 94]. However, the fitting routines are based on the total energy. Eq. (5.2) is solved numerically in each iteration of the fit to calculate the rescaled total energy.

5.4 Correlation of muon scale and total energy

The total energy E is fixed to its initial value while N_μ is a free parameter. Because the different contributions to the total signal in a tank are not measured separately there is an ambiguity between the total energy and the overall muon scale of the shower. This causes a strong correlation of both parameters. An example is shown in Fig. 5.4: The total muonic signal in a single tank can be obtained by lowering the total energy and increasing the muon scale at the same time.

The ambiguity between N_μ and E is solved in part because the ratio of electromagnetic to muonic signal depends on the position of the station in the shower plane. The distance to X_{max} sets an additional constraint (it determines the size of the electromagnetic contribution). N_μ and E can be fitted both at the same time. There is no bias, but the reconstruction spread of both variables increases considerably.

5.5 Correlation and coupling of X_{max} and X_0

In principle, the fitting algorithm allows to reconstruct the depth of shower maximum X_{max} and the depth of first interaction X_0 independently. The curvature of the shower front and thus the start time of the signal in the tanks is mainly determined by the depth of first interaction. The shape of the signal depends mainly on X_{max}. However, there is a strong correlation between X_{max} and X_0: A shower with a deep X_0 is likely have a deep X_{max} and vice versa (see also [95]). This correlation makes it difficult to fit both X_{max} and X_0 at the same time and increases the spread as well as the bias especially for events with low station multiplicity. If not explicitly mentioned, X_{max} and X_0 are *coupled* using a model derived from simulations (see Appendix A.3).

This introduces a dependence on model and primary particle. While the influence of the primary mass is small (meaning that a single model for the description of both iron and proton can be found, Fig. A.8), the correlation is different depending on the hadronic interaction model. Furthermore, the dependence is different for photon primaries. This introduces a systematic error in the reconstruction of X_{max} (Section 6.7).

The standard parametrization for all the analyses in this thesis is based on an equal mixture of proton and iron showers, simulated with QGSJet II-03 and EPOS 1.99 (Fig. A.9). The correlation based only on QGSJet II-03 is shown in Fig. A.10, for EPOS 1.99 in Fig. A.11.

5.6 Example of a reconstructed shower

To visualize the results of the new reconstruction, a simulated proton shower with $E = 10^{19.5}$eV and $\theta = 36°$ was chosen. Due to the complexity of the fit, some projection has to be chosen for the visualization. In Fig. 5.5, the lateral shape of the signal is shown. In this case, four stations are selected for the bin-by-bin time fit. The shape of the signal in these stations is shown in Fig. 5.6. The likelihood is calculated using only the total (time-dependent) signal. With the universality parameters obtained from the fit, the whole time dependence of the four signal components can be predicted. The measurement and prediction of the shower front curvature is shown in Fig. 5.7.

Figuratively speaking, in Fig. 5.5, the reconstruction code fits the black line to the black points. The colored parts of the example plots are predictions based on the reconstructed parameters. The reconstructed parameters describe the simulated signal components very well. The variance of the start time as predicted by this algorithm is larger than in the standard method.

In some cases, the minimization does not converge. These fits are not used further on. The fraction of events where the minimization converges in shown in Fig. 5.8. There is no systematic difference on mass introduced by rejecting these events. This issue could not be solved completely but is likely due to geometrical properties, i.e. arrival direction or distance of the shower axis to the nearest station.
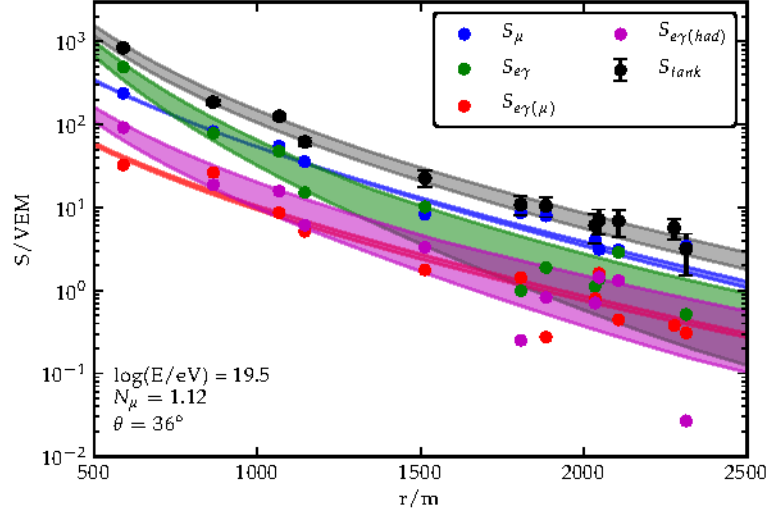
Figure 5.5: Lateral shape of the signal. Figuratively speaking, the black band is fitted to the black points. The colored bands show the prediction for the four signal components compared to the simulated values (colored points). The size of the signal asymmetry is indicated by the width of the bands: The upper and lower boundaries show the extreme case of $\Psi = 0°$ and $180°$. The large asymmetry of both electromagnetic compared to the muonic components is apparent.
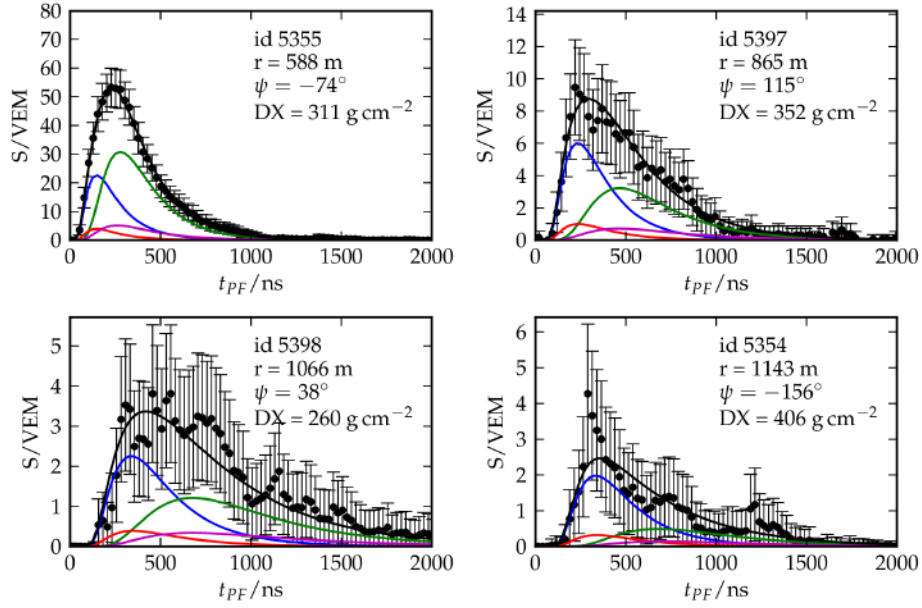

Figure 5.6: Time dependence of the signal in the four *hottest* stations. The model (black line) is fitted to the bin entries of the VEM trace (black points). The position in the shower plane coordinate system and the distance to X_{max} is shown for each station. From the fitted parameters, a prediction for the time dependence of the components is obtained (colored lines).
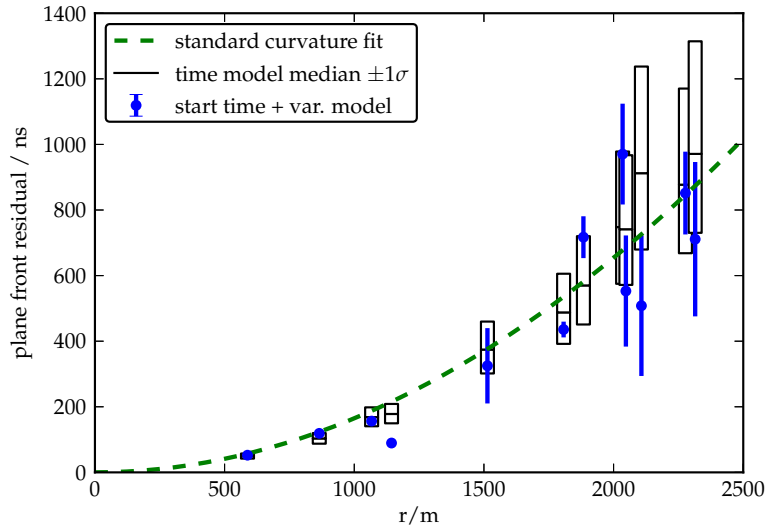
Figure 5.7: Prediction of the shower front curvature from extreme value transformation of the time model. The dashed line is the curvature fitted by the standard SD reconstruction, along with the measured start times (blue) and their respective uncertainties from the time variance model [50]. The upper and lower edges of the black rectangles indicate the 1σ quantiles of the p.d.f. for the start time, the center line is the median value. The standard uncertainty model underestimates the variance at large distance due to single muons. This is solved with the time model presented herein.

5.7 Discussion and outlook

Several extensions of the Pierre Auger Observatory are planned or being deployed. The reconstruction can be improved with a comparatively simple upgrade of the readout electronics. Increase of the sampling rate from (or higher). With faster sampling (i.e. 120 MHz instead of 40 MHz), the arrival time can be measured more precisely, which will improve the reconstruction of arrival direction and shower front curvature. Faster sampling will also improve muon counting algorithms that rely on the time dependence of the signal.
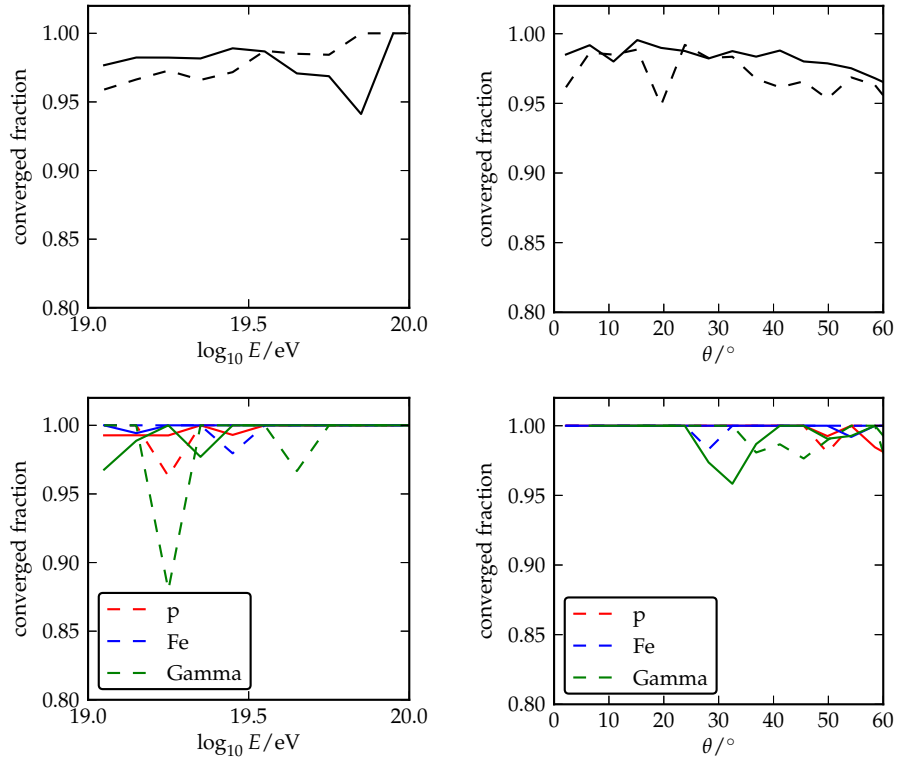
Figure 5.8: The fraction of events where the minimization converges for data (top) and simulated showers (bottom). Events without (solid lines) and with saturation (dashed lines). Photon showers with saturation are the most challenging candidates for the reconstruction. Due to the steep lateral slope, very few stations can be considered for the time trace fit.

6

Validation of shower universality in simulated showers

In this chapter the predictive power of shower universality is studied based on simulated showers. All the results presented in this section are obtained using the simulated showers described in Section 4.2. It is shown that the models developed in Chapter 4 predict the signal in the water Cherenkov detectors (WCDs) accurately. The accuracy of the reconstruction of X_{max} and N_μ and several sources of systematic uncertainties are studied in detail.

6.1 Prediction of the WCD signals

To check the accuracy of the model predictions, the result needs to be independent of the reconstruction algorithm. Therefore, the true values of E, X_{max}, X_0 and the geometry of the shower are used to predict the signal. N_μ is fitted in each event with the time contribution in the likelihood turned off. Note that the model prediction was rescaled by 13 % to account for the mismatch shown in Fig. 4.12. For this study, the continuous library is used. Saturated stations are not used. A cut on the expected signal $S > 10\,\text{VEM}$ was set to avoid a bias from upward fluctuations of the signal (*trigger bias*).

On average, the model predicts the simulated signal well. In most cases, the deviations are below 0.5σ. In Fig. 6.1, the core position was fixed to the true value (N_μ is the only free parameter). In Fig. 6.2, the core position is fitted in addition. In both cases, the signals are predicted accurately, while the NKG function has a distance-dependent bias. When the core position is fitted using universality, there is a small improvement in the residuals. This effect is in agreement with the small remaining systematic bias of the core position to the early region of the shower (Fig. 6.3). It suggests that the description of the azimuthal asymmetry of the signal is not perfect. Part of the discrepancy of the NKG function is because the shape of the lateral distribution is optimized for hadronic mass composition. In particular, this explains the bad performance of the NKG function in photon simulations. For a fair comparison, a different lateral shape has to be used, e.g. [57]. Nevertheless it shows that the same universal models can be used for hadronic and photon showers. For the case of the NKG function, the shape model (dependence of the slope on zenith angle) i.e. the type of the primary particle needs to be known before the fit is done. Because there are more muons in data than in simulations, especially the discrepancy at large distances can be understood because of the flatter distribution of the muonic LDF. The comparison for data is shown in Section 7.2.1.
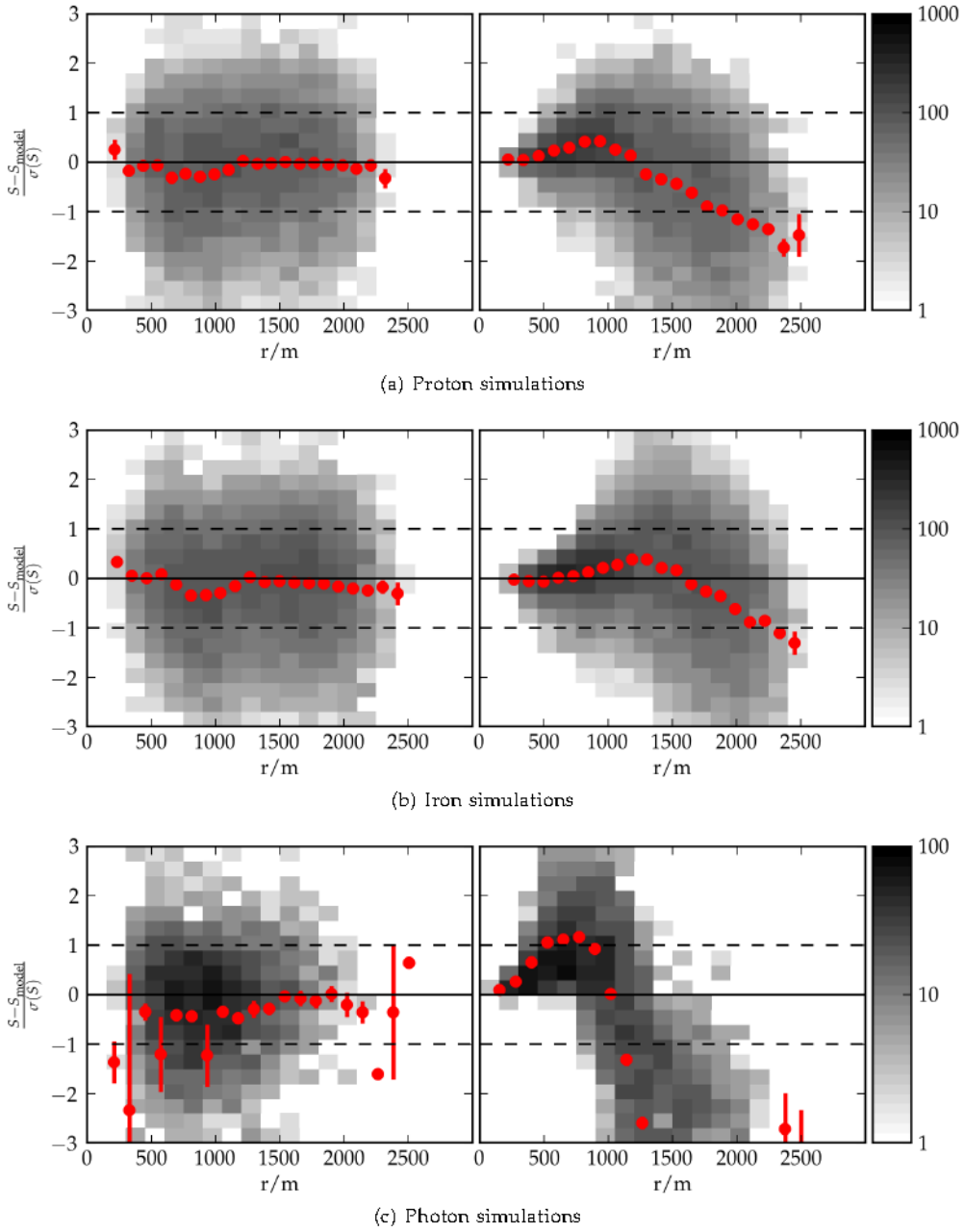
(a) Proton simulations

(b) Iron simulations

(c) Photon simulations

Figure 6.1: Residuals of the WCD signals and the model prediction for simulated showers. **Universality** (left column), **one dimensional NKG shape** (right column). The distribution of individual values is indicated by the shaded area. The residuals to the universal model are obtained by fitting N_μ to the total signals (no time model is used), while E, X_{max}, X_0, axis and core are set to the true values. The comparison for data is shown in Section 7.2.1.

(a) Proton simulations

(b) Iron simulations
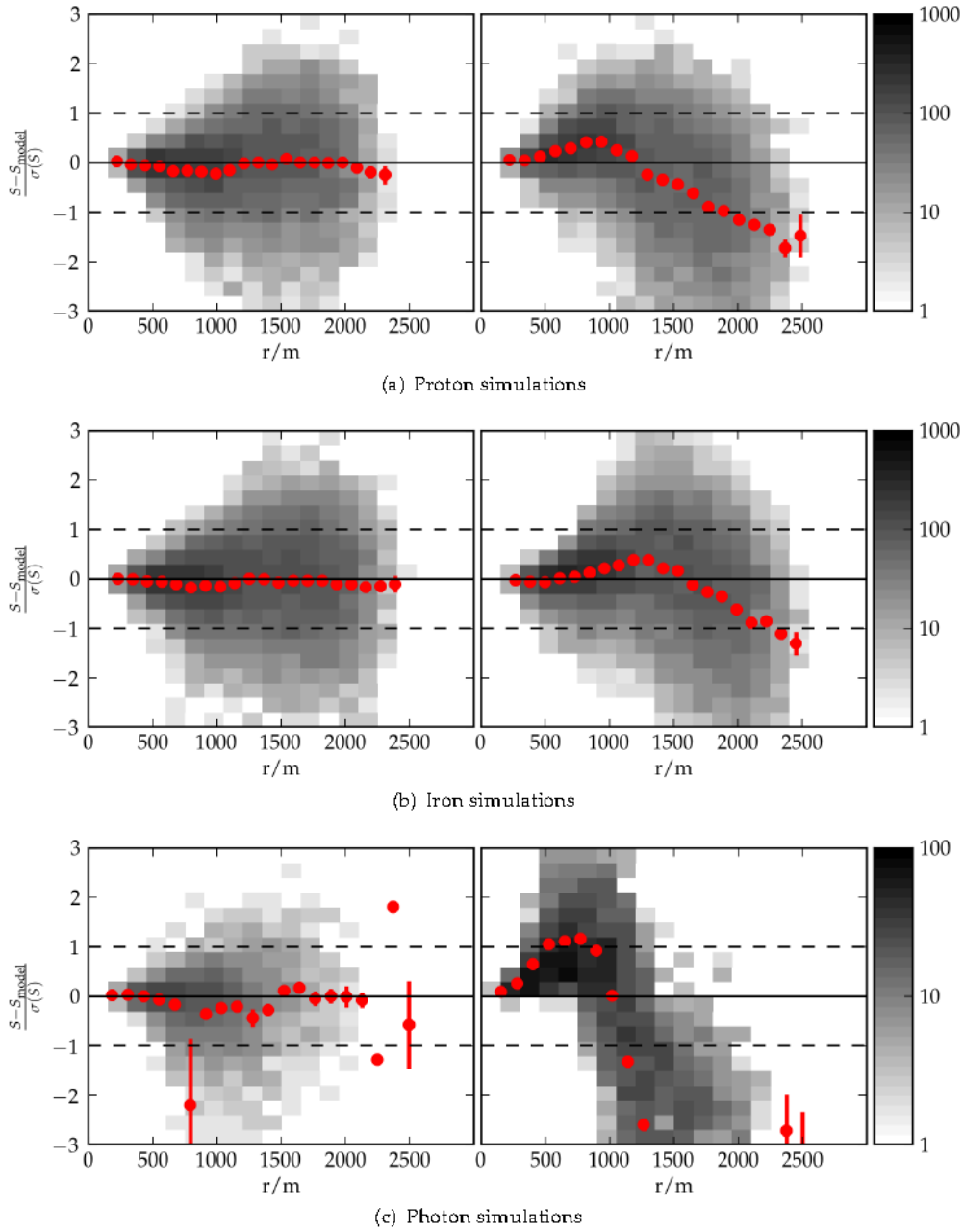

(c) Photon simulations

Figure 6.2: The same as Fig. 6.1, except that for the comparison to the universal model, the core was fitted in addition.

6.2 Accuracy of core position and axis (shower geometry)

The signal model used in the reconstruction includes all signal asymmetries due to atmospheric attenuation and detector effects (Section 4.5). It is therefore expected to give a bias-free (without systematic shift) estimate of the signal on ground regardless of the position in the shower plane and the distance to X_{max}. The standard reconstruction uses a NKG-type LDF that ignores azimuthal asymmetries. Therefore, the core is shifted systematically to the early region of the shower because asymmetries are ignored (referred to as the *core bias* further on). This core bias is expected to vanish. The reconstruction of the shower axis is also expected to be bias-free. However, compared to the core position, this is a minor effect.

The reconstructed core position is calculated in the shower plane coordinate system of the true geometry. In Fig. 6.3, the results are shown for 100 proton showers at 10^{19}eV and $\theta = 45°$. The effect of the increasing attenuation on the core bias can be clearly seen. When shower universality is used, the bias (and its zenith-dependence) vanishes completely in the whole range $\theta = 0° - 60°$ (except for small sampling fluctuations due to the finite size of the data set). The core positions for each fixed zenith angle are shown in Fig. A.27. Above 55° the electromagnetic component of the shower starts to vanish rapidly. Because the muonic part of the shower is only weakly attenuated in the atmosphere, the bias in the core estimate from the NKG fit decreases above $\theta = 55°$. In the FD reconstruction, the shower core is also expected to be unbiased (because it is independent of signal asymmetries on ground). This is studied in Section 7.3.

The reconstruction of the arrival direction is almost unbiased in both reconstruction methods (Fig. 6.4). The bias in zenith angle is smaller for intermediate angles in the universal method, which indicates a better description of the shower when considering asymmetries. The discrepancy in azimuth is a result of the degeneracy of ϕ in spherical coordinates for vertical showers. The angular resolution is shown for proton showers at 10^{19}eV and $10^{19.5}$eV in Fig. 6.5. The accuracy is comparable in both reconstruction algorithms. The universal method performs better at intermediate angles. The results are similar for other energies and for iron showers.

The effect of saturation on the geometry reconstruction was checked. The reconstruction becomes more difficult with saturated stations. The resolution in both core position and axis is worse while the core position remains unbiased. However, no fundamentally different behavior was found in events with saturated stations.

6.3 Reconstruction of the depth of shower maximum

In this section, the reconstruction accuracy of the depth of shower maximum X_{max} is shown. The dependency on primary particle, energy, zenith angle and FADC saturation is studied in detail. For the studies in this section, the continuous library is used. In principle, the shower models describe the signal in the WCDs accurately starting at $10^{18.6}$eV. However, at this energy the average number of triggering stations per event is very low (only 3 in the extreme case of vertical events) Therefore, the reconstruction of X_{max} is difficult and the spread becomes very large. Moreover, the event statistics available from the FD in the low-energy range is very large. Hence, only events $E > 10^{19.0}$eV are considered. The correlation of the true and reconstructed X_{max} is shown in Figs. A.12 to A.14.
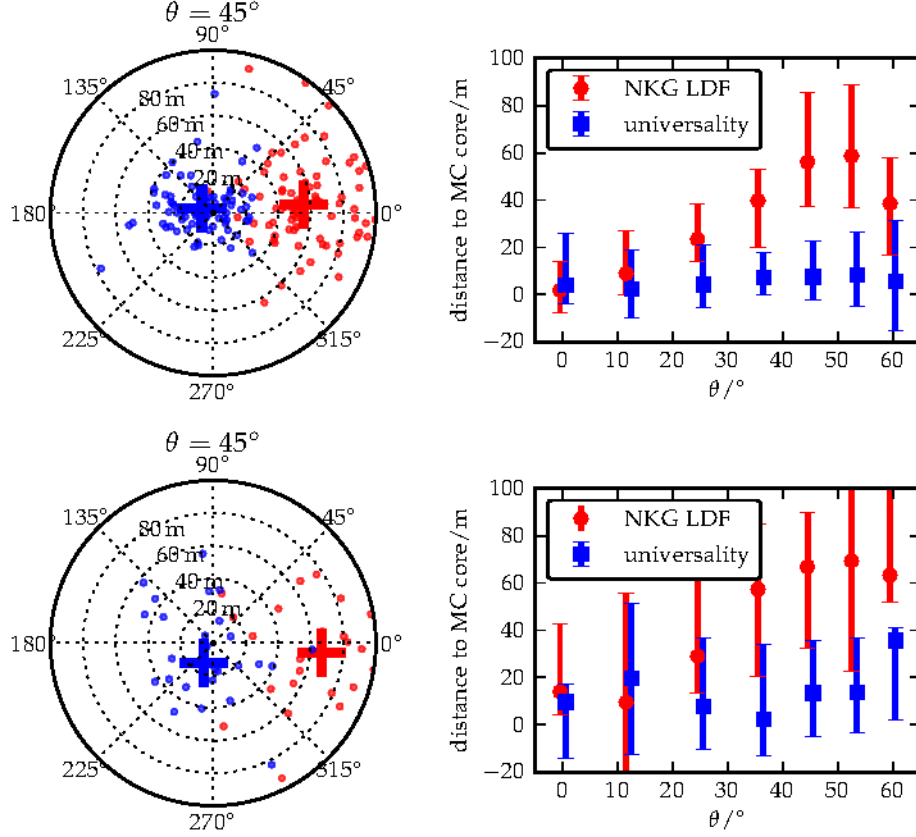
Figure 6.3: Bias of the reconstructed core position in MC shower plane coordinates for proton simulations at $10^{19.5}$eV. **Left:** $\theta = 45°$. Showers are rotated in ϕ such that the incoming direction is to the right. The large cross markers indicate the mean value of all points. **Right:** average bias of the reconstructed core position. **Top:** no saturation. **Bottom:** events with saturation. **Red:** standard reconstruction (`LDFFinderKG`). **Blue:** this work, taking into account signal asymmetries. Points are shifted for better readability.

6.3.1 Bias of the reconstructed X_{max}

The X_{max} based on timing information of the WCDs has a reconstruction bias. In most cases, X_{max} is shifted systematically to smaller values. This bias depends on primary energy and zenith angle. It is corrected empirically by assuming a linear shape in θ and $\log_{10} E$,

$$\Delta[X_{max}] = f(\log_{10} E, \theta) = p_0 + p_1 \log_{10} E /\text{eV} + p_2 \theta/° \, . \tag{6.1}$$

The same reconstruction bias is apparent in the fixed library (for details, see Fig. A.28). At the current stage, the bias is not fully understood. A detailed discussion is given in Section 6.3.1.5.
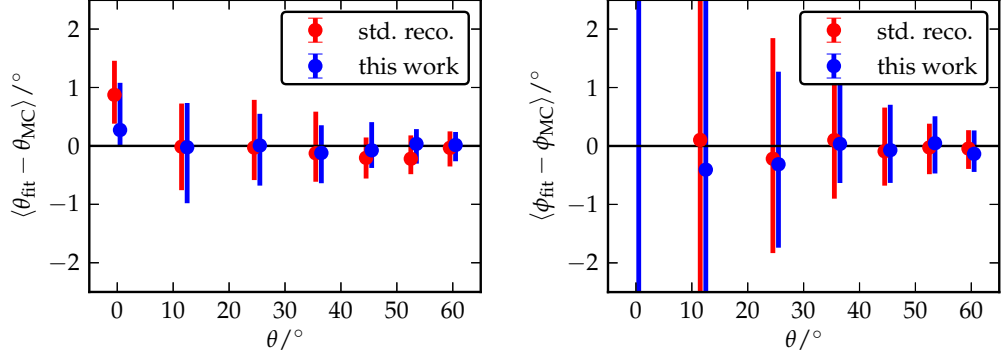
Figure 6.4: Average bias of the reconstructed shower axis for proton showers at 10^{19}eV **Left:** zenith angle **Right:** azimuth angle (the large spread for small θ comes from the ambiguity of ϕ in spherical coordinates). **Red:** standard reconstruction (`LDFFinderKG`), **Blue:** this work. Points are shifted for better readability.
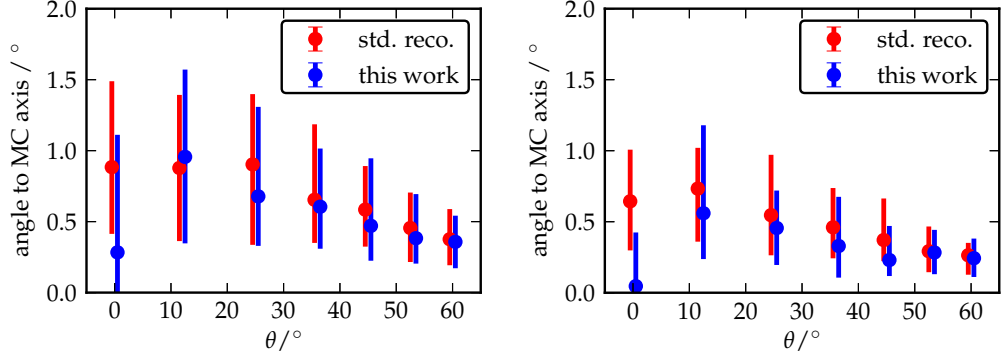

Figure 6.5: Resolution of the reconstruction of the shower axis for proton showers. **Left:** 10^{19}eV, **Right:** $10^{19.5}$eV. **Red:** standard reconstruction (`LDFFinderKG`), **Blue:** this work. Points are shifted for better readability.

6.3.1.1 Events without saturated stations

The X_{max} bias in events without saturated stations is subtracted using Eq. (6.1). The average bias before and after correction is shown in Fig. 6.6. The remaining bias due to the non-linear shape is comparatively small. If X_0 is coupled to X_{max}, there is a small mass dependence but the resolution improves because the ambiguity introduced by X_0 and X_{max} is reduced. With X_0 coupled to X_{max}, a dependence on primary mass is expected because the X_{max}-X_0-model is based on a mixture of proton and iron showers (Section 5.5). The systematic error introduced by the coupling is studied in Section 6.7. In the case of fitted X_0, both proton and iron showers show the same reconstruction bias. In this case however, the resolution is worse, as is shown in the next section. The remaining systematic uncertainty after the correction is below 10 g/cm^2.

If only showers with $25° < \theta < 50°$ are accepted, the systematic error due to the remaining

bias can be reduced and it is possible to correct for the bias uniformly over the whole energy and zenith angle range (Fig. A.17). This comes naturally at the expense of reduced statistics. The cut efficiency for $\theta > 25°$ is 0.81, for $\theta < 50°$ it is 0.77. After both cuts, 62 % of all events pass the cut in θ.

6.3.1.2 Events with saturated stations

In events with saturated stations, the shape of the reconstruction bias is the same as without saturation. However, the difference between proton and iron is much larger (Fig. 6.7). The bias can be corrected with the same approach as in Eq. (6.1), but the systematic uncertainty after correction is in the order of $20\,\text{g/cm}^2$ to $30\,\text{g/cm}^2$.

6.3.1.3 Photon-induced showers

The reconstruction bias of photon showers[1] is similar compared to hadronic showers. Photon showers can be subtracted with the same correction parameters as hadronic showers. in Eq. (6.1). If, in the reconstruction, X_0 is coupled to X_{max} according to the model derived from photons, the remaining systematic uncertainty is very small (Fig. 6.8).

The same coupling function has to be used for all events because the nature of the primary particle is not known a priori. If the coupling model based on a mixture of proton and iron is used (Fig. A.9) a systematic shift of $-20\,\text{g/cm}^2$ is introduced. Hence, the X_{max} for photons is shifted towards the mean value for protons. This is expected because an assumption about the mass is made in the reconstruction.

For the calculation of the bias in X_{max}, showers are accepted only if the shower maximum is above the ground surface. Due to this restriction, the bias is only shown for showers above $\approx 35°$.

6.3.1.4 Primary masses between proton and iron

A small library of CORSIKA simulations based on QGSJet II-03 was produced to check the behavior of the fit for intermediate masses. The primary energy is $10^{19.5}$eV. The primary particles are helium, carbon and silicon. The resolution in X_{max} is similar to the results obtained for proton and iron showers. The reconstruction bias is comparable to proton and iron simulations and can be corrected with the same parameters (Eq. (6.1)). The remaining bias after correction is smaller than $10\,\text{g/cm}^2$ in most cases (Fig. A.30).

Although there is a reconstruction bias, these results are reassuring. The intermediate mass simulations are completely independent of the showers used for the models, the reconstruction and to derive the bias correction parameters. Nevertheless the accuracy of the reconstruction is similar as in proton and iron showers.

---

[1]The simulation of photon events is based on the CORSIKA showers from http://augerdb.lal.in2p3.fr:8080/augerdb/simdb/Library-en.do?libraryId=32025780

(a) X_0 coupled to X_{max}

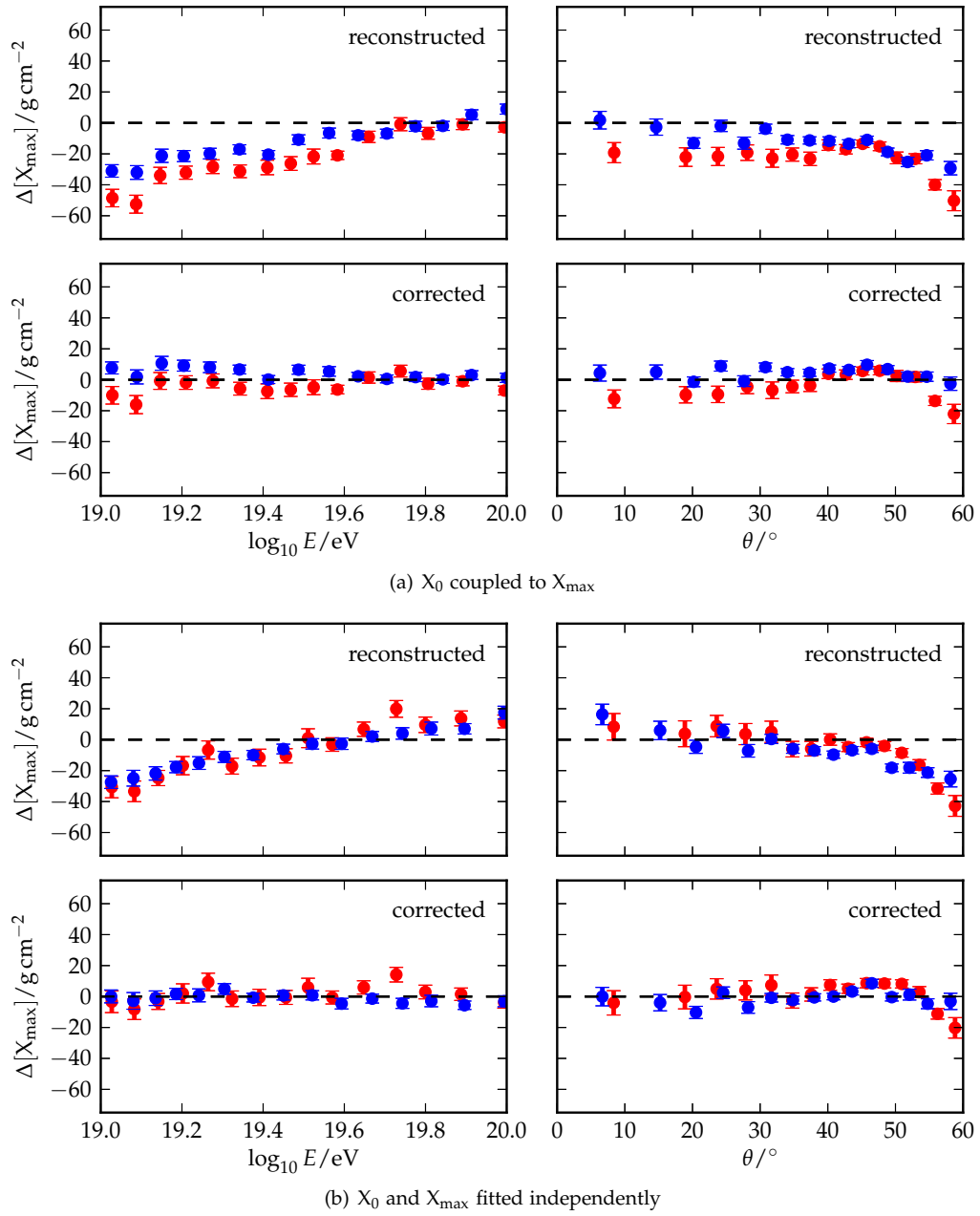(b) X_0 and X_{max} fitted independently

Figure 6.6: Bias of the reconstructed X_{max}. The plots show that there is a trade-off between the systematic uncertainty and the resolution. When X_{max} and X_0 are coupled (upper four plots), a mass dependence is introduced. When X_{max} and X_0 are fitted independently, the reconstruction spread increases (see Fig. 6.9). **Red:** proton, **Blue:** iron
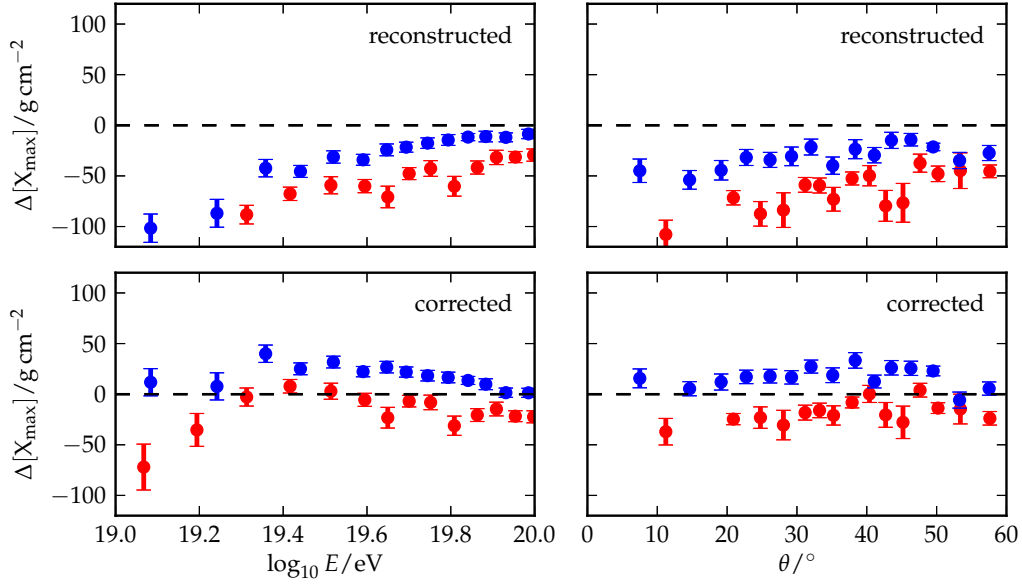
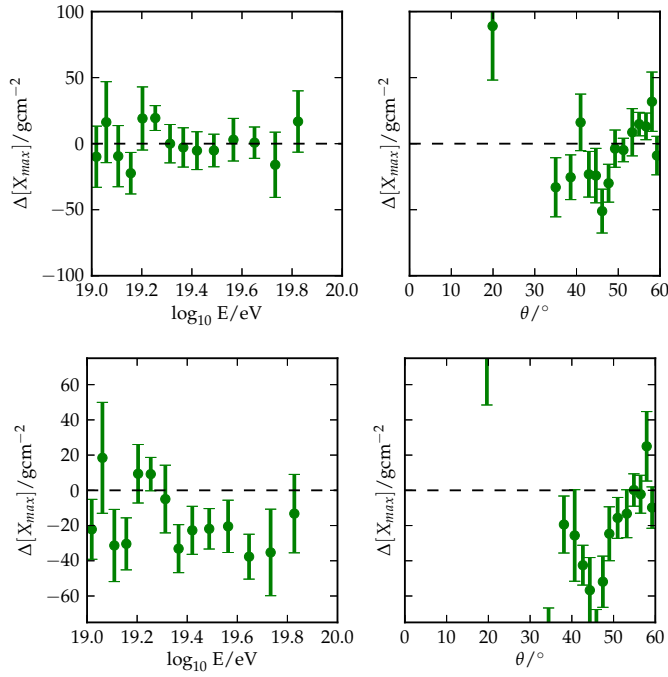**Figure 6.7:** The same as Fig. 6.6(a) in events with saturation.

Figure 6.8: Bias of the reconstructed X_{max} for photons. Only events with X_{max} above ground are accepted. Photon showers develop very deep in the atmosphere, consequently the maximum can only be observed with $\theta \gtrsim 35°$. X_0 is coupled to X_{max}. **Top:** X_{max}-X_0-coupling for photons, **bottom:** X_{max}-X_0-coupling for proton and iron

6.3.1.5 Conclusions on the X_{max} bias

The reconstruction bias of X_{max} is the most important issue that is not fully understood. There are several possible explanations. The 13 % systematic difference (Fig. 4.12) in the signal predicted by universality and the $\overline{\text{Off}\underline{\text{line}}}$ detector simulation is basically ruled out. The prediction from universality is rescaled (called *fudge factor*) to account for the mismatch. There is a difference of around 1 % between the full tank simulation based on Geant4 and the interpolated tank response (Fig. 4.5). It can be caused by different tank geometries. In any case, the difference is too small to explain the bias and can not explain the zenith dependence.

The residuals of the $\overline{\text{Off}\underline{\text{line}}}$ simulation and the model are shown in Fig. 4.12. Within each zenith angle bin, there is an increase of the residuals with DX. This effect is more pronounced for the components that depend on the muon scale. The same shape is also apparent in the DX-dependence of the X_{max} bias. This effect vanishes on average for each zenith angle and therefore can not explain the zenith dependence of the bias. Nevertheless, it indicates that the model could be improved by using the maximum of the muonic profile X_{max}^{μ}. Another explanation for the bias is an intrinsic correlation of N_{μ} and X_{max}. The zenith-dependence of the bias of N_{μ} is opposite in sign to X_{max} (Fig. 6.12). This effect compensates an incorrectly reconstructed X_{max} to give a correct prediction of the ground signals. In this case, a separate measurement of the signal components helps to break the correlation and reduce the biases. Extensions of the SD for this purpose are discussed in Chapter 9.

In events with saturated stations, the station configuration is often inconvenient. The station close to the core can not be used. Due to the geometry of the array, there are (in the extreme case) six stations at almost the same distance to the core. This makes the fit of a lateral distribution function difficult. If there is no station below ≈ 1000 m, the whole measurement is mainly sensitive to the muonic cascade because most of the information on the electromagnetic part is concentrated in a few stations close to the core. Hence the sensitivity to X_{max} is small.

Each simulated shower contains around 100 virtual (*dense*) stations that are placed on a regular grid around the shower axis (Fig. 4.3), the positions are independent of the impact w.r.t. the regular array. If the virtual stations are used instead of the regular ones, effects of the triangular geometry of the array on the reconstruction can be excluded. The results are shown in Appendix A.8. It is clear that the total signal on ground is very well described by the model because the core bias vanishes completely (Fig. A.26). The bias in the angular reconstruction is also very small (Fig. A.25). However, the angular resolution is almost the same as in the case of the regular array (Fig. A.24). The resolution in X_{max} improves drastically when the dense array is used (Fig. A.23). However, the structure of the bias is very similar to the results obtained with the regular array (Fig. 6.6) This suggests that the signal and time models describe the VEM traces accurately y but the FADC sampling rate is the limiting factor, especially for the angular resolution. Faster sampling of the FADC in the tanks is likely to improve also the quality of the reconstruction regarding X_{max}.

There is a systematic mass dependence due to the X_{max}-X_0-coupling. When the start time contribution is turned off, the mass dependence in the X_{max} bias vanishes and the overall bias decreases (Fig. A.19). This comes at the expense of worse X_{max} resolution (similar to the freely fitted X_0 in Fig. 6.9) and much worse angular spread which increases by a factor six (Fig. A.18).

6.3.2 Resolution of the shower maximum

The resolution of X_{max} depends strongly on the number of stations considered in the fit. Hence, it is correlated with energy and zenith angle. The resolution is obtained from the spread w.r.t. the true X_{max},

$$\sigma[X_{max}(\text{fit}) - X_{max}(\text{MC})].$$

The resolution as a function of energy and zenith angle is shown in Fig. A.20. In most cases, the resolution is in the order of $20\,\text{g/cm}^2$ to $50\,\text{g/cm}^2$.

The shower-to-shower fluctuations of X_{max} are of special interest because the systematic uncertainty from the model dependence at the highest energies is very small compared to the mean X_{max}. These are the physical in contrast to the measured fluctuations. The physical fluctuations are obtained from the measurement by correcting for the reconstruction spread (data analysis in Section 8.2.4). For this purpose, the (one dimensional) energy dependence of the resolution is needed. According to the argument in [96], it can be obtained from simulated showers if the simulation sample is representative for the distribution of showers in real data. The zenith angle distribution in the continuous library follows a $\sin\theta\cos\theta$ distribution (Fig. 4.2). The core position is sampled randomly within the whole array. Consequently, concerning the parameters the X_{max} resolution depends on, the simulations have the same distribution as the data. To obtain the energy dependence, it is enough to bin the spread of X_{max} by primary energy to obtain the spread $\sigma[X_{max}]$ for each energy bin.

With the variance V, the standard deviation σ and the fourth central moment m_4 of the X_{max} distribution within one energy bin, the uncertainty of the spread is given by

$$\sigma[\sigma] = \sqrt{\frac{1}{N}\left(m_4 - \frac{N-3}{N-1}V^2\right)}.$$

The energy dependence of the resolution of proton and iron showers is shown in Fig. 6.9 for both coupled and freely fitted X_0. For the case of coupled X_0 it ranges from $50\,\text{g/cm}^2$ to $20\,\text{g/cm}^2$ depending on energy and primary particle. The resolution is worse if X_0 is fitted independently (however, in this case the systematic error in X_{max} is smaller). If only showers with $25° < \theta < 50°$ are accepted, the resolution can be improved by $5\,\text{g/cm}^2$ to $10\,\text{g/cm}^2$ (Fig. A.21).

The resolution for photon showers is shown in Fig. 6.10. With $70\,\text{g/cm}^2$ to $80\,\text{g/cm}^2$, the spread is much larger than for proton and iron showers. However, the separation in X_{max} between proton and photon showers is also larger. Hence, the resolution is sufficient to separate photon and proton samples. The spread is smaller for $\theta < 55°$ (Fig. A.22).

In $\overline{\text{Off}}\underline{\text{line}}$, simulations are reconstructed with the same energy calibration as the data. Therefore, due to the mismatch of the muon scale in data and simulations, the energy of simulated showers is underestimated (typically by 20% to 30%). As a consequence, the reconstructed energy can not be used as input for the universality reconstruction because it leads to an overestimated N_μ. Therefore, the energy is fixed to the true value in the fit. On the downside, this results in an underestimation of the X_{max} and N_μ spread. A change in energy means a change in the predicted ground signal. This is compensated in the fit by a change in N_μ and X_{max} (Fig. 6.19): If the energy is decreased, N_μ and X_{max} are increased and vice versa. An estimate of the resolution that included the uncertainty in the energy

(a) Events without saturation. **Left:** X_0 coupled. **Right:** X_0 fitted

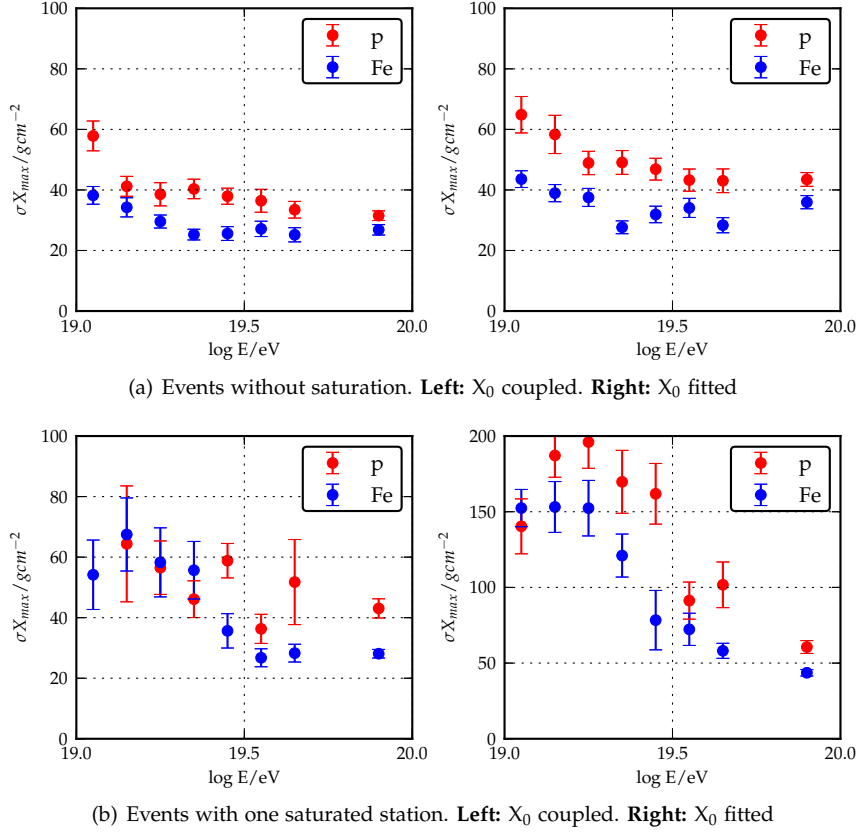(b) Events with one saturated station. **Left:** X_0 coupled. **Right:** X_0 fitted

Figure 6.9: Energy dependence of the X_{max} resolution. The resolution is better for iron showers due to larger signals and higher station multiplicity (see also Fig. 5.1).

reconstruction is obtained by randomizing the energy according to the energy resolution. The energy resolution of the SD is shown in Fig. A.15. The resolution of N_μ and X_{max} obtained by smearing the energy according to a normal distribution is shown in Fig. 6.11. While the resolution of X_{max} changes only by $5\,g/cm^2$, N_μ is affected strongly by the energy fluctuation. Because N_μ is strongly correlated with the energy (Fig. 5.4) a change in energy translates directly to a change in N_μ. The difference is $0.05 - 0.10$.

6.3.3 Dependence of the resolution on the T5 quality selection

At the highest energies, it is necessary to get the largest possible sample of events with good reconstruction accuracy, especially for the study shown in Section 8.4. Usually, the 6T5 quality selection is used. All six stations around the station with the largest signal are required to be in data acquisition at the time of the event. If only 5 stations out of 6 are required, the size of the data sample can be increased by 20 % to 30 %.

It was checked using simulated showers, how the accuracy of X_{max} is affected by a missing station in the first crown. For this study, one randomly selected station in the first crown is discarded and not used in the fit. This reproduces the 5T5 situation in real data where the
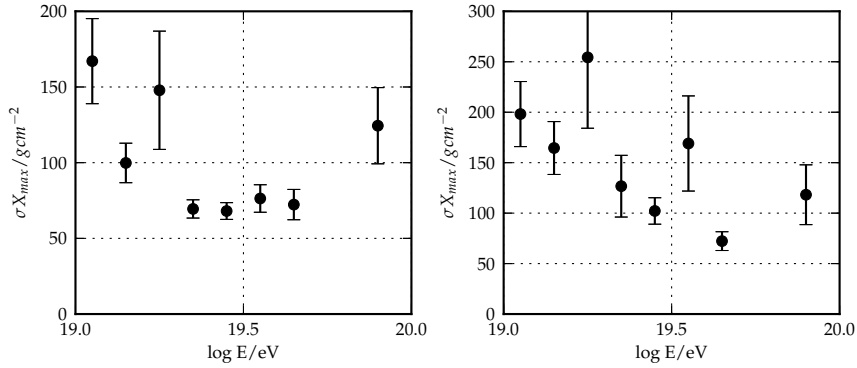
Figure 6.10: Energy dependence of the X_{max} resolution for photons (X_{max} coupled to X_0). **Left:** events without saturation. **Right:** events with one saturated station.
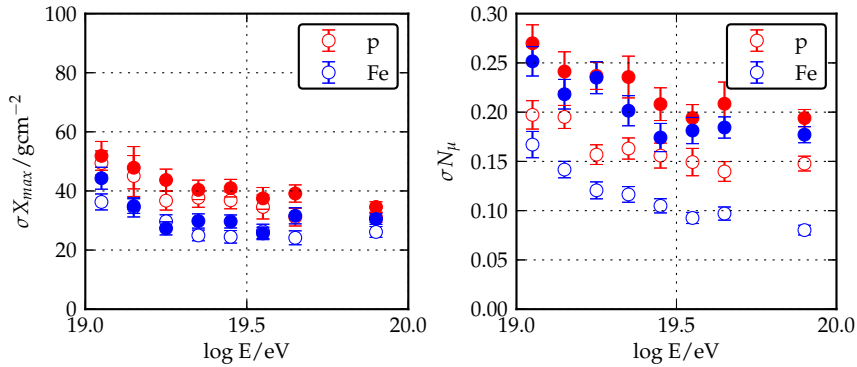

Figure 6.11: The resolution in X_{max} and N_μ taking into account the energy resolution of the SD reconstruction (values for the shift are taken from Fig. 6.19). Open markers refer to the spread if the true energy is used, filled markers taking into account the energy resolution.

position of the missing station is random in the sense that it does not depend on the shower itself. The resulting X_{max} resolution is shown in Fig. A.16. The effect of leaving out one station on the resolution of X_{max} is very small. Events that fulfill the 5T5 criterion still have enough remaining stations to provide a good lever arm for the fit.

6.4 Reconstruction of the muon scale

The energy and zenith-dependence of the average reconstructed N_μ in simulated showers is shown in Fig. 6.12. The expected average for proton is 1.0 by definition, for iron ≈ 1.3. For photons, the average is ≈ 0.3. Photon showers are only accepted if the true X_{max} is located above the ground to ensure a reliable reconstruction. The same cut as in Section 6.3.1.3 is used. Therefore, the average N_μ is only shown for showers above $30°$.

The spread of the reconstructed N_μ is shown in Fig. 6.13. It corresponds to 30% to 50% of the difference between proton and iron. The same analysis was also done with showers at fixed zenith angles, with comparable results (Fig. A.29). The spread is similar for photon
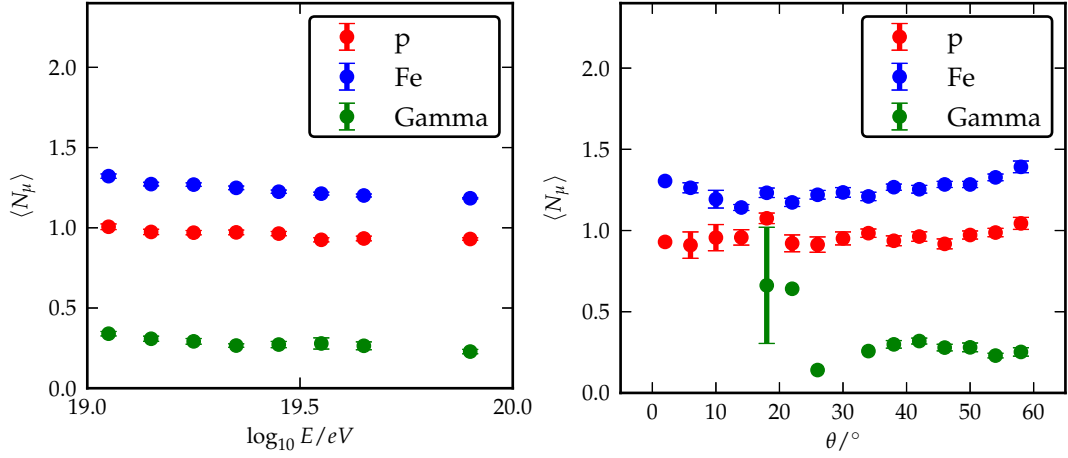
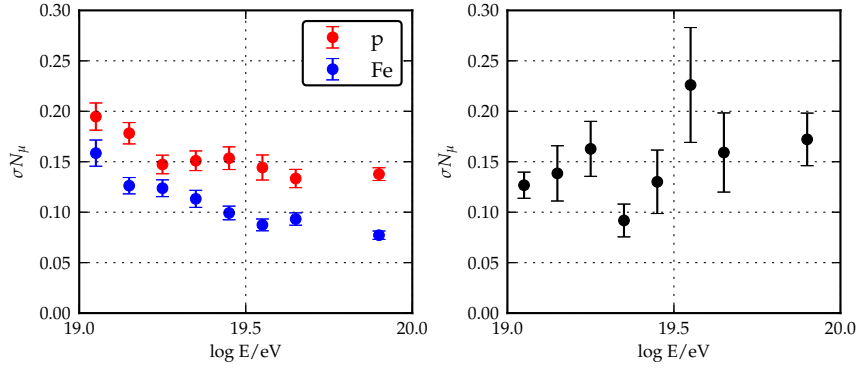**Figure 6.12:** Energy dependence of the average reconstructed N_μ

Figure 6.13: Energy dependence of the resolution of N_μ for proton and iron (left) and photon showers (right).

showers but corresponds to a larger relative separation due to the large difference of N_μ between proton and photon showers.

6.5 Mass discrimination based on X_{max} and N_μ

The easiest case of mass discrimination is the separation in light and heavy (the extreme cases are proton and iron). Several mass-sensitive observables are available: X_{max} (SD) or X_{max} (FD) and N_μ. Each one or a combination of them can be used to classify an event as light or heavy. In the context of photon search, showers are classified as muon-rich/poor and shallow/deep. Usually, there is considerable overlap in the distributions of N_μ and X_{max}. This results in a trade-off between *purity* (the fraction of events assigned to one class actually belonging to it) and *efficiency* (the fraction of events that are accepted) that needs to be done for the classification. This is illustrated in Fig. 6.14. The connection of purity and efficiency is obtained by scanning the whole parameter range (e.g. from light to heavy). In the ideal case, the purity is 1 regardless of the efficiency (no overlap of the two distributions). In the worst case the

purity is anti-correlated to the efficiency (complete overlap of both distributions). The purity-efficiency-plot is shown in Fig. 6.14. The whole zenith angle range is used ($\theta = 0° \ldots 60°$). The energy resolution of the SD reconstruction was propagated to X_{max} and N_μ by smearing the total energy according to a normal distribution Fig. 6.11. X_{max} (SD) performs worse than X_{max} from the FD due to the larger reconstruction spread and the remaining systematic uncertainty after the bias correction. N_μ has a better discrimination power.

Several parameters (e.g. N_μ and X_{max} (SD)) can be combined with a linear Fisher discriminant. It is an analytical algorithm that projects the n-dimensional distribution of parameters to one dimension such that the variance within two classes (proton and iron) is minimized while the difference of the mean values along the projection axis is maximized. In this case, the value on the projection axis is a measure for the mass of the primary particle. This is the simplest algorithm in the plethora of classification algorithms. For this two-dimensional case, more sophisticated algorithms are not expected to improve the separation significantly. The parameters follow a normal distribution approximately and it can be shown that, in this case, the linear discriminant separates the two populations in an optimal way [97]. The discriminant is obtained from the covariance V of N_μ and X_{max} in simulations,

$$V^{\mathrm{P}}, V^{\mathrm{Fe}}.$$

The projection axis w reads as

$$\vec{w} = (V^{\mathrm{P}} + V^{\mathrm{Fe}})^{-1} \cdot (\vec{\mu}^p - \vec{\mu}^{\mathrm{Fe}}),$$

where

$$\vec{\mu} = \begin{pmatrix} \langle N_\mu \rangle \\ \langle X_{max} \rangle \end{pmatrix}.$$

The Fisher value F for an individual (simulated or measured) event is obtained as

$$F = \vec{w} \cdot \begin{pmatrix} N_\mu \\ X_{max} \end{pmatrix}.$$

The separation power increases if N_μ and X_{max} are combined (Fig. 6.14). The combined separation is even superior to X_{max} (FD).

For the case of (approximately) Gaussian-distributed observables, the separation power can be estimated with a *merit factor M*. For proton and iron, it is estimated from the mean difference of the averages normalized by the combined spread as

$$M = \frac{|\mu_{\mathrm{p}} - \mu_{\mathrm{Fe}}|}{\sqrt{\sigma_{\mathrm{P}}^2 + \sigma_{\mathrm{Fe}}^2}}. \tag{6.2}$$

The larger the merit factor the better the separation ($M = 0$ means no separation at all). The merit factor for N_μ and X_{max} (SD) is shown in Fig. 6.15. The increase of M due to the improving accuracy of the reconstruction is apparent.

6.6 Selection bias from saturation cut

The reconstruction bias of X_{max} in events with a saturated station is comparatively large (Fig. 6.7). It is difficult to correct for in real data because an assumption about the mass composition needs to be done. If a mixed composition of 50 % proton and 50 % iron is assumed,
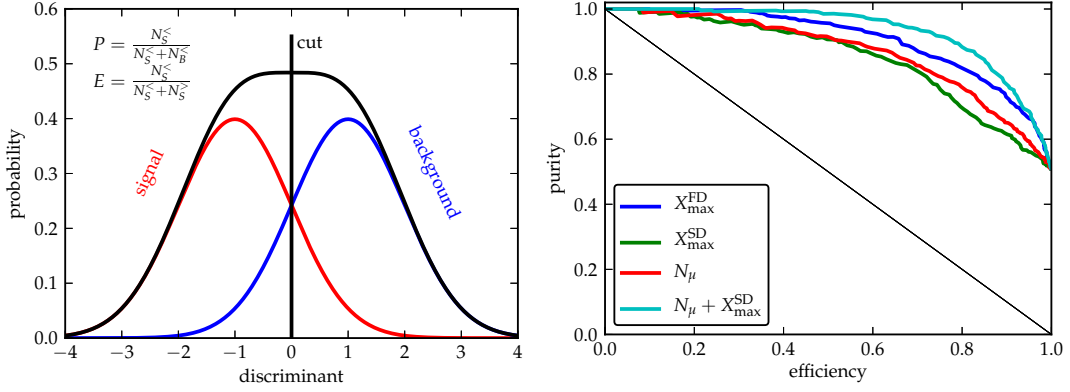
Figure 6.14: Discrimination power for proton/iron separation using different mass-sensitive variables. When X_{max} and N_μ are combined based on a linear Fisher discriminant, the separation improves.
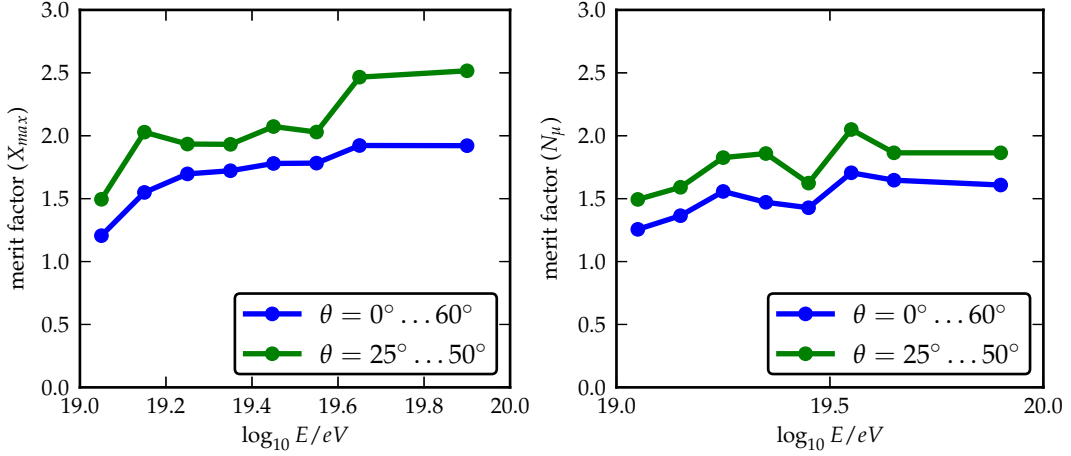

Figure 6.15: The merit factor (Eq. (6.2)) is a measure for the separation of two distributions. Merit factor for X_{max} (left) and N_μ (right). The separation improves with a cut on $25° < \theta < 50°$.

the remaining systematic error is in the order of $20\,\mathrm{g/cm^2}$ to $30\,\mathrm{g/cm^2}$. To obtain a data sample with small systematic uncertainties, it can be advisable not to use events with saturation.

If events with saturation are discarded, it might introduce a selection bias in X_{max}, because the signals on ground depend on X_{max}: Deeper showers have larger signals. Such a bias can be excluded if the distribution of the true X_{max} is the same for events with or without saturated stations. The distributions are shown in Fig. 6.16 for proton, iron and photon primaries simulated with QGSJet II-03 at $10^{19.5}$eV. Throughout all primary particles and energies, the mean X_{max} is larger for events with saturated stations but the difference is less than $<1\,\mathrm{g/cm^2}$. The saturation is almost completely determined by the distance to the shower core. The depth of the shower has a comparatively small influence on the signal. No selection bias is introduced to the mean X_{max}.
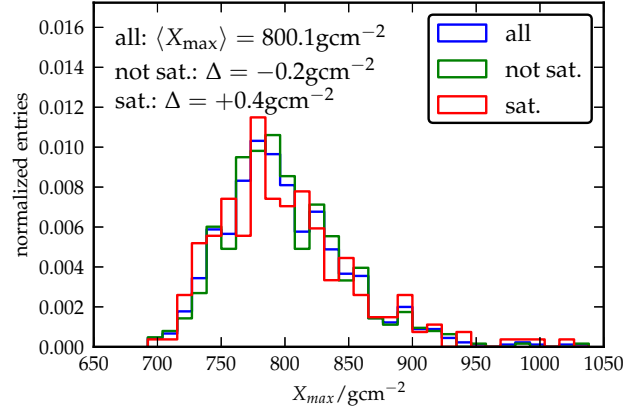
(a) Proton simulations
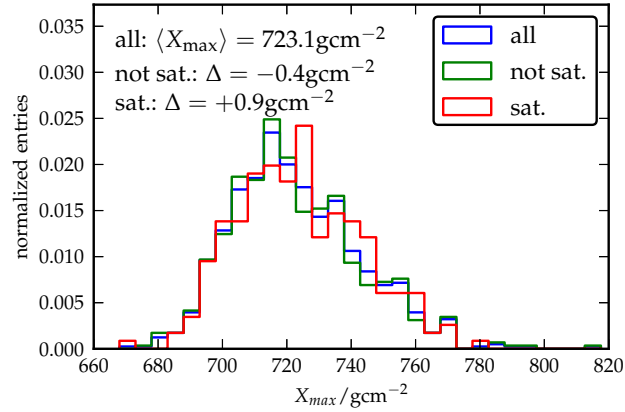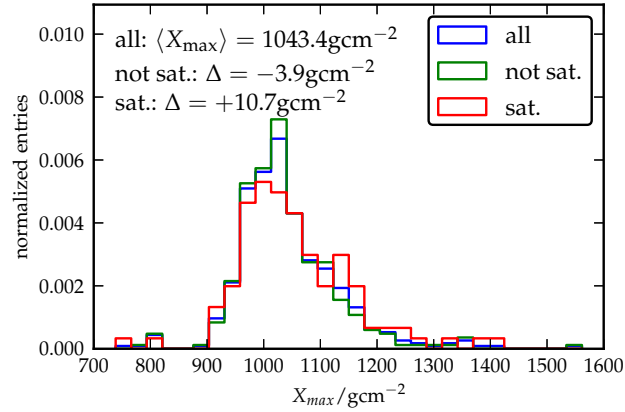
(b) Iron simulations

(c) Photon simulations

Figure 6.16: Distribution of the true X_{max} for showers at $10^{19.5}$eV. The depth of the shower is almost completely uncorrelated with saturation. For photon showers, saturation tends to be caused by deeper showers. In all cases, a possible selection bias is negligible.

6.7 Sources of systematic uncertainties

There are several sources of possible systematic errors. In Section 4.9 it was shown that the time traces are not completely universal in r, Ψ and DX. The model used in the reconstruction is based on a mixture of all available showers. This is done assuming a negligible dependence of the time shape on hadronic interaction model, primary particle and energy. This assumption causes a systematic uncertainty in the reconstruction.

To estimate the size of the systematic error, several time models for all combinations of model, primary and energy are derived according to the method in Sections 4.7 and 4.8. The simulated showers are reconstructed using the different time models. The effect on the reconstruction of X_{max} and N_μ is shown in Fig. 6.17. The systematic uncertainty in N_μ is below 0.01. This reflects the fact that N_μ is mainly determined by the shape of the LDF and not by the time shape. For X_{max} the difference is below $5\,g/cm^2$ except for showers at $60°$.

The function for the correlation of X_0 and X_{max} (Section 5.5) is based on the same mixture of showers that is used to derive the time model. For a specific combination of model and primary, the average correlation function does not describe the dependence of X_{max} and X_0 perfectly. The simulated showers are reconstructed with the mean coupling function and the one based only on QGSJet II-03 showers (see Appendix A.3). The difference of the reconstructed values is shown in Fig. 6.18. The systematic error is very small for N_μ while X_{max} can change by up to $5\,g/cm^2$ to $10\,g/cm^2$.

The monthly models for the atmosphere describe the height dependence of the depth very accurately. In contrast to the FD reconstruction, the choice of atmospheric model has only a minor effect on the result because the grammage is only calculated at the height of the detector. In addition, the slant depth calculated at this height for different months varies by less than $3\,g/cm^2$ (for more details, see Fig. 6.20).

The largest systematic error is caused by the uncertainty of the energy scale. If the energy is increased, the prediction for the ground signal is larger. This is compensated by a smaller N_μ and X_{max}. For a purely muonic shower, the expected change in N_μ is exactly $10\,\%$. If an electromagnetic part is present, the ground signal has a weaker dependence on N_μ. Therefore, N_μ has to be decreased by a larger amount to compensate for the change caused by the increased energy. For $\theta = 0°$, the change is $\approx -16\,\%$. It increases to $-10\,\%$ at $\theta = 60°$. The increase in the electromagnetic signal is compensated by difference in X_{max} of $-10\,g/cm^2$ (Fig. 6.19).
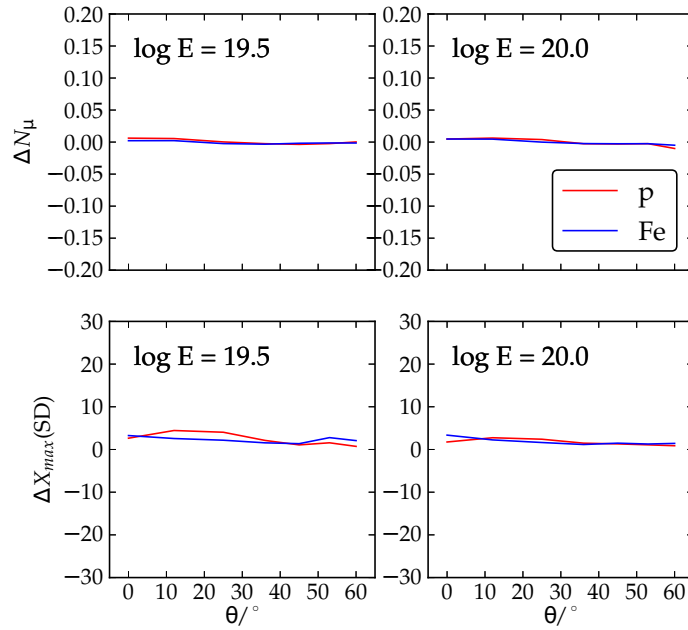
(a) Time model based on a mixture of proton and iron showers simulated with QGSJet II-03 and EPOS 1.99 at $10^{19.5}$eV.
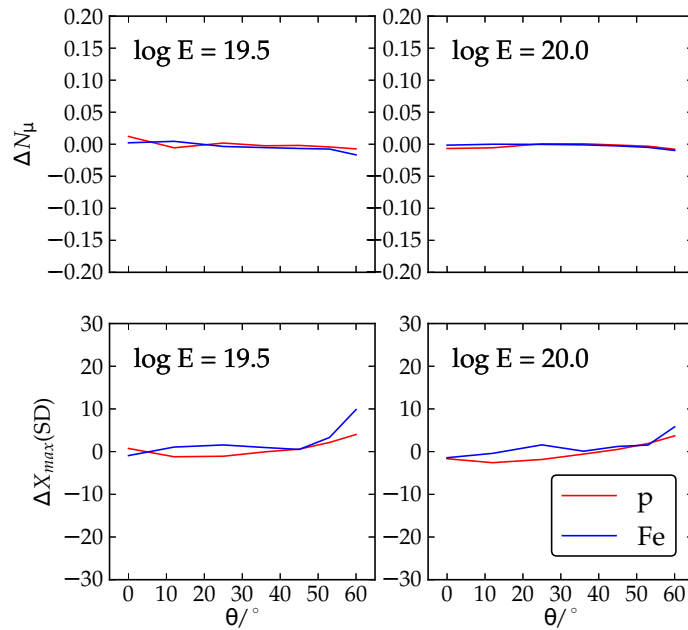
(b) Time model based on a mixture of proton showers simulated with EPOS 1.99 at $10^{19.0}$ eV, $10^{19.5}$ eV and $10^{20.0}$ eV.

Figure 6.17: Systematic error in the reconstructed X_{max} and N_μ introduced by the violation of universality in the time model. The difference of the reconstructed X_{max} and N_μ to the reference model is shown. In all cases, the shift in N_μ is negligible. When the time model is derived from $10^{19.5}$ eV only (upper four plots), X_{max} is increased by $\approx 3\,\mathrm{g/cm^2}$. A similar effect is apparent when the time model is derived from EPOS 1.99 showers only (lower four plots).
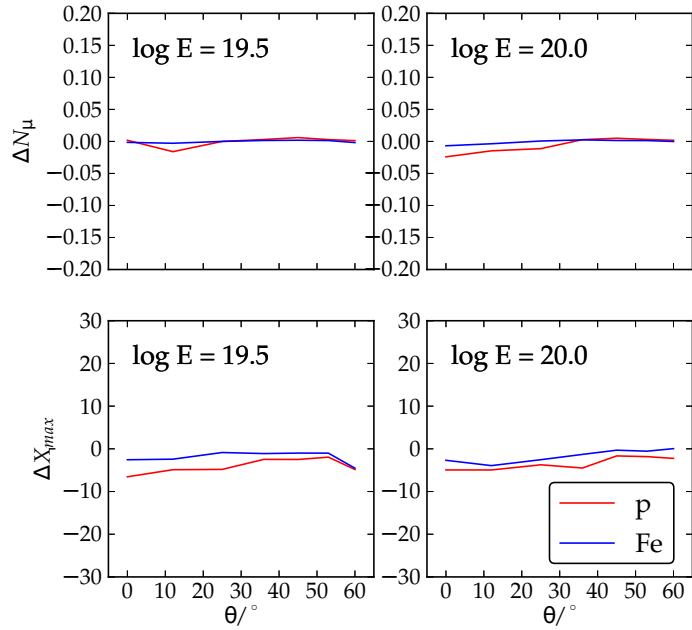
Figure 6.18: Systematic error in the reconstructed X_{max} and N_μ introduced by X_{max}-X_0-coupling function. When the coupling function is based only on QGSJet II-03 showers, the reconstructed X_{max} decreases. The influence on N_μ is negligible.
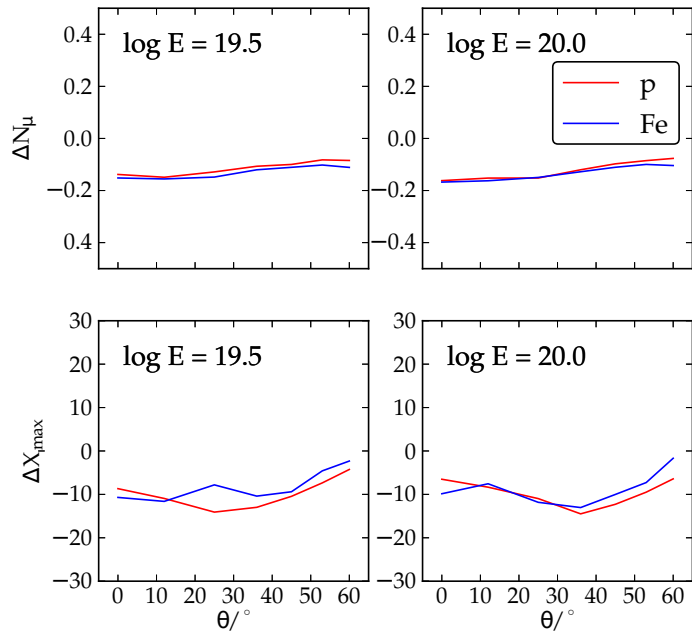

Figure 6.19: Systematic error in the reconstructed X_{max} and N_μ introduced by the energy scale. When the energy is increased by 10 %, this is compensated by the signal model. N_μ decreases by 10 % to 15 %, X_{max} by $10\,g/cm^2$.
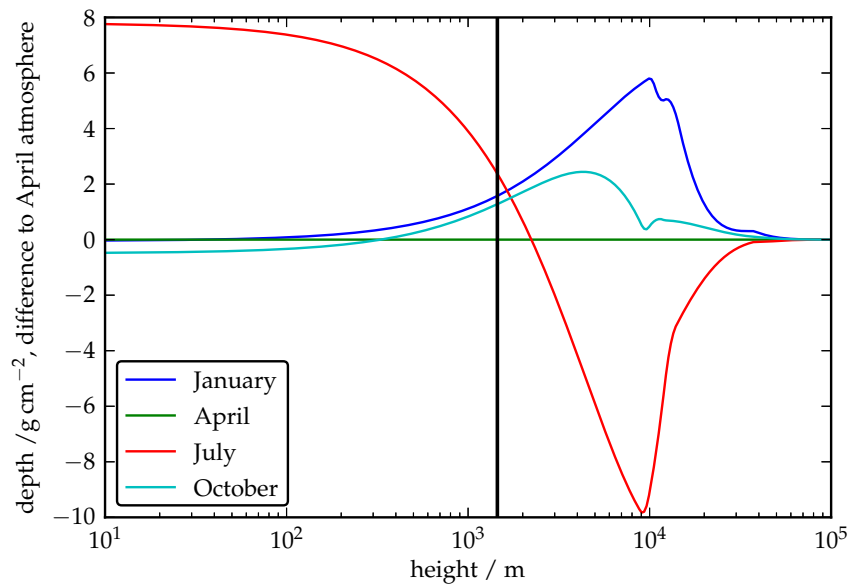
Figure 6.20: The slant depth on ground for $\theta = 36°$ for various monthly models of the atmosphere. The difference to the April atmosphere is shown. At the height of the SD (solid vertical black line), the slant depths differ by at most $3\,\mathrm{g/cm^2}$.

7

Validation of shower universality with data

In Chapter 6 the signal and time models and the reconstruction algorithm are tested in simulated showers. Clearly, the models describe the total signal as well as its time shape well in simulations. In this section, the validity of the models is checked with real data. Ideally, the measurement is predicted from observables taken by an independent detector to avoid any fit to the data that should be validated. In SD-only events this is not possible. Golden hybrid events (data that contains both SD and FD data), this requirement is fulfilled except for the overall muon scale N_μ. The total energy E, the depth of maximum X_{max} and the geometry of the shower are given by the FD reconstruction. N_μ is the only parameter that still needs to be fitted. To minimize the dependence on the models (Chapter 4), the contribution of the timing to the likelihood is switched off. The fit is expected to perform similarly as with the timing likelihood switched on because N_μ is completely determined by the lateral shape (integrated signals).

7.1 Description of the data set

For the analysis of hybrid events, the standard quality cuts are used: X_{max} is required to be in the field of view of the telescope and the uncertainty on X_{max} has to be smaller than $40\,\mathrm{g/cm^2}$. In this case, the energy cut ($E > 10^{19}$eV) is based on the FD energy. The uncertainty of the energy has to be smaller than 20 %. The minimum angle between the shower axis and the axis of the telescope is $20°$ (*minimum viewing angle*). At least 5 pixels have to be available for the axis fit. The reduced χ^2 of the Gaisser-Hillas profile to the longitudinal fluorescence profile has to be smaller than 2.5 to ensure a reliable fit.

In version `v9r3` as of June 2013 of the official reconstruction, the FD energy scale was updated. The effect results in an increase of the calorimetric energy by 10 % to 15 % depending on the energy. The energy is a fixed input parameter for the universality reconstruction. The energy scale is very important for the reconstruction of X_{max}. Hence, the analyses concerning X_{max} are shown for the current (`v9r3`) and the previous (`v9r1`) version of the official reconstruction.

7.2 Prediction of the VEM traces using FD data

The prediction of the time quantiles in simulations is shown in Section 4.10. In the following sections, several checks are done that show the ability of shower universality in the prediction of the time traces in real data.

7.2.1 Prediction of the integrated signal

On average, the model predicts the measured signal well in pure SD as well as in golden hybrid events. In most cases, the deviations are well below 0.5σ (Fig. 7.1), while the NKG function has a distance-dependent bias. Note that the model prediction was rescaled by 13 % due to the mismatch shown in Fig. 4.12. Saturated stations are not used. A cut on the expected signal $S > 10$ VEM was set to avoid a bias from upward fluctuations.

In SD events, all shower parameters are reconstructed using the time information. The fact that the signals are predicted well is only a weak argument for universality because possible discrepancies could be absorbed partly in the fitted parameters. However, it shows that the lateral shape is described reasonably well. The residuals are shown in Fig. 7.1(a).

In golden hybrid events, E, X_{max} and the geometry are taken from the FD reconstruction while N_μ is fitted using only the total signals. The residuals for the whole data sample of such golden hybrid events are shown in Fig. 7.1(b).

The uncertainty of the core in the FD reconstruction is comparatively large. Due to the steep lateral shape of the signal, this translates to a very large error in the prediction of the signal (*LDF effect*). To avoid this effect, the distance of the core positions reconstructed by the SD and the FD is required to be smaller than 50 m. This approach is not entirely correct because the SD core is not a bias-free estimator of the true core position. To correct for this, the SD core is shifted by 1 m$/°$ (Fig. 6.3) towards the late region of the shower beforehand. This shift corrects for zenith-dependence of the core bias. The residuals of this reduced high quality data sample are shown in Fig. 7.1(c).

7.2.2 Prediction of the time quantiles

In this section, the time quantiles of the VEM traces are predicted and compared to the measured values. The rise time is the time it takes for the signal to rise from 10 % to 50 % of its integrated value. Any quantile can be calculated from the model. The rise time is chosen because it is a mass-dependent observable that is widely used in other studies (e.g. [85, 86, 87]).

The time quantiles are obtained from the four component time models $f_c(t)$ using the cumulative distribution functions as

$$F_c(t) = \int_0^t f_c(t')dt'\,.$$

The c.d.f. of the total trace reads as

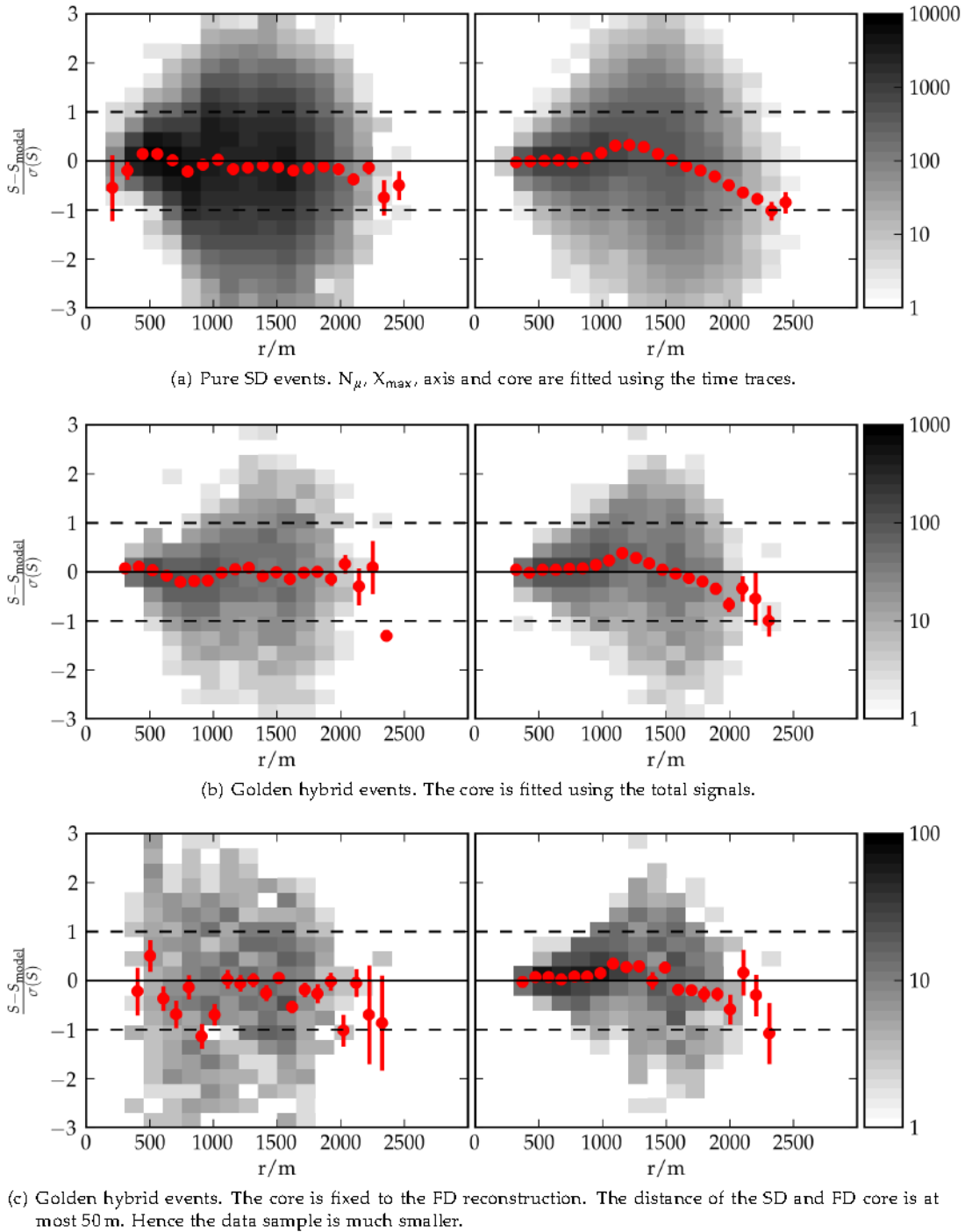$$F_{\text{tot}}(t) = \frac{\sum_c F_c(t) \cdot S_c}{\sum_c S_c}\,,$$

(a) Pure SD events. N_μ, X_{max}, axis and core are fitted using the time traces.

(b) Golden hybrid events. The core is fitted using the total signals.

(c) Golden hybrid events. The core is fixed to the FD reconstruction. The distance of the SD and FD core is at most 50 m. Hence the data sample is much smaller.

Figure 7.1: Residuals of the measured signals and the model prediction. The residuals to the universal model are obtained by fitting N_μ to the total signals (no time model is used), while E, X_{max}, axis and core are taken from the FD reconstruction. **Universality** (left column), **one dimensional NKG shape** (right column). **SD events** (top), **golden hybrid events** (middle and bottom). In the last row, due to the cut on the distance to the SD core, the data sample is smaller. The distribution of individual values is indicated by the shaded area.

where S_c denotes the integrated trace signal of a component c. The time t of a quantile q is obtained by finding the inverse of

$$F_{\text{tot}}(t) = q \,,$$

which is done numerically.

The result is shown in Fig. 7.2. The data sample was divided into the stations that *would* contribute to the bin-by-bin time fit according to the criteria in Section 5.1 and those that *would* only contribute with the total signal.

The time model gives a good prediction of the rise time ($t_{50} - t_{10}$) for a wide range of distances to the shower core. The absolute quantiles t_{10}, t_{50} are also predicted correctly. This shows there is no hidden offset that is not accounted for. Note that for this study, the time information is not used at all. The distinction is made to show that the time shape of stations that would contribute to the time likelihood is described significantly better than for the remaining stations. The prediction is less accurate for t_{90} and consequently for the fall time $t_{90} - t_{50}$. The t_{90} is probably underestimated because the falling edge of the lognormal distribution is too steep, i.e. the late part of the trace is not described precisely enough. The differences can also be caused by the dependence of the time model on primary and hadronic interaction model. For more details, see the discussion of the systematic uncertainties induced by the dependence on model, primary and energy in Section 4.9).

7.2.3 Prediction of the shape of the VEM traces

The time quantiles are parameters that condense the information of the whole time trace to a few numbers. Naturally, the best test of the model is a comparison of the whole trace. However, care needs to be taken to select an event that gives a meaningful result. Due to the LDF effect discussed in Section 7.2.1, only a few events are suitable. In the event 200708201779, the distance of the SD and FD core reconstruction is below 50 m. The result of the prediction of the time shape is shown in Fig. 7.3 for the four traces that *would* be selected for the bin-by-bin time fit. First, the fit was done using the standard configuration (fitting everything except for the total energy). Naturally, the agreement of the traces and the model is very good because almost everything is fitted to match the measurement. This is not yet a strong test of universality. In the second step, the energy, X_{max} and the geometry are taken from the FD and not modified further while N_μ is fitted without using the time model. The shape of the traces is in good agreement with the model prediction. This is a strong argument for universality, because the time shape is predicted based on an independent measurement. However, there is an overall time offset. It can be explained by the violation of universality shown in Section 4.10 or by a systematic offset in the timing of the FD and the SD [98, 99]. Another source of systematic shift is the prediction of the start time from the curvature of the shower front. If the mass composition assumed for the calculation of X_0 is wrong, it can cause a shift of the start time. In the last set of plots, the model prediction is allowed to shift in time by minimizing the χ^2 to the trace. This was done to show that the model prediction is in good agreement with the traces except for the overall offset. Note that the shape of the signal was not modified in this step.
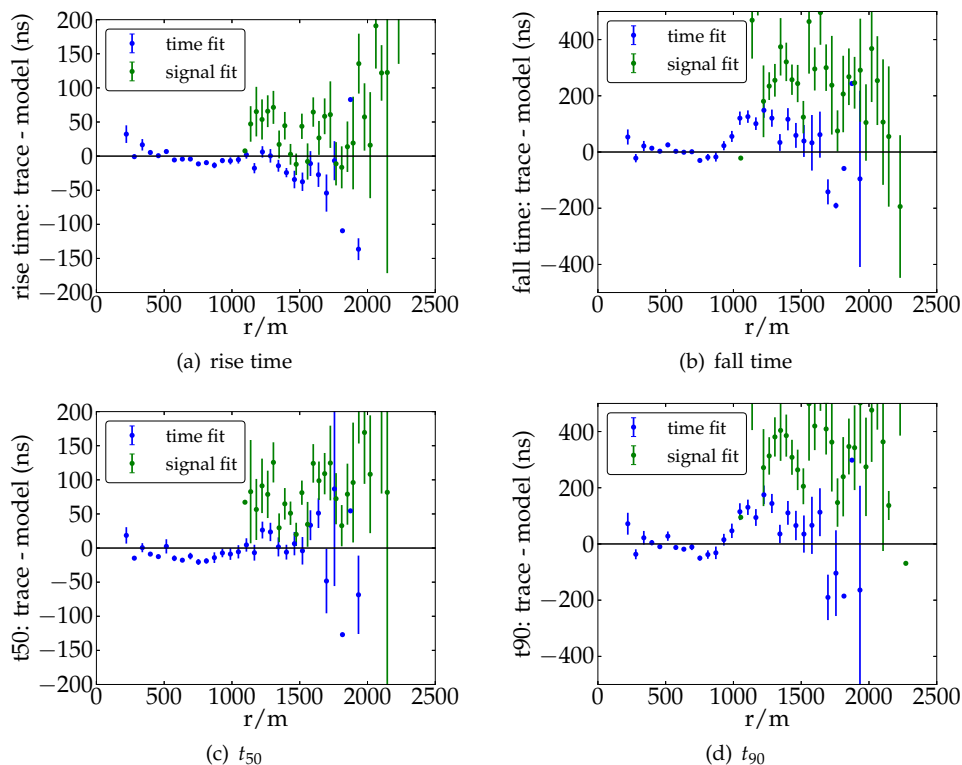
(a) rise time

(b) fall time

(c) t_{50}

(d) t_{90}

Figure 7.2: Using X_{max}, E and geometry from the FD reconstruction, the time quantiles of the VEM trace are predicted. **Top:** rise and fall time (relative quantiles), **bottom:** t_{50} and t_{90} (absolute quantiles). Stations that would contribute to the bin-by-bin time fit in the reconstruction according to the criteria in Section 5.1 are shown in blue (time fit). Stations that would only contribute to the fit of the total signal are shown in green.

7.3 Accuracy of core position and axis (shower geometry)

In the FD reconstruction, the shower axis is fitted based on the triggered pixels in the camera and on the start time of a single SD station (Section 3.2.2). It does not depend on the signal on ground. Hence, the signal asymmetry does not influence the result. On average, the FD reconstruction is expected to give an unbiased estimate of the true core position and the shower axis.

In the following, the estimate of the core position from the FD reconstruction and the universality algorithm are compared. Two FDs (Loma Amarilla and Coihueco) are not considered due to systematic errors in the reconstruction of the shower axis. Only showers without saturated tanks are used. The resulting core coordinates are calculated in the shower plane coordinate system referred to the hybrid geometry (Fig. 7.4).

The same effect as in simulated showers (Section 6.2) is apparent. Universality gives a bias-free estimate of the core position. There is no dependence on zenith angle, in contrast to the SD reconstruction based on the NKG function. However, the effect is less pronounced than
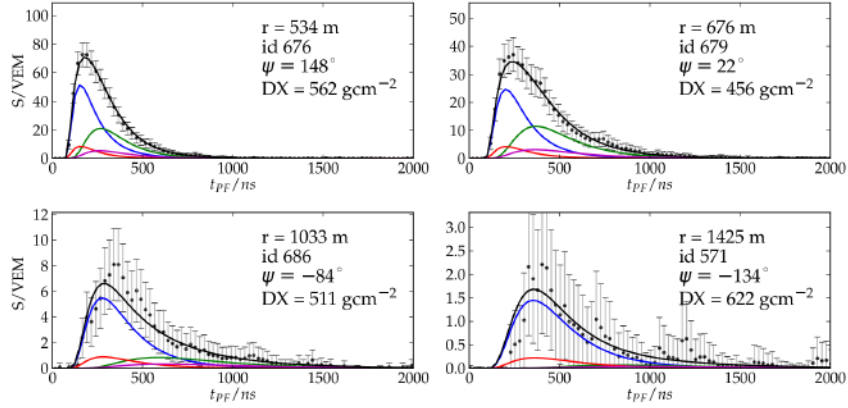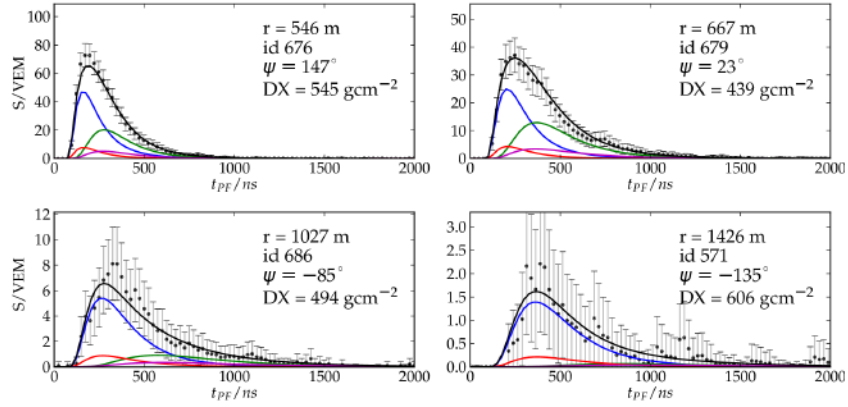
(a) Geometry, X_{max} and N_μ fitted to the VEM traces (standard configuration).
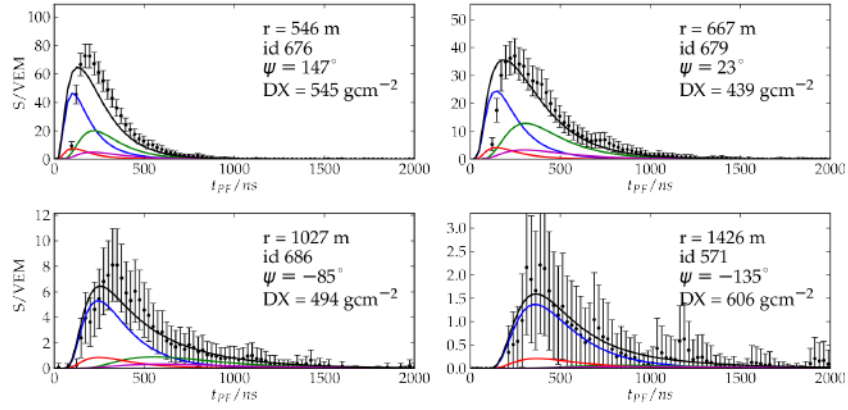
(b) Geometry, X_{max} and total energy fixed to the values reconstructed by the FD, only N_μ fitted. The shape of the time traces is predicted correctly except for an overall shift.

(c) The same as in the middle panel. The model is shifted by $\approx 50\,$ns to show that the shape of the signal is predicted correctly.

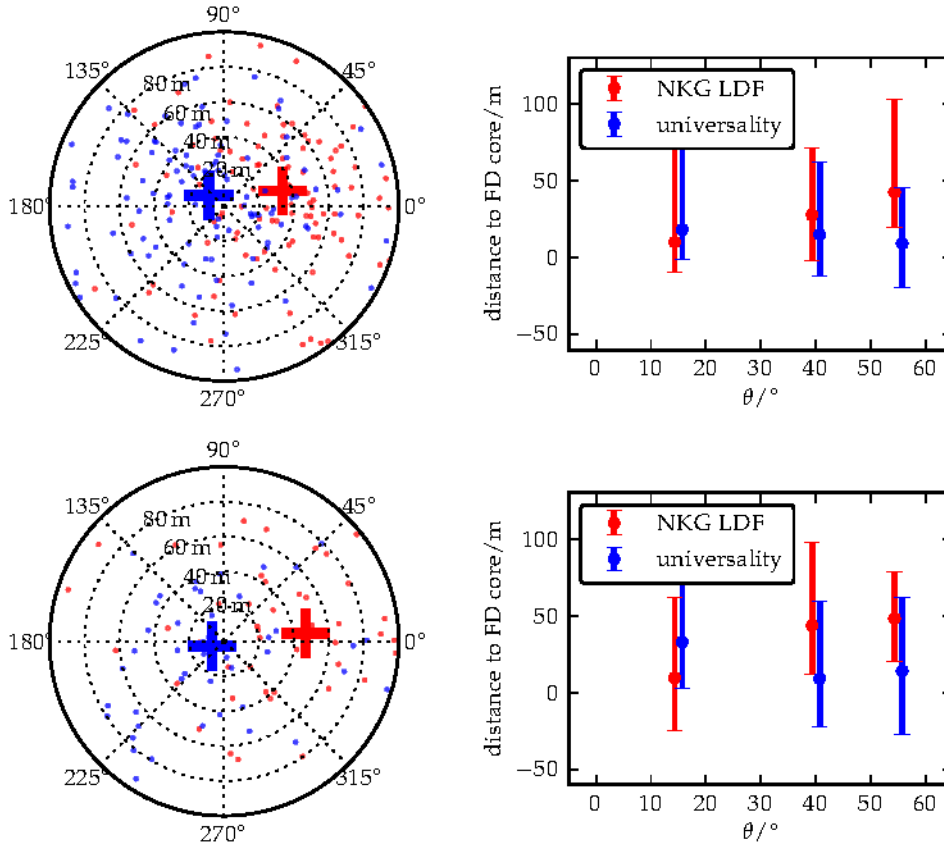**Figure 7.3:** Prediction of the VEM traces in real data using golden hybrid events.

Figure 7.4: Bias of the reconstructed core position in FD shower plane coordinates. **Left:** showers with $35° < \theta < 55°$ were selected to maximize the asymmetry effect. Showers are rotated in ϕ such that the incoming direction is to the right. **Right:** average distance of the reconstructed core position to the position from the FD reconstruction. **Top:** no saturation. **Bottom:** events with saturation. **Red:** standard reconstruction (LDFFinderKG). **Blue:** this work, taking into account signal asymmetries. Points are shifted for better readability.

in simulated showers for two reasons. For this comparison, the uncertainties of the FD and the universality reconstruction are combined, which increases the total spread considerably. Furthermore, the fraction of muons is underestimated in the simulation. Muons are much less absorbed in the atmosphere. Hence, an increase of the muon fraction decreases the signal asymmetry on ground. Consequently, a smaller shift of the core position is expected.

7.4 Comparison of the shower maximum X_{max}

In Fig. 7.5, X_{max} (SD) is compared to X_{max} (FD). Before calculating the residuals, X_{max} (SD) was corrected for the reconstruction bias according to 67.

In `v9r1`, the agreement is very good. There is no remaining systematic shift as a function of zenith angle or energy. In `v9r3` however, there is a clear systematic increase of the residuals as a function energy and an overall shift as a function of zenith angle. A bias of up to $-20\,\text{g/cm}^2$ to $-30\,\text{g/cm}^2$ remains even after the bias correction.

In both cases, the bias correction function is derived from simulated showers using the true energy and geometry. The change of energy scale does not affect the correction itself. The change of the residuals with the new energy scale is expected because of there energy dependence of the bias correction. If an increased energy is assigned to the measured events the bias estimate changes.

These results suggest that, judging only based on shower universality, the energy scale in `v9r1` is correct and is rather overestimated in the new version `v9r3`. The energy is not fitted in the current stage of the universality reconstruction. Hence, the discrepancy can not be resolved completely. With additional muon detectors (Chapter 9), the energy can be fitted independently of N_μ. An example of the prediction of the signal in muon detectors is shown in Fig. 7.6. Even if this will be applicable only for a small subset of the hybrid data set, the energy scale could be derived from the SD alone.

7.5 Prediction of the integrated signal in CDAS

There are two independent codes for the reconstruction of data taken by the Auger Observatory, CDAS[1] and $\overline{\text{Off}}\underline{\text{line}}$. This thesis is mainly based on $\overline{\text{Off}}\underline{\text{line}}$. Triggered by this work, the universality models were also introduced in CDAS. Based on the same approach as in the previous sections, the residuals of the signal are calculated. E, X_{max} and the geometry are taken from the CDAS FD reconstruction, N_μ is fitted [100].

The lateral as well as the temporal shape of the SD signal is predicted very well by shower universality (Fig. 7.7). This is very reassuring. The algorithms implemented in CDAS code are completely independent from the code used to derive the time models and from the reconstruction algorithm used in this thesis. The fact that both codes give compatible results gives further confidence in the validity of shower universality.

Currently, there is no large data sample that contains a direct measurement of the muons hitting the ground. Therefore, the muon scale needs to be fitted in all comparisons shown in this section. A very small data sample with muon information is available, obtained from underground scintillators in a part of the infill array (AMIGA). In a preliminary analysis it is shown that the universal signal model can describe also the scintillator signal. The predictions are obtained from a description based on universality that is extended to scintillators placed above ground [101]. The underground signal is calculated by estimating the attenuation in the soil above the scintillator. For this comparison, a hybrid event with SD, FD and scintillator

---

[1]Abbreviation for *central data acquisition system*. This software collects the data from all detectors of the Auger Observatory and performs reconstructions of SD data. https://auger.colostate.edu/private/herald
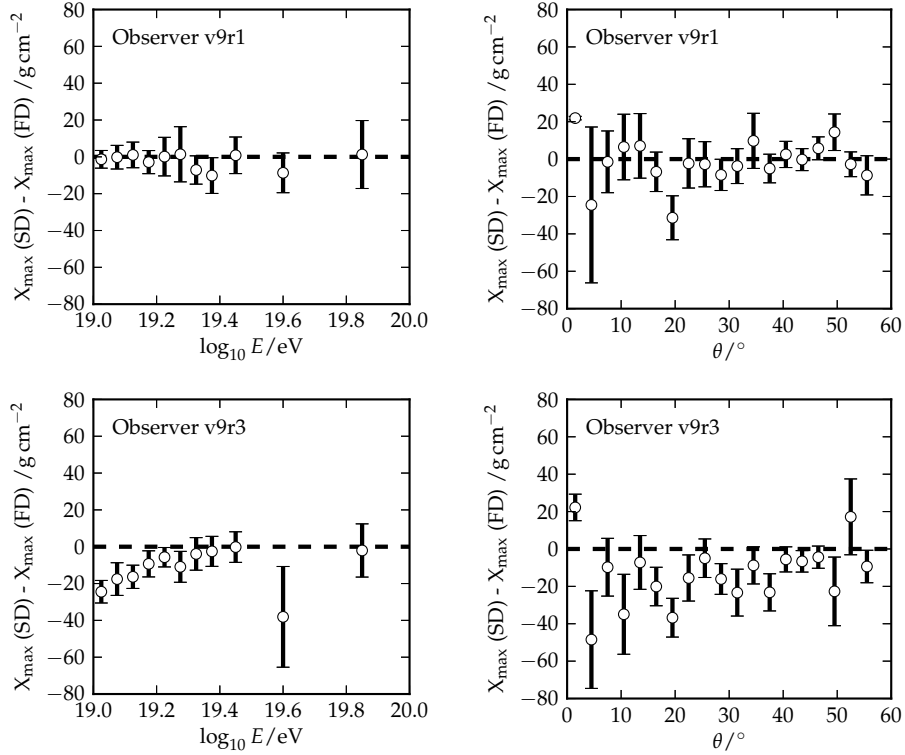
Figure 7.5: The difference of X_{max} in FD and the reconstruction based on universality. Old energy scale (top), new energy scale (bottom). Events without saturation are selected.

data is used. E and X_{max} are fixed to the value obtained from FD. The core position is fitted within the uncertainty of the FD reconstruction. The result is shown in Fig. 7.6. It is clear that universality gives a good description of the muon measurement, although a detailed analysis still needs to be done (e.g. a comparison based on a model of the underground scintillator response).
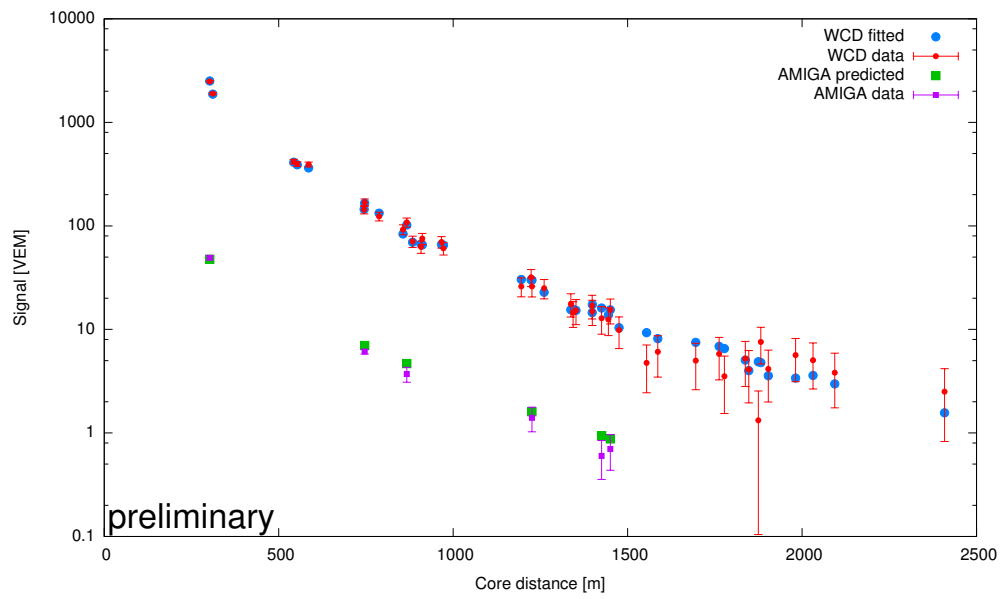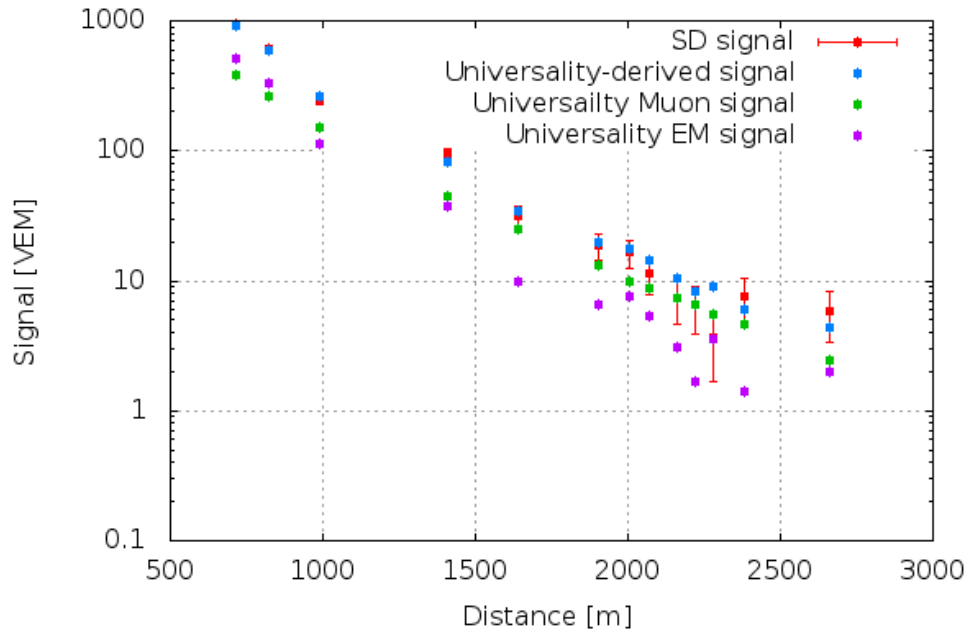
Figure 7.6: Prediction of the underground muon detector signal from universality. Shown is hybrid event with FD, SD and scintillator measurement. The energy and X_{max} are taken from the FD reconstruction. N_μ and the core position are fitted to the WCD signal. The model gives a good description of the muon signal. Preliminary analysis from [102].

(a) Prediction of the lateral shape of the signal in CDAS.
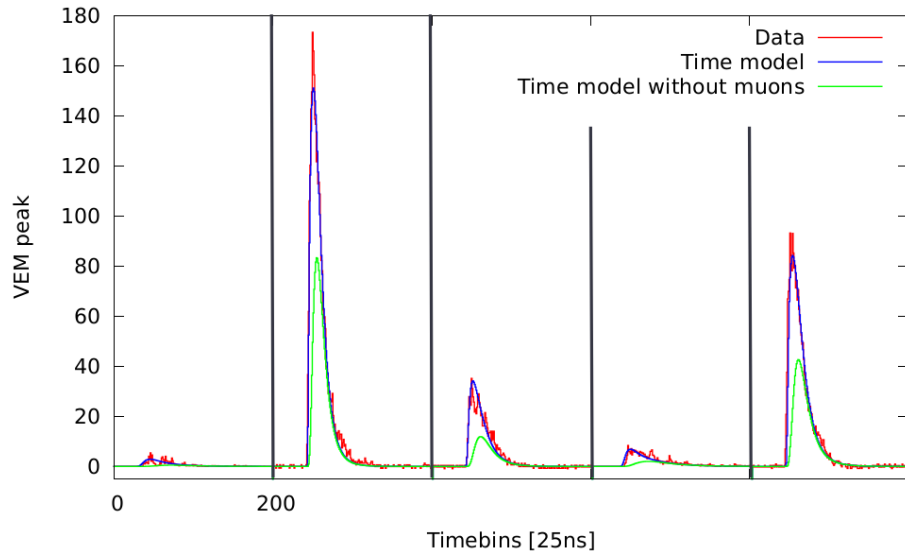
(b) Prediction of the time shape of the four largest signals in CDAS.

Figure 7.7: Triggered by this work, the time-dependent WCD signal in golden hybrid events was calculated with the CDAS (an independent reconstruction algorithm). The plot shows the signal traces (red lines) of the four stations with the highest signal (separated by the vertical lines) and the prediction of the time model (blue lines). The highest energy hybrid event without saturation was chosen. E, X_{max} and geometry are taken from the FD reconstruction, N_μ is fitted. From [100].

Results on mass composition and hadronic interactions

In the previous chapters, it is shown that the reconstruction algorithm (Chapter 5) works well in simulated (Chapter 6) as well as in real events (Chapter 7). In this chapter the results of the analysis of real air showers is presented. The data is analyzed in terms of the mass composition and hadronic interactions in the energy range 10^{19}eV to 10^{20}eV. The dependence on energy and zenith of N_μ and X_{max} is compared to the model predictions, in particular to the models tuned to LHC data. For the studies presented in this chapter, the reconstruction is based exclusively on data taken by the surface detector (SD). Data from the fluorescence detector (FD) is not used directly for the reconstruction. The mean and fluctuations of X_{max} are compared in the SD and the FD.

N_μ and X_{max} are observables sensitive to the primary mass and to the hadronic interactions at the onset of the particle cascade. A classification in light and heavy data samples on a single event basis can be done. More generally, showers are classified as muon-poor (muon-rich) and deep (shallow). This is applied to a mass-dependent search for correlations with astrophysical sources and to the search for ultra-high energy photons.

8.1 Description of the data set

The data set used in this thesis is based on the official *Observer* reconstruction[1]. In some cases, the data is not reliable due to communication problems of the central data acquisition system (CDAS) and the array or other problems with the data acquisition in the detectors. Data collected in these *bad periods*[2] is rejected.

The minimum energy (obtained from the standard SD reconstruction) is set to 10^{19}eV. Below that energy, the universality fit becomes increasingly difficult in terms of bias and resolution. Furthermore, the data sample available from the FD at low-energy is very large.

Only events with $\theta < 60°$ are considered. This restriction is mainly imposed by the models, which are built for this zenith angle range. At least five of the stations neighboring the

---

[1] http://augerobserver.fzk.de/doku.php?id=datatree:root
[2] http://ipnweb.in2p3.fr/~auger/AugerProtected/AcceptBadPeriods.html

station with the largest signal are required to be in data acquisition at the time of the event (5T5 quality selection).

The reconstruction is more difficult when a SD station saturates (*saturated events*). The reasons for this are discussed in detail Section 6.3.1. In particular the X_{max} resolution and the systematic uncertainties are larger than without saturation. Therefore, saturated events are studied separately in the following sections. In Chapter 9, measures to get rid of saturation as often as possible and the expected improvements of this analysis are discussed.

One of the most important changes in version `v9r3` of the reconstruction is an update of the energy scale [103, 104]. With the new energy calibration function, the energy estimate for SD events is increased by 10 % to 15 %. The effect of a change in energy on the reconstruction of X_{max} and N_{μ} was estimated for simulated showers in Section 6.7. This change in energy affects both the reconstructed N_{μ} and X_{max} (an increase in energy is compensated by a decrease in X_{max} and N_{μ}). The difference of the previous and the current version is shown.

The number of high quality events above $10^{19.5}$ eV can be doubled if the saturation of the FADC counters is avoided. This can be achieved, if the dynamic range is increased from 10 bits to 14 bits (this upgrade is currently discussed within the collaboration).

8.2 Depth of the shower maximum X_{max}

8.2.1 Distribution of the mean X_{max}

The reconstructed X_{max} has a systematic bias that depends on primary energy and zenith angle. It is corrected for empirically using Eq. (6.1) on page 67. The correction function is derived from simulations, assuming a mass composition of 50 % proton and 50 % iron. The mean X_{max} for events without saturation is shown in Fig. 8.2 with an estimate of the systematic uncertainties. The trend from to heavier masses with increasing energy seen in the FD reconstruction is also apparent in the SD reconstruction and continues up to the highest energies. The mass composition is not known a priori. Therefore, the bias correction introduces a systematic uncertainty in the mean X_{max}. In events without saturation it is comparatively small (5 g/cm^2 to 10 g/cm^2). In events with saturated stations, the uncertainty is in the order of 25 g/cm^2 (Fig. 6.7).

For saturated events, the correction function is derived from the mean X_{max} of events without saturation as follows: For each energy bin, a proton fraction w_p is derived based on the prediction of EPOS 1.99 and the derivation in Section 8.2.3. The energy dependence $w_p(E_i)$ is obtained by linear interpolation. The correction function $f(\log_{10} E, \theta)$ is fitted to all simulated proton and iron events with saturation. In Fig. 6.7, this was done with equal weights for proton and iron (no dependence on energy). In this case, a modified χ^2 is used to account for the energy-dependent proton fraction. The χ^2 contribution of each simulated shower with energy E and bias $\Delta[X_{max}]_i$ is modified according to $w_p(E)$:

$$\chi^2 = \chi_p^2 + \chi_{Fe}^2 \,,$$

where χ_p^2 (χ_{Fe}^2) is the contribution for proton (iron) and

$$\chi_p^2 = \sum_i \left(\frac{\Delta[X_{max}]_i - f(\log_{10} E_i, \theta_i)}{\sigma[X_{max}]_i} \cdot \frac{1}{1 - w_p(E_i)} \right)^2$$

$$\chi_{Fe}^2 = \sum_i \left(\frac{\Delta[X_{max}]_i - f(\log_{10} E_i, \theta_i)}{\sigma[X_{max}]_i} \cdot \frac{1}{w_p(E_i)} \right)^2$$

and

$$f(\log_{10} E, \theta) = p_0 + p_1 \log_{10} E/\text{eV} + p_2 \theta/^\circ \,.$$

Based on this correction function, the mean X_{max} for saturated events is obtained. The results are shown in Fig. 8.3. The resulting values after correction are in good agreement with non-saturated events. With this method however, the result for saturated and non-saturated events are no longer independent but it shows the consistency.

The largest systematic in X_{max} is caused by the uncertainty in the energy scale and amounts to 10 g/cm^2 to 15 g/cm^2. The remaining uncertainties are caused by the choice of the time model and the showers used for the coupling of X_{max} and X_0. The combined systematic uncertainty amounts to 5 g/cm^2 to 10 g/cm^2. The sources of systematic uncertainties are discussed in more detail in Section 6.7.
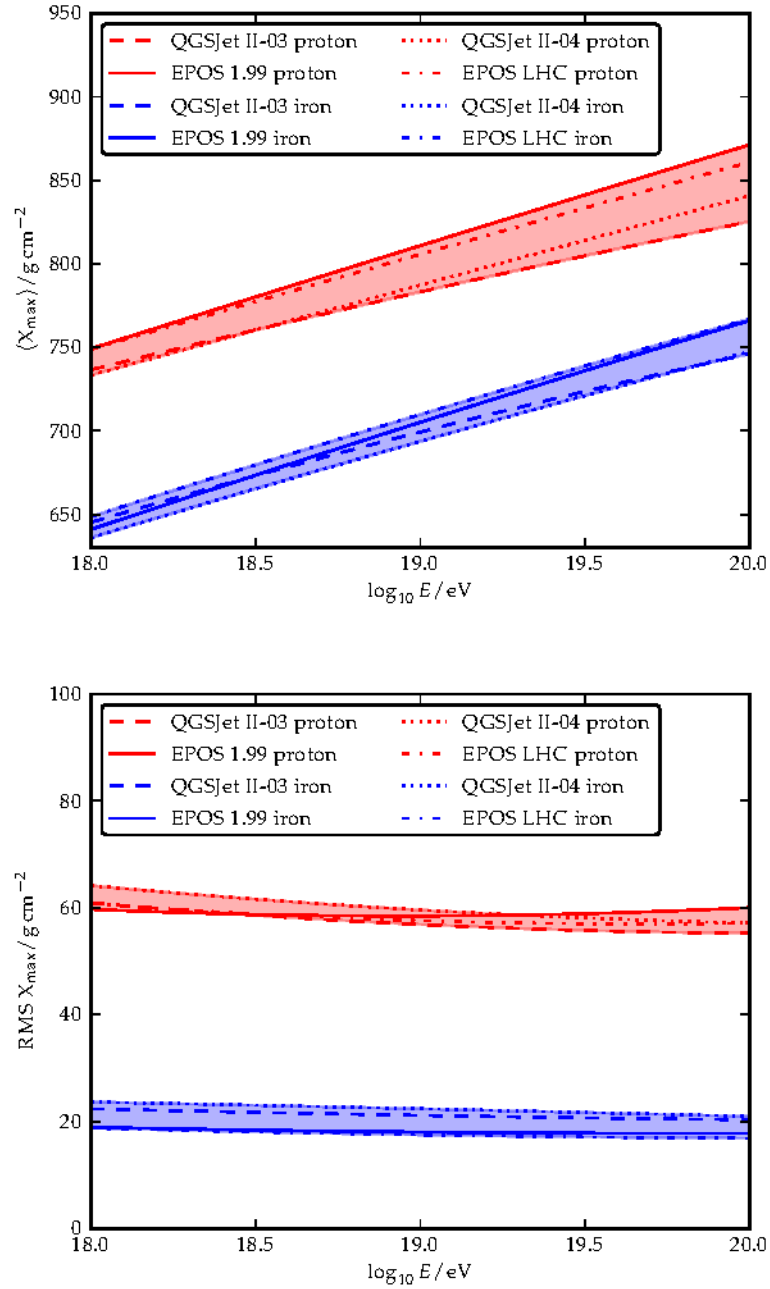
Figure 8.1: Model predictions of X_{max} for proton and iron. **Top:** mean X_{max}. **Bottom:** fluctuations of X_{max}. The values predicted by QGSJet II-03 and EPOS 1.99 (pre LHC) and QGSJet II-04 and EPOS-LHC (post LHC) are shown. The colored bands enclose the whole range of model predictions.
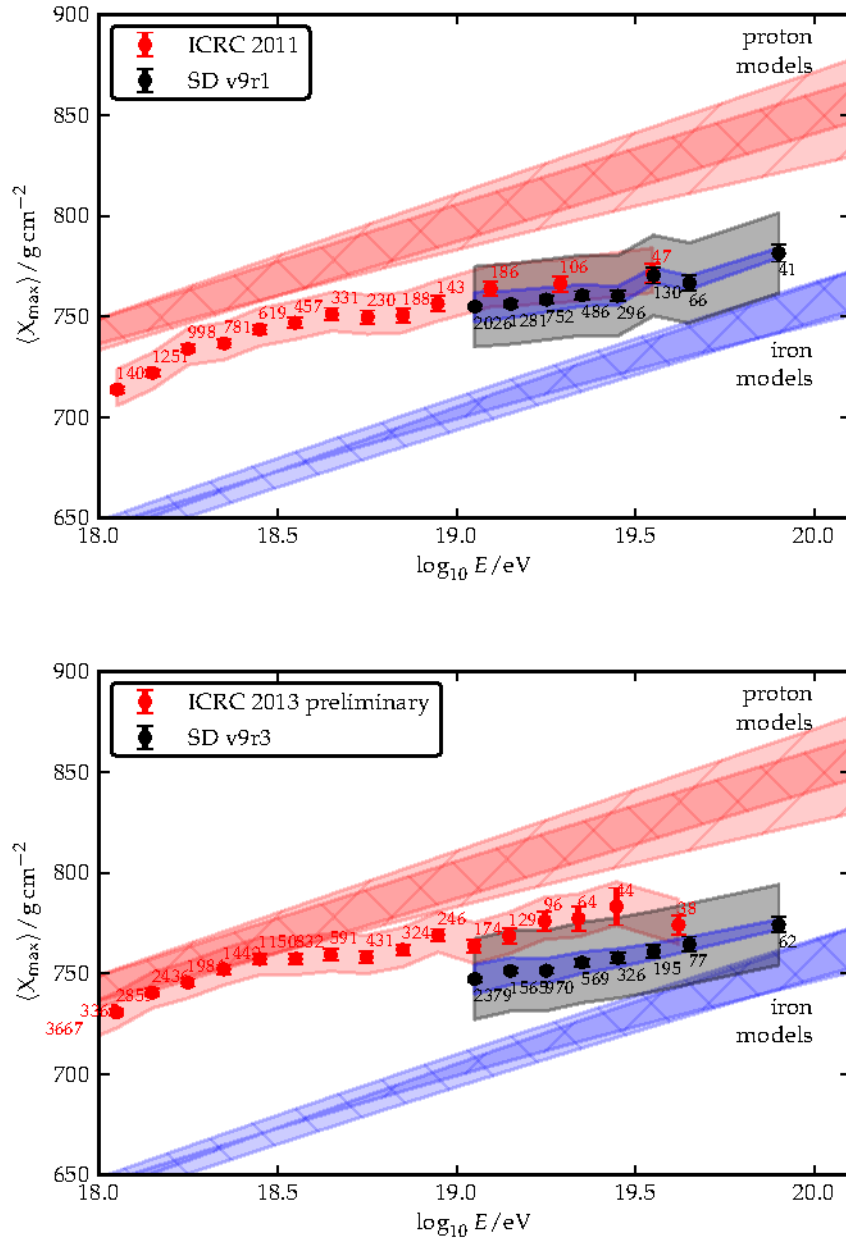
Figure 8.2: The mean X_max for events without saturated stations. The FD measurement [105] (red points) and the results from universality (black points). The blue band in the center indicates the systematic uncertainty from the bias correction. The black band is an estimate of the total systematic uncertainty. The range of the model predictions is shown by the upper and lower bands (for details, see Fig. 8.1). The number of events is given for each energy bin. There are more events in v9r3 due to the increased energy scale. The exact values for each point are given in Appendix A.10.
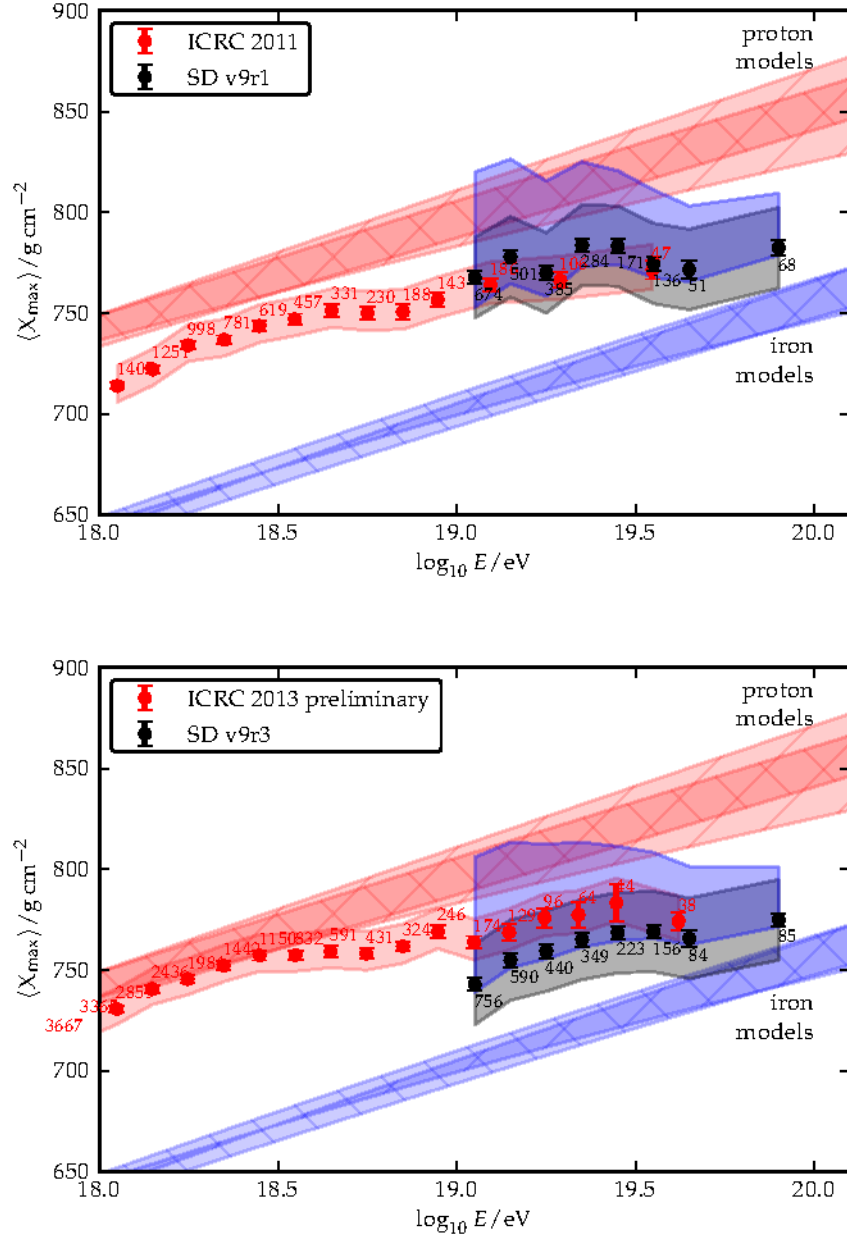
Figure 8.3: The same as Fig. 8.2 for events with saturation. The blue band in the center is a very conservative estimate of the systematic uncertainty due to the bias correction. The exact values for each point are given in Appendix A.10.

8.2.2 Mean logarithmic mass

The semi-superposition model states that the interaction of a nucleus of mass A and energy E with the nuclei in the atmosphere can be described by a superposition of A nucleons with energy E/A [106]. This is justified because the kinetic energy per nucleon of the primary particle is much larger than the average binding energy. The nucleons can be considered as moving in parallel without interacting with each other. It can be shown that in this case, the mean X_{max} is proportional to the mean logarithmic mass $\ln A$ [6]. Under the assumption of a specific interaction model, the mean mass is obtained from the mean X_{max} as

$$\langle \ln A \rangle = \frac{\langle X_{max}^{P} \rangle - \langle X_{max}^{data} \rangle}{\langle X_{max}^{P} \rangle - \langle X_{max}^{Fe} \rangle} \ln 56 \,.$$

The mean logarithmic mass based on EPOS 1.99 is shown in Fig. 8.4. Due to large differences in the model predictions for X_{max} especially at the highest energies, the mass has a large model dependence. A general trend to heavier composition is apparent, although no precise mass measurement can be derived. The range of the model predictions is indicated by the width of the bands.

8.2.3 Proton fraction

The proton fraction is obtained from $\ln A$. This is needed for the bias correction of saturated events (Section 8.2.1) and for the resolution correction of the X_{max} fluctuations (Section 8.2.4).

Assuming a two-component mixture of proton and iron nuclei, the proton fraction is obtained as

$$w_p = \frac{\ln A(\mathrm{Fe}) - \ln A}{\ln A(\mathrm{Fe}) - \ln A(\mathrm{p})}$$
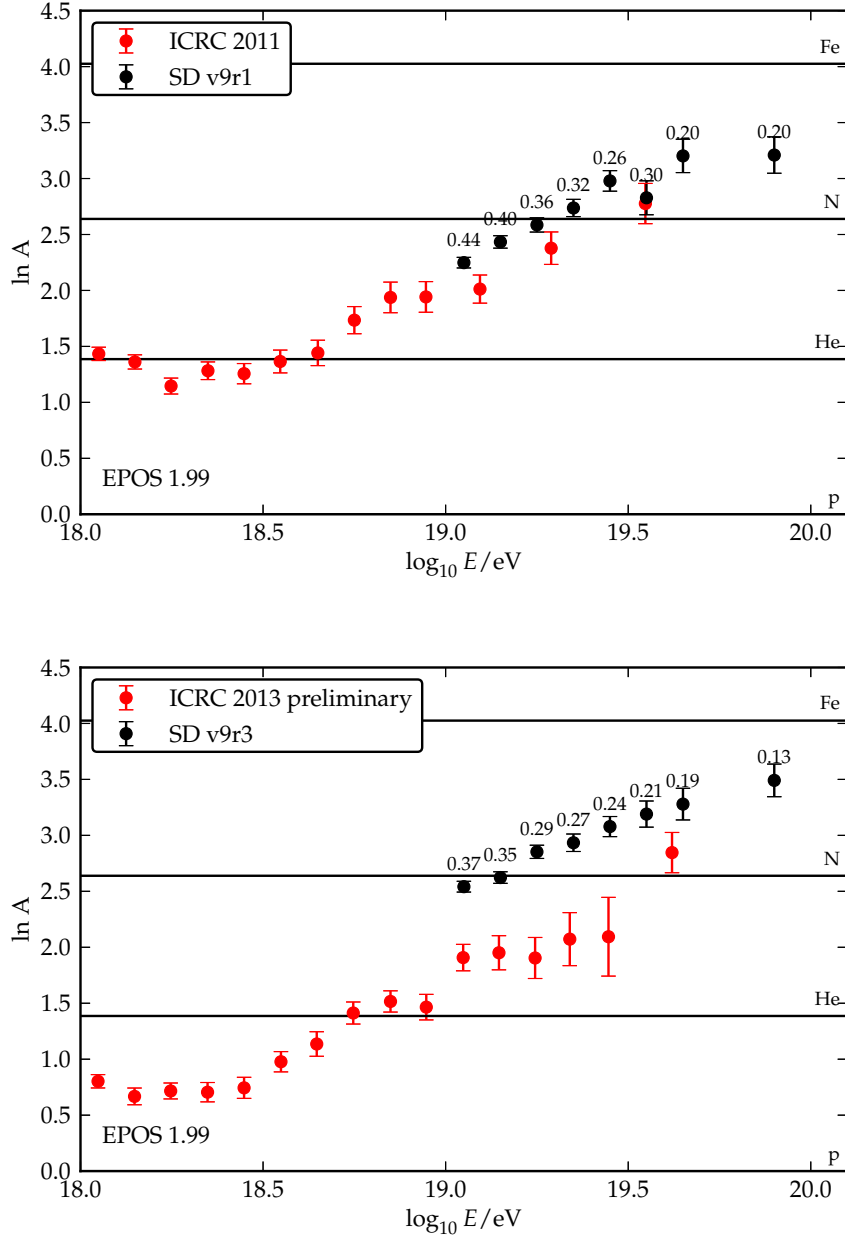$$w_p = \frac{\ln 56 - \ln A}{\ln 56} \,.$$

Figure 8.4: The mean logarithmic mass calculated from the X_{max} prediction of EPOS 1.99 (for details, see Section 8.2.2). The FD measurement [105] (red) and the results from universality (black).

8.2.4 Fluctuations of X_{max}

The fluctuations of the shower maximum (RMS of X_{max}) are of special interest, because there is only a small model dependence (see the model predictions in Fig. 8.5). The mass inferred from the X_{max} fluctuations has a comparatively small systematic uncertainty.

The measured fluctuations are a combination of physical and reconstruction effects. To obtain the real (shower to shower) fluctuations, the data needs to be corrected for detector effects. The measured spread $V[X_{max}]$ is corrected for the detector resolution σ to obtain the resolution corrected spread $RMS[X_{max}]$. It follows

$$RMS[X_{max}] = \sqrt{V[X_{max}] - \sigma[X_{max}]^2}\,.$$

Within one energy bin, the resolution depends only on the zenith angle of the shower. It is shown in [96] that the simple correction above can be applied to obtain a good estimate of the fluctuations in data if the sample of showers used to derive the resolution is a representative sample of the data. This requirement is fulfilled, because in the simulated shower library, θ is distributed uniformly in $\sin\theta\cos\theta$ (Fig. 4.2). The resolution obtained from simulations is shown in Fig. 6.11.

With the variance V, the standard deviation σ and the fourth central moment m_4 of the X_{max} distribution within one energy bin, the uncertainty of the spread reads as

$$\sigma[RMS[X_{max}]] = \sqrt{\frac{1}{N}\left(m_4 - \frac{N-3}{N-1}V^2\right)}\,.$$

The uncertainty of the resolution corrected spread is obtained from error propagation as

$$\sigma[RMS[X_{max}]]_{corrected} = \frac{\sqrt{V}}{RMS[X_{max}]}\sigma[RMS[X_{max}]]\,.$$

The situation is complicated by the fact that the detector resolution of X_{max} is mass-dependent. Assuming pure proton composition means subtracting too much from the observed X_{max} spread while assuming pure iron composition means subtracting not enough. Similar to the approach to correct the mean X_{max} in saturated events, the energy dependence of the resolution is obtained from the average of proton and iron weighted by the proton fraction w_p (the proton fraction is calculated using EPOS 1.99).

In an energy bin k, the mean μ_k and uncertainty σ_k of the detector X_{max} resolution is obtained from the weighted average as

$$\mu_k = \frac{\sum_i w_i \mu_i}{\sum_i w_i}$$
$$= \frac{w_p \mu_{\mathrm{p}} + (1 - w_p)\mu_{\mathrm{Fe}}}{w_p + (1 - w_p)}$$
$$= w_p \mu_{\mathrm{p}} + (1 - w_p)\mu_{\mathrm{Fe}}$$
$$\sigma_k = \sqrt{\frac{\sum_i w_i^2 \sigma_i^2}{\sum_i w_i^2}}$$
$$= \sqrt{\frac{w_p^2 \sigma_{\mathrm{p}}^2 + (1 - w_p)^2 \sigma_{\mathrm{Fe}}^2}{w_p^2 + (1 - w_p)^2}}$$
$$i = \mathrm{p, Fe}\,.$$

The measured spread of X_{max} as well as the resolution corrected values are shown in Fig. 8.5. It is important to note that already the uncorrected spread has a strong falling shape. Furthermore, the influence of the reconstruction bias on the fluctuations is comparatively small. Note that by doing this, the results for the mean and the spread of X_{max} are no longer independent and a decision has to be made about the model used to calculate $\ln A$ (in this case, EPOS 1.99 is used).

8.2.5 Summary on X_{max}

The mean X_{max} obtained with the SD matches well the FD results. The energy range of the X_{max} measurement is extended to the highest energies. The large systematic uncertainty of X_{max} in events with saturation can be reduced by combining the bias correction function with the proton fraction obtained from events without saturation. With this correction, also the X_{max} in events with saturation matches the FD measurement reasonably well. However, the results of the two SD data samples are no longer independent. In the range $25° < \theta < 50°$, the resolution and systematic uncertainty of X_{max} is improved. In saturated events, X_{max} is obtained up to 10^{20}eV. In the energy range that is only covered by the SD, the trend towards heavier mass composition is confirmed, but the composition remains mixed on average. The same conclusion can be drawn from the RMS measurement.

The discrepancy between version v9r1 and v9r3 of the reconstruction is well within the systematic uncertainties. The shift to smaller X_{max} in v9r3 is in very good agreement with the expectation when the energy is rescaled (Fig. 6.19). The results for version v9r1 agree even within the small systematics from the time model and the coupling of X_0 and X_{max}. Judging from universality, the discrepancies can be explained by a few factors. The comparison of X_{max} (FD) and X_{max} from universality shown in Fig. 7.5 suggests that the new energy scale is systematically too high. Within the systematics of the calorimetric energy (14 %) and the model systematics of the universality reconstruction, the FD results and universality agree. The models for the time shape and the X_{max}-X_0-coupling are based on an equal mixture of simulated proton and iron showers. If the change in average is taken into account, a systematic shift of the X_{max} distribution in the SD reconstruction towards the FD result is possible.
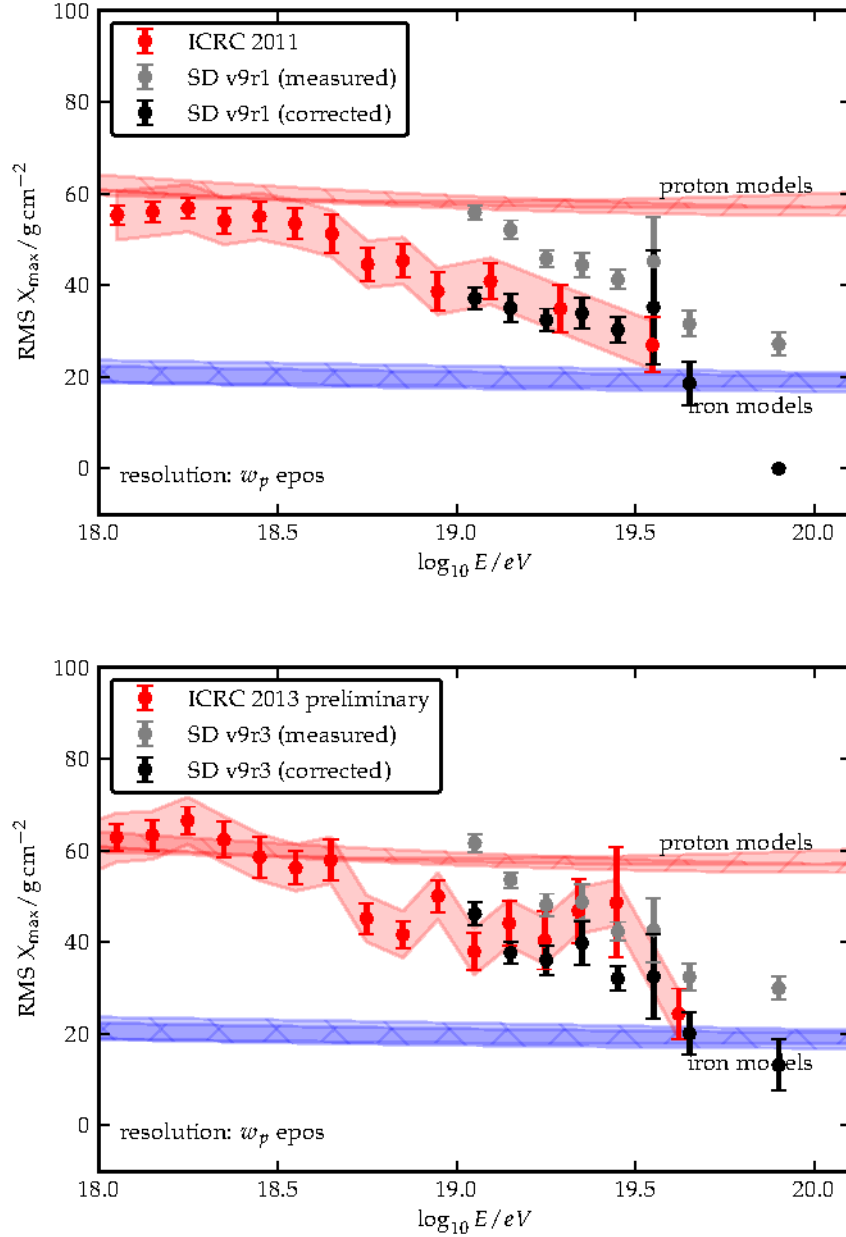
Figure 8.5: Fluctuations of X_{max} for events without saturated stations. Detector effects have been subtracted from the measured spread to obtain the physical fluctuations. The correction is calculated based on the mean X_{max} and the average logarithmic mass obtained from EPOS 1.99. The FD measurement [105] (red) and the results from universality (black). In the last two bins, the estimate of the detector resolution is larger than the measured spread and the corrected value becomes invalid (either the estimated iron fraction is too small or the two-component model needs to be improved). The range of the pre (post) LHC model predictions is indicated by the light (dark) colored bands (for details, see Fig. 8.1). The exact values for each point are given in Appendix A.10.

8.3 Muon scale N_μ

In this section, the muon scale N_μ is studied and compared to the model predictions. The muon content of air showers at the highest energies is not described properly by the hadronic interaction models. This was found in several other analyses (e.g. [7, 8, 9, 10]) and is also shown in this section. The effect of fluctuating the energy in simulated showers to account for the SD energy resolution (Fig. 6.11) was checked.

Part of the study in this section is based on a different detector simulation. To account for the muon discrepancy the thinning weight of all particles correlated with the muon scale is increased (all signal components except the pure electromagnetic). The weights are increased by $R_\mu = 1.6$. The muon scale discrepancy is further discussed in Section 8.3.3.

8.3.1 Distribution of the mean N_μ

The energy dependence of N_μ in pure SD events is shown in Fig. 8.6. Even the most extreme model (EPOS 1.99 iron) does not predict enough muons to account for the reconstructed N_μ at the highest energies.

N_μ has a strong dependence on zenith angle, even if a zenith-dependent bias stemming from the reconstruction is subtracted. The entire range of the model prediction between proton and iron is covered by the data. This indicates a discrepancy in the description of the muon attenuation in the atmosphere. A harder muon spectrum at production in data compared to simulations leads to an apparent increase of the muon scale for inclined events.

With the new energy scale in `v9r3`, the mean N_μ decreases by ≈ 0.1. This value is in good agreement with the expected systematic effect shown in Fig. 6.19. However, the value is still above the model predictions at 10^{20} eV.

An interpretation of the N_μ measurement in terms of primary mass remains difficult due to the difference in scale between simulations and real data. Nevertheless, while the reconstructed N_μ of simulated showers decreases as a function of energy as expected, it remains rather constant in data. If the muon discrepancy does not depend on the primary energy (this assumption is justified by the Fig. 8.8), a trend from intermediate to heavy composition is apparent in the data in agreement with the X_{max} measurement.

The dependency of the mean N_μ on energy and zenith angle was also studied using golden hybrid events (Fig. 8.6). With the same approach as in Chapter 7, E, X_{max} and the geometry of the shower are determined by the FD reconstruction (and not modified further during the fit). N_μ is the only remaining parameter to be fitted. The mean N_μ in SD events is compatible with the results derived in golden hybrid events. If the rescaled simulations are used, the mean reconstructed N_μ is also scaled by a factor $R_\mu = 1.6$. It is not changed when the energy in simulations is smeared.

8.3.2 Fluctuations of N_μ

In contrast to the studies for X_{max} (Section 8.2.4), there is no parametrization of the shower-to-shower fluctuations of N_μ. Therefore, the detector resolution is not subtracted but the reconstructed simulations and data are compared directly.

The spread of N_μ derived from SD events is shown in Fig. 8.6. When the energy resolution of the SD reconstruction is taken into account in the simulation, the spread in data is not compatible with the simulations. This is because part of N_μ is absorbed in the energy in the SD reconstruction: A muon-rich shower is assigned a higher energy due to the larger signals. This results in a smaller reconstructed N_μ. The opposite effect is apparent for muon-poor showers. As a result, the width of the N_μ distribution in SD events gets smaller.

In golden hybrid events, because the energy is derived from the electromagnetic part of the shower, N_μ can be reconstructed. When the energy resolution is taken into account, the golden hybrid data is compatible with the simulations.

8.3.3 Compatibility of N_μ and X_{max}

The muon scale difference in data and simulation can be obtained also by a different approach. An air shower is created by a single particle, hence all the observables must give compatible predictions for the primary particle if the models and the reconstruction describe the data well. This leads to the requirement to obtain the same value for the primary mass from N_μ as well as from X_{max}.

Similar to X_{max}, N_μ is assumed to scale linearly as a function of $\ln A$. This was checked with showers of intermediate mass (Fig. A.30 for details).

Due to the muon scale discrepancy, the estimate for the mass from N_μ is above the iron prediction. $\ln A(X_{max})$ and $\ln A(N_\mu)$ can be made compatible by scaling down the muon content by a factor f as

$$\ln A(N_\mu/f) = \ln A(X_{max}).$$

With the assumption of linearity, $\ln A(N_\mu)$ is given by

$$\langle \ln A \rangle = \frac{\langle N_\mu^P \rangle - \langle N_\mu^{data} \rangle}{\langle N_\mu^P \rangle - \langle N_\mu^{Fe} \rangle} \ln 56 .$$

Requiring that the rescaled N_μ gives the same $\ln A$ as X_{max},

$$\frac{N_\mu/f - N_\mu^{Fe}}{N_\mu^P - N_\mu^{Fe}} = \frac{X_{max} - X_{max}^{Fe}}{X_{max}^P - X_{max}^{Fe}} .$$

Finally, the scale factor is obtained as

$$f = \frac{N_\mu}{\frac{X_{max} - X_{max}^{Fe}}{X_{max}^P - X_{max}^{Fe}} \cdot (N_\mu^P - N_\mu^{Fe}) + N_\mu^{Fe}} .$$

The dependence on energy and zenith angle of the scale factor is shown in Fig. 8.8. The dependence on primary energy is small while there is a strong dependence on zenith angle. Using this approach, the change of the mass composition with energy is subtracted automatically. The scale factor purely reflects the mismatch of the model predictions and the data.
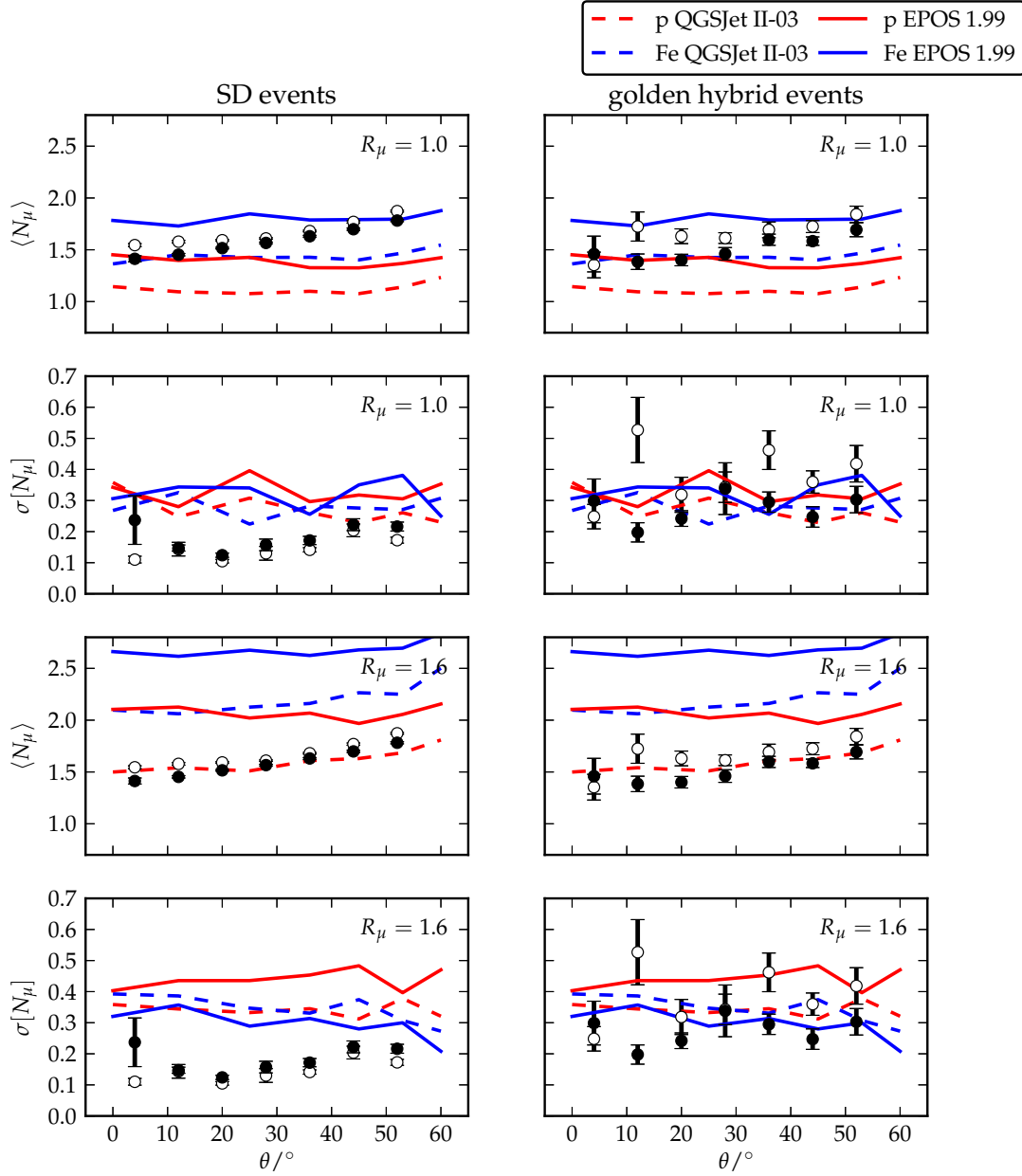
Figure 8.6: Energy dependence of N_μ in SD events (left column) and golden hybrid events (right column). Data: $\theta = 30° - 40°$. MC: $\theta = 36°$. Standard simulations (upper four plots) and after rescaling of the thinning weight by $R_\mu = 1.6$ (lower four plots). For the reconstruction of simulated showers, the energy is smeared according to Fig. 6.11. The mean N_μ is compatible with the rescaled simulations. The measured spread does not match the reconstructed SD simulations. This is because part of the fluctuations of N_μ are absorbed to the energy by the SD reconstruction, which leads to smaller fluctuations of the reconstructed N_μ. With the energy estimated from the FD reconstruction, the fluctuations are estimated correctly.

Figure 8.7: The same as Fig. 8.6 as a function of zenith angle. Data: $\log_{10} E/\text{eV} = 19.0 - 19.1$. MC: $\log_{10} E/\text{eV} = 19.0$.
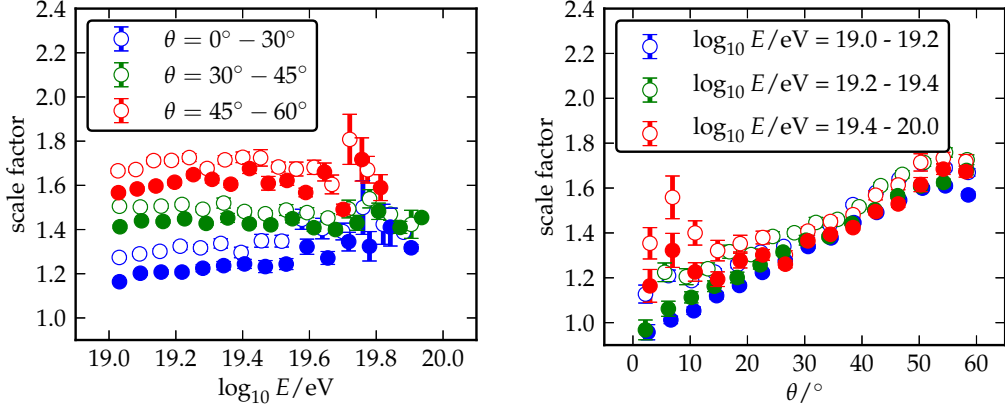
Figure 8.8: From the requirement of compatibility of ln A derived from X_{max} and N_μ the discrepancy of the muon scale in data and simulations is derived. The energy-dependent change in mass composition is compensated for automatically. The muon scale difference is rather independent of the energy (left) while there is a strong dependence on zenith angle (right). Empty markers: `v9r1`, filled markers: `v9r3`.

8.3.4 Signal predictions for simulations and data

In this section, the model prediction for the four signal components is studied. The predictions for data are compared to simulated proton and iron showers. For the comparison, simulations at the same energy and zenith angle as in data are chosen.

Given E, N_μ and X_{max} (fitted or true values), the contribution of the signal components in each station is determined. An example of the reconstructed component LDFs is shown in Fig. 5.5).

In Fig. 8.9, the prediction for the ratio of the components to the total signal is shown. This was done for the pure electromagnetic magnetic component and the sum of the remaining three components (those that depend on N_μ). The signal ratio is bracketed by the simulations. The ratio tends to be better described by the prediction for iron.

A different way of comparing the signal predictions is shown in Fig. 8.10. Here, the estimate for the components is directly compared to the prediction for simulated showers. The ratio R is

$$R_{e\gamma} = \frac{S_{e\gamma}(\text{data})}{S_{e\gamma}(\text{QGSJet II-03})}$$

$$R_{\text{had}} = \frac{S_{\text{had}}(\text{data})}{S_{\text{had}}(\text{QGSJet II-03})},$$

where S_{had} comprises all signal components that depend on the muon scale,

$$S_{\text{had}} = S_\mu + S_{e\gamma_\mu} + S_{e\gamma_{\text{had}}}.$$

The ratio is calculated both for proton and iron showers simulated with QGSJet II-03. If the models were a perfect description of the data, $R = 1$ is expected, independent of the
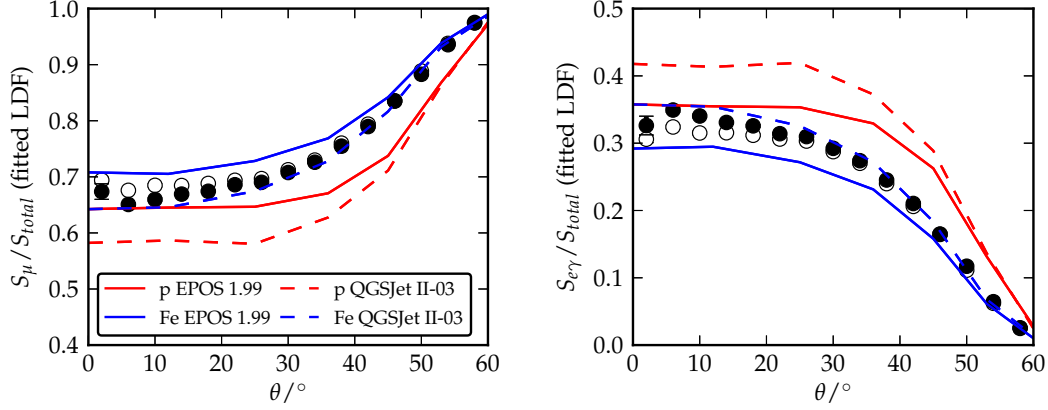
Figure 8.9: The ratio of the signal components to the total signal. S_μ contains all the parts of the signal that depend on the hadronic cascade (left), $S_{e\gamma}$ contains the purely electromagnetic part (right). The signal components are predicted from the fitted values of N_μ and X_{max}. The data is clearly described better by iron simulations while no inference can be made from this plot about the interaction model. Empty markers: `v9r1`, filled markers: `v9r3`.
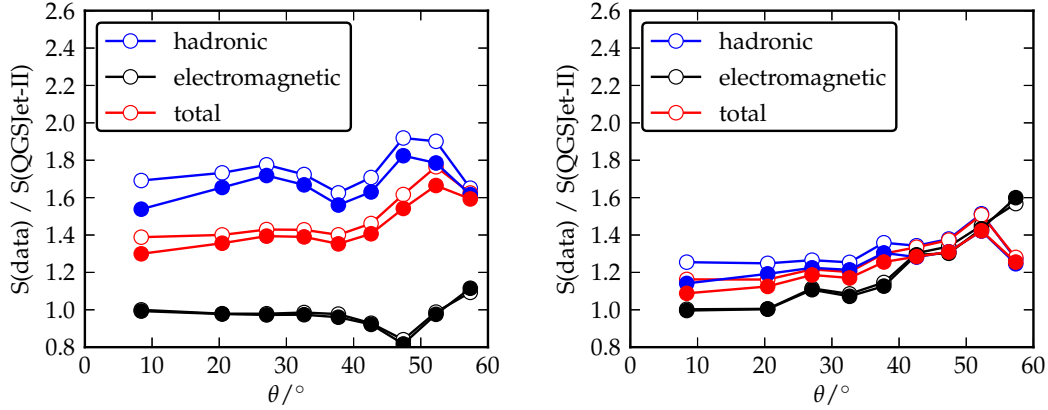

Figure 8.10: The ratio of the estimated signal components in data and simulation, as predicted from the fitted N_μ and X_{max}. The parts of the signal that depend on the hadronic cascade are considered separately from the purely electromagnetic part. Assuming proton composition (left), not only the muonic component has to be rescaled but also the electromagnetic part. This hints to a mismatch in the energy scale. It decreases with the new energy scale in Observer `v9r3`. If iron composition is assumed (right) the necessary rescaling is almost the same for the muonic and the electromagnetic part. Empty markers: `v9r1`, filled markers: `v9r3` Data: $\log_{10} E/\text{eV} = 19.0 - 19.1$. MC: $\log_{10} E/\text{eV} = 19.0$.

zenith angle. The electromagnetic part of the signal ($R_{e\gamma}$) is in good agreement with the model predictions. The discrepancy in the prediction of the hadronic part (R_{had}) is clearly visible. The ratio is fits better to the iron prediction. Part of the discrepancy vanishes with the updated energy scale. The rise as a function of zenith angle that can also be seen in the mean N_μ remains.

8.3.5 Summary on N_μ

With the updated energy scale, a large part of the original *muon problem* is solved. The mean and fluctuations of N_μ in real data are compatible with a trend to heavier composition in the energy range 10^{19}eV to 10^{20}eV. Moreover, the signals measured on ground are described in a more consistent way by iron simulations. The spread of N_μ in golden hybrid events is bracketed by simulations when the energy resolution of the SD is considered. This holds for the mean N_μ as well, however based on the most extreme assumption of EPOS iron showers. The largest remaining discrepancy is apparent in the zenith-dependent increase of N_μ. This is not expected if the models are just off by an overall scale. It can be explained if the muon injection spectrum at the point of production in real showers extends to higher energies than in simulations. At higher zenith angles, more muons are able to travel to the ground surface and thus increase the apparent muon content. The data exhibits a trend towards heavier masses at the highest energies, although no statement about the preferred model can be made from the spread of N_μ alone.

8.4 Mass measurement for individual events

The most meaningful statements about the sources and propagation processes of cosmic rays can be made if the primary mass is known for each individual event. The average mass dependence of X_{max} and N_μ was shown in the previous sections. Based on each parameter or a combination of both, it is possible to assign a mass estimate to every event measured by the SD. The situation is complicated by the fact that the prediction of the number of muons is smaller than in the data. However, the mismatch is expected to be independent of the primary mass, meaning that the overall distribution of N_μ is shifted to larger values. It is not possible to assign an exact mass value, but it is possible to select samples from the data that are relatively light or heavy compared to the overall distribution.

A light (heavy) sample can be chosen by selecting deep (shallow) showers or muon-poor (muon-rich) showers. A combination of N_μ and X_{max} can be done to increase the separation power. This is done based on a linear Fisher discriminant. The details on the discriminant are described in Section 6.5). The separation function is obtained from proton and iron simulations at $E = 10^{19.5}$eV.

The distribution of N_μ and X_{max} in simulations as well as data is shown in Fig. 8.11.

8.4.1 Rescaling of X_{max}

The Fisher discriminant is derived from simulations at a fixed energy ($10^{19.5}$eV). The energy dependence of X_{max} in data has to be subtracted for a meaningful mass classification. The measured X_{max} of each shower is shifted according to the elongation rate of proton showers to the value that the shower would have if the energy was exactly $10^{19.5}$eV (the choice of the model and primary particle for the subtraction is arbitrary). For the transformation, the parametrization for the mean X_{max} is taken from Fig. 8.1. Using the elongation rate

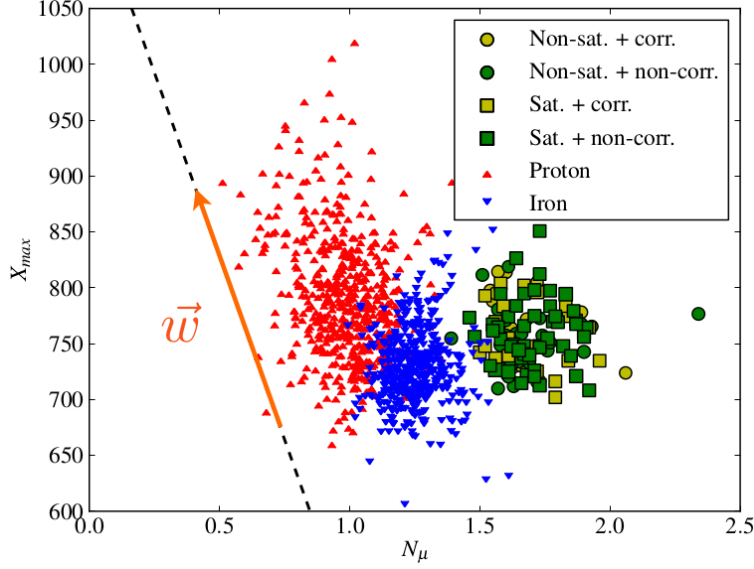$$\frac{\partial X_{max}}{\partial \log_{10} E}$$

Figure 8.11: Distribution of N_μ and X_{max} in simulations and data. The simulations are at a fixed energy of $10^{19.5}$eV. The real events are selected according to the prescription described in Section 8.5. The arrow ($\vec{w}$) indicates the direction of maximum separation. The mass estimator decreases along the direction of the arrow.

for a shower with $E = E_{rec}$, the transformed $X_{max}^{rescaled}$ reads as

$$X_{max}^{rescaled} = X_{max} + (\log_{10} E_{rec} - \log_{10} E_{MC}) \cdot \frac{\partial X_{max}}{\partial \log_{10} E} \, .$$

At the highest energies, a large fraction of the events has a saturated station. It was shown in Section 6.6, that events with and without saturation have the same distribution of the true X_{max}. Therefore, the depth of the shower has a negligible influence on whether a station saturates. The difference in the mean of the distributions is well below $1 \, g/cm^2$. Under this assumption, the observable differences in the reconstruction bias (for details, see Section 6.3.1) and resolution of X_{max} in events with saturation are purely due to the reconstruction. Hence, the observed distributions are generated from the same basic population. The distributions of X_{max} can be brought to agreement by an overall shift and rescaling of the spreads as follows.

The rescaled value X_{max}^{renorm} for events with saturation is obtained as

$$X_{max}^{renorm} = (X_{max}^{sat} - \langle X_{max}^{sat} \rangle) \cdot \frac{\sigma_{X_{max}}^{not \, sat.}}{\sigma_{X_{max}}^{sat.}} + \langle X_{max}^{not \, sat.} \rangle \, .$$

It was shown in the previous section, that the discrepancy in the prediction of the muon content has only a small energy dependence. In this case, the distribution of the measured parameters can be shifted along the N_μ axis to match the simulations. This is done only for visualization. The shift has no influence on the direction of the mass discrimination vector. The Fisher discriminant can be directly applied to the data without any shift in N_μ to select light and heavy samples.

8.5 Correlations with point-like astrophysical sources

First evidence for the correlation of arrival directions with astrophysical sources was published in [29]. In the first step of the analysis, a definition of correlation is needed. The deflection of charged particles in magnetic fields depends on the energy (more generally on the rigidity) and the distance traveled. Therefore, part of the data was used to scan the parameter space. The strongest correlation was found for a minimum energy $E > 55 \times 10^{18}$eV, a maximum redshift $z < 0.018$ (corresponding to a maximum distance of about 75 Mpc) and a deflection angle $\Psi < 3.1°$. As of 2007, out of the 27 events satisfying these cuts, 69 % correlated with the position of active galactic nuclei from the VCV catalog [28]. The probability P to find this correlation if the underlying distribution of arrival directions is isotropic is $P < 10^{-5}$. Since the first publication, the correlation was updated. The fraction went down to 38 % in an update of the first publication [30]. In the most recent analysis of the correlation, 30 out of 110 events correlate. This corresponds to a chance probability of 7 % ($< 3\sigma$).

At the current stage, there is no conclusive explanation for the decrease of the correlation fraction. Possible reasons are the aging of SD tanks or a drift in the energy scale. The latter would allow lower energy events to degrade the correlation fraction.

Regardless of these effects, it is especially worthwhile to study the correlation with light primary particles. The deflection in the intergalactic magnetic fields is proportional to the rigidity and to the distance to the source. Protons from nearby sources are therefore expected to have the strongest correlation to possible astrophysical sources. Iron nuclei can also point back to astrophysical sources but the minimum energy for a correlation to be observable is 26 times higher than for protons and hence above the energy range accessible to the Pierre Auger Observatory.

Therefore, each event in the data sample of AGN candidates is classified as light or heavy according to the procedure described in Section 8.4. The events are sorted according to the mass estimate (the projection of N_μ, X_{max} onto the discriminant $\vec{w}$). Based on the fluctuations of X_{max} measured by the FD, 10 % to 15 % protons are expected at the highest energies (Fig. 8.12) [31]. Therefore, the 10 events with the smallest mass estimate are considered as proton candidates. The 35 heaviest are considered as iron candidates. The distribution of N_μ and X_{max} of the candidate events is shown in Fig. 8.13. With those samples the correlating fraction is calculated. Without any anisotropy in the true distribution of arrival directions, $p = 21$ % of all events are expected to correlate with at least one source due to random coincidence. This fraction corresponds to the area of the sky (weighted by the exposure of the SD) that is covered by the regions at angular separation less than $\Psi = 3.1°$ of the source.
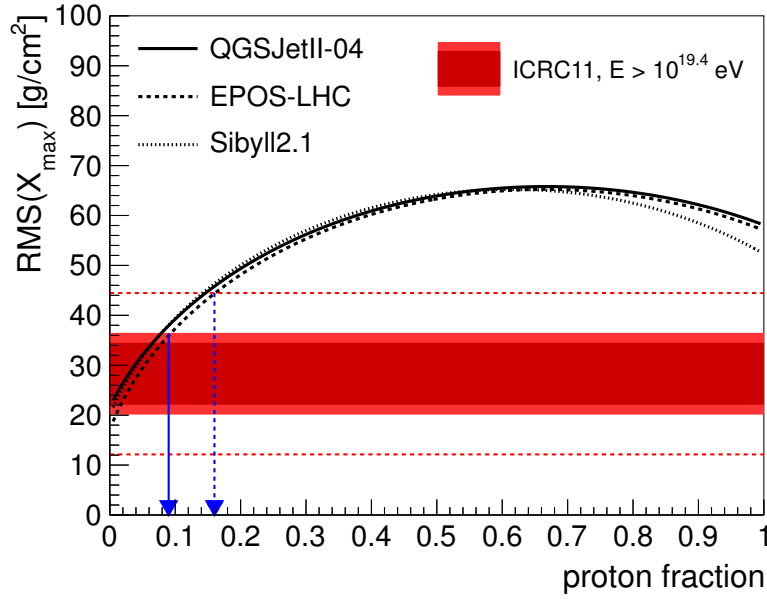
Figure 8.12: The proton fraction as a function of the X_{max} fluctuations, assuming only proton and iron nuclei are present in the data. At the highest energies, a proton fraction of 10 % to 15 % is compatible with the measurement. From [31].
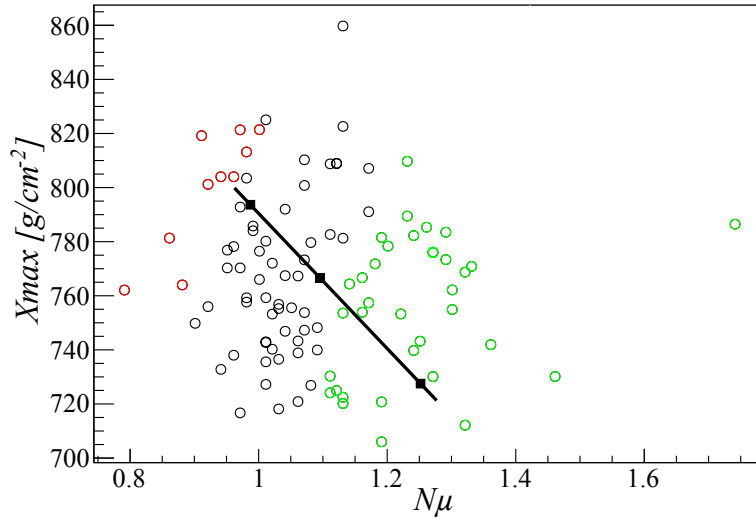

Figure 8.13: N_μ and X_{max} for the SD events in the AGN selection (all points). Showers are classified as light (red) and heavy (green). The solid black line connects the mean values in proton (top), data (middle) and iron (bottom). For better visibility, the data sample was shifted along the x axis to coincide with the MC prediction (black squares connected by the solid line), i.e. to correct for the muon discrepancy. Note that the analysis is independent of this shift. From [107].
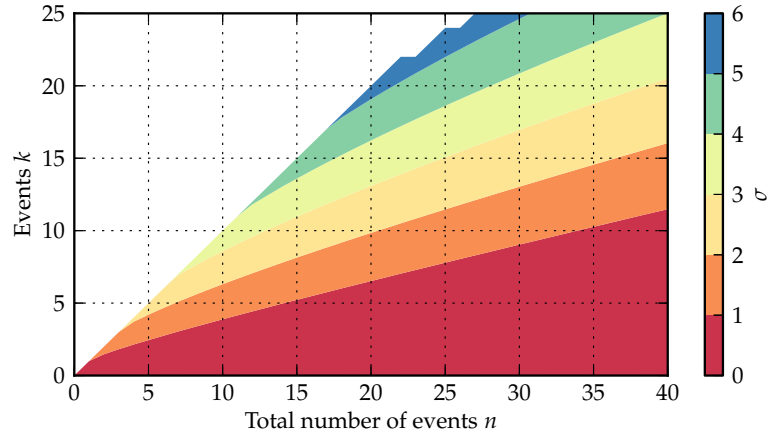
Figure 8.14: The confidence level for the rejection of the null hypothesis (isotropy) given a data set of size N and the number of correlating events k.

The time dependence of the correlating fraction is shown in Fig. 8.15 for the complete data set and the light and heavy sample. The correlating fraction of the light component as of today is over 60 %. 6 correlating events out of 10 corresponds to a chance probability $P = 0.009$ for the events to originate from an isotropic distribution. For the heavy sample the fraction is mainly consistent with the expectation for isotropy The chance probability is $P = 0.105$ [107]. The expected confidence level for the rejection of the isotropy hypothesis is shown in Fig. 8.14 (e.g. for 10 proton candidates, the confidence level is 2σ if 50 %).

The arrival directions of the full event sample from the AGN selection is shown in Fig. 8.16. The light and heavy selection is shown in Fig. 8.17. The arrival directions of the heavy sample are distributed uniformly over the whole sky. The light sample seems to be concentrated closer to the super galactic plane. However, due to the very limited size of the data sample, no firm conclusions can be drawn.

(a) Light sample

(b) Heavy sample

(c) All events
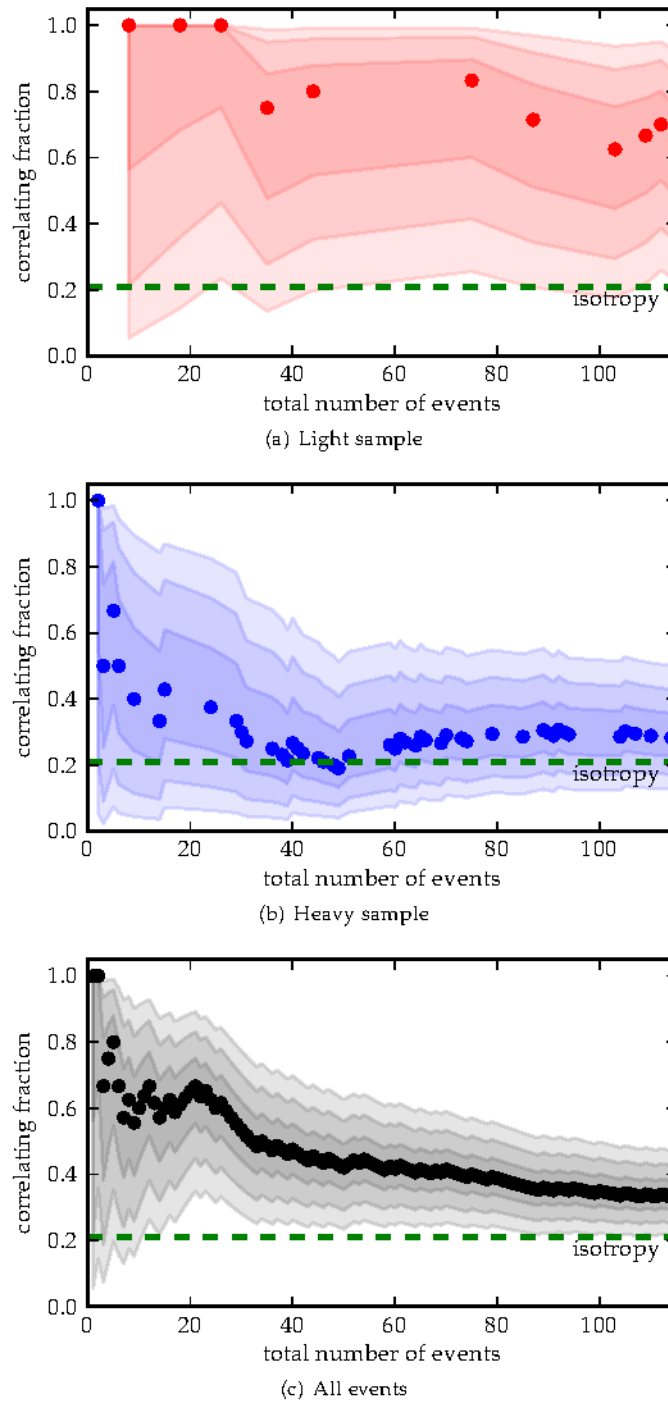
Figure 8.15: The correlating fraction as a function of the total number of events (ordered in time. The correlation is stronger for the light (70 %) than for the heavy sample (30 %). Adapted from [107].
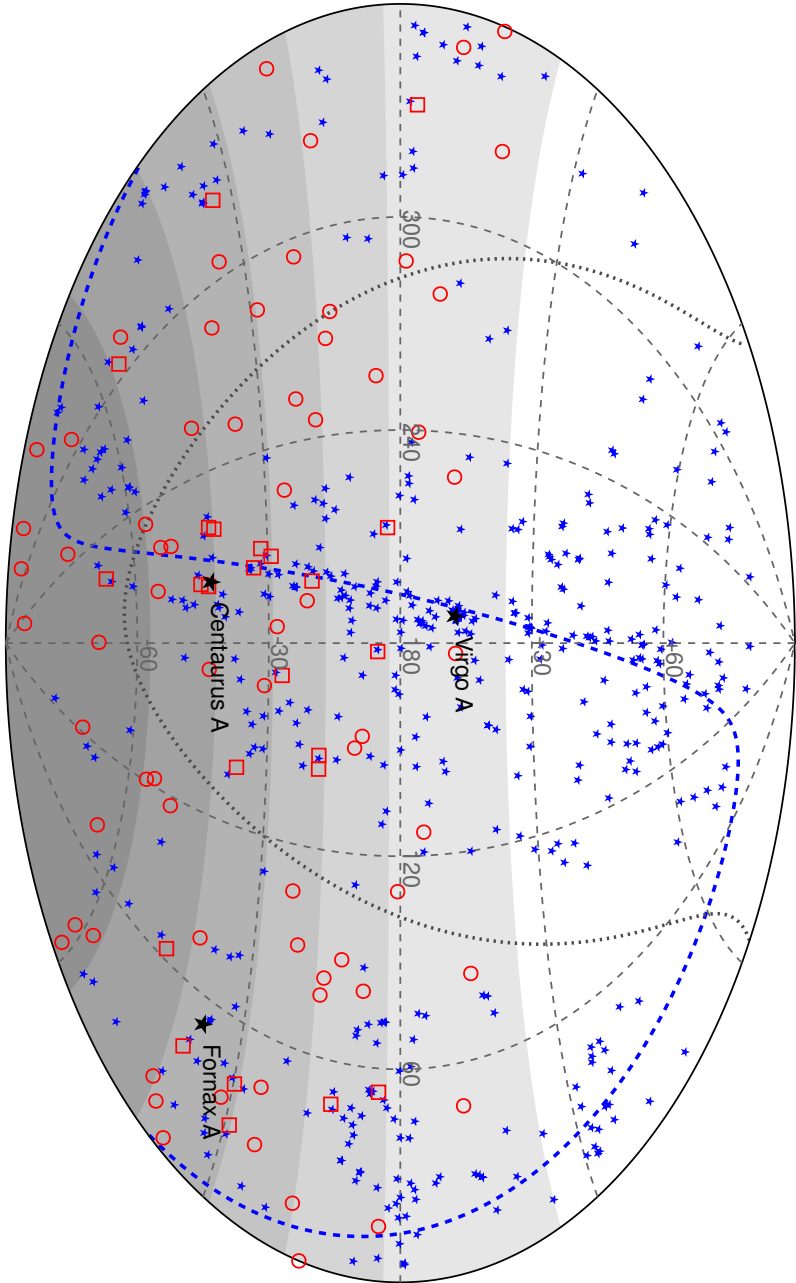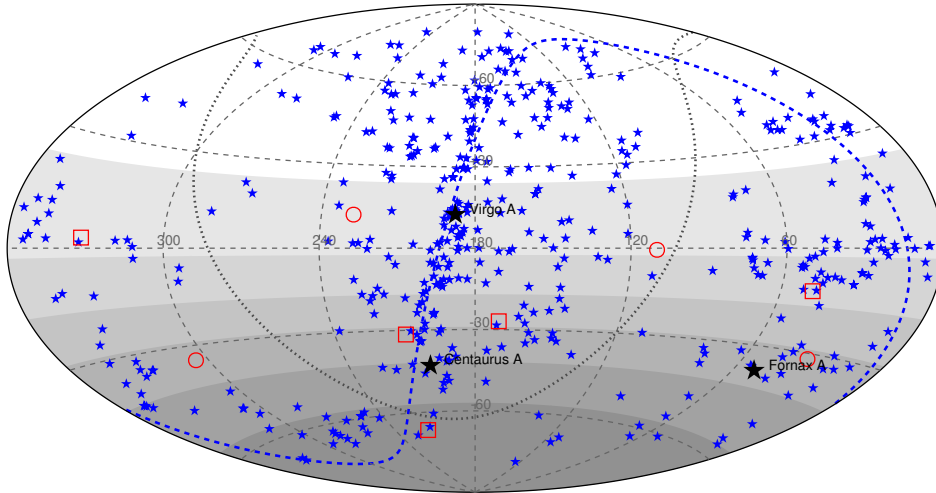
Figure 8.16: The position of the 472 AGNs with z < 0.018 from the VCV catalog (blue stars) and the selected AGN candidates (red markers) in equatorial coordinates. The super galactic plane is indicated by the dashed blue line. **Circles:** non-correlating events, **Squares:** correlating events. The shaded areas indicate the relative exposure of the surface detector. From [107].

(a) Light sample
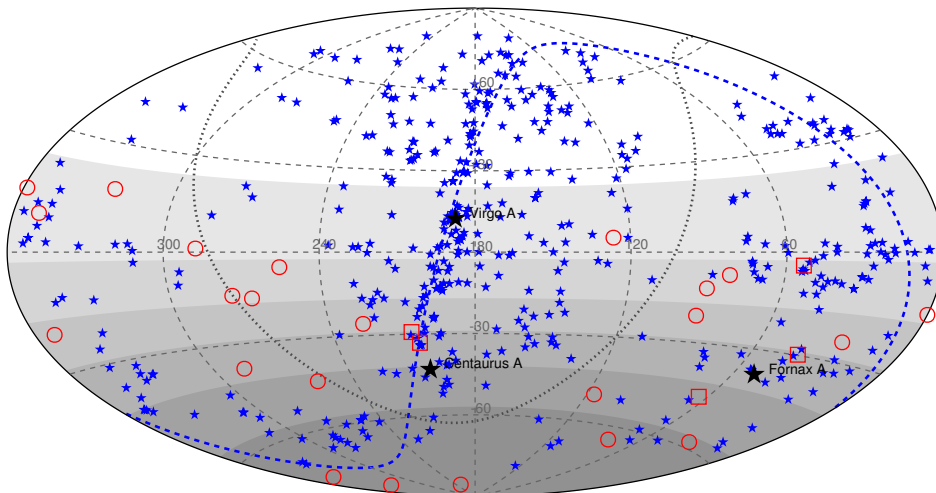
(b) Heavy sample

Figure 8.17: The same as Fig. 8.16 for the light and heavy sample. **Circles:** non-correlating events, **Squares:** correlating events. From [107].
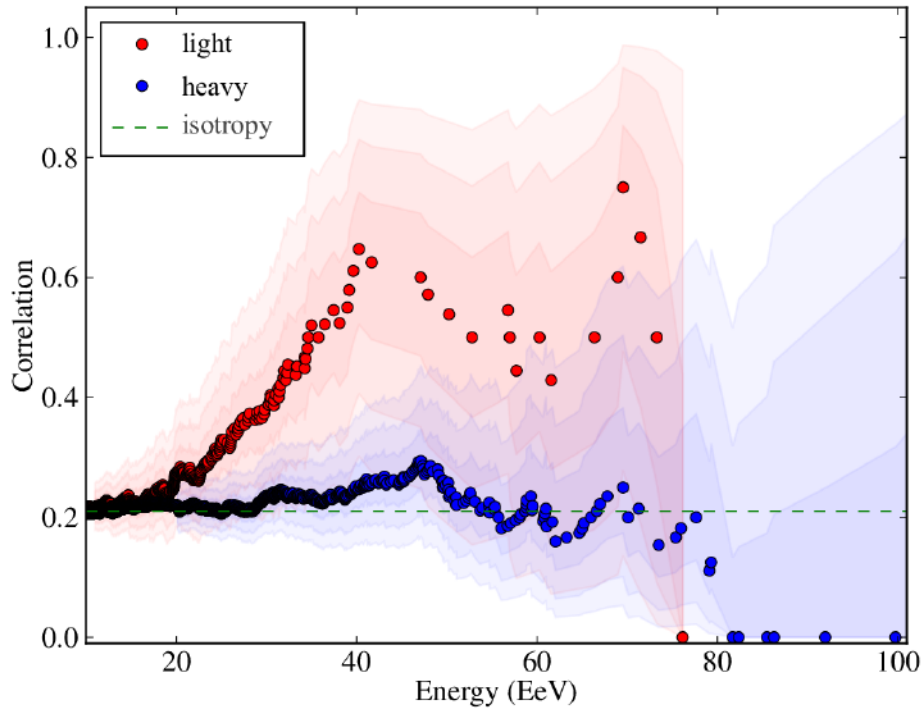
Figure 8.18: The fraction of events correlating to sources from the VCV catalog as a function of energy. In each energy bin E_i, the fraction refers to all events where $E > E_i$. The correlation of the heavy component is compatible with an isotropic distribution while the strength of correlation of the light component increases with energy. The red and blue shaded areas are the confidence intervals of the correlating fraction.

Lowering the energy threshold

The energy threshold $E > 55 \times 10^{18}$eV was chosen because it maximizes the correlation in the data set (in the first publication). It is natural to expect that the correlation does not suddenly start at that energy. Rather, one expects also correlations at lower energy, for example from very close sources. Hence, the correlating fraction is calculated as a function of energy. The maximum opening angle and the distance cuts are unchanged.

For the light and heavy sample, the fraction of correlating events is shown in Fig. 8.18. In each energy bin E_i, the fraction is showed for all events where $E > E_i$. The correlating fraction for the heavy sample is mainly compatible with the expectation for isotropy across the whole energy range. The correlating fraction for the light sample deviates from isotropy above $E = 20$ EeV and rises up to 60 % above $E = 40$ EeV. The energy where the correlating fraction starts to deviate from isotropy hints to the strength of the intergalactic magnetic fields. However, no precise conclusion about the field strength can be concluded from this plot. The same result is expected for a shower sample that starts to correlate abruptly above a certain energy threshold.

8.6 Search for ultra-high energy photons

The current status of photon searches is shown in Fig. 2.6. No photon candidates were found up to now. However, the GZK effect can not be excluded yet with the current upper limits. This is in part due to poor statistics and due to the insufficient separation power of the variables used up to now. Photon searches are possible based on shower universality. The true distribution of X_{max} and the number of muons on ground (individual particles) is shown for simulations in Fig. 2.3. The reconstructed distributions are shown in Fig. 8.20. It is clear that the combination of X_{max} and N_μ provides strong separation power for the selection of photon candidates (or to set a strong upper limit).

Generally, the cross section for photo-nuclear interaction of photon primaries is very small. Photon showers develop mainly in the electromagnetic cascade. The mean X_{max} is deeper than for proton showers due to the smaller cross sections. Hence, photon showers have very few muons. Above 10^{19}eV, interference effects of subsequent interactions become important. After each scattering process, the interaction probability of electromagnetic particles is suppressed due to the time it takes to build up the electromagnetic fields around the charge (*formation zone suppression*). If this time scale becomes comparable to the proper time between subsequent scattering targets, the interaction probability is reduced (LPM effect [108, 109]). This effect is especially important for photon showers because the formation time of electromagnetic fields is much larger than for the strong interaction (relevant for hadronic interactions). As a result, the mean X_{max} and the shower to shower fluctuations increase significantly. Above $10^{19.5}$eV, photons can interact with the geomagnetic field. Magnetic bremsstrahlung and pair production is possible. A shower of several hundred secondary photons is created. Due to superposition, shower to shower fluctuations are reduced. The mean X_{max} becomes smaller. This dominates the LPM effect, because the energy per secondary photon is smaller. Between $10^{19.5}$eV and $10^{20.0}$eV, the elongation rate becomes negative, depending on the arrival direction of the photon w.r.t. the orientation of the geomagnetic field. The influence of these effects on the mean X_{max} is shown in Fig. 8.19.

The reconstructed X_{max} has a bias well within $\pm 30\,\text{g/cm}^2$. The bias has the same energy dependence as for proton and iron showers (Fig. 6.8) and is corrected for empirically by a function that is based only on proton and iron showers. Due to strong correlations of X_{max} and the first interaction X_0, both parameters are coupled during the reconstruction. If the coupling function is derived from photon showers, the energy dependence of the reconstruction bias can be subtracted completely. However, the true primary particle is not known beforehand. Therefore, the reconstruction algorithm has to be the same for all types of simulations and for real data. If the coupling function is derived from proton and iron showers (the standard configuration), the reconstructed X_{max} is pulled closer to the expectation for proton. On average a bias of $-20\,\text{g/cm}^2$ remains. The resolution of X_{max} is $70\,\text{g/cm}^2$ to $100\,\text{g/cm}^2$ (Fig. 6.10). If showers above $55°$ are rejected, the resolution can be further improved to $70\,\text{g/cm}^2$ to $80\,\text{g/cm}^2$ above $10^{19.2}$eV (Fig. A.22).

The cross section for photo-nuclear interactions is very small. As a consequence, most of the energy of photon primaries is deposited in the electromagnetic cascade. The number of muons on ground is one order of magnitude smaller than for hadronic showers (Fig. 2.3).

The reconstructed N_μ is ≈ 0.25 with a small energy dependence (Fig. 6.12). The spread in the reconstructed N_μ is in the order of 0.15 (Fig. 6.13). Hence, N_μ alone provides strong discrimination power to distinguish photons from hadronic showers on average.

It is worthwhile to mention that the reconstruction of N_μ and X_{max} (and also the bias correction) works well also for photon showers although the signal and time models and the bias correction function are built using only proton and iron showers. This is another strong argument for the validity of the universality approach.

The energy is not reconstructed with the algorithm presented in this thesis. The main reason is that the water Cherenkov detectors are not able to separate the muonic and electromagnetic contributions to the signal completely. This leads to a strong correlation between N_μ and the total energy (Fig. 5.4). In simulated showers, the energy is fixed to the true value. In real data, the energy is fixed to the value obtained from the SD reconstruction. The SD energy calibration is valid if the data is mainly composed of hadronic events, i.e. if the average mass lies between proton and iron. If the energy of a photon shower is reconstructed with this calibration function, the energy is underestimated due to the significantly smaller signals and the steeper slope of the lateral distribution. This mismatch is compensated in the reconstruction by incrementing N_μ. The effect is opposite if hadronic showers are reconstructed with a photon LDF. As a result, the distributions of N_μ of photon and proton showers are pulled closer together and the separation power decreases. In [57], a parametrization of the shape of the LDF is given for photon showers.

Photons can already be discriminated from hadronic showers using only the reconstructed shape of the LDF, without referring to shower universality. Simulated and real showers are reconstructed both with the shape parametrization for hadronic and for photon showers. The likelihood to obtain the signals $\vec{S}$ given a specific shape model is

$$L(\vec{S}|\text{shape model}) \,.$$

The discriminating variable is the *likelihood ratio*

$$t(\vec{S}) = \frac{L(\vec{S}|\text{hadron LDF})}{L(\vec{S}|\text{photon LDF})} \,.$$

If $t < 1$ ($t > 1$) the shower is photon-like (hadron-like). The discrimination is trained with simulations of photon showers and part of the SD data sample, assuming a small contribution from photons. The distribution of the t is shown in Fig. 8.21. The likelihood ratio is a very robust estimator, but the discrimination power can be increased by combining t with N_μ and X_{max}. The distribution of the Fisher discriminant that combines all three variables is shown in Fig. 8.22.

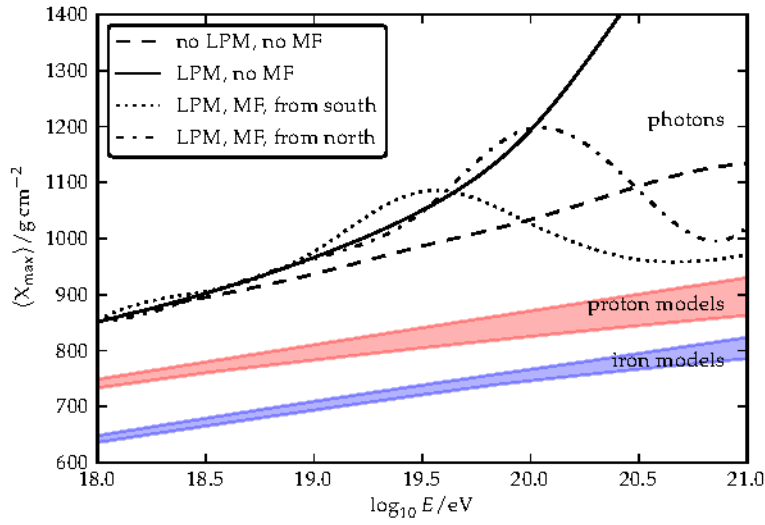Both variables are used to derive a limit on the flux of ultra-high energy photons. The results are shown in [110].

Figure 8.19: Model predictions of the mean X_{max} for photon showers [111]. Above 10^{19} eV the cross sections are suppressed by the LPM effect. The turnover is due to pair production in the geomagnetic field (MF), depending on the incoming direction of the primary photon. The predictions for hadronic showers are summarized in the red and blue band (see Fig. 8.1 for details).
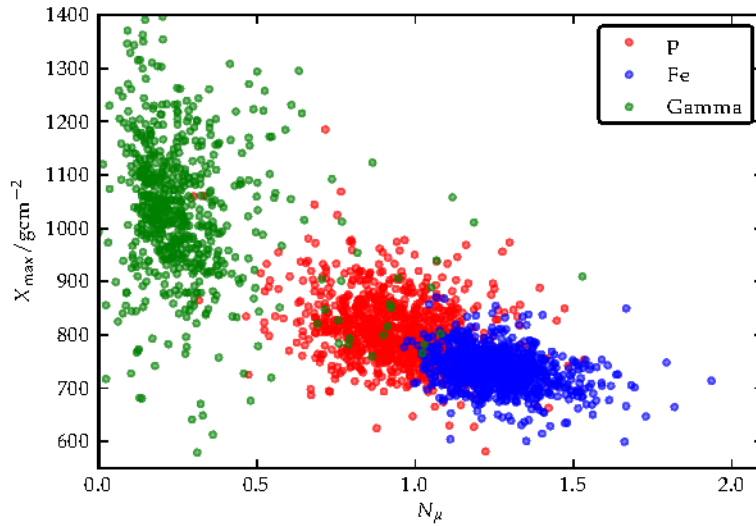

Figure 8.20: The reconstructed N_μ and X_{max} for proton, iron and photon simulations in the range 10^{19} eV to 10^{20} eV
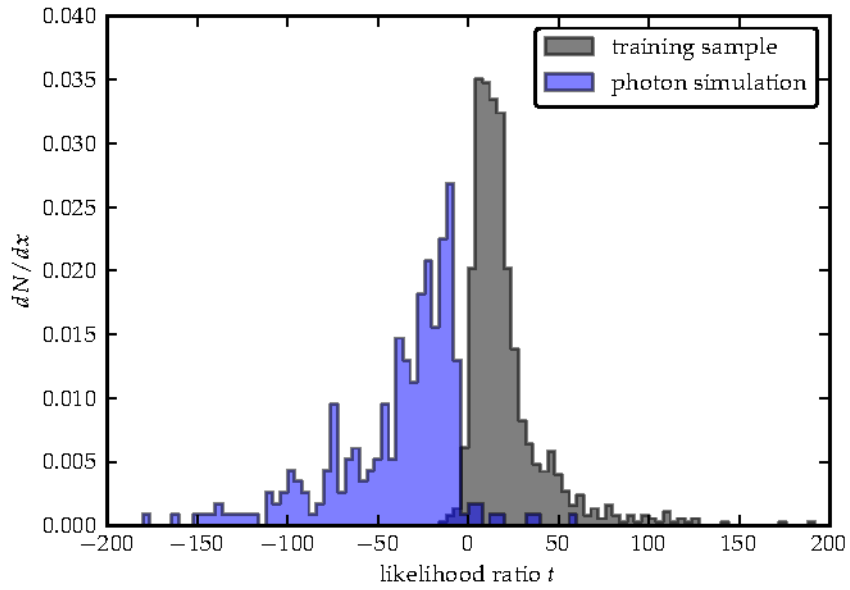
Figure 8.21: Distribution of the likelihood ratio *t* for simulated photon showers and part of the SD data used as training sample. Adapted from [110].
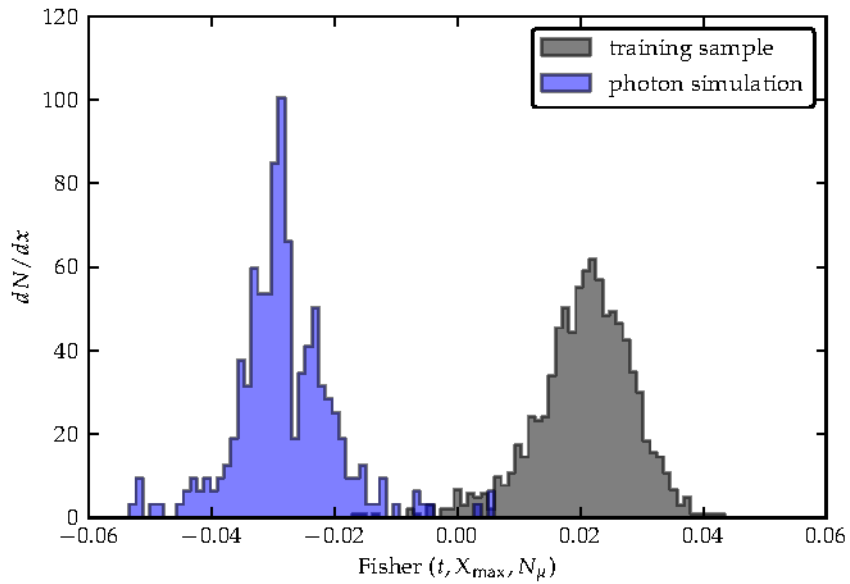
Figure 8.22: The same as Fig. 8.21 using a linear Fisher discriminant based on the likelihood ratio, N_μ and X_{max}. Adapted from [110].

9

Summary and conclusions

Throughout the last 100 years, a plethora of experiments were conducted to understand the properties of ultra-high energy cosmic rays (UHECR). The energy spectrum was measured precisely up to 10^{20}eV. While UHECR are reasonably well understood up to 10^{16}eV, the mechanisms of acceleration and propagation at the highest energies remain essentially unknown.

The energy spectrum alone is not sufficient to discriminate among different source and propagation scenarios. Therefore, it is crucial to measure the primary mass of UHECR on a single event basis. The aim of this thesis was to benefit from the large data sample collected by the surface detector and to develop a method for an event-based measurement of the primary mass. It was shown that shower universality can be used to describe the measurements taken by the Pierre Auger Observatory in the energy range above 10^{19}eV. It was applied successfully to the reconstruction of data taken by the surface detector.

The main achievements are:

- Correlations with astrophysical sources. The arrival directions of the highest energy events were compared with the positions of active galactic nuclei from the VCV catalog. Due to the mass dependence of acceleration and propagation processes and the deflection in extragalactic magnetic fields, light particles are expected to correlate more than heavy particles. Indications for a strong correlation of light particles and possibly an energy-dependent onset of the correlation were found.

- Measurement of the shower maximum and muon content with the SD. Using N_μ and X_{max}, the energy dependence of the primary mass was estimated. The average and fluctuations of X_{max}, as well as the average and fluctuations of N_μ consistently show a trend to heavy mass composition in the energy range 10^{19}eV to 10^{20}eV. The FD measurement was confirmed and extended to higher energies.

- A search for photon primaries was started. Ultra-high energy photons are expected as by-products of the GZK effect on protons or from photo-dissociation of heavy nuclei with the cosmic microwave background (CMB). It was shown that, using N_μ, X_{max} and the shape of the lateral distribution, photon showers can be discriminated from proton showers.

The results are based on several new developments that are summarized as follows.

- Development of a model that describes the signal response of the surface detector. The model is based on the concept of air shower universality. It uses the total energy E, the depth of maximum of the air shower cascade (X_{max}), the depth of first interaction (X_0) and the overall muon content (N_μ) to predict the average time-dependent signal in the water Cherenkov detectors.

  It is worthwhile to mention that shower universality is a remarkable property, given the vast number of secondary particles and interactions. Simulated showers derived from different interaction models in a wide range of primary masses, photon-induced showers and real events can be described in the same framework with just a few parameters.

- Development of a new reconstruction algorithm that uses the time traces of the water Cherenkov detectors to reconstruct X_{max} and N_μ. The implementation was designed with the rapid development cycle in mind that is common in many physics analyses. It can be easily extended to include data from other types of detectors.

- Validation of the predictions. The model is based on simulations conducted with the $\overline{\text{Off}}\underline{\text{line}}$ framework. The consistency of the model and the reconstruction algorithm was checked with simulations. Note that, while the model is based only on simulations of proton and iron showers, it works well also for intermediate masses and photon-induced showers. In a reduced data sample with information from both the SD and the FD (*golden hybrid events*), the model was validated with real data.

- Independent validation. Triggered by this work, the universality approach was tested with a different implementation of the reconstruction (CDAS), with similar results.

The main next steps that are possible with the current detector design are:

- Extension of the universal models to lower energies, ideally to 10^{17} eV and reconstruction using data taken by the infill array.

- Improvement of the models by including the depth of maximum of the muonic cascade (X_{max}^μ) in the parametrizations.

- Further reduction of the dependence on a specific detector design by factorizing the description of the shower and the time dependence of the detector response.

- Extension of the reconstruction algorithm to include time information of detectors far from the shower core.

The expected benefits from improvements of the detectors are as follows. Faster sampling of the PMT response will improve the estimate of the start time and therefore the measurement of the shower front curvature as pointed out in Section 5.7. Hence, faster sampling will increase the sensitivity to the depth of first interaction X_0, which is important for the distinction of different hadronic interaction models. A direct measurement of the muon density on ground will allow to validate the universality models in a way that is completely independent of the reconstruction. Furthermore it will break the correlation of the energy and the muon scale and allow to reconstruct both at the same time (see also Section 4.11).

Acknowledgments

The number of people who contributed to the success of my thesis is (almost) countless. First of all, I would like to thank Johannes Blümer for agreeing to accept me as a Ph. D. student at the Institut für Kernphysik in Karlsruhe. I am grateful to Michael Feindt for accepting my thesis as a co-referee.

Many thanks go to Markus Roth for supervising my work. His door was always open for me. He took a great interest in the topic I worked on for the past three years. His competent (and demanding) nature helped a lot to advance my work and to achieve the results at hand.

I want to thank Javier Gonzalez with whom I had the honor to share an office for two years. His commitment and interest in my work and his outstanding knowledge on programming was most helpful.

With his universal signal model, Maximo Ave laid the foundation for the results in this thesis. I am most grateful to him for the insights I gained in countless phone conferences and collaboration meetings.

I want to thank Balazs Kegl, Lorenzo Cazon, Diego Garcia-Gamez, Ralph Engel and Michael Unger for some interesting discussions. I would like to thank all my colleagues in Karlsruhe. Special thanks go to my office colleagues Hans Dembinski and Alexander Schulz for creating a very enjoyable working atmosphere. Benjamin Fuchs, Nunzia Palmieri and Alessio Porcelli, thank you for taking the time to read this thesis carefully. Many thanks go to Sabine Bucher for all her organizational support at the institute.

Although they did not directly contribute to the physics results, I am deeply indebted to countless people in the open source community. They created a software ecosystem that is perfectly suited for the type of analysis presented in this thesis. In particular, I want to mention Matplotlib [112], SciPy [113] and Scikit-learn [114].

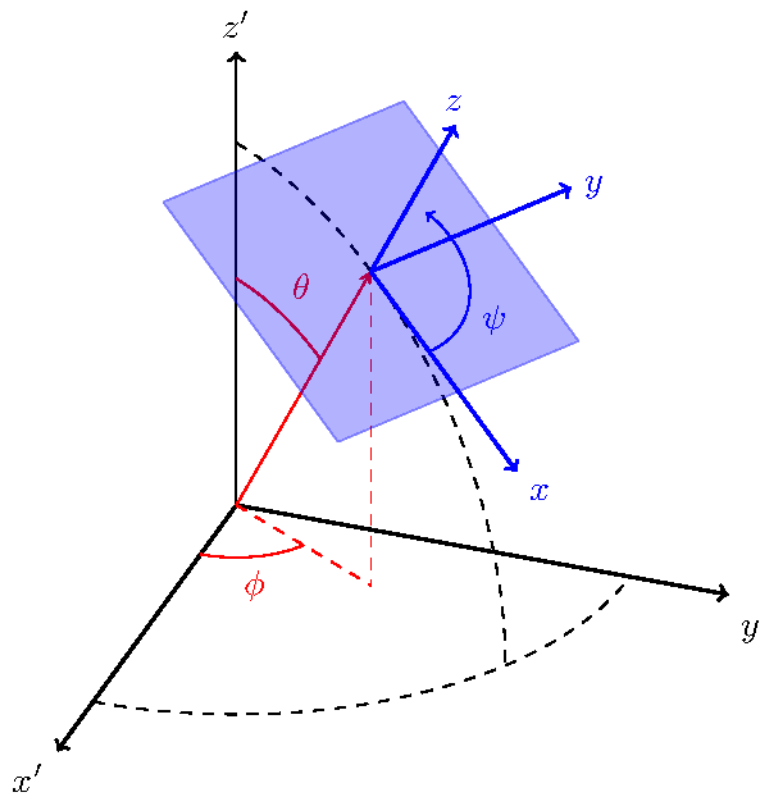Finally, my most sincere thanks go to my family who supported me at all times.

Appendix

Figure A.1: The convention for the Cartesian ground-based coordinate system x', y', z', where x' points to the geographic east and y' to the north (black lines), and the shower plane coordinate system (blue lines). From [72].

A.1 Dependence of the time model on interaction model, primary mass and energy
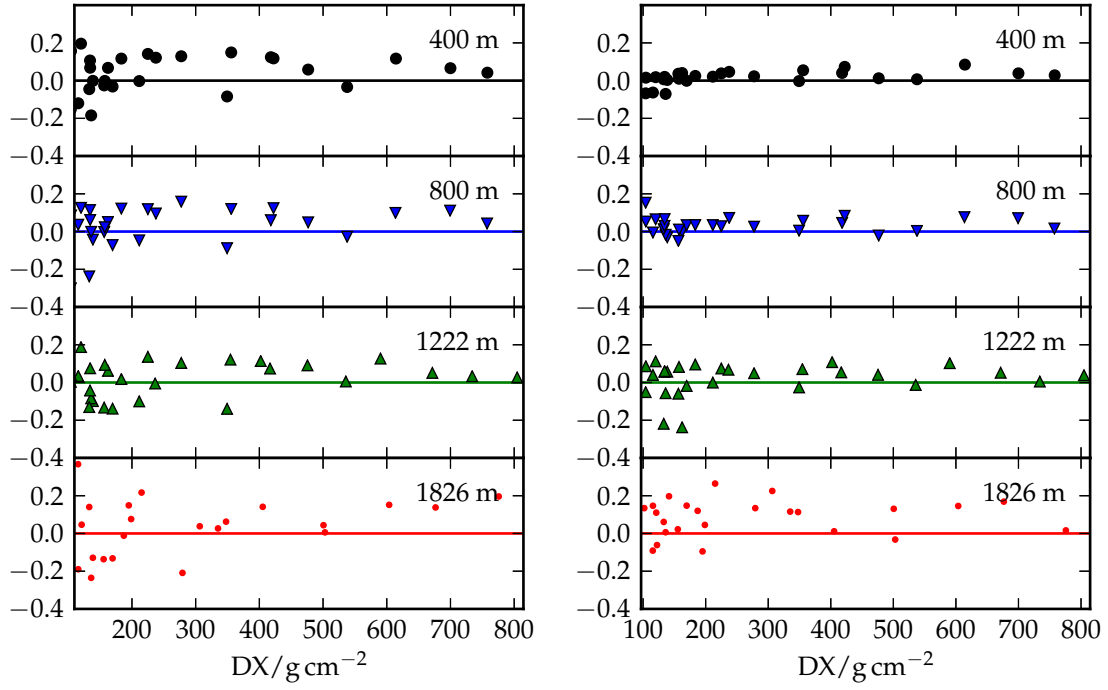
(a) Purely muonic component. Average component trace based on QGSJet II-03 photon.

(b) Purely electromagnetic component. Average component trace based on QGSJet II-03 photon.

Figure A.2: Violation of universality of the time shape of the purely muonic component. Each points corresponds to one average component trace. The difference of the *m* parameter of the lognormal to the prediction of the reference model (proton and iron, QGSJet II-03 and EPOS 1.99 mixed) is shown.

(a) Time model derived from QGSJet II-03 proton

(b) Time model derived from QGSJet II-03 iron

(c) Time model derived from EPOS 1.99 proton

(d) Time model derived from EPOS 1.99 iron
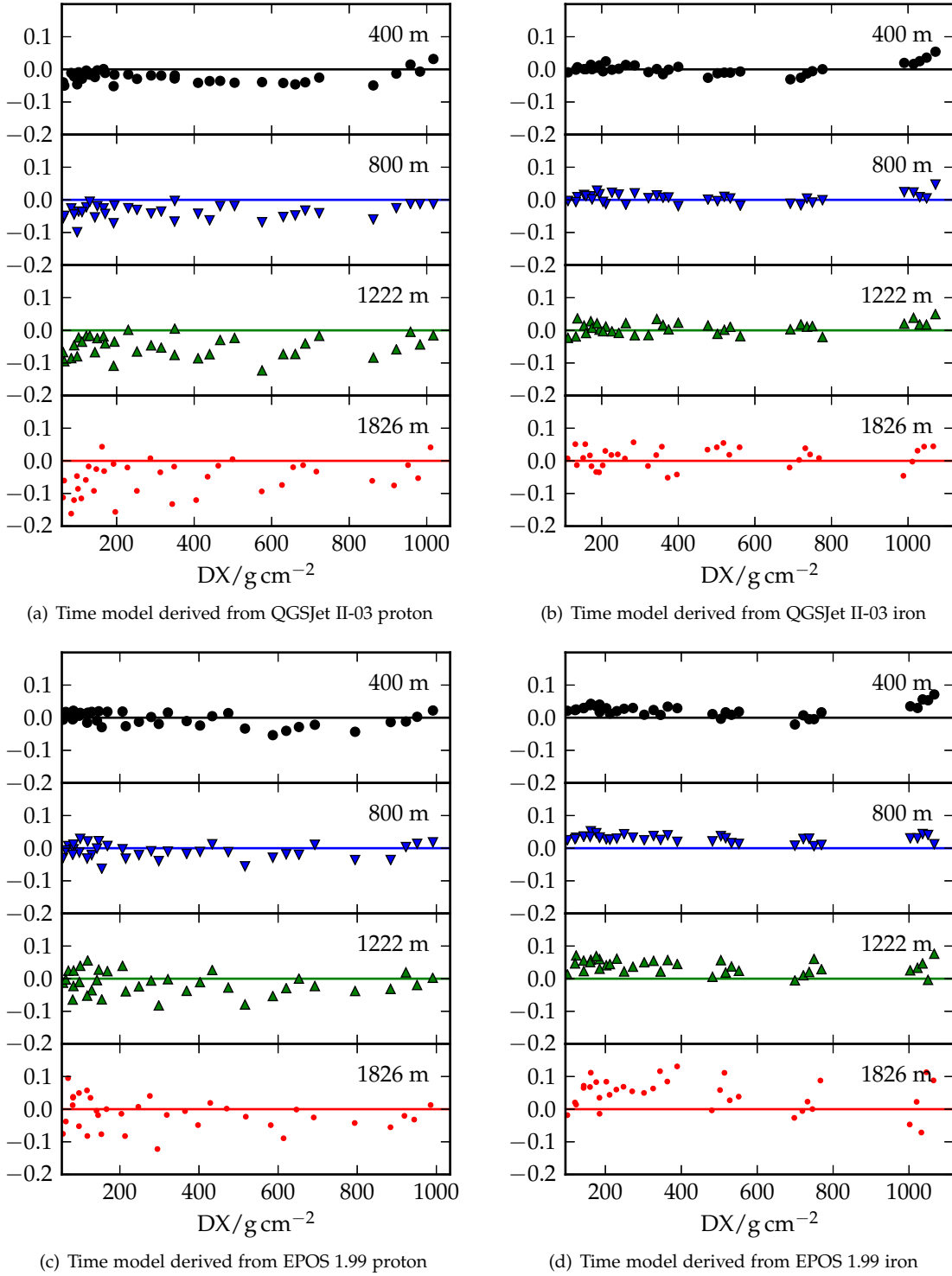
Figure A.3: Non-universality of the time shape of the purely muonic component. The difference to the reference model (proton and iron, QGSJet II-03 and EPOS 1.99 mixed) of the *m* parameter is shown for different combinations of model and primary particle.

(a) Time model derived from QGSJet II-03 proton

(b) Time model derived from QGSJet II-03 iron

(c) Time model derived from EPOS 1.99 proton

(d) Time model derived from EPOS 1.99 iron
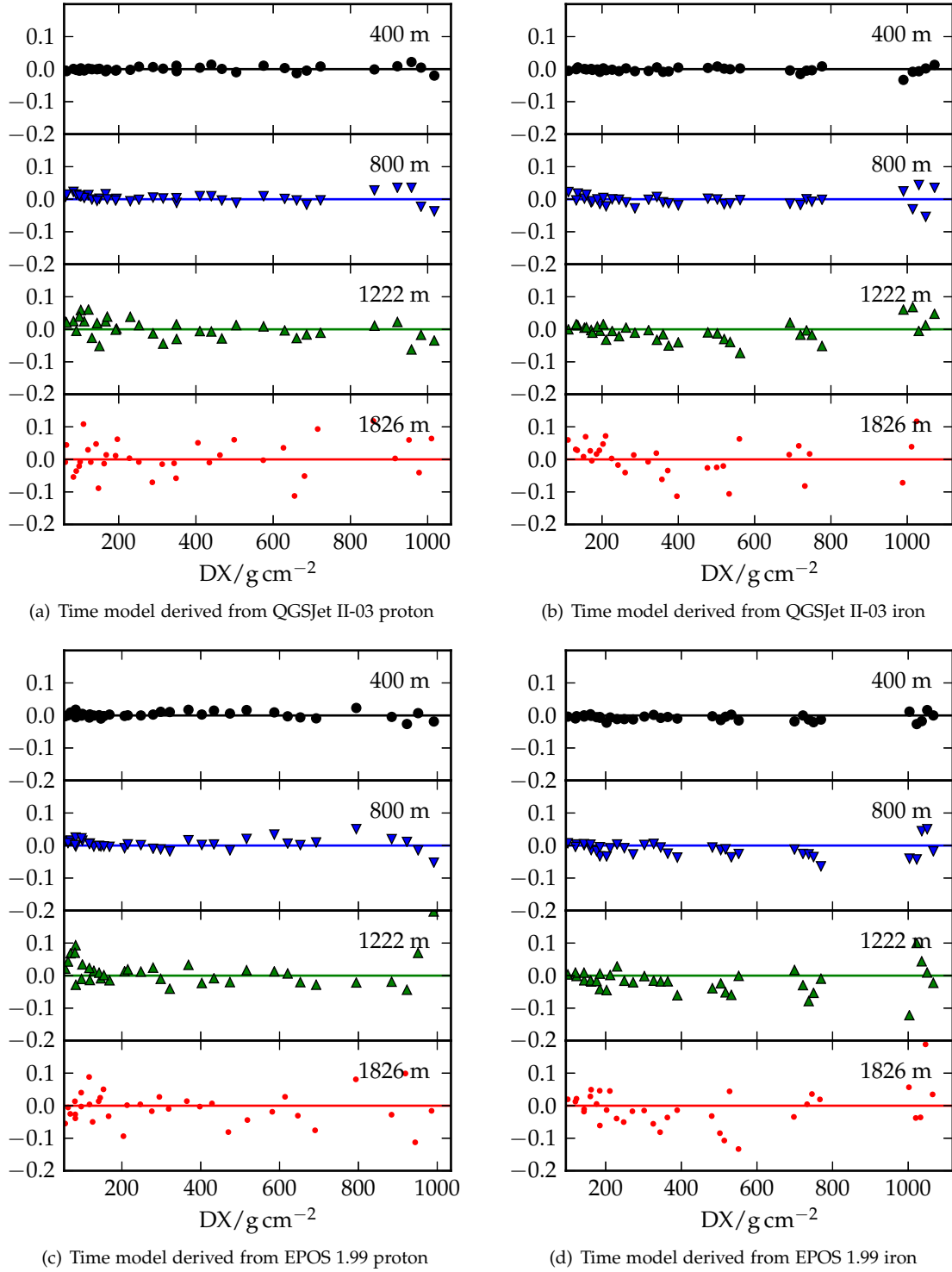
Figure A.4: Non-universality of the time shape of the purely electromagnetic component. The difference to the reference model (proton and iron, QGSJet II-03 and EPOS 1.99 mixed) of the *m* parameter is shown for different combinations of model and primary particle.

A.2 Prediction of the absolute time quantiles of the component traces
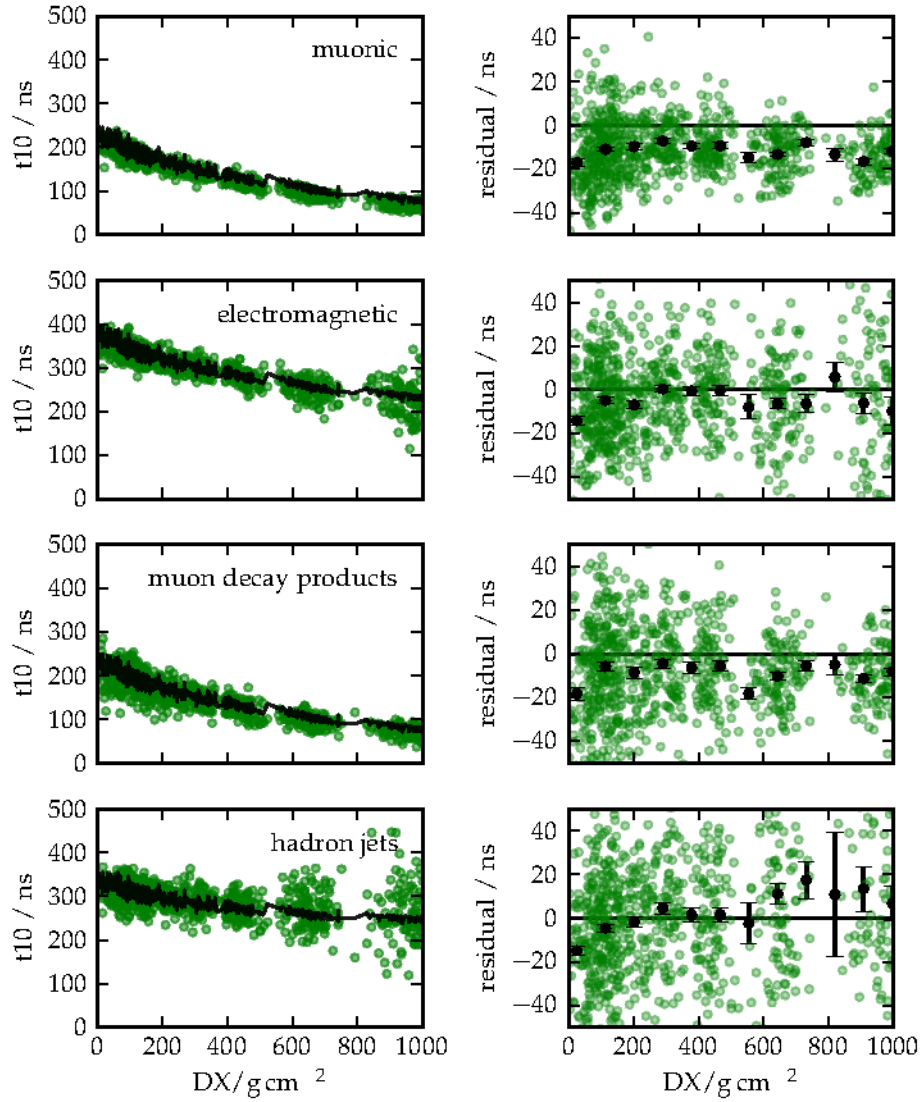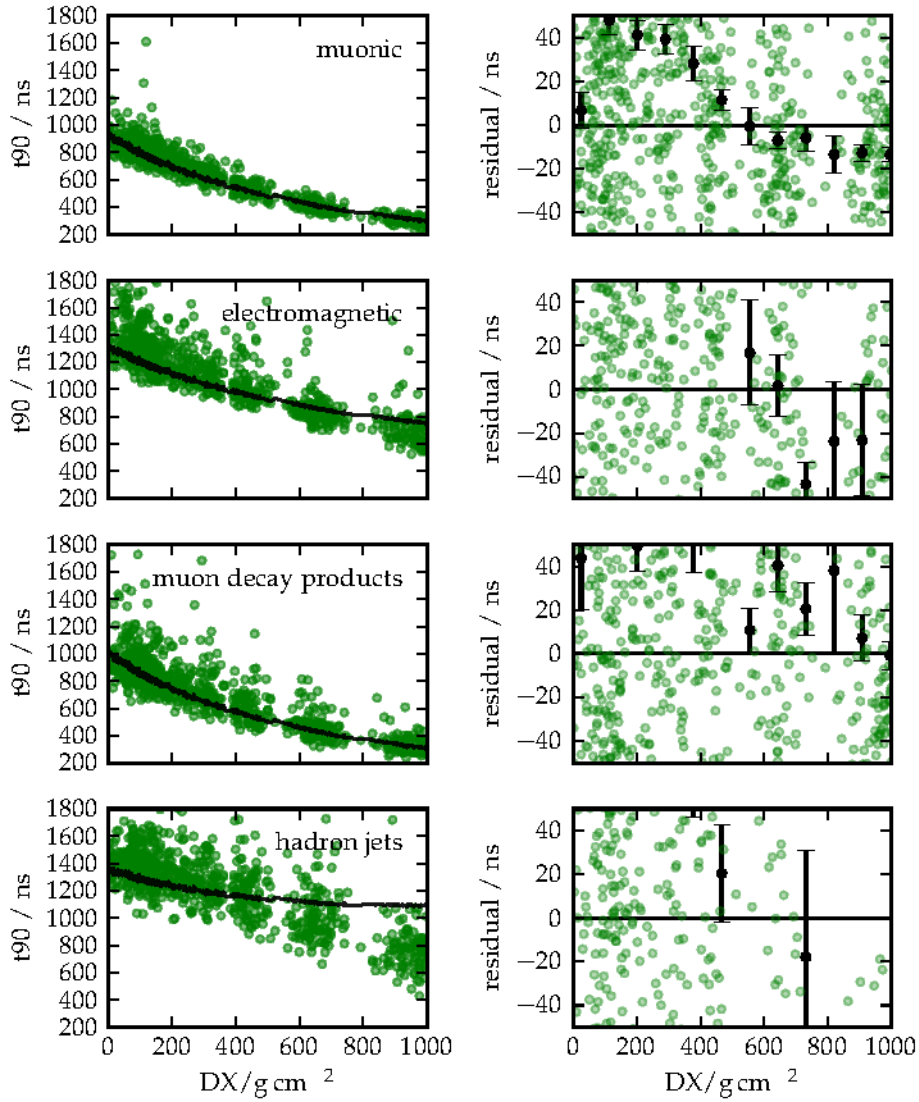

Figure A.5: The t_{10} quantile obtained from the simulated traces (green points) and the model prediction (solid black line). Dense stations at $r = 800\,\mathrm{m}$ and $\Psi = 90°$ are used. The residuals (simulation-prediction) are shown on the right. The jumps in the model prediction are due to different X_0 at the same DX, which leads to different predictions for the start time.
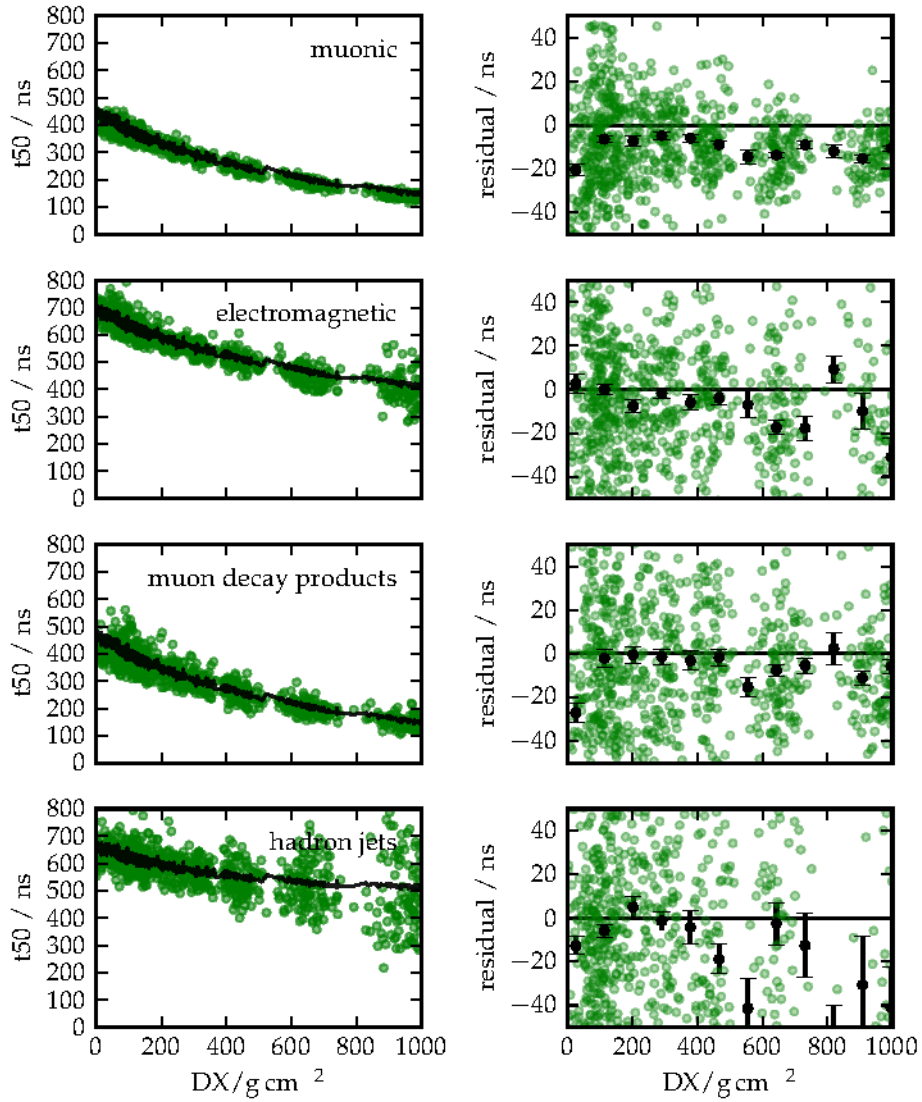
Figure A.6: The t_{50} quantile obtained from the simulated traces (green points) and the model prediction (solid black line). Dense stations at $r = 800\,\mathrm{m}$ and $\Psi = 90°$ are used. The residuals (simulation-prediction) are shown on the right. The jumps in the model prediction are due to different X_0 at the same DX, which leads to different predictions for the start time.

Figure A.7: The t_{90} quantile obtained from the simulated traces (green points) and the model prediction (solid black line). Dense stations at $r = 800\,\text{m}$ and $\Psi = 90°$ are used. The residuals (simulation-prediction) are shown on the right. The jumps in the model prediction are due to different X_0 at the same DX, which leads to different predictions for the start time.
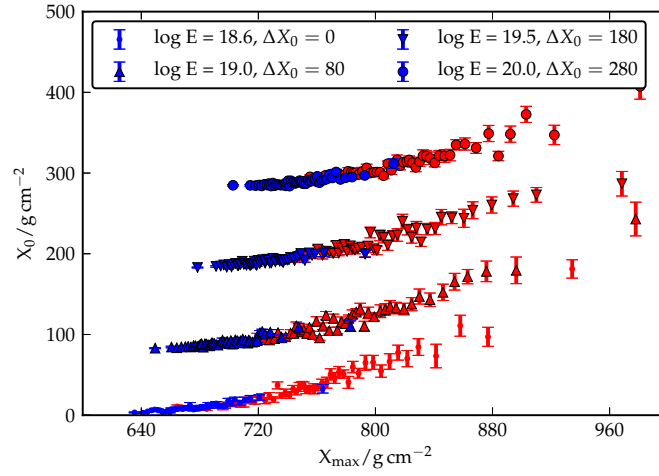
A.3 X_0- X_{max}- model

Figure A.8: Correlation of X_{max} and X_0 for QGSJet II-03. The same correlation function can be used to describe proton (red) and iron (blue).
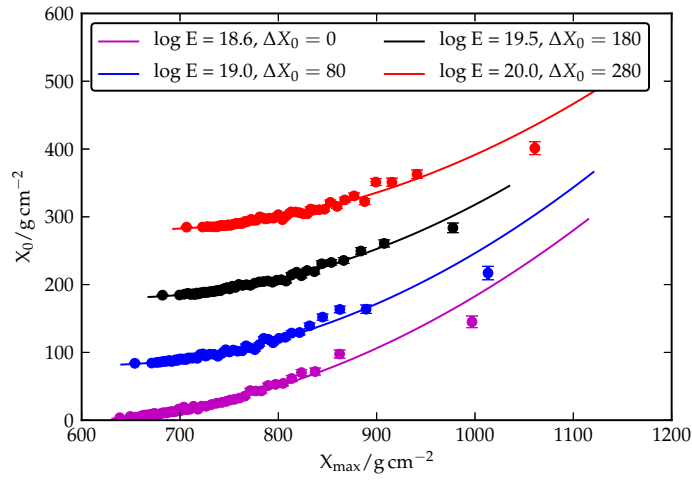
Figure A.9: Correlation of X_{max} and X_0. Since the primary mass and hadronic interactions are not known in the reconstruction, this intermediate correlation function is used. The same number of proton and iron showers simulated with QGSJet II-03 and EPOS 1.99 is mixed.
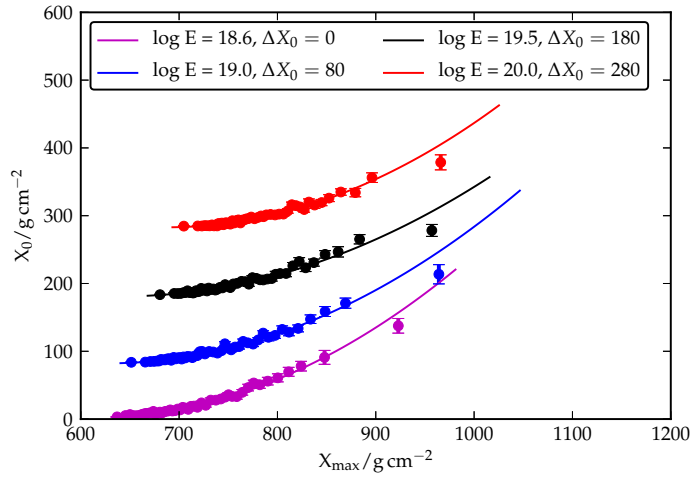
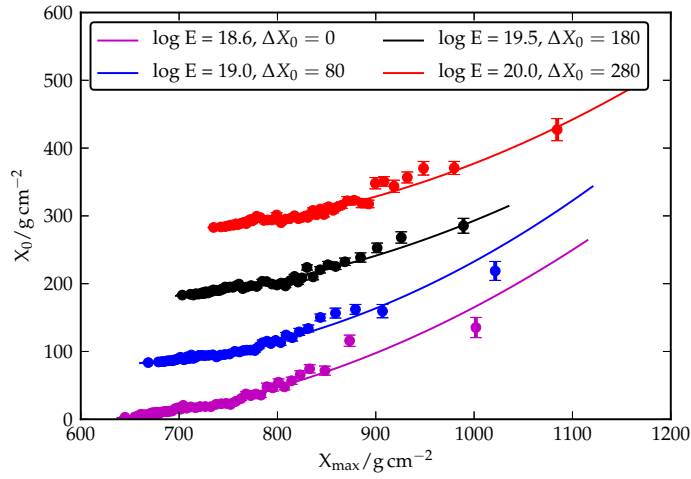**Figure A.10:** Correlation of X$_{max}$ and X$_0$. Showers are simulated with QGSJet II-03.

Figure A.11: Correlation of X$_{max}$ and X$_0$. Showers are simulated with EPOS 1.99.

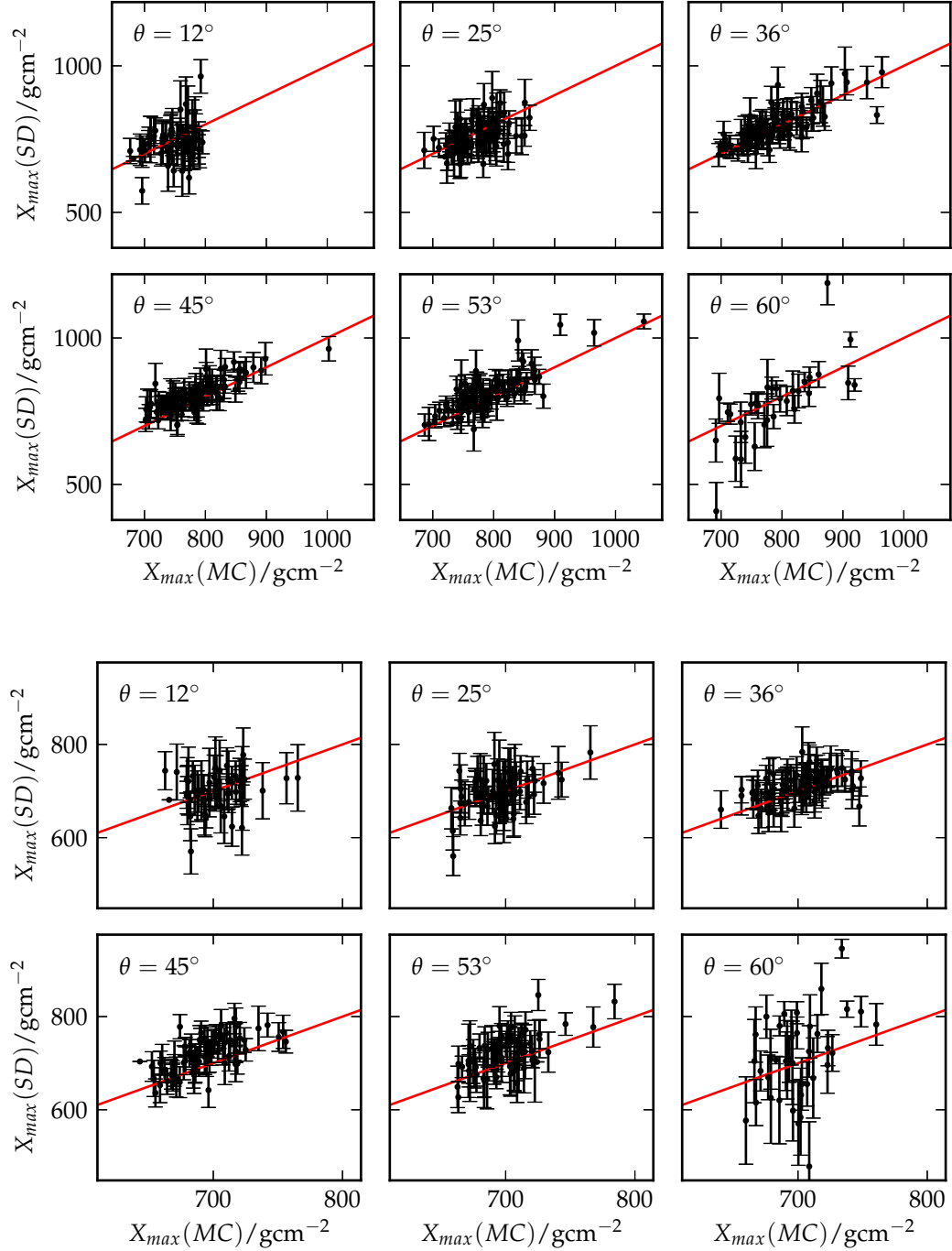## A.4 Details on the reconstruction accuracy

Figure A.12: Correlation of the true and the reconstructed X_{max} at $E = 10^{19.0}$eV. Perfect correlation is indicated by the red line. **Top:** proton. **Bottom:** iron. Interaction model: QGSJet II-03.
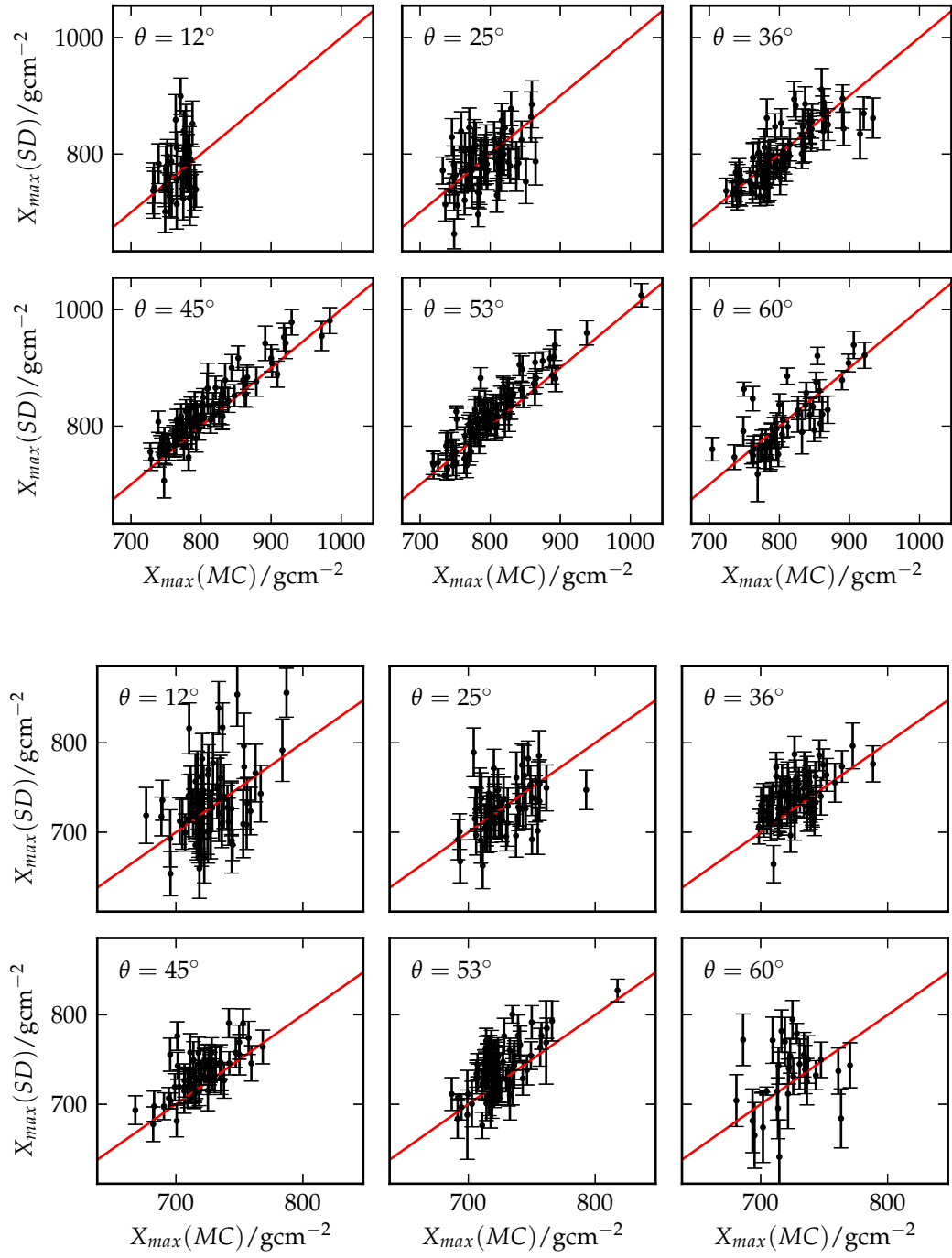
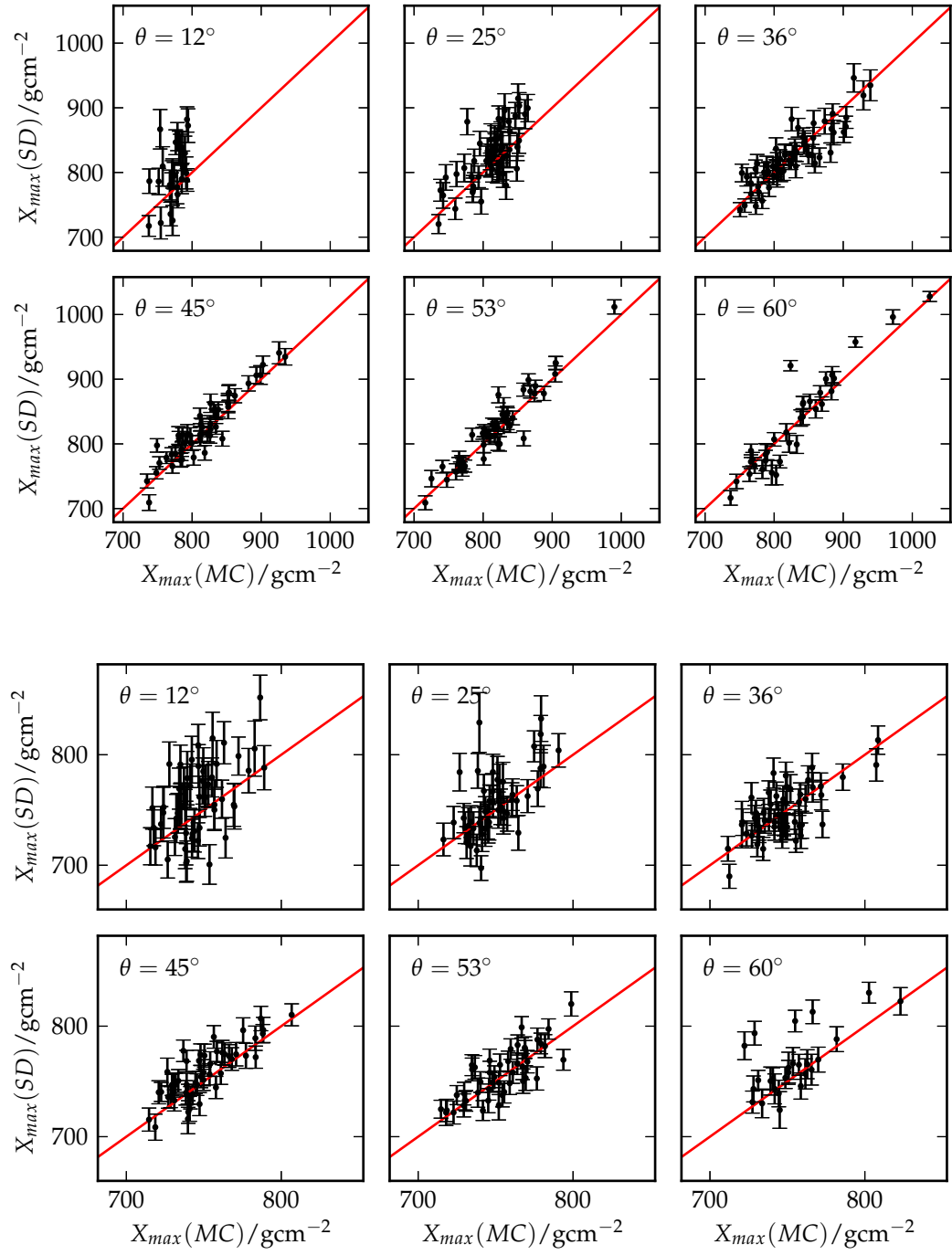**Figure A.13:** The same as Fig. A.12 for $E = 10^{19.5}$eV.

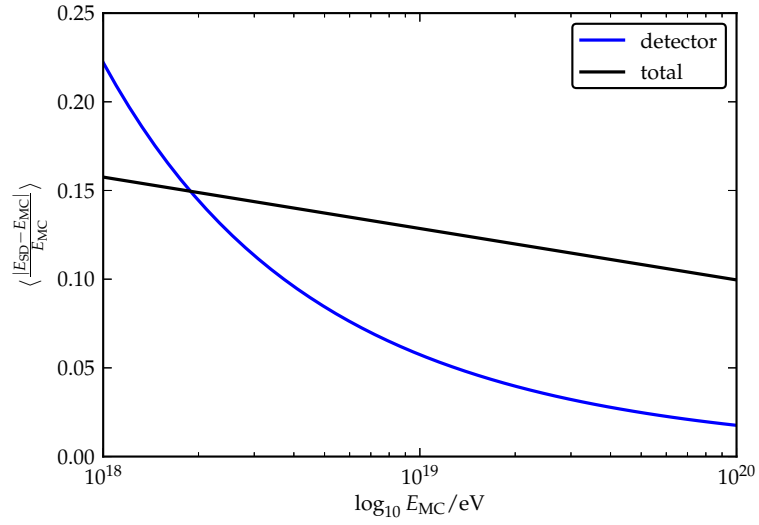**Figure A.14:** The same as Fig. A.12 for $E = 10^{20.0}$eV.

Figure A.15: The energy resolution of the SD. The blue line indicates the pure accuracy from the reconstruction. The black line estimates the resolution when shower-to-shower fluctuations are included. From [115].
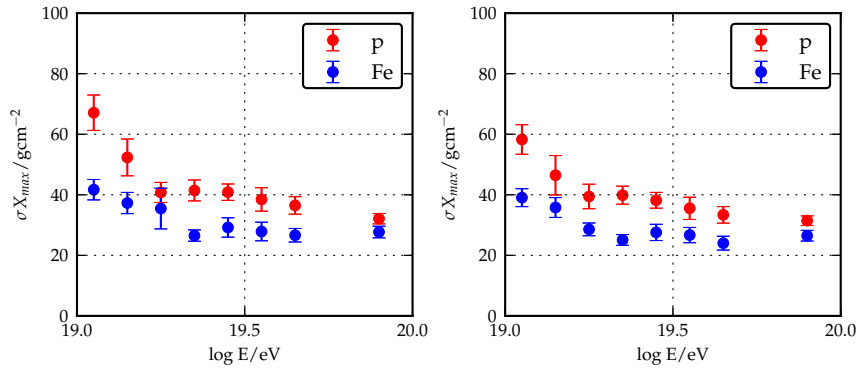

Figure A.16: Resolution in X_{max} depending on the type if `T5`. **Left:** one station left out (`5T5`). **Right:** all six stations in the first crown have a signal (`6T5`). There is a very small improvement of the resolution for the second case.

143

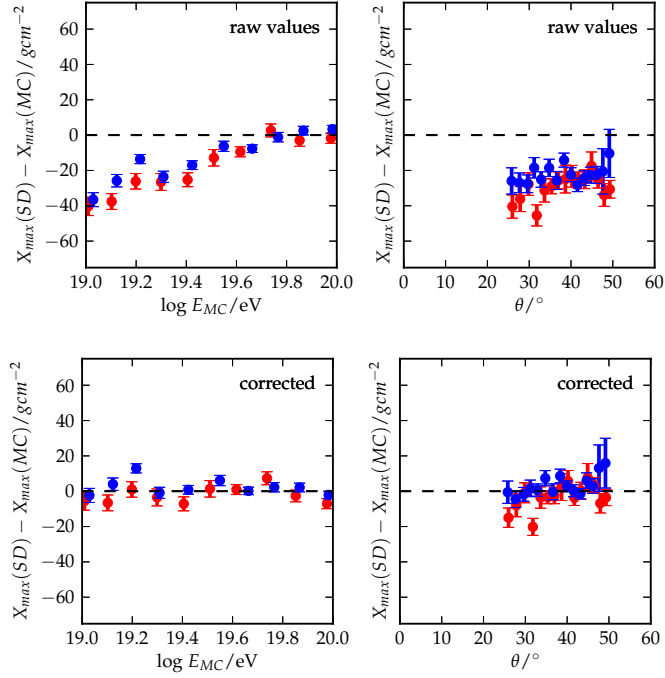## A.5 Reconstruction bias with restricted zenith angle range

Figure A.17: Bias of the reconstructed X_{max} (X_0 coupled to X_{max}). Before (top) and after bias correction (bottom). Showers in the range $25° < \theta < 50°$ are selected. The systematic uncertainty from the bias correction is reduced. **Red:** proton, **Blue:** iron.

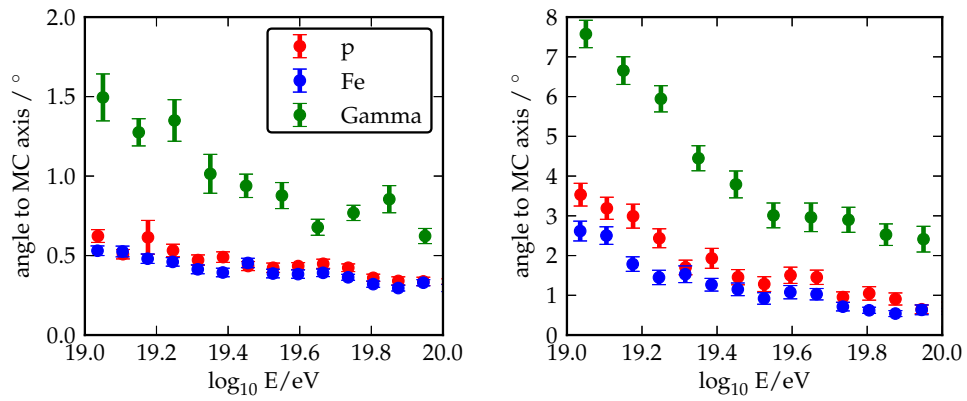## A.6 Reconstruction without start time fit

Figure A.18: Effect of the start time contribution on the reconstruction of the arrival direction. The spread in the arrival direction increases by a factor six when the start time is not considered in the fit.
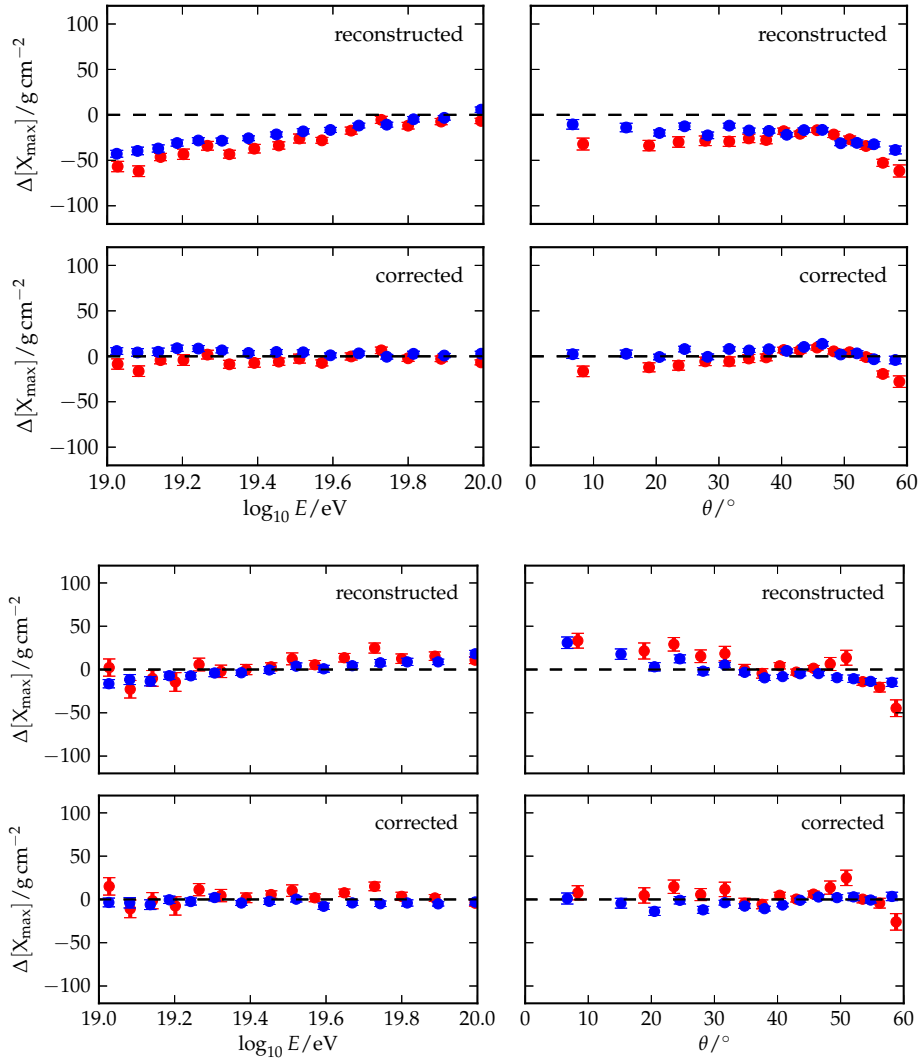
Figure A.19: Effect of the start time contribution on the reconstruction of X_{max}. The upper four plots show the bias of X_{max} when the start time is used. When only the shape fit contributes to the fit, the mass dependence in the X_{max} bias vanishes (lower four plots). This is expected because the dependence on the X_{max}-X_0-coupling is switched off. Furthermore, the difference of the bias from lowest to highest energies decreases from 50 to 30 g/cm^2 and the overall shape of the bias is shifted upwards. **Red:** proton, **Blue:** iron.

A.7 Resolution of X_{max}
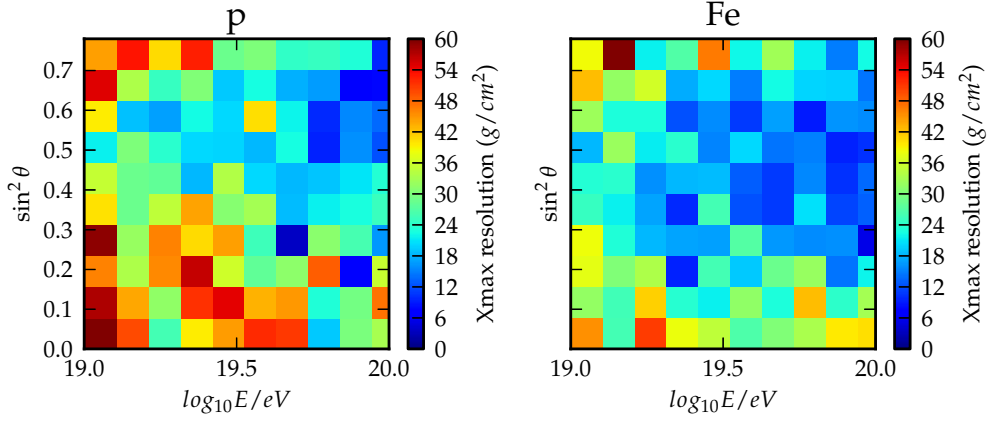
Figure A.20: Resolution of X_{max} for proton and iron simulations as a function of $\log E$ and θ
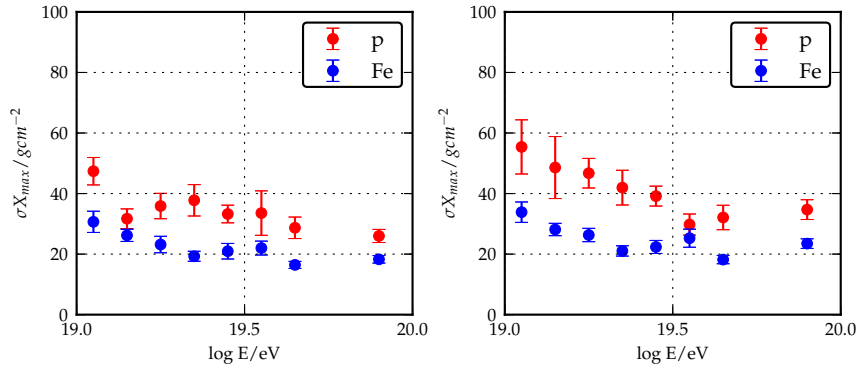
Figure A.21: Resolution of X_{max} as a function of energy in the range $25° < \theta < 50°$. **Left:** X_0 coupled to X_{max}. **Right:** X_0 fitted independently.
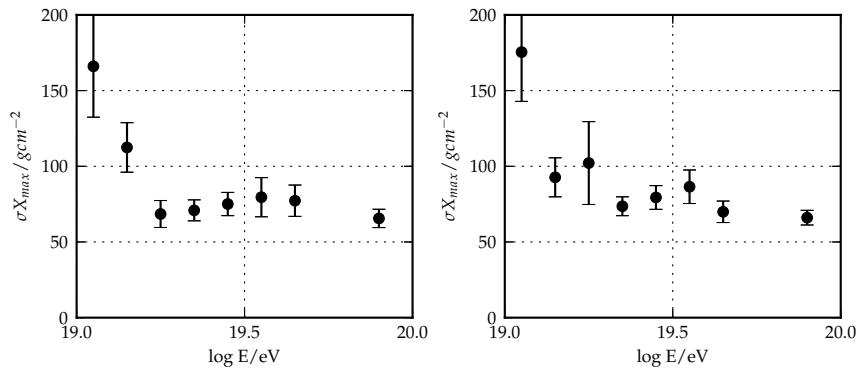
Figure A.22: Resolution of X_{max} as a function of energy for photon primaries in the range $25° < \theta < 50°$. **Left:** X_0 coupled to X_{max}. **Right:** X_0 fitted independently.

147

A.8 Reconstruction based on dense detector spacing
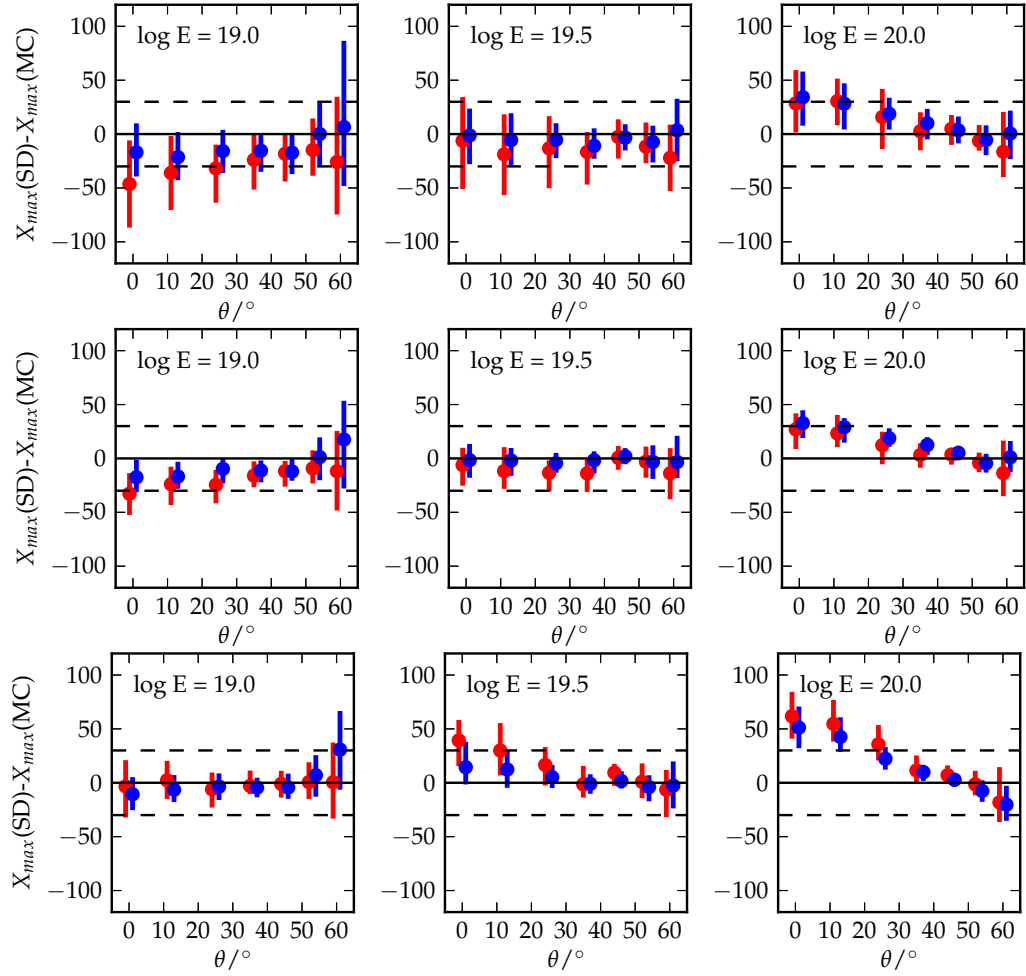
Figure A.23: Reconstruction based only stations in the dense array. **Top:** one third of all stations selected for the fit at random (X_0 coupled). **Center:** fit based on all dense stations (X_0 coupled). **Bottom:** fit based on all dense stations (X_0 free). The markers for proton and iron shifted for better readability.
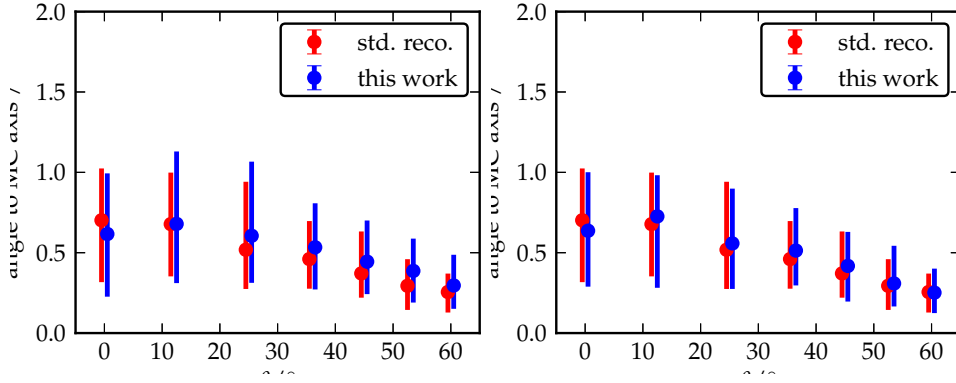
Figure A.24: Angular resolution for proton showers at $10^{19.5}$eV. The standard reconstruction uses the regular stations. The universality reconstruction (blue markers) is based on the dense stations. **Left:** one third of all stations selected for the fit at random. **Right:** fit based on all dense stations. The markers for proton and iron shifted for better readability.
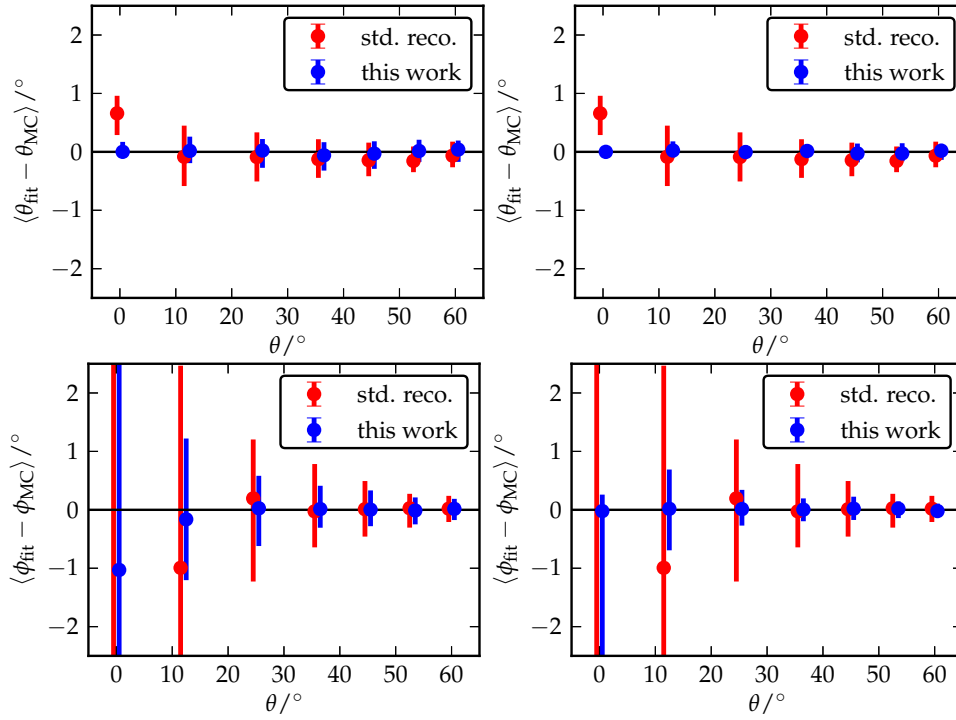
Figure A.25: Angular bias for proton showers at $10^{19.5}$eV. The standard reconstruction uses the regular stations. The universality reconstruction (blue markers) is based on the dense stations. **Top:** one third of all stations selected for the fit at random. **Bottom:** fit based on all dense stations. The markers for proton and iron shifted for better readability.
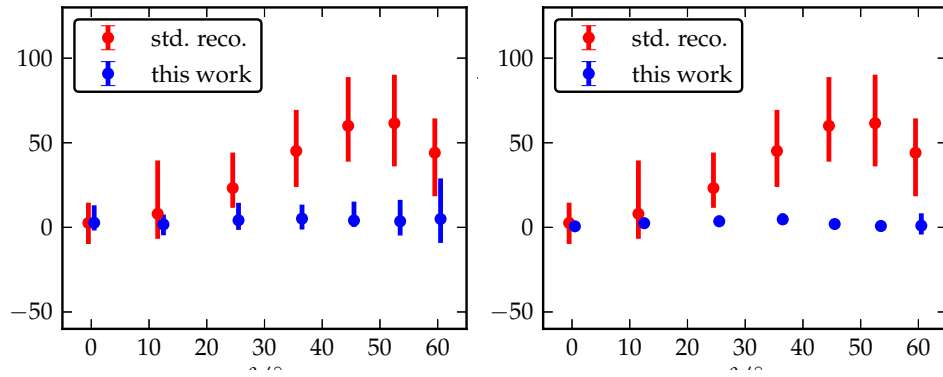
Figure A.26: Bias of the core position for proton showers at $10^{19.5}$eV. The standard reconstruction uses the regular stations. The universality reconstruction (blue markers) is based on the dense stations. **Left:** one third of all dense stations selected for the fit at random. **Right:** fit based on all dense stations. The resolution clearly improves. The bias is very close to zero, which proves that the geometry is described very well by the model. The markers for proton and iron shifted for better readability.

A.9 Accuracy of the reconstruction at fixed energies and zenith angles
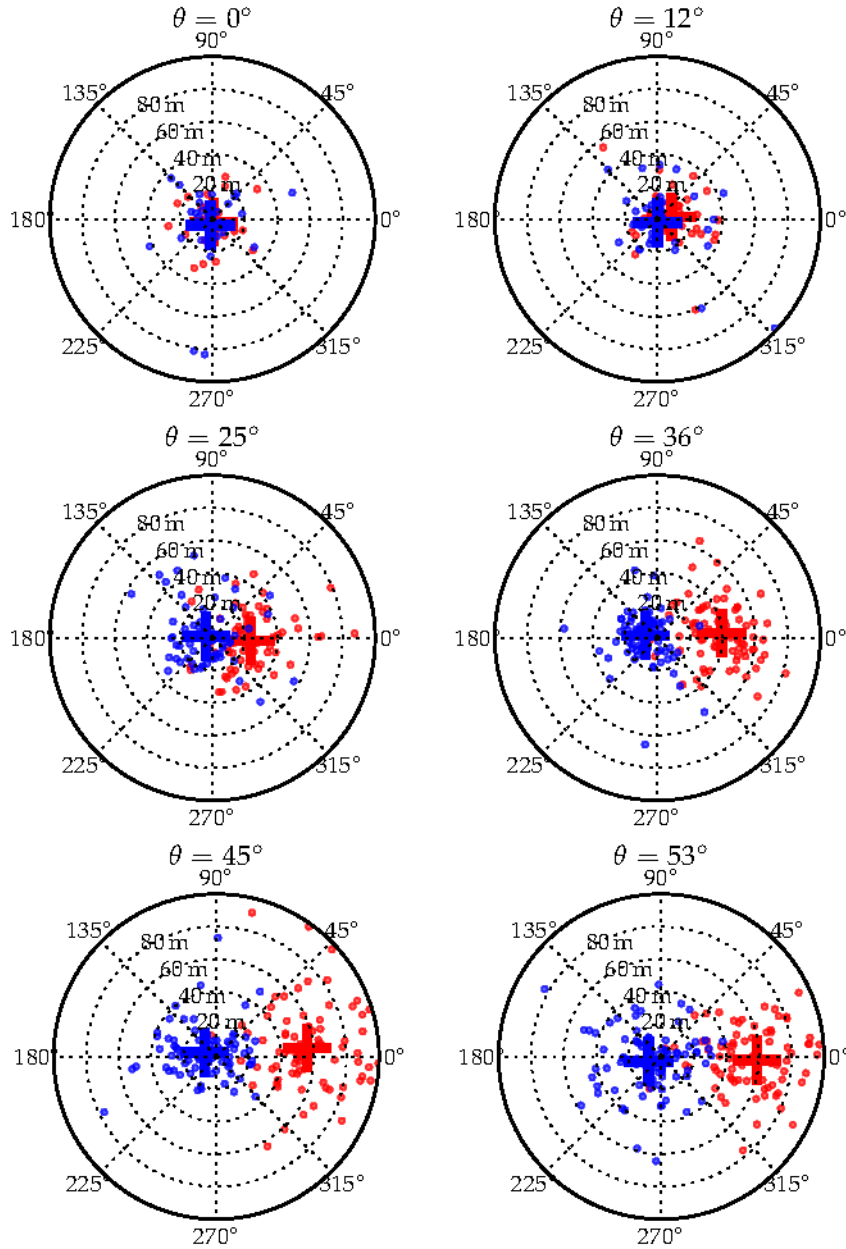
Figure A.27: The core position reconstructed with the standard algorithm (red points) and based on universality (blue points). When the NKG function is used (standard case) the core position is shifted systematically to the early region of the shower (to the right in this projection) because the asymmetry in the ground signal is ignored (*core bias*). The core bias is correlated to the zenith angle because of the increasing atmospheric attenuation. For details, see Fig. 6.3.
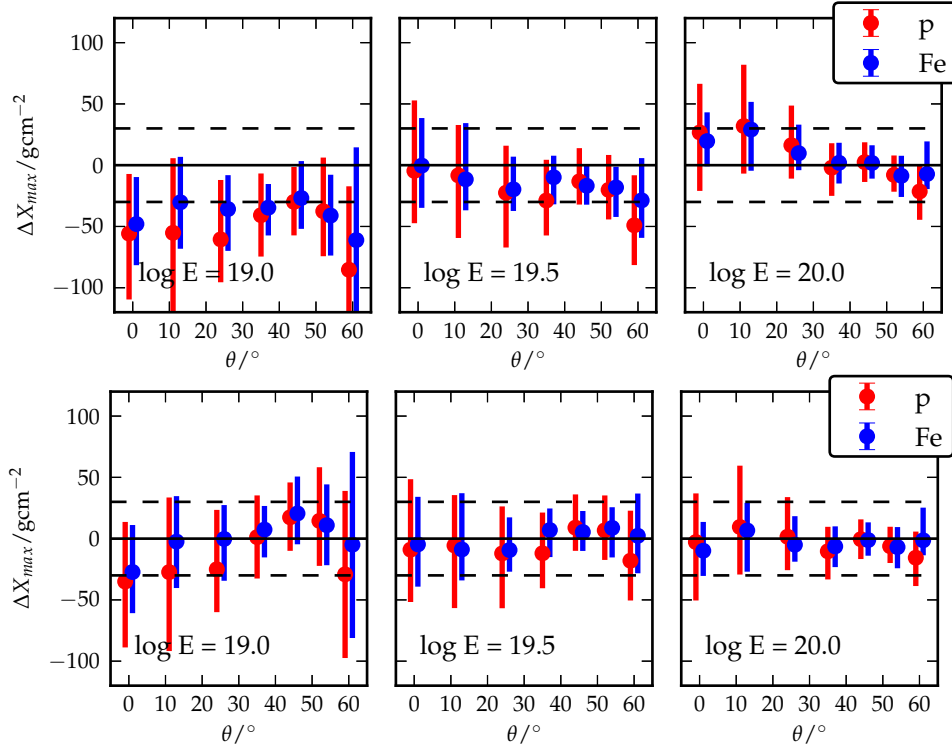
Figure A.28: Reconstructed X_{max} in simulated showers at fixed zenith angles before (top) and after bias correction (bottom). Note that the bias correction is derived from an independent set of showers, the continuous library.
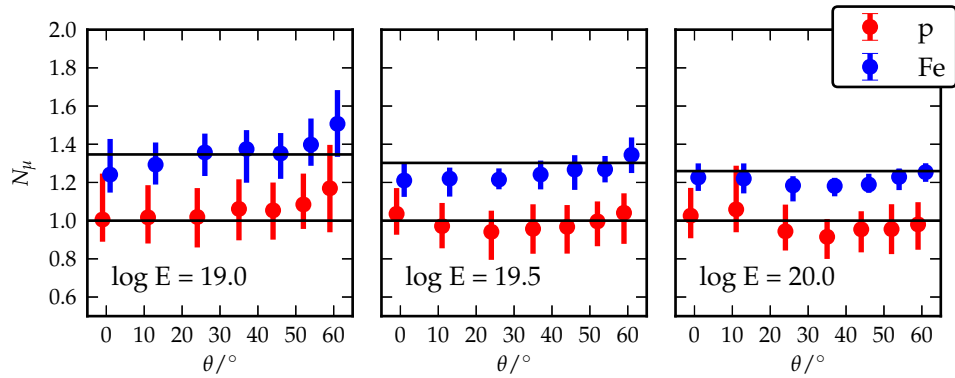
Figure A.29: Reconstructed N_μ in simulated showers at fixed zenith angles. The horizontal lines indicate the model expectation. The difference to the prediction is caused by the bias of the reconstruction.

Figure A.30: X_{max} bias (left) and N_μ for showers with intermediate mass. X_{max} is corrected for the reconstruction bias. Note that the bias correction is derived only from proton and iron simulations in the continuous library.

A.10 Depth of shower maximum reconstructed with the SD and the FD

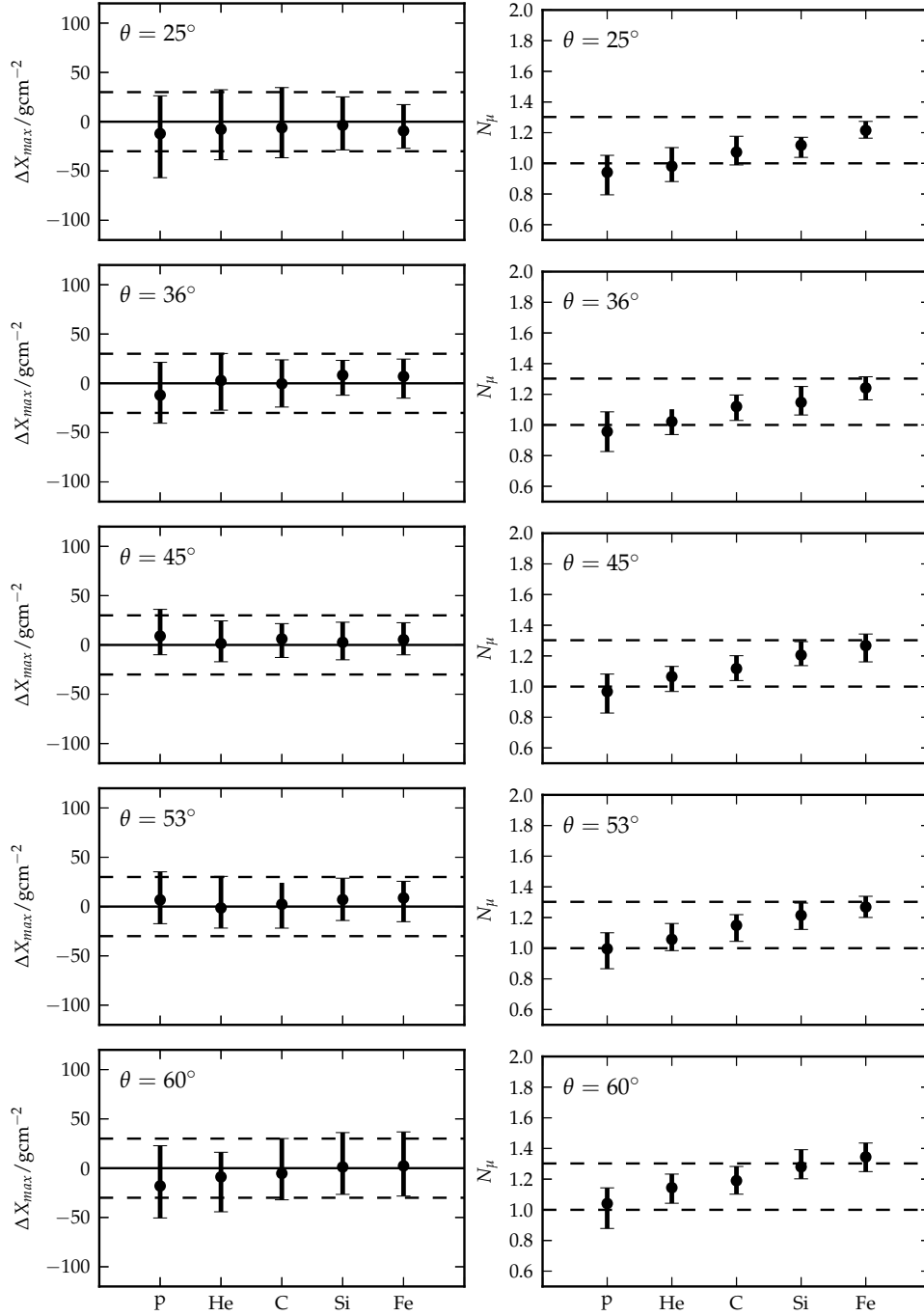| $log_{10}E$/eV	$\langle X_{max} \rangle$/gcm^{-2} $\pm$ stat. $\mp$ syst.	RMS(X$_{max}$)/gcm^{-2} $\pm$ stat. $\mp$ syst.	N
	SD v9r1, no saturation		
19.05	754.9 $\pm$1.2 -20.0 +20.0	37.2 $\pm$2.4	2026
19.15	756.2 $\pm$1.5 -20.0 +20.0	35.1 $\pm$3.1	1281
19.25	758.4 $\pm$1.7 -20.0 +20.0	32.4 $\pm$2.5	752
19.35	760.5 $\pm$2.0 -20.0 +20.0	33.9 $\pm$3.4	486
19.45	760.3 $\pm$2.4 -20.0 +20.0	30.3 $\pm$2.8	296
19.55	770.3 $\pm$4.0 -20.0 +20.0	35.2 $\pm$12.5	130
19.65	766.6 $\pm$3.9 -20.0 +20.0	18.6 $\pm$4.7	66
19.90	781.4 $\pm$4.2 -20.0 +20.0	0.0 $\pm$0.0	41
	SD v9r1, with saturation		
19.05	767.5 $\pm$3.1 -20.0 +20.0	69.0 $\pm$6.3	674
19.15	777.8 $\pm$3.4 -20.0 +20.0	63.7 $\pm$7.1	501
19.25	769.9 $\pm$3.4 -20.0 +20.0	59.0 $\pm$7.6	385
19.35	783.7 $\pm$3.3 -20.0 +20.0	44.8 $\pm$8.1	284
19.45	783.2 $\pm$3.4 -20.0 +20.0	32.6 $\pm$6.9	171
19.55	774.6 $\pm$3.4 -20.0 +20.0	27.3 $\pm$3.8	136
19.65	771.6 $\pm$4.7 -20.0 +20.0	21.2 $\pm$7.2	51
19.90	782.3 $\pm$3.6 -20.0 +20.0	11.0 $\pm$6.4	68
	FD ICRC11		
18.05	713.8 $\pm$1.6 -8.1 +10.0	55.4 $\pm$2.1 -5.5 +5.3	1407
18.15	722.0 $\pm$1.7 -8.1 +10.1	56.1 $\pm$2.2 -5.3 +5.2	1251
18.25	734.0 $\pm$1.9 -8.1 +10.2	56.9 $\pm$2.3 -5.2 +5.2	998
18.35	736.7 $\pm$2.1 -8.2 +10.3	54.1 $\pm$2.7 -5.2 +5.1	781
18.45	743.6 $\pm$2.4 -8.3 +10.5	55.1 $\pm$3.3 -5.1 +5.1	619
18.55	746.9 $\pm$2.7 -8.3 +10.6	53.5 $\pm$3.4 -5.1 +5.1	457
18.65	751.3 $\pm$3.0 -8.5 +10.8	51.3 $\pm$4.2 -5.1 +5.1	331
18.75	749.8 $\pm$3.2 -8.6 +11.0	44.6 $\pm$3.7 -5.1 +5.1	230
18.85	750.6 $\pm$3.6 -8.7 +11.2	45.4 $\pm$3.6 -5.1 +5.1	188
18.95	756.5 $\pm$3.6 -8.9 +11.3	38.7 $\pm$4.1 -5.1 +5.1	143
19.09	763.8 $\pm$3.3 -9.1 +11.6	40.9 $\pm$3.9 -5.1 +5.1	186
19.29	766.2 $\pm$3.8 -9.4 +12.0	34.9 $\pm$5.1 -5.2 +5.1	106
19.55	771.5 $\pm$4.7 -9.7 +12.5	27.0 $\pm$6.0 -5.4 +5.2	47

$log_{10}E/$eV	$\langle X_{max}\rangle/$gcm^{-2} $\pm$ stat. $\mp$ syst.	RMS(X_{max})/gcm^{-2} $\pm$ stat. $\mp$ syst.	N
	SD v9r3, no saturation		
19.05	747.2 $\pm$1.3 -20.0 +20.0	46.2 $\pm$2.6	2379
19.15	751.2 $\pm$1.4 -20.0 +20.0	37.7 $\pm$2.3	1565
19.25	751.4 $\pm$1.5 -20.0 +20.0	36.2 $\pm$3.2	970
19.35	755.4 $\pm$2.0 -20.0 +20.0	39.8 $\pm$4.7	569
19.45	757.7 $\pm$2.3 -20.0 +20.0	32.1 $\pm$2.7	326
19.55	760.9 $\pm$3.1 -20.0 +20.0	32.5 $\pm$9.2	195
19.65	764.6 $\pm$3.7 -20.0 +20.0	20.1 $\pm$4.7	77
19.90	774.1 $\pm$3.8 -20.0 +20.0	13.2 $\pm$5.7	62
	SD v9r3, with saturation		
19.05	742.7 $\pm$3.2 -20.0 +20.0	79.4 $\pm$5.3	756
19.15	754.8 $\pm$3.6 -20.0 +20.0	78.0 $\pm$6.3	590
19.25	759.3 $\pm$3.5 -20.0 +20.0	65.6 $\pm$7.5	440
19.35	765.1 $\pm$3.5 -20.0 +20.0	58.0 $\pm$8.0	349
19.45	768.4 $\pm$3.2 -20.0 +20.0	38.8 $\pm$5.7	223
19.55	769.0 $\pm$3.1 -20.0 +20.0	27.3 $\pm$2.9	156
19.65	765.6 $\pm$4.1 -20.0 +20.0	27.9 $\pm$4.1	84
19.90	774.8 $\pm$3.2 -20.0 +20.0	11.0 $\pm$5.8	85
	FD ICRC13 preliminary		
17.85	714.3 $\pm$1.5 -7.8 +9.9	55.8 $\pm$2.8 -6.4 +5.9	3667
17.95	723.3 $\pm$1.7 -7.8 +9.9	60.0 $\pm$3.1 -5.7 +5.5	3365
18.05	730.6 $\pm$1.6 -7.8 +10.0	62.9 $\pm$2.9 -5.4 +5.3	2859
18.15	740.5 $\pm$2.0 -7.8 +10.1	63.4 $\pm$3.4 -5.3 +5.2	2436
18.25	745.4 $\pm$1.9 -7.8 +10.2	66.6 $\pm$3.0 -5.2 +5.1	1984
18.35	752.0 $\pm$2.3 -7.9 +10.3	62.4 $\pm$3.9 -5.1 +5.1	1442
18.45	757.2 $\pm$2.5 -8.0 +10.4	58.6 $\pm$4.4 -5.1 +5.1	1150
18.55	757.3 $\pm$2.4 -8.1 +10.6	56.3 $\pm$3.6 -5.1 +5.1	832
18.65	759.2 $\pm$2.9 -8.2 +10.7	57.9 $\pm$4.5 -5.1 +5.1	591
18.75	758.1 $\pm$2.6 -8.3 +10.9	45.2 $\pm$3.3 -5.1 +5.1	431
18.85	761.7 $\pm$2.5 -8.5 +11.1	41.7 $\pm$3.0 -5.1 +5.1	324
18.95	769.1 $\pm$3.0 -8.6 +11.3	50.1 $\pm$3.5 -5.1 +5.1	246
19.05	763.7 $\pm$3.1 -8.8 +11.5	38.0 $\pm$4.0 -5.1 +5.1	174
19.15	768.6 $\pm$4.0 -8.9 +11.7	44.2 $\pm$4.9 -5.1 +5.1	129
19.25	775.9 $\pm$4.8 -9.1 +11.9	40.4 $\pm$6.3 -5.1 +5.1	96
19.34	777.3 $\pm$6.2 -9.2 +12.1	46.9 $\pm$7.0 -5.1 +5.0	64
19.45	783.2 $\pm$9.2 -9.3 +12.3	48.7 $\pm$12.0 -5.1 +5.0	44
19.62	774.1 $\pm$4.7 -9.6 +12.6	24.4 $\pm$5.5 -5.4 +5.2	38

Bibliography

[1] Cosmic rays from the knee to the highest energies, J. Blümer, R. Engel, J. Hörandel, Prog. Part. Nucl. Phys. 63 (2009) 293, http://www.sciencedirect.com/science/article/pii/S0146641009000362.

[2] Extensive air Showers and hadronic interactions at high energy, R. Engel, D. Heck, T. Pierog, Annu. Rev. Nucl. Part. S. 61 (2011) 467, http://www.annualreviews.org/doi/abs/10.1146/annurev.nucl.012809.104544.

[3] Observation of the Suppression of the Flux of Cosmic Rays above 4×10^{19} eV, J. Abraham et al., Phys. Rev. Lett. 101 (2008) 061101, http://link.aps.org/doi/10.1103/PhysRevLett.101.061101.

[4] Energy spectrum and mass composition of high-energy cosmic rays, A. Haungs, H. Rebel, M. Roth, Rep. Prog. Phys. 66 (2003) 1145, http://stacks.iop.org/0034-4885/66/i=7/a=202.

[5] A Heitler model of extensive air showers, J. Matthews, Astropart. Phys. 22 (2005) 387, https://www.sciencedirect.com/science/article/pii/S0927650504001598?np=y.

[6] Measurements of the cosmic ray composition with air shower experiments, K.-H. Kampert, M. Unger, Astropart. Phys. 35 (2012) 660, http://www.sciencedirect.com/science/article/pii/S0927650512000382.

[7] Interpretation of the signals produced by showers from cosmic rays of 10^{19} eV observed in the surface detectors of the Pierre Auger Observatory, J. Allen for the Pierre Auger Collaboration, Proc. 32nd ICRC (2011), http://arxiv.org/abs/1107.4804.

[8] A measurement of the muon number in showers using inclined events recorded at the Pierre Auger Observatory, I. Valiño for the Pierre Auger Collaboration, Proc. 33rd ICRC (2013), http://arxiv.org/abs/1307.5059v1.

[9] The muon content of hybrid events recorded at the Pierre Auger Observatory, G. Farrar for the Pierre Auger Collaboration, Proc. 33rd ICRC (2013), http://arxiv.org/abs/1307.5059v1.

[10] Measurement of the muon signal using the temporal and spectral structure of the signals in surface detectors of the Pierre Auger Observatory, B. Kegl for the Pierre Auger Collaboration, Proc. 33rd ICRC (2013), http://arxiv.org/abs/1307.5059v1.

[11] Non-linear amplification of a magnetic field driven by cosmic ray streaming, S. G. Lucek, A. R. Bell, Mon. Not. R. Astron. Soc. 314 (2000) 65, http://mnras.oxfordjournals.org/content/314/1/65.abstract.

[12] The Origin of Ultra-High-Energy Cosmic Rays, A. Hillas, Annu. Rev. Astron. Astr. 22 (1984) 425, http://www.annualreviews.org/doi/abs/10.1146/annurev.aa.22.090184.002233.

[13] Die Suche nach den Quellen der kosmischen Strahlung: Antworten versprechen die Luftschauerexperimente KASCADE und AUGER, H. Blümer, K. Kampert, Physik Journal 56 (2000) 39, http://dx.doi.org/10.1002/phbl.20000560311.

[14] Ultrahigh Energy Cosmic Rays without Greisen-Zatsepin-Kuzmin Cutoff, V. Berezinsky, M. Kachelrieß, A. Vilenkin, Phys. Rev. Lett. 79 (1997) 4302, http://link.aps.org/doi/10.1103/PhysRevLett.79.4302.

[15] Monopolonium, C. T. Hill, Nucl. Phys. B 224 (1983) 469, http://www.sciencedirect.com/science/article/pii/0550321383903863.

[16] An update on a search for ultra-high energy photons using the Pierre Auger Observatory, M. Settimo for the Pierre Auger Collaboration, Proc. 32nd ICRC (2011), http://arxiv.org/abs/1107.4805.

[17] Radio detection of air showers with the Auger Engineering Radio Array, K.-H. Kampert for the Pierre Auger Collaboration, Proc. 32nd ICRC (2011), http://arxiv.org/abs/1207.4823v1.

[18] Ultra-high energy neutrinos at the Pierre Auger Observatory, P. Pieroni for the Pierre Auger Collaboration, Proc. 33rd ICRC (2013), http://arxiv.org/abs/1307.5059v1.

[19] A new composition-sensitive parameter for ultra-high energy cosmic rays, G. Ros, Astropart. Phys. 35 (2011) 140, http://www.sciencedirect.com/science/article/pii/S0927650511001319.

[20] End to the Cosmic-Ray Spectrum?, K. Greisen, Phys. Rev. Lett. 16 (1966) 748, http://link.aps.org/doi/10.1103/PhysRevLett.16.748.

[21] Upper limit of the spectrum of cosmic rays, G. Zatsepin, V. Kuzmin, JETP Lett. 4 (1966) 78, http://www.jetpletters.ac.ru/ps/1624/article_24846.shtml.

[22] Extragalactic propagation of ultrahigh energy cosmic-rays, D. Allard, Astropart. Phys. 39–40 (2012) 33, http://www.sciencedirect.com/science/article/pii/S092765051100199X.

[23] The measurement of the cosmic ray spectrum above 3×10^{17} eV with the Pierre Auger Observatory, A. Schulz for the Pierre Auger Collaboration, Proc. 33rd ICRC (2013), http://arxiv.org/abs/1307.5059v1.

[24] Inferences about the mass composition of cosmic rays from data on the depth of maximum at the Auger Observatory, E.-J. Ahn for the Pierre Auger Collaboration, Proc. 33rd ICRC (2013), http://arxiv.org/abs/1307.5059v1.

[25] Measurements of the Longitudinal Development of Air Showers with the Pierre Auger Observatory, D. Garcia-Pinto for the Pierre Auger Collaboration, Proc. 32nd ICRC (2011), http://arxiv.org/abs/1107.4804.

[26] Measurement of Atmospheric Production Depths of muons with the Pierre Auger Observatory, D. Garcia-Gamez for the Pierre Auger Collaboration, Proc. 32nd ICRC (2011), http://arxiv.org/abs/1107.4804.

[27] Observations of the longitudinal development of extensive air showers with the surface detectors of the Pierre Auger Observatory, D. Garcia-Gamez for the Pierre Auger Collaboration, Proc. 33rd ICRC (2013), http://arxiv.org/abs/1307.5059v1.

[28] A catalogue of quasars and active nuclei: 12th edition, M.-P. Véron-Cetty, P. Véron, Astron. Astrophys. 455 (2006) 773, http://dx.doi.org/10.1051/0004-6361:20065177.

[29] Correlation of the highest-energy cosmic rays with nearby extragalactic objects, The Pierre Auger Collaboration, Science 318 (2007) 938, http://www.sciencemag.org/content/318/5852/938.abstract.

[30] Update on the correlation of the highest energy cosmic rays with nearby extragalactic matter, The Pierre Auger Collaboration, Astropart. Phys. 34 (2010) 314, http://www.sciencedirect.com/science/article/pii/S0927650510001696.

[31] Review of FD results and related sys. uncertainties, presentation at the Auger Collaboration Meeting, March 2013, M. Unger, https://indico.nucleares.unam.mx/contributionDisplay.py?contribId=129&confId=708.

[32] Measurement of the Depth of Maximum of Extensive Air Showers above 10^{18} eV, J. Abraham et al., Phys. Rev. Lett. 104 (2010) 091101, http://link.aps.org/doi/10.1103/PhysRevLett.104.091101.

[33] An update on the measurements of the depth of shower maximum made at the Pierre Auger Observatory, V. de Souza for the Pierre Auger Collaboration, Proc. 33rd ICRC (2013), http://arxiv.org/abs/1307.5059v1.

[34] Interpretation of the depths of maximum of extensive air showers measured by the Pierre Auger Observatory, The Pierre Auger Collaboration, J. Cosmol. Astropart. P. 2 (2013) 026, http://stacks.iop.org/1475-7516/2013/i=02/a=026.

[35] Inferences about the mass composition of cosmic rays from data on the depth of maximum at the Auger Observatory, E.-J. Ahn for the Pierre Auger Collaboration, Proc. 33rd ICRC (2013), http://arxiv.org/abs/1307.5059v1.

[36] Evidence for a Primary Cosmic-Ray Particle with Energy 10^{20} eV, J. Linsley, Phys. Rev. Lett. 10 (1963) 146, http://link.aps.org/doi/10.1103/PhysRevLett.10.146.

[37] Properties and performance of the prototype instrument for the Pierre Auger Observatory, J. Abraham et al., Nucl. Instrum. Meth. A 523 (2004) 50, http://www.sciencedirect.com/science/article/pii/S0168900203033497.

[38] Maps of the Pierre Auger Observatory, D. Veberič, `http://sabotin.ung.si/˜darko/auger-array/auger_array-pdf/auger_array-ad.pdf`.

[39] Data Summary Trees and Shower Visualization for Reconstructed Auger Events (GAP note 2006-081), I. Maris, F. Schuessler, R. Ulrich, M. Unger, `http://www.auger.org/admin/GAP_Notes/GAP2006/GAP2006_081.pdf`.

[40] The surface detector system of the Pierre Auger Observatory, I. Allekotte et al., Nucl. Instrum. Meth. A 586 (2008) 409, `http://www.sciencedirect.com/science/article/pii/S0168900207024680`.

[41] Single muon response: The signal model (GAP note 2010-110), R. Bardenet, B. Kégl, D. Veberič, `http://www.auger.org/admin/GAP_Notes/GAP2010/GAP2010_110.pdf`.

[42] Calibration of the surface array of the Pierre Auger Observatory, X. Bertou et al., Nucl. Instrum. Meth. A 568 (2006) 839, `http://www.sciencedirect.com/science/article/pii/S0168900206013593`.

[43] Trigger and aperture of the surface detector array of the Pierre Auger Observatory, The Pierre Auger Collaboration, Nucl. Instrum. Meth. A 613 (2010) 29, `http://www.sciencedirect.com/science/article/pii/S0168900209021688`.

[44] Top-down Selection of Events and Stations in Surface Detector Triggers (GAP note 2006-072), P. Billoir, `http://www.auger.org/admin/GAP_Notes/GAP2006/GAP2006_072.pdf`.

[45] Proposition to improve the local trigger of the Surface Detector for low energy showers (GAP note 2009-179), P. Billoir, `http://www.auger.org/admin/GAP_Notes/GAP2009/GAP2009_179.pdf`.

[46] New proposal to improve the local trigger of the Surface Detector (GAP note 2011-089), P. Billoir, `http://www.auger.org/admin/GAP_Notes/GAP2011/GAP2011_089.pdf`.

[47] SD Reconstruction - Offline Reference Manual (GAP note 2005-035), D. Veberič, M. Roth, `http://www.auger.org/admin/GAP_Notes/GAP2005/GAP2005_035.pdf`.

[48] On optimal Barycenter Estimation (GAP note 2007-035), M. Horvat, D. Veberič, `http://www.auger.org/admin/GAP_Notes/GAP2007/GAP2007_035.pdf`.

[49] Reconstruction accuracy of the surface detector array of the Pierre Auger Observatory, M. Ave for the Pierre Auger Collaboration, Proc. 30th ICRC (2007), `http://arxiv.org/abs/0709.2125v1.pdf`.

[50] On Shower-Front Start-Time Variance (GAP note 2007-057), M. Horvat, D. Veberič, `http://www.auger.org/admin/GAP_Notes/GAP2007/GAP2007_057.pdf`.

[51] The lateral and the angular structure functions of electron showers, J. Nishimura, K. Kamata, Prog. Theor. Phys. Supp. 6 (1958) 93, `http://ptp.ipap.jp/link?PTPS/6/93`.

[52] The extensive air showers, K. Greisen, Progress in Elementary Particle and Cosmic Ray Physics 3 (1956) 1.

[53] An update on the signal accuracy using the infill array (GAP note 2012-012), R. Hiller, M. Roth, `http://www.auger.org/admin/GAP_Notes/GAP2012/GAP2012_012.pdf`.

[54] Estimation of Signal in Saturated Stations of Pierre Auger Surface Detector, D. Veberič for the Pierre Auger Collaboration, Proc. 33rd ICRC (2013), http://arxiv.org/abs/1307.5059v1.

[55] Influence of the reconstructed core position on S(1000) for inclined showers (GAP note 2006-035), M. T. Dova, F. G. Monticelli, H. Wahlberg, http://www.auger.org/admin/GAP_Notes/GAP2006/GAP2006_035.pdf.

[56] Measurement of the Energy Spectrum of Cosmic Rays between 0.1 EeV and 30 EeV with the Infill Extension of the Surface Detector of the Pierre Auger Observatory, A. Schulz, http://www.auger.org/admin/GAP_Notes/GAP2012/GAP2012_136.pdf.

[57] Towards a parametrization of the photon LDF (GAP note 2012-130), G. Ros, A. Supanitsky, G. Medina-Tanco, L. del Peral, M. Rodriguez-Frias, http://www.auger.org/admin/GAP_Notes/GAP2012/GAP2012_130.pdf.

[58] Energy calibration of data recorded with the surface detectors of the Pierre Auger Observatory: an update, R. Pesce for the Pierre Auger Collaboration, Proc. 32nd ICRC (2011), http://arxiv.org/abs/1107.4809.

[59] The fluorescence detector of the Pierre Auger Observatory, The Pierre Auger Collaboration, Nucl. Instrum. Meth. A 620 (2010) 227, http://www.sciencedirect.com/science/article/pii/S0168900210008727.

[60] Reliability of the method of constant intensity cuts for reconstructing the average development of vertical showers, T. Gaisser, A. Hillas, Proc. 15th ICRC (1977), http://adsabs.harvard.edu/abs/1977ICRC....8..353G.

[61] Determination of the calorimetric energy in extensive air showers, H. Barbosa, F. Catalani, J. Chinellato, C. Dobrigkeit, Astropart. Phys. 22 (2004) 159, http://www.sciencedirect.com/science/article/pii/S0927650504001239.

[62] A new method for determining the primary energy from the calorimetric energy of showers observed in hybrid mode on a shower-by-shower basis, The Pierre Auger Collaboration, Proc. 31st ICRC (2011), http://arxiv.org/abs/1107.4804.

[63] Estimate of the non-calorimetric energy of showers observed with the fluorescence and surface detectors of the Pierre Auger Observatory, M. Tueros for the Pierre Auger Collaboration, Proc. 33rd ICRC (2013), http://arxiv.org/abs/1307.5059v1.

[64] The HEAT Telescopes of the Pierre Auger Observatory. Status and First Data, H.-J. Mathes for the Pierre Auger Collaboration, Proc. 32nd ICRC (2011), http://arxiv.org/abs/1107.4807.

[65] The AMIGA muon detectors of the Pierre Auger Observatory: overview and status, F. Suarez, Proc. 33rd ICRC (2013), http://arxiv.org/abs/1307.5059v1.

[66] Measuring the accuracy of the AMIGA muon counters at the Pierre Auger Observatory, S. Maldera, Proc. 33rd ICRC (2013), http://arxiv.org/abs/1307.5059v1.

[67] Radio detection of air showers with the Auger Engineering Radio Array, F. Schröder, Proc. 33rd ICRC (2013), http://arxiv.org/abs/1307.5059v1.

[68] Probing the radio emission from cosmic-ray-induced air showers by polarization measurements, T. Huege, Proc. 33rd ICRC (2013), `http://arxiv.org/abs/1307.5059v1`.

[69] Concepts of age and universality in cosmic ray showers, P. Lipari, Phys. Rev. D 79 (2009) 063001, `http://link.aps.org/doi/10.1103/PhysRevD.79.063001`.

[70] Universality of electron–positron distributions in extensive air showers, S. Lafebre, R. Engel, H. Falcke, J. Hörandel, T. Huege, J. Kuijpers, R. Ulrich, Astropart. Phys. 31 (2009) 243, `http://www.sciencedirect.com/science/article/pii/S0927650509000292`.

[71] Applying EAS universality to ground detector data, The Pierre Auger Collaboration, Proc. 30th ICRC (2007), `http://arxiv.org/abs/0706.1990`.

[72] Prediction of the tank response from shower universality (GAP note 2011-087), M. Ave, R. Engel, J. Gonzalez, D. Maurel, M. Roth, D. Heck, T. Pierog, `http://www.auger.org/admin/GAP_Notes/GAP2011/GAP2011_087.pdf`.

[73] Thoughts for a new year: the Universality - A new paradigm in Auger? (GAP note 2013-002), X. Bertou, `http://www.auger.org/admin/GAP_Notes/GAP2013/GAP2013_002.pdf`.

[74] CORSIKA: A Monte Carlo code to simulate extensive air showers. 1998, D. Heck, G. Schatz, T. Thouw, J. Knapp, J. Capdevielle, `http://www-ik.fzk.de/corsika/`.

[75] Quark-gluon-string model and EAS simulation problems at ultra-high energies, N. Kalmykov, S. Ostapchenko, A. Pavlov, Nucl. Phys. B - Proc. Sup. 52 (1997) 17, `http://www.sciencedirect.com/science/article/pii/S0920563296008468`.

[76] Parton ladder splitting and the rapidity dependence of transverse momentum spectra in deuteron-gold collisions at the BNL Relativistic Heavy Ion Collider, K. Werner, F.-M. Liu, T. Pierog, Phys. Rev. C 74 (2006) 044902, `http://link.aps.org/doi/10.1103/PhysRevC.74.044902`.

[77] The offline software framework of the Pierre Auger Observatory, S. Argirò et al., Nucl. Instrum. Meth. A 580 (2007) 1485, `http://www.sciencedirect.com/science/article/pii/S0168900207014106`.

[78] A sampling procedure to regenerate particles in a ground detector from a "thinned" air shower simulation output, P. Billoir, Astropart. Phys. 30 (2008) 270, `http://www.sciencedirect.com/science/article/pii/S0927650508001394`.

[79] Geant4 - a simulation toolkit, S. Agostinelli et al., Nucl. Instrum. Meth. A 506 (2003) 250, `http://www.sciencedirect.com/science/article/pii/S0168900203013688`.

[80] Prediction of the tank response from shower universality (GAP note 2011-086), M. Ave, R. Engel, J. Gonzalez, D. Maurel, M. Roth, `http://www.auger.org/admin/GAP_Notes/GAP2011/GAP2011_086.pdf`.

[81] Can EPOS Reproduce the Auger SD and Hybrid Data? (GAP note 2007-098), M. Ave, N. Busca, L. Cazon, F. Schmidt, T. Yamamoto, `http://www.auger.org/admin/GAP_Notes/GAP2007/GAP2007_098.pdf`.

[82] Study of statistical thinning with fully-simulated air showers at ultra-high energies, The Pierre Auger Collaboration, Proc. 31st ICRC (2011), `http://adsabs.harvard.edu/abs/2011ICRC....2...39B`.

[83] Extended shower universality: A model of the time-dependent signal in water Cerenkov tanks (GAP note 2013-022), D. Maurel, J. Gonzalez, M. Ave, M. Roth, `http://www.auger.org/admin/GAP_Notes/GAP2013/GAP2013_022.pdf`.

[84] Implementation of the time model described in [83], D. Maurel, `https://devel-ik.fzk.de/wsvn/users/maurel/universal-timemodel`.

[85] The Spread in the Arrival Times of Particles in Air-Showers for Photon and Anisotropy Searches above 10 EeV (GAP note 2008-160), C. Wileman, `http://www.auger.org/admin/GAP_Notes/GAP2008/GAP2008_160.pdf`.

[86] Composition Studies of Ultra High Energy Cosmic Rays using Data of the Pierre Auger Observatory (GAP note 2010-037), K. Mora, `http://www.auger.org/admin/GAP_Notes/GAP2010/GAP2010_037.pdf`.

[87] Time Asymmetry in UHE Cosmic Ray Showers. Mass Composition Studies in the Pierre Auger Observatory (GAP note 2010-054), D. Garcia-Pinto, `http://www.auger.org/admin/GAP_Notes/GAP2010/GAP2010_054.pdf`.

[88] ROOT: An object oriented data analysis framework, R. Brun, R. Rademakers, Nucl. Instrum. Meth. A 389 (1997) 81, `http://www.sciencedirect.com/science/article/pii/S016890029700048X`.

[89] Minuit2 minimization package, L. Moneta, F. James, `http://seal.web.cern.ch/seal/work-packages/mathlibs/minuit/doc/doc.html`.

[90] SWIG: An easy to use tool for integrating scripting languages with C and C++, D. Beazley et al., Proc. 4th USENIX Tcl/Tk workshop (1996), `http://static.usenix.org/publications/library/proceedings/tcl96/full_papers/beazley/`.

[91] Muon-track studies in a water Cherenkov detector, A. Etchegoyen et al., Nucl. Instrum. Meth. A 545 (2005) 602, `http://www.sciencedirect.com/science/article/pii/S016890020500759X`.

[92] Estimating the missing energy of Extensive Air Showers at the Pierre Auger Observatory (GAP note 2013-026), A. Mariazzi, M. Tueros, `http://www.auger.org/admin/GAP_Notes/GAP2013/GAP2013_026.pdf`.

[93] The nucleus-nucleus interaction, nuclear fragmentation, and fluctuations of extensive air showers, N. Kalmykov, S. Ostapchenko, Phys. Atom. Nucl. 52 (1997) 17, `http://www.sciencedirect.com/science/article/pii/S0920563296008468`.

[94] Quark-gluon-string model and EAS simulation problems at ultra-high energies, N. Kalmykov, S. Ostapchenko, A. Pavlov, Nucl. Phys. Proc. Suppl. 56 (1993) 346, `http://adsabs.harvard.edu/abs/1993PAN....56..346K`.

[95] On the measurement of the proton-air cross section using air shower data, R. Ulrich, J. Blümer, R. Engel, F. Schüssler, M. Unger, New J. Phys. 11 (2009) 065018, `http://stacks.iop.org/1367-2630/11/i=6/a=065018`.

[96] Measurement of the Depth of Shower Maximum of Cosmic Rays above 1 EeV (GAP note 2009-078), E.-J. Ahn, J. Bellido, S. BenZvi, R. Engel, F. Schüssler, R. Ulrich, M. Unger, `http://www.auger.org/admin/GAP_Notes/GAP2009/GAP2009_078.pdf`.

[97] G. Cowan, *Statistical data analysis*, Oxford Science Publications (1998).

[98] Measurement of the time synchronization between the SD and the FD (GAP note 2005-085), J. Bellido, http://www.auger.org/admin/GAP_Notes/GAP2005/GAP2005_085.pdf.

[99] Measurements of SD-FD Time Offset Using Inclined Laser Shots (GAP note 2006-005), P. Younk, J. Chirinos Diaz, B. Fick, L. Wiencke, http://www.auger.org/admin/GAP_Notes/GAP2006/GAP2006_005.pdf.

[100] Universality, presentation at the Auger Collaboration Meeting, March 2013, X. Bertou, https://indico.nucleares.unam.mx/contributionDisplay.py?contribId=80&confId=708.

[101] Ground signal parameterization for water Cherenkov and scintillator detectors and performance of ground arrays that combine both techniques (GAP note 2012-141), M. Ave, http://www.auger.org/admin/GAP_Notes/GAP2012/GAP2012_141.pdf.

[102] private communication, X. Bertou (2013).

[103] Proposal for an update of the Auger Energy Scale (GAP note 2012-124), B. Dawson, C. Di Giulio, A. Mariazzi, R. Pesce, G. Fernandez, G. Salina, M. Tueros, J. Vazquez, V. Verzi, http://www.auger.org/admin/GAP_Notes/GAP2012/GAP2012_124.pdf.

[104] The Energy Scale of the Pierre Auger Observatory, V. Verzi, Proc. 33rd ICRC (2013), http://arxiv.org/abs/1307.5059v1.

[105] The distribution of shower maxima of UHECR air showers, P. Facal for the Pierre Auger Collaboration, Proc. 32nd ICRC (2011), http://arxiv.org/abs/1107.4804.

[106] Nucleus-nucleus collisions and interpretation of cosmic-ray cascades, J. Engel, T. Gaisser, P. Lipari, T. Stanev, Phys. Rev. D 46 (1992) 5013, http://link.aps.org/doi/10.1103/PhysRevD.46.5013.

[107] Korrelation der Ankunftsrichtungsverteilung hochenergetischer kosmischer Teilchen mit Aktiven Galaktischen Kernen, Bachelorarbeit, I. Glasner (2013).

[108] Bremsstrahlung and pair production in condensed media at high-energies, A. Migdal, Phys. Rev. D. 103 (1956) 1811.

[109] Limits of applicability of the theory of bremsstrahlung electrons and pair production at high-energies, L. Landau, I. Pomeranchuk, Dokl. Akad. Nauk SSSR 92 (1953) 535.

[110] Search for ultra-high energy photons based on air shower universality, Diplomarbeit, C. Meynen (2013).

[111] Dependence of the longitudinal shower profile on the characteristics of hadronic multiparticle production, T. Pierog et al., Proc. 29th ICRC (2005), http://icrc2005.tifr.res.in/htm/Vol-Web/Vol-17/17103-ger-engel-R-abs2-he14-oral.pdf.

[112] Matplotlib: A 2D graphics environment, J. Hunter et al., Comput. Sci. Eng. 9 (2007) 90, http://dx.doi.org/10.1109/MCSE.2007.55.

[113] SciPy: Open source scientific tools for Python, E. Jones, T. Oliphant, P. Peterson et al., http://www.scipy.org.

[114] Scikit-learn: Machine Learning in Python, F. Pedregosa et al., J. Mach. Learn. Res. 12 (2011) 2825, http://arxiv.org/abs/1201.0490.

[115] private communication, A. Schulz (2013).